Neutron Background Simulation for the CRESST – II Experiment

Dissertation

der Mathematisch-Naturwissenschaftlichen Fakultät
der Eberhard Karls Universität Tübingen
zur Erlangung des Grades eines
Doktors der Naturwissenschaften
(Dr. rer. nat.)

vorgelegt von
Stephan Michael Scholl
aus Paderborn

Tübingen
2011

Tag der mündlichen Qualifikation: 22.06.2011

Dekan:	Prof.Dr. Wolfgang Rosenstiel
1. Berichterstatter:	Prof.Dr. Josef Jochum
2. Berichterstatter:	Prof.Dr. Heinz Clement

Ich versichere an Eides statt, dass ich diese Arbeit ohne unerlaubte Hilfe und nur mit den angegebenen Hilfsmitteln angefertigt habe. Desweiteren habe ich bis jetzt noch keinen Promotionsversuch unternommen.

Tübingen, den 25. Mai 2011 .....

(Stephan Scholl)

Contents

List of Figures

List of Tables

Acknowledgments

The author acknowledges the support of the ILIAS, EUROGRAD and the SFB Transregio 27 programmes.

Zusammenfassung

In dieser Arbeit wird die Simulation des durch Neutronen induzierten Untergrunds für das **CRESST** – II Experiment zum direkten Nachweis *dunkler Materie* behandelt. Der von Neutronen induzierte Untergrund stellt einen fundamentalen, irreduziblen Untergrund für alle Experimente dar, die *Dunkle Materie* über die Messung der Rückstoßenergie eines streuenden Kerns nachweisen wollen. In dieser Arbeit geht es insbesondere um die Fragestellung, ob die vom CRESST – II Experiment beobachteten Ereignisse durch Neutronenstreuung erklärbar sind.

Die astrophysikalische Motivation zur Suche nach *dunkeler Materie* ist in dem heutigen kosmologische Standardmodell gegeben. In diesem mit ΛCDM bezeichneten Standardmodell der Kosmologie ergeben sich aus physikalischen Beobachtungen drei weitreichende Schlussfolgerungen:

- Erstens ist die Geometrie des Universums global *flach*.
- Zweitens liegen etwa 24 Prozent der Gesamtenergiedichte des Universums in der Form von kalter, nichtrelativistischer Materie vor; davon nur ein Sechstel in der Form von Hadronen, der Rest muss von einer unbekannten Form nichtbaryonischer, elektrisch neutraler *dunkler Materie* (**C**old **D**ark **M**atter) vorliegen.
- Drittens ergibt sich im kosmologischen Standardmodell eine *beschleunigte* Expansion des Universums, die hierfür verantwortliche *dunkle Energie* umfasst 76 Prozent der gesamten Energiedichte des Universums. In der einfachsten Form kann die dunkle Energie durch die kosmologische Konstante **Λ** in der Einsteingleichung der allgemeinen Relativitätstheorie beschrieben werden.

Die Natur und Physik der *dunkle Energie* ist nach wie vor rätselhaft und ist womöglich ein Artefakt vereinfachender Annahmen in der Herleitung der Evolutionsgleichungen des Universums. Für die Existenz der *dunklen Materie* spricht aber eine Vielzahl unabhängiger astronomischer Beobachtungen:

- Die beobachteten Rotationsgeschwindigkeiten von Galaxien und Galaxienhaufen sind nur dann erklärbar, wenn der überwiegende Teil ihrer Massen durch nicht – hadronische *dunkle Materie* gestellt wird.
- Die durch *Mikrolensing* beobachtbare Massen – Verteilung und die durch Beobachtung des intergalaktischen Gases im Röntgenbereich von Galaxienhaufen stimmen nicht überein. Somit kann der Effekt der *dunklen Materie* nicht durch die Modifikation der Gravitationkraft auf galaktischen Entfernungsskalen erklärt werden.

Die Teilchen der *dunkle Materie* müssen die richtige *Reliktdichte* im heutigen Universum aufweisen, woraus sich Bedingungen an die Masse und den Selbstannihilations – Wirkungsquerschnitt während der *Freeze Out* Phase im frühen Universum ableiten lassen. Die Nichtbeobachtbarkeit elektromagnetischer und starken Wechselwirkung verlangen, daß die *dunkle Materie* nur schwach wechselwirken darf. Desweiteren muß die *dunkele Materie kalt* sein, denn Teilchen mit relativistischen Energien sind mit der beobachteten Strukturbildung im Universum nicht vereinbar. Diese Bedingung schliesst den einzigen Kandidat des Standardmodels , das Neutrino, aus. Somit sind die Teilchen der *dunkle Materie* in Theorien jenseits des Standardmodells der Teilchenphysik zu suchen. Sowohl supersymmetrische Modelle als auch Theorien mit zusätzlichen Dimensionen erlauben stabile Teilchen mit Massen zwischen 50 GeV und einigen TeV, diese als WIMPs (**W**eakly **I**nteracting **M**assive **P**article) bezeichneten Teilchen sind grundsätzlich auch experimentell beobachtbar. Desweiteren stellen Axionen einen möglichen Kandidaten für die *dunkele Materie* dar.

Für den experimentellen Nachweis eines solchen Teilchens ergeben sich drei Herangehensweisen:

- Die direkte Erzeugung von Teilchen jenseits des Standardmodells im Large Hadron Collider am CERN. Das Problem besteht dann in dem Nachweis der Stabilität des gefundenen Teilchens und der Identität des gefundenen Teilchens mit der *dunklen Materie* im Universum.
- Der indirekte Nachweis der *dunklen Materie* durch astronomische Messungen der entstehenden Strahlung und Zerfallsprodukte. Die Schwierigkeit in diesem Ansatz ist die exakte Berechnung des galaktischen Strahlungshintergrundes und der Ausschluss anderer astrophysikalischer Quellen, sowie die Frage ob hinreichend hohe Konzentrationen *dunkler Materie* sich in gut beobachtbarer Position befinden.
- Der direkte Nachweis *dunkler Materie* mit Detektoren im Labor. Die Schwierigkeit ergibt sich aus der erforderlichen Sensitivität des Detektors und der grundsätzlichen Frage, ob die lokale Dichte der *dunklen Materie* ausreichend ist um den Nachweis zu ermöglichen. Zur Erhöhung der Sensitivität ist eine weitestgehende Unterdrückung des Signaluntergrunds erforderlich; der auftretende Untergrund muss im Detail verstanden sein, um ein mögliches Signal zu erkennen.

Das CRESST – II Experiment versucht den direkten Nachweis der schwache Wechselwirkung der WIMPs durch die Detektion des gestreuten Kerns. Das Experiment zeichnet sich durch eine hervorragende Diskriminierung des elektromagnetischen Untergrunds von Kernrückstössen aus. Ein nichtdiskriminierbarer Untergrund ist durch neutroneninduzierte Kernrückstösse gegeben.

Die Analyse der Wechselwirkung der Neutronen mit dem Aufbau des Experimentes und insbesondere die Energiedeposition in den verwendeten Detektoren erfordert den Einsatz von Monte – Carlo Simulationen. Hierbei wird das in der Teilchenpysik weit verbreitete GEANT4 Programmpaket verwendet.

Die Implementierung der Neutronenstreuung innerhalb von GEANT4 wird getestet und die notwendige Verbesserung des Programmcodes für die inelastische Neutronenstreuung in GEANT4 vorgestellt. Der getestete und verbesserte Code wird dann zur Simulation der bekannten Neutronenquellen für den CRESST – II Aufbau verwendet:

- Neutronen, die im Umgebungsgestein des Aufbaus erzeugt werden.
- Neutronen, die durch Verunreingungen von Uran und Thorium durch (α, n) Kernreaktionen und spontane Spaltungen erzeugt im Polyethylenschild werden.
- Neutronen, die durch Spontanspaltung von Uran und Thorium im Bleischild erzeugt werden.
- Neutronen, die durch (α, n) Reaktionen und Spontanspaltungen aufgrund der Verunreingung des Kupferschildes durch Uran und Thorium produziert werden.
- Hochenergetische kosmogene Neutronen, welche durch Muonen der Höhenstrahlung erzeugt werden. Die Simulation erfolgt hierbei von einem resultierenden Neutronenspektrum welches die Startbedingungen der Neutronen beschreibt.

Die in den Simulationen ermittelte Untergrundsrate an Kernrückstössen im Intervall von 10 bis 40 keV von 6.33×10^{-3} cts $\mathrm{kg}^{-1}\mathrm{d}^{-1}$ erreicht nur etwa ein Zwölftels des experimentell beobachteten Untergrundes. Da die Simulation des Experimentes ohne Polyethylenabschirmung mit dem gemessenen Untergrund gut übereinstimmt, ist die Diskrepanz nicht durch eine fehlerhafte Implementierung der Neutronenphysik innerhalb der Simulation zu erklären. Allerdings ist der den Untergrund dominierende kosmogene Neutronenfluss mit einer grossen Unsicherheit behaftet, daß sich der induzierte Untergrund leicht um einen Faktor drei erhöhen lässt. Selbst wenn die Divergenz von experimenteller und simulierter Untergrundrate ignoriert wird, unterscheiden sich Experiment und Simulation in einem weiteren Punkt:

Das Verhältnis von Ereignissen mit nur einem Detektortreffer zu Ereignissen mit mehreren Detektortreffern ist in den Simulationen grösser als im Experiment.

Hierzu wird ebenfalls eine Vergleichssimulation des für die in Run 32 durchgeführte Neutronenkalibration mit einer Am – Be Neutronenquelle durchgeführt. Dabei ergibt unter Annahme von Effizienz und Totzeitkorrekturen eine Übereinstimmung der beobachteten koinzidenten Streuungen in mehreren Detektormodulen in Kalibration und Simulation.

Aufgrund der doppelten Diskrepanz des von der Simulation vorgesagten Untergrunds und der fehlenden Doppeldetektortreffern lässt sich folgern, daß es unwahrscheinlich ist, daß der beobachtete Untergrund in Run 32 des CRESST – II Experimentes von Neutronen verursacht wird.

Abstract

This thesis presents the simulation of the neutron induced background for the CRESST – II experiment. This kind of background is of particular interest as the induced nuclear recoil can not be distigushed from a recoil due to the interaction of a weakly interacting massive particle (WIMP) and a nucleus. With regard to the CRESST – II experiment, the main question is if the observed background of run 32 can be explained by neutron sources.

Today's cosmological standard model, (ΛCDM) demands the existence of non – baryonic, non – relativistic *Dark Matter*. The three cornerstones of ΛCDM are:

- The Universe is globally flat, this implies that the energy density of the Universe is equal to a critical energy density.
- About 20 percent of the total energy density of the Universe Ω_{total} is given by a form of *cold*, non – baryonic *Dark Matter* (CDM) which interacts only weakly.
- The expansion of the Universe is accelerating which is the result of the effect of the *Dark Energy* which contributes 76 percent of the total energy density of the Universe. The most simple form of the *Dark Energy* is given by a cosmological constant Λ in Einstein's Equation.

The nature and the interactions of the *Dark Energy* are still mysterious and maybe an artifact of the simplistic *Ansatz* used in the derivation of Friedman's Equations. On the other hand, the existence of the *Dark Matter* is supported by many astronomical observations, among them are:

- The rotational velocities of galaxies and galaxy clusters demand that the major contribution to the mass is made up by *Dark Matter*.
- The observation of mergers of galaxy clusters show that the mass distribution and the distribution of the intergalactic gas do not match. Modifications to gravity (MOND) cannot explain such an effect whereas *Dark Matter* can.

Constraints on the annihilation – cross – section and the mass of the *Dark Matter* particles during the *freeze out* phase in the early Universe can be formulated as they have to match the correct *relict density* today. Non – observation of exotic matter rule out electro – magnetic and strong interactions of those particles. Structure formation prohibits that the *Dark Matter* particles are too energetic, they must propagate non – relativistically. This constraint rules out only candidate in the standard model of particle physics, the neutrino. Thus the search for *Dark Matter* is the search for physics beyond the standard model. Supersymmetric (SUSY) extensions of the standard model and theories with extra dimensions offer stable particles in the mass range of 50 GeV to a few TeV which are dubbed WIMPs which are generally experimentally accessible. Another well motivated candidate is the axion, a particle invented to solve the strong CP problem with masses in the sub eV range.

Three methods for the experimental detection of *Dark Matter* particles are viable:

- Production of particles beyond the standard model at the LHC may be possible. The difficulty in this approach is the proof of the stability of the particle found and if it is identical to the *Dark Matter* observed astronomically.
- Indirect detection of *Dark Matter* via the detection of its decay products. The challenge in this approach is the exact knowledge of the galactic radiation background and the fundamental question if *Dark Matter* concentrations capable of producing a detectable signal are around.
- Direct detection of *Dark Matter* in the laboratory. The key issues in this approach are the required sensitivity of the used detectors, the suppression and analysis of signal background and the open question if the local density of *Dark Matter* is sufficient to yield a measurable signal.

The CRESST – II experiment is an direct detection experiment looking for a nuclear recoil induced by the weak interaction of a WIMP on a scintillating $CaWO_4$ crystal. While charged background can be discriminated, a non discriminable background due to nuclear recoils due to neutron scattering remains.

The analysis of the interaction of the neutrons with the experimental setup and in particular the deposited energy in the detector modules requires the usage of Monte – Carlo simulations. In this work, the GEANT4 monte – carlo framework is used. The implementation of the neutron physics in the GEANT4 package is tested and a necessary correction of the inelastic neutron scattering is presented.

The validated and enhanced code is then used for the simulation of the following neutron sources using the CRESST – II setup:

- Neutrons produced in the ambient rock and concrete around the experiment.
- Neutrons produced via (α, n) and spontaneous fission (s.f.) reactions of U and Th contaminations in the polyethylene (PE) of the neutron shielding.
- S.f. neutrons produced by contaminations in the lead shielding.
- S.f. and (α, n) neutrons from contaminations of the copper shielding.
- High energetic cosmogenic neutrons produced by cosmogenic muons. The primary particles in the simulation are the neutrons.

For a setup of ten operational detectors a background of nuclear recoils of 6.33×10^{-3} cts kg^{-1}d^{-1} is found in the energetic region of interest between 10 – 40 keV, which is only one twelfth of the experimentally observed rate of events.

Since the simulation of the unshielded experimental setup is in good agreement with the experimental result, an error in the implementation of the neutron physics can be excluded. It is more probable that the uncertainty of dominating background contribution given by the cosmogenic neutron flux may reduce the discrepancy to a factor of four. There is another independent observable which can be checked, however:

The distribution of single detector hit events to double detector hit events observed in the experiment does not match the one predicted by the simulations.

On the other hand, the simulation of the neutron calibration of run 32 of the CRESST – II experiment yields a double detector event rate in agreement with the experimental one observed for the neutron calibration.

The combination of the results on background rate in the nuclear recoil band and on the double detector hit events allow the conclusion to be drawn, that it is highly unlikely that the observed background of run 32 is induced by neutrons.

Chapter 1

Cosmology

In this chapter, the basic ingredients needed for a cosmological model are presented. These ingredients are the theory of general relativity, which relates the geometry of space – time to the energy content of the Universe and the standard model of particle physics which describes the nature of the known particle content of the Universe.

In the light of the modern astronomical observations of the cosmic microwave background and its anisotropies and the redshift – luminosity measurements of distant supernovae, it is clear that two unknown forms of energy must exist that the cosmological model fits the observed data.

The enigmatic *Dark Energy* is needed in the standard cosmological model to drive the expansion of the Universe as the redshift – luminosity measurements of supernovae indicate an accelerated expansion of the Universe. The existence of non – baryonic *Dark Matter* is inferred from the anisotropies seen in the cosmic microwave background, but independent observations of galaxy clusters and single galaxies also indicate a surplus of non – luminous mass in these objects.

From the point of particle physics, well motivated ideas of particle physics beyond the Standard Model which present viable candidates for *Dark Matter* exist, i.e. supersymmetry, extra dimensions and axions.

1.1 Introduction

As soon as man looked into the night sky, he wondered about the nature and the laws governing the stars and their motion. In this light, astronomy and cosmology became the oldest sciences pursued by mankind. In our modern era, astronomy and cosmology are completely embedded into the framework of physics. The experimental science of astronomy refined its methods and techniques which allowed the ever improving exploration of the Universe. Since the invention of the telescopes, astronomers were able to investigate the Universe to ever increasing ranges. The observation of the motion of the planets reached such a accuracy, that Newton was able to formulate his law of gravity. In turn

the application of the law of gravity on Jupiter and Saturn eventually led to the discovery of Uranus, Neptune and ultimately Pluto. The fix stars were identified as distant suns. Far away galaxies were identified as vast islands of stars drifting in the void of the Universe. The last century saw the advent of several new messengers observable by astronomers, apart from the visible light, observations throughout the electromagnetic spectrum became possible. Also high energetic particles known as cosmic rays widened the window through which we can observe the Universe.

In the past century, with the advent of Einstein's theory of general relativity and quantum mechanics as the foundation of particle physics, cosmology lost its former speculative character and calculations and predictions based on the two theories became possible. However, as the observational methods and techniques improved, it became evident that not everything was understood. In 1923, Edwin Hubble observed Cepheid variable stars within the Andromeda nebula M31. This discovery allowed him to estimate its distance and size, clearly showing that spiral nebula are galaxies like our own, rather than objects within our own galaxy. He also formulated the famous Hubble law in 1929, stating that the redshift of an astronomical object is linearly proportional to its distance[Hu29]. The discovery of the expanding Universe however was made two years earlier in 1927 by Georges Lemaître [Le27] based on the discovery of the redshift by Milton Humanson and the spatial distribution of the galaxies.

From the 1930s on, the deviation of the orbital motion of single galaxies in galaxy clusters from Kepler's law observed by Fritz Zwicky first in the Coma Cluster was a puzzle in the light of the known cosmology and particle physics. His conclusion that a vast amount of non – luminous, *dark* , matter dominates the dynamics of galaxy clusters, received little attention in the following years. In 1959, Louise Volders demonstrated by observations of the Doppler shift of the 21 cm radio line that the spiral galaxy M31 does not spin as expected from Keplerian Dynamics. From the 1960s on, Vera Rubin confirmed the non – Keplerian profile of rotation velocities for a huge number of other galaxies using optical spectroscopy, giving further support for Zwicky's hypothesis. These observations revived the interest in the topic of *Dark Matter*.

With the discovery of an isotropic cosmic microwave background (CMB) in 1965, the Horizon problem became evident: As the particle horizon at the time of last scattering now has shrank to an area about 1.6° in the visible background today, no physical influence could have smoothed out initial inhomogeneities in either a matter – or radiation – dominated Universe and thus bringing points separated by more than a few degrees at the time of last scattering to the same temperature. This contradicts the observation of a nearly perfect isotropy of the CMB at large angular scales.

In the past quarter century, our view of the Universe experienced further dramatic changes. In the beginning of the 1980s the proposal of the theory of inflation offered a solution to the Horizon problem among some other outstanding cosmological puzzles, and provided a mechanism for the origin of large – scale structure, which could be tested by the observation of anisotropies in the cosmic microwave background. With the beginning of the 1990s the launch of

the Cosmic Microwave Background Explore (CoBE) satellite measured the temperature of the cosmic microwave background to three decimal places, confirmed its thermal nature and found the long sought anisotropies. The Wilkinson Microwave Anisotropy Probe (WMAP) and several other experiments showed that these anisotropies are in accordance of with the inflationary theory. The multipole spectrum of the observed anisotropies demanded the existence of an new type of matter, non – baryonic and non – luminous, i.e. *Dark Matter*. In the late 1990s, the measurement of the luminosity – distance relation of Type Ia supernovae led to the discovery that the expansion of the Universe is accelerating, implying that most of the energy in the Universe is some exotic *Dark Energy*, characterized by its negative pressure – density ratio. This was confirmed by analysis of the microwave background anisotropies, and by massive surveys of galaxies like the Sloan Digital Sky Survey (SDSS). Both observations combined provided increasingly accurate values for cosmological parameters.

Meanwhile the progress of the classical instruments and methods used in astronomy steadily improved independent constraints on the same cosmological parameters. The spectroscopic discovery of thorium and uranium in the atmosphere of old stars, in combination with refined studies of the turn-off point from the stellar main sequence in globular clusters, narrowed estimates of the age of the Universe. The measurement of the deuterium to hydrogen ratio in interstellar absorption together with calculations of the cosmological nucleosynthesis has given a good value for the cosmological density of ordinary baryonic matter and established that its energy density is only a fifth of the mysterious non – baryonic dark matter. Countless observations with the Hubble space telescope and ever improving ground based telescopes have yield increasingly precise values for the Hubble constant.

1.2 Standard cosmology

In this section the fundamental theoretical building blocks of the standard cosmology of today are presented. Contemporary standard model of cosmology is given by the *Big Bang* scenario, which describes the Universe as a system evolving from a extremely compressed state existing around 10^{10} years ago. The oldest structure observed by astronomers today is the cosmic microwave background, which formed when the decreasing temperature of the Universe allowed the combination of electrons and protons into neutral hydrogen atoms, rendering the Universe transparent for electromagnetic radiation.

Six fundamental ingredients are necessary for the formulation of the cosmological model:

- Einstein equations, which relate the geometry of the Universe with its matter and energy content.
- A metric, which mirror the space – time symmetries of the Universe.
- Equation of state, governing the physical properties of the matter and energy content.
- Inflation, a mechanism which realizes the *Cosmological Principle*, i.e. ensures the homogeneity and isotropy of the observed Universe.
- The Standard Model of particle physics, which is important for the early formation of the Universe as it describes the available particles and their properties.
- Big Bang Nucleosynthesis, the nuclear physics which explain the amount of primordial elements found in the Universe.

1.2.1 General Relativity, a Metric and the Equation of State

The Einstein equation of gravity can be derived from first principles, under the following assumptions:

- Invariance under general coordinate transformations.
- The weak field limit is given by Newton's law of gravity.
- The equation is of second differential order and linear in second derivatives.

The resulting equation is then given by

$$R_{\mu\nu} - \frac{1}{2} g_{\mu\nu} = -\frac{8\pi G_N}{c^4} T_{\mu\nu} + \Lambda g_{\mu\nu}. \tag{1.1}$$

In this equation, $R_{\mu\nu}$ and R are the Ricci tensor and scalar, $g_{\mu\nu}$ is the metric tensor, G_N is Newton's constant, $T_{\mu\nu}$ is the energy – momentum tensor and Λ is the cosmological constant.

If the cosmological constant is ignored for a moment, the meaning of the equation is rather simple; the geometry of the Universe, given by the left hand side of the equation, is dictated by its energy content, found on right hand side. The cosmological constant represents a *vacuum energy* of the space – time itself instead of the matter content. While Einstein's equation looks rather innocent and its meaning is straightforward, unconstrained calculations are not achievable generally. Thus space – time symmetries must be adopted to cope with the equations mathematically.

The observation of the near exact isotropy of the cosmic microwave background together with the assumption that our spatial position is not special – the *Copernican* or *Cosmological* principle – leads to the conclusion that to a reliable degree of approximation, we live in a globally homogeneous and isotropic Universe which can be characterized by a Friedmann – Lemaître – Robertson – Walker (FLRW) geometry. The properties of homogeneity and isotropy imply that this specific metric, is given by:

$$ds^2 = -c^2dt^2 + a(t)^2\left(\frac{dr^2}{1-kr^2} + r^2d\Omega^2\right). \tag{1.2}$$

In this equation of the FLRW metric, $a(t)$ is the *scale factor* governing the evolution of the Universe and the constant k describes the spatial curvature of the Universe with the three possible choices $k = -1, 0, +1$. For $k = 0$, the spatial part of the Robertson – Walker metric reduces to the metric of ordinary Euclidean space.

Einstein's equation can be solved analytically in the FLRW metric, leading to the Friedman – Lemaître equations:

$$H^2 = \left(\frac{\dot{a}}{a}\right)^2 = \frac{8\pi G_N}{3}\rho - \frac{k}{a^2} + \frac{\Lambda}{3}, \tag{1.3}$$

$$\frac{\ddot{a}}{a} = \frac{\Lambda}{3} - \frac{4\pi G_N}{3}\left(\rho + 3p\right), \tag{1.4}$$

where ρ_{tot} is the total average matter density of the Universe, p is the isotropic pressure and H is the Hubble parameter.

In addition to the Hubble parameter, several other useful cosmological parameters can be defined. The critical density can be derived from Eq. 1.3 such that the curvature of the Universe is flat, $k = 0$, under the assumption that the cosmological constant Λ vanishes:

$$\rho_{crit} = \frac{3H^2}{8\pi G_N}. \tag{1.5}$$

A useful quantity replacing the scale factor $a(t)$ is the redshift z, which is astronomically observable by the shift of spectral lines. The connection between the measurable redshift of a past epoch z and the not directly measurable scale parameters $a(t_1)$ (the scale factor at the past moment t_1) and $a(t_0)$ (todays

scale factor) is given by the equation below:

$$1 + z = \frac{a\,(t_0)}{a\,(t_1)}. \tag{1.6}$$

It also convenient to express the abundance of a substance Ω in the Universe in units of ρ_{crit}. This leads to the definition:

$$\Omega = \sum_i \Omega_i \equiv \sum_i \frac{\rho_i}{\rho_{crit}}. \tag{1.7}$$

As the equation of state for the various species in the Universe differs, the Friedmann equation can be cast in the following form:

$$\frac{H^2(z)}{H_0^2} = \Omega_X\,(1+z)^{3(1+\alpha_X)} + \Omega_K\,(1+z)^2 + \Omega_M\,(1+z)^3 + \Omega_R\,(1+z)^4\,. \tag{1.8}$$

In the equation above, z is the redshift, M and R are labels for non – relativistic matter and radiation, respectively. $\Omega_K = -k/a_0^2H_0^2$ and X refers to a generic substance with the equation of state:

$$p_X = \alpha_X \rho_X\,. \tag{1.9}$$

The measurement of the Hubble parameter is a very important task in cosmology and much effort is devoted to reduce the statistical and systematic uncertainties. A recent evaluation of the three year WMAP data in Ref. [Sp07] fits the value of the Hubble parameter at present day in the ΛCDM model as $H_0 = 73.2^{+3.1}_{-3.2}\ {}^{\mathrm{km}}/_{\mathrm{s\cdot Mpc}}$.

Recently, it was questioned if the approach described by the Friedman equations above is not an approximation too crude. Although the matter distribution was certainly very homogeneous at the epoch of last scattering when the CMB was imprinted, since then the growth of structure made it very inhomogeneous.

The problem of fitting a smooth geometry to a Universe with a lumpy matter distribution [El84] is central to relating observations to the numerical values of the averaged parameters which govern the evolution of the Universe. While the conventional interpretation of observations within the FLRW models has yielded a standard model of cosmology in broad agreement with observations, this model requires that most of the energy density in the Universe is in the form of clumped non – baryonic *Dark Matter* and smooth *Dark Energy*. Especially the nature of the *Dark Energy* seems to be the greatest challenge to physics. In standard cosmology the best – fit parameters give a model with a number of open questions.

Among these puzzles are the early formation of the first galaxies [Gl04, Ci04], signs of ellipticity in the CMB anisotropies consistent with the geodesic mixing expected from average negative spatial curvature [Gu07] and the low quadruple

power in the CMB anisotropy spectrum combined with the unexplained alignment of low multipoles [Co06a]. Furthermore, the standard models of structure formation fail to predict the observed *emptiness* in the voids which dominate Universe observed today [Pe01].

In Ref. [Wi07] the author proposes to resolve the puzzles by a more rigorous application of general relativity to cosmology to an inhomogeneous Universe. In such an Universe, the appropriate averaged Einstein equations describing the dynamical evolution is not the Friedmann equation, but modified equations obtained by a suitable averaging scheme, for which a number of possible solutions exist [Bu00, Za92, Co05a]. A virtue of this *Ansatz* is that no new physics or changes to general relativity are postulated. Additionally, upcoming CMB measurements should reach the precision needed to support or refute this interesting new model. In such a model, concordance with the supernova data and the baryonic acoustic oscillation scale is achievable without the assumption of *Dark Energy*, also the tension with early structure formation and the ellipticity in the CMB anisotropies vanishes. If the magnitude of the claimed effects of this model is confirmed by ongoing work, the cosmological parameters will change considerably. It should be stressed that such a model requires still a large amount of *Dark Matter* to be in agreement with the astronomical observations.

Nonetheless, throughout this work, the parameters of standard cosmology will be cited and applied.

1.2.2 Inflation

Another cornerstone for todays cosmology is a process called *Inflation* which is a mechanism for realizing the *Cosmological Principle* which is the basis of the standard model of physical cosmology. It accounts for the observed homogeneity and isotropy of the Universe. Additionally, it accounts for the observed flatness and absence of exotic relics from the very early Universe.

The formulation of the *Flatness Problem* is related to the discovery of the nearly isotropic cosmic microwave background in the 1960s. Since then, it is known that the total energy density of the Universe must have been very close to the critical density necessary for a flat Universe. Regardless of the shape of the Universe the contribution of spatial curvature to the expansion rate of the Universe could not be much larger than the matter contribution. When the Universe expands, curvature is redshifted away slower than the matter and the radiation content. A fine – tuning problem emerges as the primordial energy density contribution due to curvature of the Universe is required to have been exponentially small:

At the time of Big Bang Nucleosynthesis curvature energy density must have been 16 orders of magnitude smaller than the radiation energy density. Observations of the cosmic microwave background exacerbate this problem since they show that the Universe is flat to the accuracy of a few percent.

The question why the Universe appears statistically homogeneous and isotropic as demanded accordance by cosmological principle is known as the *Horizon Problem*. Without inflation, equilibrium cannot be attained in the early Universe as the gravitational expansion is too quick. With matter and radiation contributions only, two sufficiently separated regions of the observable Universe are unable to equilibrate as they diverge superluminally from each other. Being in equilibrium, they must have been causally connected sometime ago, however. Since they have been causally disconnected throughout the history of the Universe, it is not obvious to explain how these regions should have equilibrated thermally.

A solution to these two problems was given by A. H. Guth in the early 1980s [Gu81], proposing that a delayed first order phase transition called *Inflation* occurred in the very early Universe. In this phase transition, a scalar field, the *inflaton* was trapped in a local minimum of a potential initially. Subsequently it tunneled through the potential barrier and rolled toward a true minimum.

This original formulation of the theory of Inflation was flawed by the fact that domain walls accumulate the latent heat of the phase transition resulting in an anisotropic and inhomogeneous Universe [Ha82, Gu83]. A solution has been proposed assuming a number of scalar fields ϕ which are subjected to a flat potential $V(\phi)$ [Li82, Al82]. Under such conditions, the scalar fields ϕ roll down the potential $V(\phi)$ slowly in the beginning; this translates into a slow decrease of the Hubble constant H. A nearly exponential inflation happens before the field ϕ changes too much.

The energy scale of *Inflation* in the range of 10^{15} – 10^{16} GeV is uncomfortably close to the *Planck Scale* of 10^{19} GeV, which prohibits direct experimental exploration of its physics. Nonetheless, the analysis of the power spectrum of the large scale structure of the Universe yields indirect constraints on the theory of *Inflation*.

Observations of the cosmic microwave background show that the Universe is flat to an accuracy of at least a few percent, and that it is homogeneous and isotropic to the order of 10^{-5}. *Inflation* predicts that the visible structures in the Universe today were formed through the gravitational collapse of perturbations which were formed as quantum mechanical fluctuations in the inflationary epoch. The detailed form of the spectrum of these perturbations is a nearly – scale – invariant Gaussian random field. This very specific Harrison-Zel'dovich spectrum is characterized by its amplitude and a spectral index which measures the slight deviation from scale invariance predicted by inflation [Ha70, Ze72]. This shape for the spectrum of inhomogeneities of the perturbations has been confirmed by the WMAP satellite and other cosmic microwave background experiments, and galaxy surveys like the Sloan Digital Sky Survey (SDSS). Moreover, the slight deviation from scale invariance has been measured. The spectral index, n_s is equal to one for a scale – invariant spectrum. The simplest models of inflation predict that this quantity is between 0.92 and 0.98. A confirmation of the theory of inflation can be seen in the observations of the WMAP satellite, which has measured $n_s = 0.960 \pm 0.014$ and shown that it differs from unity at the level of two standard deviations.

1.2.3 The Standard Model of Particle Physics

In this subsection the Standard Model of particle physics is presented. For the evolution of the particle content of the Universe, it is important to know the existing particles, their masses and their interactions. This is important for the calculation of relic densities of the various particle species found in the Universe and as input parameters for Big Bang Nucleosynthesis (BBN). From the cosmological point of view, the Standard Model of particle physics is the effective theory which governs the evolution of the Universe from the point when electro – weak symmetry breaking occurred.

The Standard Model (SM) of particle physics accounts since many years for all observed particles and interactions up to now. Mathematically the SM is a relativistic quantum field theory, based on the $SU(3)_c \otimes SU(2)_L \otimes U(1)_Y$ gauge group, which exhibits a spontaneous symmetry breakdown:

$$SU(3)_c \otimes SU(2)_L \otimes U(1)_Y \rightarrow SU(3)_c \otimes U(1)_Q. \tag{1.10}$$

The three gauge groups shown above are the $SU(3)_c$ of color (strong) interaction, known as Quantumchromodynamics (QCD), the $SU(2)_L$ of weak interaction acting only on left handed fermions and a $U(1)_Y$ symmetry acting on the weak hypercharge, Y. After spontaneous symmetry breakdown, a $U(1)$ symmetry acting on Q is the electric charge generator emerges.

The fundamental constituents of matter are massless spin – $^1/_2$ particles, fermionic *quarks* and *leptons*. The left – handed fermions are arranged into three generations of $SU(2)_L$ doublets, while the corresponding right – handed fields transform as singulets under $SU(2)_L$:

$$\begin{pmatrix} \nu_e^w \\ e \end{pmatrix}_L \quad \begin{pmatrix} \nu_\mu^w \\ \mu \end{pmatrix}_L \quad \begin{pmatrix} \nu_\tau^w \\ \tau \end{pmatrix}_L$$

$$\begin{pmatrix} u \\ d^w \end{pmatrix}_L \quad \begin{pmatrix} c \\ s^w \end{pmatrix}_L \quad \begin{pmatrix} t \\ b^w \end{pmatrix}_L$$

$$(\nu_e)_R \qquad (\nu_\mu)_R \qquad (\nu_\tau)_R$$

$$e_R \qquad \mu_R \qquad \tau_R$$

$$u_R \qquad c_R \qquad t_R$$

$$d_R^w \qquad s_R^w \qquad b_R^w$$

The superscript w indicates that these fields are *electroweak eigenstates* instead of physical *mass eigenstates*. The quark fields carry *baryon number* $B = {}^1/_3$ and *lepton number* $L = 0$, while the lepton fields carry $B = 0$ and

$L = 1$. Each particle also has a corresponding antiparticle with the same mass and opposite quantum numbers. Their interactions are mediated by massless spin one *gauge bosons*. The strong interactions are mediated by gluons G^a_μ obeying the $SU(3)$ color symmetry; the electroweak interaction is mediated by the B_μ $U(1)_Y$ hypercharge singlet, the W_μ $SU(2)$ triplet field, which both are massless, too.

$$\begin{array}{cc} & G^a_\mu \\ W_\mu & B_\mu \end{array}$$

For the generation of particle masses in the standard model, a massless complex scalar Higgs doublet $\phi \equiv \binom{\phi^+}{\phi^0}$ has to be introduced. Under spontaneous electroweak symmetry breaking, the electroweak and the Higgs field merge to the observable massive vector bosons $W^\pm_\mu$, Z^0_μ, a massless γ_μ and a massive Higgs boson H^0 .

The search for the Higgs boson is one of the main motivations for the construction of the LHC collider.

The masses of the fermionic fields are generated their Yukawa coupling to the Higgs field. The quarks in the *weak eigenstate* representation are related to the *mass eigenstates* by the Cabibbo – Kobayashi – Maskawa (CKM) matrix. This mixing arise from the Yukawa interactions of the quark fields with the Higgs condensate,

$$\mathcal{L} = -Y^d_{ij}\overline{Q^w_{Li}}\phi d^w_{Rj} - Y^u_{ij}\overline{Q^w_{Li}}\epsilon\phi^* u^w_{Rj} + h.c., \tag{1.11}$$

where $Y^{u,d}$ are 3×3 complex matrices, ϕ is the Higgs field, i and j label the quark generations and ϵ is the 2×2 antisymmetric tensor. Q^w_L are the left handed quark doublets, and d^w and u^w are right handed down – and up – type quark singulets, respectively. The superscript w denotes that these fields are in the electroweak eigenstate basis. When the Higgs field ϕ acquires a vacuum expectation value, $\langle\phi\rangle = \left(0, v/\sqrt{2}\right)$, Eq. 1.11 yields mass terms for the quarks. The mass matrices for the *physical states* are then obtained by diagonalizing $Y^{u,d}$ by four unitary matrices $V^{u,d}_{L,R}$, as $M^{u,d} = V^{u,d}_L Y^{u,d}\left(V^{u,d}_R\right)^\dagger\left(v/\sqrt{2}\right)$. As a result, the charged current interactions by $W^\pm$ couple to the physical quarks with couplings given by the CKM matrix:

$$V_{CKM} \equiv V^u_L\left(V^d_L\right)^\dagger = \begin{pmatrix} V_{ud}V_{us}V_{ub} \\ V_{cd}V_{cs}V_{cb} \\ V_{td}V_{ts}V_{tb} \end{pmatrix}. \tag{1.12}$$

This unitary 3×3 matrix may be parameterized by three mixing angles and a CP – violating phase δ [Ca63, Ko73].

Analogous to the quark sector, a unitary 3×3 mixing matrix emerges for the leptonic sector called the Pontecorvo – Maki – Nakagawa – Sakata (PMNS)

matrix. The mass matrices for the physical eigenstates of the leptonic sector can be be constructed as in the quark sector by diagonalizing the respective Yukawa matrices $Y^{\nu,e}$ by four unitary matrices $U^{\nu,e}_{L,R}$. The PMNS matrix which relates the mixing between weak eigenstates and mass eigenstates in the leptonic sector has the following form:

$$U_{PMNS} \equiv U^{e}_{L} \left(U^{\nu_e}_{L}\right)^{\dagger} = \begin{pmatrix} U_{e1}U_{e2}U_{e3} \\ U_{\mu 1}U_{\mu 2}U_{\mu 3} \\ U_{\tau 1}V_{\tau 2}V_{\tau 3} \end{pmatrix}. \tag{1.13}$$

The indices one to three stand for the different physical eigenstates of the neutrino. Note that by convention the PMNS changes neutrino states, while the CKM matrix changes down – type quark states. Like the CKM matrix, the PMNS matrix can be described by three angles and a CP-violating phase δ. As it is still an open question if the neutrino is a Dirac or a Majorana fermion, two additional phases α_1 and α_2 which are only nonzero if the neutrino is a Majorana particle are possible.

Despite its success, several theoretical problems in particle physics point to fact that the SM is only the low – energy limes of a more fundamental theory, as some questions remain unanswered:

- The generation problem, or why are there exactly three generation of the fundamental fermions?
- The hierarchy problem, or why do the fundamental interactions have vastly different coupling strengths?
- How to include gravity into the framework of the SM.
- Leptogenesis and Baryogenesis cannot be explained with the CP – violation found in the standard model.
- The strong CP – problem, or why there is no CP – violation observable in QCD?
- Does the Higgs boson exist with the predicted properties?
- The SM has 18 free parameters which must be obtained by measurements, are these parameters predictable by a more general theory?

The crucial input for cosmology from the SM is the particle dynamics during the early Universe. While leptogenesis and baryogenesis is not explainable within the SM, it does contain the elementary fields of all experimentally confirmed particles and forces. It is the foundation for the understanding of the *freeze – out* of neutrons and protons and for the subsequent Big Bang Nucleosynthesis. Furthermore, there is no particle within the Standard Model which has the right properties to explain the effects of *Dark Matter*.

1.2.4 Big Bang Nucleosynthesis

In this subsection, Big Bang Nucleosynthesis (BBN) is presented. BBN offers a reliable probe on the early Universe as it is based on experimentally validated nuclear physics [Wa67]. Predictions on the abundances of the lightest elements synthesized in the early Universe are in good agreement with the primordial abundances inferred from observational data: This is understood as a validation of the standard hot Big Bang Cosmology [St06].

BBN provides powerful constraints on possible deviations from the cosmological Standard Model as well as on new physics beyond the Standard Model of particle physics. Big Bang Nucleosynthesis constraints *cold Dark Matter* to be non – baryonic as interactions between *Dark Matter* spoil the observed abundances of the primordial elements as seen in Fig. 1.1 . Furthermore, the reheating of the Universe by the decay of hypothetical particles at the epoch of Big Bang Nucleosynthesis is constrained by its interference with the formation of the primordial elemental abundances.

The synthesis of light elements is sensitive to physical conditions in the early radiation dominated Universe at temperatures $T \lesssim 10^4$ K ≈ 1 MeV, thus nucleons can be treated as being at rest, essentially.

The weak interaction allows neutron – proton conversion through three different channels:

$$n + \nu_e \leftrightharpoons p + e^-, \qquad n + e^+ \leftrightharpoons p + \bar{\nu}_e, \qquad n \leftrightharpoons p + e^- + \bar{\nu}_e. \tag{1.14}$$

As the nucleons are at rest, the initial and final lepton energies are related by the following equations:

$$E_e - E_{\nu_e} = Q(n + \nu_e \leftrightharpoons p + e^-), \tag{1.15}$$
$$E_{\nu_e} - E_e = Q(n + e^+ \leftrightharpoons p + \bar{\nu}_e), \tag{1.16}$$
$$E_e + E_{\nu_e} = Q, \text{ for n} \leftrightharpoons \text{p} + \text{e}^- + \bar{\nu}_\text{e}, \tag{1.17}$$

where $Q = 1.293$ MeV is the neutron to proton mass difference. In thermal equilibrium at higher temperatures, the ratio of neutron to proton number density is given by $n/p = \exp(\frac{-Q}{T})$, As the temperature drops , chemical equilibrium is departed and the *freeze – out* of the neutron occurred at a temperature defined by:

$$T_{fr} \propto \left(g_* G_N / G_F^4\right)^{1/6} \simeq 1\text{MeV} \tag{1.18}$$

Here g_* is the number of relativistic particle species determining the energy density in radiation, G_N is Newton's constant of gravity and G_F is Fermi's constant of weak decay. The neutron fraction at this time, given by $n/p = \exp(-Q/T_{fr}) \simeq {}^1/_6$ is thus very sensitive to every physical interaction known,

as Q depends on the strong and the electromagnetic interaction while T_{fr} depends on both the weak and gravitational interactions. After the *freeze – out*, the neutrons were free to β – decay, resulting in a neutron fraction of $\simeq {}^1/_7$ at the time when nuclear reactions between neutrons and protons began. At this time, the baryon density was too low, for any but two body reactions between nuclei. A simplified analytic model of the *freeze – out* allows the calculation of the n/p ratio with good accuracy [Be89a, Mu04].

The rates of the nuclear reactions depend on the density of baryons, which is conventionally given with respect to the relic photon density as:

$$\eta \equiv \frac{n_B}{n_\gamma} \tag{1.19}$$

The photon density n_γ is fixed by the present CMB temperature 2.725 K The formation of deuterium in the process $p\,(n,\gamma)\,\mathrm{D}$ starts the nucleosynthesis chain. The formation of heavier nuclei proceeds via:

$$\mathrm{D}\,(\mathrm{D},\mathrm{T})\,\mathrm{p}, \qquad \mathrm{D}\left(\mathrm{T},{}^4\mathrm{He}\right)\mathrm{n}, \tag{1.20}$$

$$\mathrm{D}\left(\mathrm{D},{}^3\mathrm{He}\right)\mathrm{n}, \qquad \mathrm{D}\left({}^3\mathrm{He},{}^4\mathrm{He}\right)\mathrm{p}, \tag{1.21}$$

as well as slower processes involving photons,

$$n\,(\mathrm{D},\mathrm{T})\,\gamma, \qquad p\left(\mathrm{D},{}^3\mathrm{He}\right)\gamma. \tag{1.22}$$

Photo dissociation by high energetic photons prevents the production of the light nuclei tritium T and ^{3}He via Eq. 1.21 well after T below the deuterium binding energy of 2.23 MeV. Since deuterium is rare at this point, the rates of the two deuteron processes are suppressed. The radiative capture processes given in Eq. 1.22 processes are not affected by the rarity of deuterium, but have intrinsically small cross sections. The production of deuterium becomes possible when, the ratio of the number of sufficiently energetic photons to baryons drops below unity:

$$\exp(\frac{2.23\mathrm{MeV}}{T})\frac{1}{\eta} \lesssim 1 \tag{1.23}$$

This happens at a temperature of $T \simeq 100$ keV, slightly above the deuterium break – up energy; at this time the remaining neutrons are rapidly fused to ^{4}He. The nuclear reactions leading to the formation of ^{4}He are not perfectly efficient, but leave a small residue of the light elements, D, T, ^{3}He, ^{7}Li and ^{7}Be. The absence of stable nuclei with nucleon numbers five and eight prevents the further formation of further nuclei. Later, tritium decays by β – decay to ^{3}He and ^{7}Be decayed by electron capture to ^{7}Li. Thus the primordial nucleosynthesis leaves us with protons, D, ^{3}He, ^{4}He and ^{7}Li. The calculated and the observed abundances are shown in Fig. 1.1 . Additionally, the matter abundance inferred from the WMAP analysis of the cosmic microwave background are shown. The good agreement of BBN and WMAP predictions on the one hand and the experimental observations on the other hand are seen as a confirmation of the cosmological standard model.

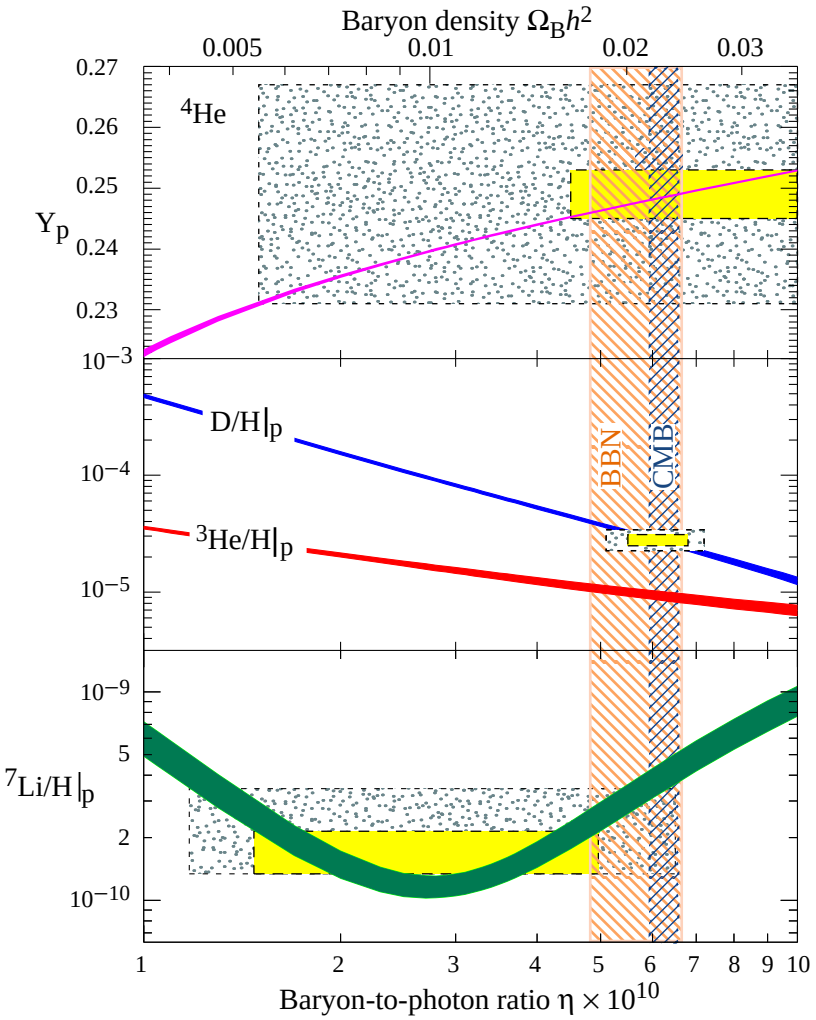

Figure 1.1: Big Bang Nucleosynthesis light nuclei abundances; on the horizontal axis, the photon to baryon ration is plotted, while the light nuclei abundances can be found on the vertical axis. The colored bands are theoretical predictions, also the predictions from Big Bang Nucleosynthesis and WMAP observations of the cosmic microwave background can be found. The boxes indicate the observed abundances. The plot can be found as Fig. 20.1. in Ref. [Am08] .

1.2.5 The Standard Cosmology Model: ΛCDM

In the previous sections the building blocks of the cosmology have been presented. In this section the standard model of cosmology and its defining parameters are discussed.

The current standard model of cosmology demands the existence of *Dark Energy* in form of a cosmological constant Λ added to the Einstein's equation (Eq. 1.1) of general relativity, with the equation of state $p_\Lambda = -1 \times \rho_\Lambda$. Furthermore, it is assumed that the *Dark Matter* found in the Universe is *cold*, i.e. it is non – relativistic. The bulk of matter is required to be in the form of non – relativistic, hence cold *Dark Matter*(CDM). In this model, the Universe is taken to be a perturbed Robertson – Walker space – time with dynamics governed by Einstein's equations. In the ΛCDM model a vanishing global space – time curvature is assumed, i.e. $k = 0$.

A successful standard model of cosmology must be able to explain two functions; the correlation spectra of the cosmic microwave anisotropies and the power spectrum. Both functions are governed by key cosmological parameters. Nine key cosmological parameters are encoded in the CMB if a simple adiabatic ΛCDM is employed:

$$\Omega_{\mathrm{CDM}}h^2, \quad \Omega_b h^2, \quad \Omega_{\mathrm{total}}, \quad H_0, \quad n_s, \quad n_t, \quad Q, \quad \tau, \quad r. \tag{1.24}$$

Of these parameters, the Ω_i's are the densities of the various types of matter. The total energy density Ω_{total} and H_0, the Hubble constant, are degenerate, so prior knowledge of the Hubble parameter is required. The parameters n_s and n_t are the scalar and tensor perturbation power spectra indices. Q is the overall amplitude of the spectrum and τ is the optical depth for Compton Scattering at the Reionization epoch. The parameter r gives the ratio of tensor to scalar perturbations, i.e. it is the ratio of gravitational perturbations to curvature perturbations. and is defined by:

$$r \equiv \frac{\Delta^2_{\mathrm{grav}}(k_0)}{\Delta^2_{\mathrm{scalar}}(k_0)}. \tag{1.25}$$

The power spectrum depends on five parameters:

$$n, \quad H_0, \quad \Omega_b, \quad \Omega_{\mathrm{CDM}}, \quad \sigma_8. \tag{1.26}$$

The parameter σ_8 measures the overall amplitude of the spectrum; it is the linear theory mass dispersion σ_8, which is defined as a box with an edge length of $8h^{-1}$ Mpc, measuring the cluster density. This scale can be conveniently probed directly via weak gravitational lensing and via its effect on the abundance of galaxy clusters. The spectral index n has to be constrained by data on the anisotropies in the CMB. A few more parameters can be added to the list of fundamental cosmological constants, the density of radiation density of relativistic particles and the neutrino mass contribution. The radiation density

Parameter	Value
Primary Parameters	
Primordial curvature fluctuations $\Delta^2_{\mathcal{R}}(k_0)$	$2.547(^{+92}_{-93}) \times 10^{-9}$ [a]
Primal fluctuations power index n_s	0.960(14)
Tensor to scalar perturbation ratio r	< 0.22 (95% C.L.)
Dark Energy density Ω_{total}	0.726(15)
Non – relativistic *Dark Matter* density $\Omega_{\text{CDM}}h^2$	0.1131(34)
Baryon energy density $\Omega_b h^2$	$0.02267(^{+58}_{-59})$
Photon energy density $\Omega_\gamma h^2$	2.469×10^{-5} [b]
Thompson scattering optical depth τ	0.084(16)
Combined neutrino mass of all species $\sum_i m_{\nu_i}$	< 0.67 eV (95% C.L.)
Hubble constant H_0	70.5(13)km/sMpc
Derived Parameters	
Reionization redshift z_{reion}	10.9(14)
Cluster number density σ_8	$0.813(^{+26}_{-27})$
Present day age of the Universe t_0	13.72(12) Ga

Table 1.1: Parameters of the cosmological standard ΛCDM model. The value of h is given by the Hubble constant H_0 in units of 100 $^{\text{km}}/_{\text{sMpc}}$. The errors are given at the 68% C.L. unless noted otherwise. Most values have been taken from Ref. [Ko09]. The total photon energy density has been measured by the CoBE FIRAS experiment[Ma99]. All energy densities are given as present day values.

[a] The primordial curvature fluctuations are given for $k_0 = 0.002\ ^1/_{\text{Mpc}}$. It is related to the primordial curvature fluctuation spectrum by $\Delta^2_{\mathcal{R}} = k^3 P_{\mathcal{R}}(k)/(2\pi^2)$.

[b] No error is given in Ref. [Ko09] for the photon density parameter Ω_γ.

can be split into two components, one for the photons and one for the neutrinos:

$$\Omega_{\text{rad}} = \Omega_\gamma \times (1 + 0.2271 N_{\text{eff}})\,. \tag{1.27}$$

In the equation above, the photon energy density Ω_γ is related to the relativistic neutrino energy density of the effective number N_{eff} of neutrino species which is set to its standard value 3.04. The effective number of neutrinos decreases to the physical number of neutrino, three, as the number of relativistic neutrinos declines. The non – relativistic neutrino density Ω_ν can be retrieved from the relation:

$$\Omega_\nu = \frac{\sum m_\nu}{94 h^2 \text{eV}}, \tag{1.28}$$

These parameters are presented in Tab. 1.1 and define the ΛCDM model of cosmology. The numbers of parameters is by no means fixed, as more sophisticated theoretical models emerge and experimental progress requires new parameters to be defined.

1.3 Astronomical Constrainsts on ΛCDM

In this section, the fundamental various astronomical observations required to determine the parameters of ΛCDM model are presented.

The first subsection addresses the Hubble constant H_0 which describes the expansion of the Universe. It is an important prior parameter for the analysis of anisotropies of cosmic microwave background (CMB) data. As the data of the CMB analysis alone yield a degenerated set of cosmological parameters, additional sources of information resolving the degeneracy are required. Measuring the redshift and the distances of SN Ia and the analysis of the power spectrum of the large scale structure (LSS) of the Universe observed today lift the degeneracy in the set of cosmological parameters. In the last section, the detection of *Dark Matter* effects on the kinematics of celestial objects is presented, which yields an additional test on the prevalence of *Dark Matter*.

1.3.1 Direct Measurements of the Hubble Constant

The Hubble constant $H(t)$ is defined as the time derivative of the scale factor $\dot{a}(t)$ divided by the scale factor $a(t)$ itself. For small distances compared to the size of the observable Universe, it is the factor of proportionality of the approximately linear relation between the distance D and the redshift z of a observed galaxy. The product $c \cdot z$ is often interpreted as the recession velocity of the observed object.

$$H = \frac{\dot{a}}{a} \approx \frac{c \cdot z}{D} = \frac{v_r}{D} \tag{1.29}$$

The Hubble Space Telescope Key H_0 project has measured today's Hubble constant H_0 to be 72 ± 8 $^{\mathrm{km}}/_{\mathrm{sMpc}}$ by the observation of Cepheid stars in other galaxies [Fr01]. Analysis of X – ray data from the Chandra X – ray telescope for distant ($0.14 < z < 0.89$) galaxy clusters assuming a ΛCDM model with 30 percent matter and 70 percent *Dark Energy* content yielded $H_0 = 77.6^{+4.8+10.1}_{-4.3-8.2}$ as result [Bo06]. Combining large scale structure surveys and WMAP data employing the basic ΛCDM model, a value of $71.9^{+2.6}_{-2.7}$ $^{\mathrm{km}}/_{\mathrm{sMpc}}$ is obtained. More general models yield a reduced H_0 of about 60 – 67 $^{\mathrm{km}}/_{\mathrm{sMpc}}$ [Ko09] . The agreement between these independent measurements is generally taken as a confirmation of the ΛCDM model.

1.3.2 Redshift – Luminosity Measurements of Distant Supernovae Ia

In a supernova (SN) of the type Ia a white dwarf in a binary system accretes sufficient matter from its partner to push its mass to the Chandrasekhar limit, which is the maximum possible mass that can be sustained by electron degeneracy pressure [Fo60]. Upon reaching this limit, the white dwarf destabilizes and the increasing density and temperature of its core allow the rapid conversion of carbon and oxygen to ^{56}Ni, triggering a thermonuclear explosion observable at

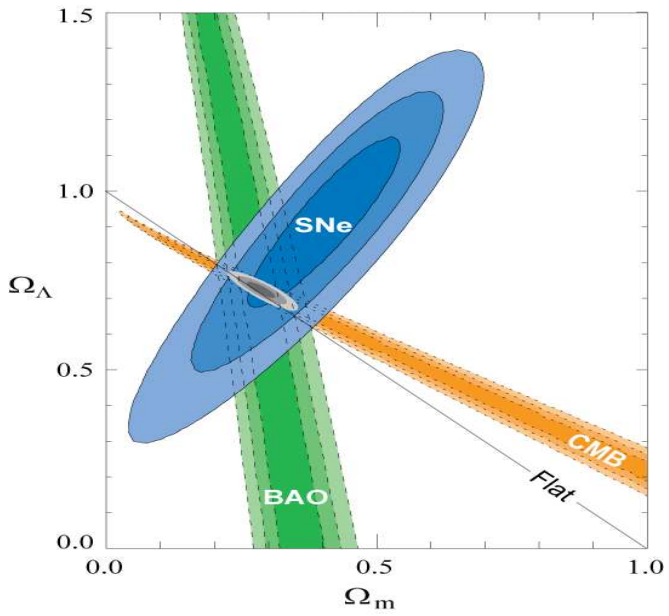

Figure 1.2: Experimental constraints on the energy density of the cosmological constant Ω_Λ and the total matter density Ω_M from the CMB, BAO and the supernova data. The figure above has been taken from Ref. [Ko08].

distances of several 1000 Mpc. As the exploding star always has a mass close to the Chandrasekhar limit, there is only little variation in the absolute luminosity of these explosions, making them nearly ideal distance indicators [Br98]. Furthermore, the brightness of the supernovae allows the detection of galaxies farther away then the host galaxies of the Cepheid variable stars.

Assuming a flat Universe, the SN Ia redshift measurements put a strict constraint in the Ω_M – Ω_Λ plane. Furthermore, another constraint on the equation of state parameter w can be placed in the Ω_M – w plane.

The accelerated expansion of Universe since at least $z = 0.5$ has been discovered in 1998 [Pe98, Ri98]. For a flat ΛCDM Universe, the dark energy density content obtained is $\Omega_\Lambda = 0.713^{+0.027+0.036}_{-0.029-0.039}$. Fig. 1.2 shows the constraints of the combined data sets on the Ω_Λ – Ω_M plane. The latest constraints from supernova data on w, the constant equation of state parameter, combined with the measurements of the CMB and BAO yield $w = -0.969^{+0.059+0.063}_{-0.063-0.066}$ for $z < 1$. This results are consistent with a cosmological constant, with only weak constraints on a redshift dependent w [Ko08].

1.3.3 The Anisotropical Cosmic Microwave Background

The most accurate determination of the cosmological parameters is based on measurements of the anisotropies of the cosmic microwave background (CMB) first observed in 1965 [Pe65, Di65]. At this place, a thorough description of the cosmological parameters and the underlying physical effects of the CMB is presented. While the CMB offers access to a lot of crucial parameters, other observations are necessary to resolve parameter degeneracies and to provide consistency checks.

The energy spectrum of the CMB photons can be described by a blackbody radiation spectrum with a temperature of 2.725 K. The lack of any observed deviations from the blackbody spectrum constrains physical processes over the cosmic history at redshifts $\lesssim 10^7$.

Local variation in temperature seen in the microwave sky to another allows further investigation of the physics of the early Universe [Wh94, Hu02]. Since the first detection of these anisotropies by the COBE satellite [Sm92], there has been intense activity to map the sky at increasing levels of sensitivity and angular resolution by ground – based and balloon – based measurements*. In 2003, the first results of the WMAP satellite were published [Be03a], which were improved upon the analysis of the three and five years WMAP data [Hi09, Ko09]. In the near future improved CMB maps including the polarization of the CMB are expected from the PLANCK satellite.

Observations show that the CMB contain anisotropies at the 10^{-5} level over a wide range of angular scales. In combination with other astrophysical data, the CMB anisotropy measurements place quite precise constraints on a number of cosmological parameters. Usually these anisotropies are presented in a spherical harmonic expansion of the CMB sky:

$$T(\theta,\phi) = \sum_{\ell m} a_{\ell m} Y_{\ell m}(\theta,\phi) \,. \tag{1.30}$$

Most of the cosmological information is contained in the temperature two – point function, i.e. the variance as a function of angular separation θ. The monopole moment a_{00} is given by the mean CMB temperature $T_\gamma = 2.725 \pm 0.001$ K(1σ) [Ma99], measurable by absolute temperature devices only. The measurements are consistent with a blackbody distribution over more than three decades in frequency. From the measured blackbody temperature the photon number n_γ and the energy density ρ_γ can be calculated at the epoch of recombination at $z \simeq 1100$, when the expansion of the Universe cools the plasma to the point where neutral hydrogen and helium atoms can be formed [Hi09]. The photon number density is evaluated to be $n_\gamma = \left(2\zeta(3)/\pi^2\right) T_\gamma^3 \simeq 411\text{cm}^{-3}$, while the energy density is given by $\rho_\gamma = \left(\pi^2/15\right) T_\gamma^4 \simeq 0.260$ eVcm^{-3}.

*Several collaborations ran balloon-based experiments, here we will mention ARCHEOPS [Be03b]; CDMP & MAT/TOCO [Mi02a]; BOOMERANG [Ru03]; MAXIMA [Le01]; DASI [Ha02]; CBI [Pe03]; ACBAR [Ku04] and VSA [Di04].

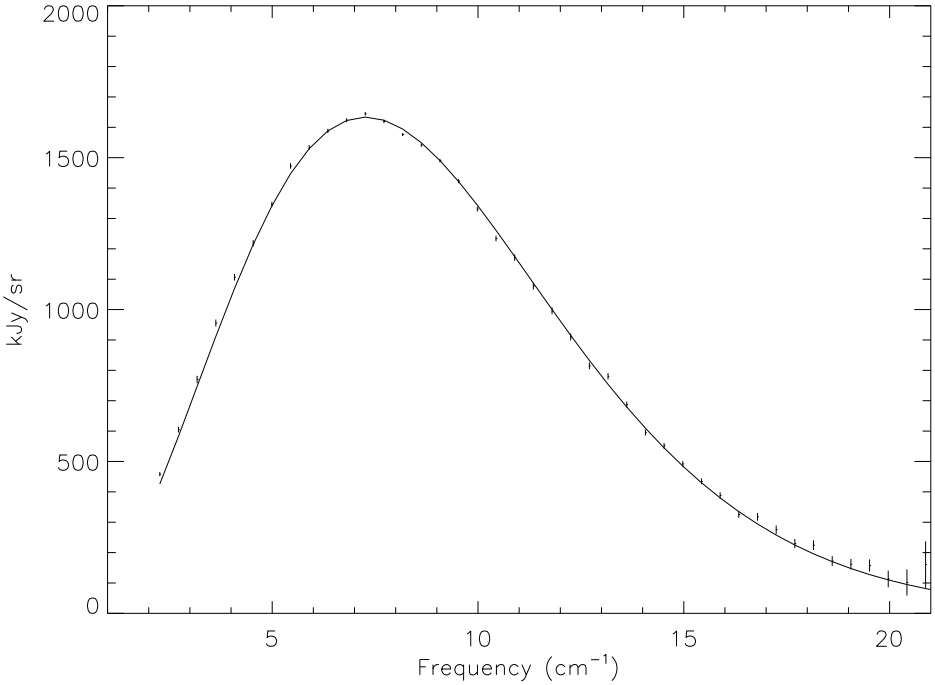

Figure 1.3: Comparison of the measured radiation intensity observed with the FIRAS radiometer of the COBE satellite with a blackbody spectrum of 2.728 K. The vertical axis gives the intensity in kiloJansky $\left(1\text{Jy} \equiv 10^{-30}\text{Jcm}^{-2}\text{s}^{-1}\text{Hz}^{-1}\right)$ per steradian, while the horizontal axis gives the reciprocal wavelength in cm^{-1}. This figure is taken from Ref. [Fi96].

The dipole moment is the largest anisotropy in the CMB with an amplitude of 3.355 ± 0.008 mK, it is the strongest multipole moment of the temperature Doppler shift due to the relative motion of the solar system with respect to the nearly isotropic blackbody radiation, as confirmed by measurements of the radial velocities of local galaxies [Hi09]. As a frame dependent quantity, it can be used to determine the *absolute rest frame* of the Universe where the CMB dipole moment vanishes. Artefacts from any relative motion must be removed for studies of the CMB anisotropies. Remaining excess variances at higher multipole moments is interpreted as a result of perturbations in the density of the early Universe, manifesting themselves at the time of the last scattering of the CMB photons.

Theoretical models generally predict that the higher $a_{\ell m}$ modes are Gaussian random fields to high precision. Tests show that Gaussianity is an extremely good approximation, with only weak indications for non – Gaussianity or statistical anisotropy at large scales [Hi09]. Non – Gaussian contributions from the phase of inflation are expected to be one to two orders of magnitude below current observational limits. Assuming Gaussianity and Isotropy, the variance of the temperature field carries the cosmological information rather than the individual multipole moments $a_{\ell m}$. It is important to understand that theories predict the expectation value of the power spectrum while the sky is a single

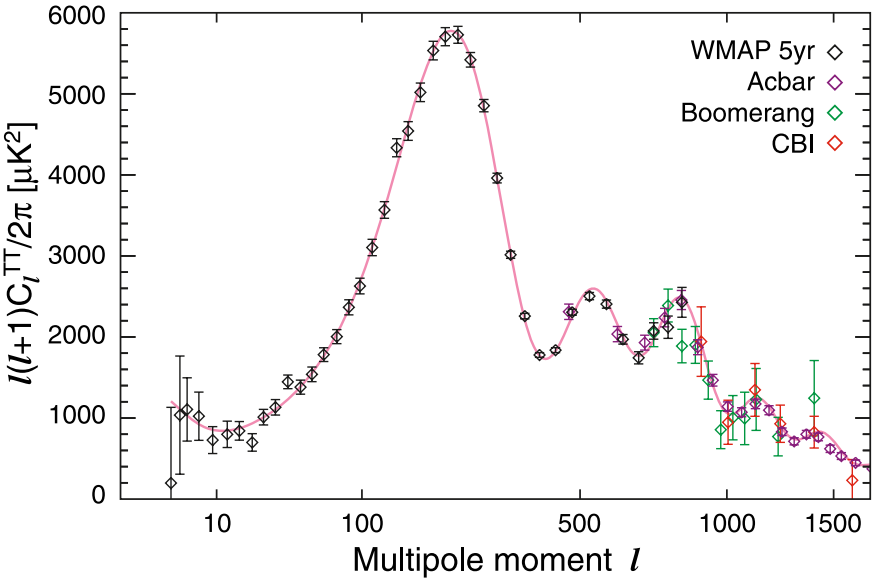

Figure 1.4: The TT auto – correlation power spectrum of the CMB anisotropies. On the vertical axis the band – power estimates $\ell\,(\ell+1)\,C_\ell^{TT}/2\pi$ in $\mu\mathrm{K}^2$ are shown, while on the horizontal axis the multipole moment ℓ and the corresponding angular size are shown. The uncertainties include both the statistical instrumental noise and cosmic variance. The red curve is the best – fit ΛCDM model to the WMAP 5 years data. The shown plot combines data from the WMAP 5 year data, ACBAR [Re09], BOOMERANG [Jo06] and CBI [Re04] experiments. The figure above is taken from Fig. 2 in Ref. [No09].

realization. Hence the cosmic variance is an unavoidable source of uncertainty when constraining models; it dominates the scatter at lower multipole moments, while the effects of instrumental noise and resolution dominate at higher multipole moments.

The angles subtended by the Hubble radius at last scattering correspond to a multipole moment of $\ell \simeq 100$. The anisotropies at larger scales have not evolved significantly and reflect the *initial conditions* at the epoch of recombination. The combination of gravitational redshift and intrinsic temperature fluctuations give rise to the Sachs – Wolfe effect [Sa67]:

$$\frac{\delta T}{T} \simeq \frac{\delta\phi}{3c^2}, \tag{1.31}$$

where $\delta\phi$ is the perturbation of the gravitational potential. The assumption of a nearly scale – invariant spectrum of density perturbations demands that $\ell\,(\ell+1)\,C_\ell \simeq$ constant for multipoles $\ell \lesssim 100$. The C_ℓs of the lowest multipoles ℓ are enhanced by time variations of the potentials. Correlations of large – scale CMB anisotropies and large – scale structures confirm the *integrated* Sachs – Wolfe effect[Fo03, Bo04, Pa05].

The multipole modes in the range of 100 to 1000 contain the acoustic peaks of the anisotropy spectrum, which are a consequence of gravity – driven acoustic oscillations of the plasma before recombination. Perturbations within the horizon at last scattering had been able to evolve causally and produced the observed anisotropy at recombination. The frozen phases of these sound – waves imprint relations of the total matter density to the baryonic matter density, giving the CMB anisotropies its constraining power on cosmological models.

Before recombination, the proton – electron plasma was tightly coupled to the photons, forming a *photon – baryon fluid*. Small, evolving density perturbations of the order $\delta\rho/\rho \sim 10^{-5}$ dominated by the dark matter component drove oscillations in the *photon – baryon fluid*. The radiation pressure of the photons provided the restoring force and the baryons gave extra inertia. As these perturbations evolved linearly, their oscillation frequency was determined by the speed of sound in the fluid. As the fluid density oscillated it gave rise to time variations in temperature and a velocity effect which is shifted $^{\pi}/_{2}$ in phase with an amplitude reduced by the sound speed. After baryons and photons decoupled, the photons propagated freely and the phases of the oscillations were frozen into the sky as a harmonic series of peaks in the anisotropy spectrum. The main peak is the mode which reached maximum compression as it went through one quarter of a full period. Even peaks represent maximum under – densities, with smaller amplitudes as the rebound had to overcome the pull of the inert *Dark Matter* accumulation. The troughs are partly filled by the Doppler effect as they are at velocity maxima of the oscillations.

The scale associated with the peaks is the sound horizon at last scattering, which size can be calculated. The projection of this length onto the sky yields an angular scale which is sensitive to the spatial curvature of the Universe and thus its total energy content, $\Omega_{\rm tot}$ if the Hubble constant is known.

Another effect arises after reionization, as a fraction of photons is isotropically scattered at times $z < z_{\rm reion}$, partially erasing the anisotropies at angular scales smaller than those subtended by the Hubble radius at $z_{\rm reion}$, which corresponds to ℓs above a few tens, depending on the used reionization model. Thus the amplitude of these acoustic peaks is reduced by a factor $e^{-2\tau}$ relative to the Sachs – Wolfe plateau, where τ is the Thomson scattering optical depth:

$$\tau = \int_0^{z_{\rm reion}} \sigma_T n_e\left(z\right) \frac{dt}{dz} dz, \tag{1.32}$$

where σ_T is the Thomson scattering cross – section, $n_e(z)$ is the free electrons number density at redshift z and dt/dz is fixed by the background cosmology.

The peaks in the CMB were a theoretical prediction going back to the early 1970s [Pe70, Su70]. They can be seen as a snapshot of stochastic standing waves with a rich structure and simple underlying physics encoding extractable information about the cosmological parameters. The picture of the acoustic peak has been confirmed by the imprint of the baryonic acoustic oscillations in the power spectrum of galaxies at small redshifts [Co05b].

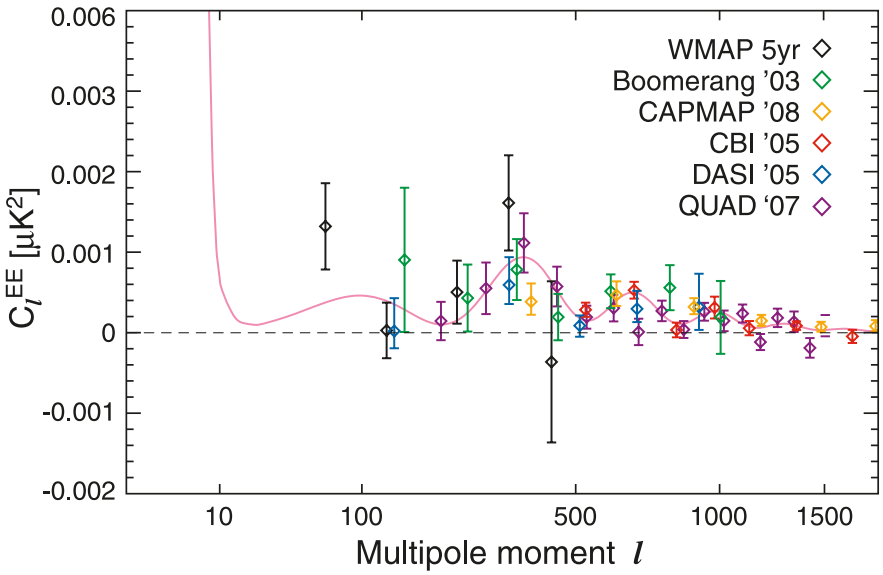

Figure 1.5: Auto – power spectrum of the E – mode polarization signal from the WMAP experiment 5 year data, combined with results from BOOMERANG [Mo06], CBI [Si07a], CAPMAP [Bi08], QUAD [Ad08] and DASI [Le05] experiments. On the vertical axis the band – power estimates C_ℓ^{EE} in μK^2 are shown, while on the horizontal axis the multipole moment ℓ are shown. The pink curve is the best fit theory spectrum from the ΛCDM/WMAP Markov Chain [Du09]. The figure above is taken from Fig. 10 in Ref. [No09].

The highest multipole moments ($\ell \gtrsim 1000$) are exposed to *Landau* damping as their corresponding scales are smaller than the thickness of the surface of last scattering, which size is the result of the fact that the opacity of the Universe does not vanish instantaneously at recombination. *Silk* damping describes the effect that the amplitude of a sound wave whose physical wavenumber k larger than the inverse mean free path of a particle in a relativistic medium is damped by viscosity and heat conduction [Si72]. An additional effect at high ℓ occurs due to gravitational lensing by non – linear structures at low redshifts. The peaks are partially flattened, as the anisotropies C_ℓ are convoluted with a smoothing function in a calculable way, generating a power – law tail at the highest multipoles and complicating the polarization signal [Za98]. Another important effect is the Sunyaev – Zel'dovic effect [Su80], which arises from the Compton scattering of the CMB photons by hot electron gas, distorting the CMB spectrum by the transfer of energy from the electrons to the photons.

Since Thompson scattering of an anisotropic radiation field also generates linear polarization, the CMB is predicted to be polarized at a five percent level [Hu97]. The most convenient decomposition of the linear polarization pattern is given by the splitting into a part which comes from a divergence (E – *mode*), and a part with a curl (B – *mode*). Primal scalar fluctuations generate only E – *modes*, while tensor fluctuations generate both E – *modes* and B – *modes*.

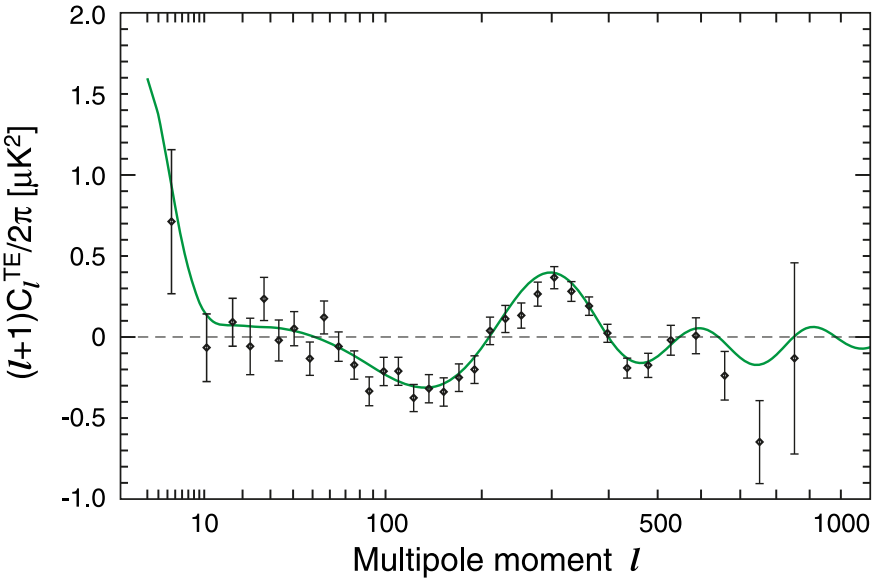

Figure 1.6: Cross power spectrum of the temperature anisotropies and E – mode polarization signal from the WMAP experiment 5 year data. On the vertical axis the band – power estimates $(\ell + 1)\, C_\ell^{TE}/2\pi$ in μK^2 are shown, while on the horizontal axis the multipole moment ℓ are shown. The green curve is the best fit theory spectrum from the ΛCDM/WMAP Markov Chain [Du09]. The figure above is taken from Fig. 5 in Ref. [No09].

From the allowed six different cross power spectra for this linear polarization, two, the C_ℓ^{TB} and the C_ℓ^{EB} are set to zero by parity symmetry requirements, i.e. if there is no preferred sense of rotation in the Universe. The remaining four spectral observables, C_ℓ^{TT}, C_ℓ^{TE}, C_ℓ^{EE} and C_ℓ^{BB} can be determined from data measuring the full temperature and polarization anisotropy information. The B – mode power spectrum can be generated by vectors or tensors only as scalar perturbations have no handedness. A nonzero B – mode signal allows the measurement of the tensor contributions on top the primordial fluctuations, but such a measurement is troubled by foreground contributions and other systematic effects. The five year WMAP data is consistent with the no contribution from tensor fluctuations [No09].

The oscillating photon – baryon fluid results in a series of acoustic peaks in the polarization C_ℓs, too. The main C_ℓ^{EE} spectrum shown in Fig. 1.5 has peaks which are out of phase with those of the C_ℓ^{TT} spectrum shown in Fig. 1.4 as the polarization anisotropies are generated by the photon – baryon fluid velocity. The C_ℓ^{TE} part of the temperature and polarization patterns results from correlations between density and velocity perturbations on the last scattering surface of either sign and exhibits a larger amplitude than the C_ℓ^{EE} spectrum. As no Sachs – Wolfe effect is present, no large – angle plateau is observed in the polarization anisotropy spectrum. Scattering during a recent period can create a polarization *bump* at large angular scales, however.

Even more important than the precise values of the cosmological parameters are the lessons learnt about the general features of our observable Universe. Beyond a confirmation of the basic hot Big Bang model, lessons from the CMB include:

- The Universe recombined at $z \simeq 1100$ and reionized at $z \simeq 10$. This sets the times when the CMB formed and when the first stars formed, respectively.
- The geometry of the Universe is close to flat as the density of the Universe matches the critical density very closely $\left(\Omega_{total} = 1.003^{+0.013}_{-0.017}\right)$.
- Both *Dark Matter* and *Dark Energy* are required within the frame of the ΛCDM model.
- Gravitational instabilities are sufficient to grow all observed large structures in the Universe.
- Topological defects were not important for structure formation.
- Synchronized *super – Hubble* modes were existent in the early Universe.
- The initial perturbations seen in the CMB were adiabatic in nature.
- The perturbations were initially maximal randomized, i.e. they had gaussian initial conditions.

For the search for *Dark Matter*, the CMB is important as it shows clearly that *Dark Matter* is not just an observable feature of todays Universe, but was present in the early Universe with observable unique consequences. The formation of the acoustic oscillation peaks requires *Cold Dark Matter*, as free – streaming relativistic *Hot Dark Matter* could not accrete.

1.3.4 Large Scale Structure of the Universe

The simplest model for the generation of cosmological structure is gravitational instability acting on some tiny primordial fluctuations. If the density of radiation and the density of matter are perturbed equally in these fluctuations, i.e. they are *adiabatic*, then the linear growth law for matter perturbations δ is given by:

$$\delta \sim \begin{cases} a(t)^2 & \text{(era of radiation domination)} \\ a(t) & \text{(era of matter domination)} \end{cases} \tag{1.33}$$

For low density Universes, the present – day amplitude is suppressed by a factor $g(\Omega)$, which can be obtained as accurate fit for models with matter and cosmological constant by the formula:

$$g\left(\Omega\right) \simeq \frac{5\Omega_M}{2} \frac{1}{\Omega_M^{4/7} - \Omega_\nu + \left(1 + \frac{\Omega_M}{2}\right)\left(1 + \frac{\Omega_\nu}{70}\right)}, \tag{1.34}$$

in this equation Ω_M is the total non – relativistic mass density, Ω_ν is the neutrino mass density.
Alternatively, *isocurvature* perturbations may exist, in this case the total density is initially unperturbed but the equation of state changes. These modes perturb the total entropy density, inducing additional large – scale anisotropies in the CMB [Ef86]. Although the character of perturbations in the simplest inflationary theories is purely adiabatic, many models predict correlated adiabatic and isocurvature modes. For such models, the simplest example is the scalar *curvaton*, whose decay yields a perturbed radiation density. If the matter content already exists at this time, the overall perturbation field is expected to reveal a significant isocurvature component. Such a prediction is contradicted by the current WMAP data [Ko09], and most analyses of CMB and LSS data assume that the adiabatic perturbation mode holds exactly.

The linear evolution preserves the shape of the power spectrum. Several processes ensure that growth actually depends on the matter content of the Universe. During the radiation dominated epoch, pressure opposes gravity effectively for wavelengths below the Horizon length. Thus the *comoving* horizon size D_H at the redshift of radiation – matter equality z_{eq} yields an important scale:

$$D_H(z_{eq}) = \frac{2\left(\sqrt{2}-1\right)}{\sqrt{\Omega_M z_{eq}} H_0} = \frac{16.0}{\Omega_M h^2}\text{Mpc}, \tag{1.35}$$

in the formula above, H_0 is today's Hubble constant and h is the Hubble constant in units of 100 $^{\text{km}}/_{\text{sMpc}}$. At early times, free – streaming *Dark Matter* particles will erase all scales up to the horizon until these particles become non – relativistic. This allows to determine an upper bound on the amount of relativistic *Dark Matter* particles in the early Universe. For example, light massive neutrinos become non – relativistic at z_{eq}, implying that all structure up to the

horizon – scale power – spectrum is erased. A further important scale is set by the process of *Silk damping* in which photon diffusion can erase perturbations in the matter – radiation fluid. The overall effect is imprinted in the transfer function T_k which relates the ratio of the late – time amplitude of a mode of its initial value. The overall power spectrum P_k is thus the primordial power spectrum times the square of the transfer function:

$$P(k) \propto k^n T_k^2. \tag{1.36}$$

This power spectrum can be measured by statistical analysis of the spatial distribution of galaxies in today's Universe.

As seen in Sec. 1.3.3 the physics of the propagation of the baryonic density waves in the early universe is simple enough to allow the prediction the size of the sound horizon at recombination. Additionally, the CMB provides a high precision measurement of this scale [Hi09].

The expansion of the Universe since recombination and today is well supported by observations and is considered one of the foundations of the Big Bang Model. As mentioned in Sec. 1.3.2, observations of supernova Ia in the 90s have proven that the Universe is expanding at an accelerated rate today. In order to understand and test the ΛCDM model, it is important to have a variety of independent ways of measuring its key parameters and to resolve degeneracies which can only be disentangled if the different observations are combined. The detection of Baryonic Acoustic Oscillations (BAO) adds to the knowledge about the accelerated expansion of Universe and its content by comparing observations of the sound horizon today (using the Large Scale Structure of Universe) to the sound horizon at the time of recombination (using the CMB) [Ei05].

The Sloan Digital Sky Survey (SDSS) has been a five – year survey taking images and spectra of millions of celestial objects. The result of this survey is a three-dimensional map of the objects in the nearby universe up to distances of $z = 0.47$. The SDSS catalog provides a picture of the distribution of matter in the Universe today which can be searched for a increased probability of galaxies been separated by the distance of the sound horizon. The SDSS collaboration successfully detected this BAO signal as a bump in the correlation function at a comoving separation equal to the sound horizon of ≈ 150 Mpc [Ei05], which is in good agreement with the result from the WMAP data.

1.3.5 Dynamics of Galaxies and Galaxy Clusters

This section will address the detection of the effect of *Dark Matter* on the kinematics of celestial objects on more local scales ($z \lesssim 1.0$). This is important for two reasons: First, the kinematics of celestial objects are independent from the cosmological model driving the evolution of the Universe. Second, as the general existence of *Dark Matter* in the early Universe does not exclude its absence on more local scale like our galaxy or solar system, an astronomical confirmation of the effects of *Dark Matter* in such systems justify more experimental effort to determine the physical properties of the *Dark Matter*.

The first evidence for dark matter was found almost eighty years ago, when F. Zwicky measured the circular velocity distribution of galaxies in the Coma cluster to estimate the mass of the cluster [Zw33]. His conclusion was that the Coma cluster must contain far more non – luminous matter than observed luminous matter. Today, the observations of galaxy clusters involve the measurement of the peculiar velocities of its galaxies, which gives a measure of the potential energy of a virialized cluster. Additionally, the X – ray temperature of the hot inter – galactic gas bound in the cluster is measured and detection of the weak gravitational lensing of background galaxies due to the mass of the cluster is possible. This allows a accurate determination of the ratio of *Dark matter* to standard baryonic matter.

With modern instrumentation, it has become possible to measure rotational curves of single galaxies since the early 1960s. The circular motion of outward stars circling around the galaxy allows the measurement of the total mass of the galaxy inside the orbit. In the context of classical Newtonian gravitation the connection of the angular velocity of an orbiting satellite around a mass in a virialized system is straightforward; the rotational velocity v of an object on a stable Keplerian orbit with radius r scales like $v(r) \propto \sqrt{M(r)/r}$, where $M(r)$ is the mass inside the orbit. If the radius of the orbit lies outside the visible part of the galaxy and if the mass distribution coincides with the distribution of the luminous parts of the galaxy, it is expected that $v(r) \propto 1/\sqrt{r}$.

Experimentally rotation curves are obtained by combining observations of the hydrogen 21 cm line with optical surface photometry. Rotation curves usually exhibit a characteristic flat behavior at large distances from the galactic center and even far beyond like the example shown in Fig. 1.7 . This observation implies the existence of a *dark* halo (i.e. a mass distribution made by non – luminous and non – absorbing matter) with a mass density $\rho(r) \propto 1/r^2$.

From the observational point of view, the most interesting objects for *Dark Matter* detection via measurement of the rotational velocities are low surface brightness (LSB) galaxies[Bo97]. Most LSBs are dwarf galaxies and are estimated to provide up to 90% of all galaxies. The measured mass to luminosity ratios of the LSBs are very high and they show no overdensities of stars, i.e. they do not have a central bulge like normal spiral galaxies. Those two properties allow to avoid the difficulties associated with the disentanglement of the dark and the visible contributions to the rotational curves, i.e. LSBs allow more precise measurements of the effects of *Dark Matter* than normal spiral galaxies .

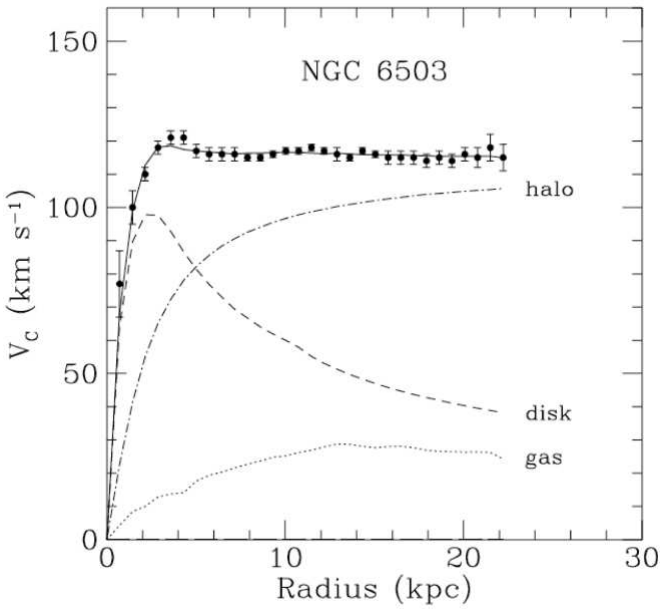

Figure 1.7: Rotation curve of the galaxy NGC6503. The points are the measured circular velocities as a function of distance to the center of the galaxy. The dotted, dashed and dash – dotted lines are the contributions of gas, disk and *Dark Matter*, respectively. The figure above is taken from Ref. [Be91].

Some elliptical galaxies show evidence for dark matter via strong gravitational lensing [Ko03]. If this observations are converted to a lower bound on the dark matter density, one arrives at a value of $\Omega_{\rm DM} \gtrsim 0.1$ where $\Omega_X \equiv \rho_X/\rho_{\rm crit}$, $\rho_{\rm crit}$ is the critical mass density (i.e. $\Omega_{\rm tot} = 1$ corresponds to the matter density which leads to a flat Universe in the Robertson – Walker metric). The observations of galaxy clusters indicate also the existence of non – luminous, non – absorbing dark matter, the *Dark Matter* densities derived from these observations are considerably larger, in the range of $\Omega_{\rm DM} \simeq 0.2$ to 0.3.

An alternative to the postulation of dark matter is to tinker with Newton's law of gravity and propose alterations to the gravitational force law [Be04, Br07] or the particles response to it [Mi83]. These theories are commonly dubbed MOdified Newtonian mechanics (MOND) or MOdified Gravity (MOG). In the MOND theories, Newton's second law is modified to the form:

$$F = m\mu(\frac{a}{a_0})a \tag{1.37}$$

In this equation above $\mu(x)$ is a function which is unity for large argument, while its value is $^a/_{a_0}$ for small arguments. This allows to avoid contradictions with observations for standard acceleration, while the deviation from Newton's second law are effective for the tiny acceleration on galactic cluster scales.

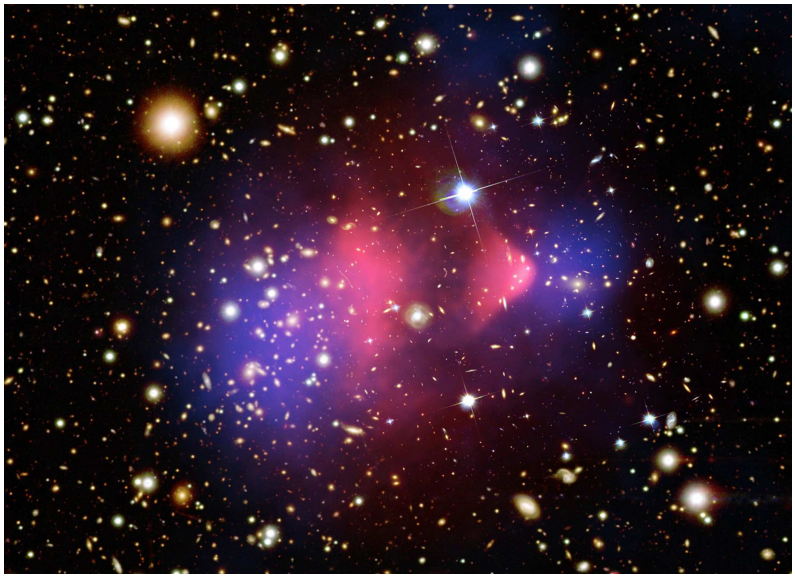

Figure 1.8: Composite picture of the bullet cluster. On top of the optical image, the red hues show the X – ray emitting hot gas making up most of the baryonic mass of the galaxy clusters. The blue hues show the distribution of the matter content according to gravitational lensing.
Composite Credit: X-ray: NASA/CXC/CfA/ M.Markevitch et al.;
Lensing Map: NASA/STScI; ESO WFI; Magellan/U.Arizona/ D.Clowe et al.
Optical: NASA/STScI; Magellan/U.Arizona/D.Clowe et al.

Since the observation of the bullet cluster shown in Fig. 1.8, the MOND approach lost its validity as substitute for the existence of dark matter [Cl06]. The bullet cluster 1E 0657 – 56 consists actually of two colliding galaxy clusters. The mass of the intra – cluster gas dominates the mass of the visible galaxies generally by a factor of three to six. The bow shock at the smaller subcluster reveals a relative velocity between the two subclusters is $\approx 4700\ {}^{\mathrm{km}}/_{\mathrm{s}}$ [Ma04]. The two subclusters collided about 100 – 150 Ma ago and the merger of the two subclusters occurred nearly in the plane of the sky. The galaxies behave like collisionless particles during this merger while the plasma is slowed by ram pressure. In a post merger system like the bullet cluster, the galaxies have thus decoupled from their associated plasma clouds. In the absence of dark matter the gravitational potential will trace the dominant visible mass content, the X – ray plasma. On the other hand, if the total mass of the system is dominated by collisionless, i.e. weakly interacting, dark matter the gravitational potential will trace the *Dark Matter* distribution. The discrepancy between the mass – distribution obtained by weak gravitational lensing and the one due to the visible galaxies and intra – cluster gas leads to the conclusion that collisionless *Dark Matter* provides the bulk of the mass of the clusters. A similar situation can be encountered in the other galaxy clusters like Abell 520 [Ma07].

However, small MOND effects on top of non – baryonic *Dark Matter* are not excluded.

1.3.6 Constraints on the Nature of Dark Matter

In the previous sections it was shown that the ΛCDM model of Cosmology is well supported by the independent measurements of the cosmic microwave background, the large scale structure of today's Universe, supernovae Ia distance measurements and celestial dynamics of galaxies and galaxy clusters.

While the nature of the enigmatic *Dark Energy* is still under debate, *Dark Matter* faces more constraints on its properties:

- The constraints derived from abundances of light elements observed in the Universe and the abundances demanded from the theory of Big Bang Nucleosynthesis require *Dark Matter* to be non – baryonic and electro – magnetically inert. Additionally, the inertness of *Dark Matter* with respect to baryons and radiation is mandatory for the mechanisms which create the observed acoustic oscillations in the CMB and the BAO of the large scale structure of the Universe.

- For simulations of the large scale structure of the Universe to be in agreement with observations, the amount of relativistic *Dark Matter* must be limited severely. As the free streaming relativistic particles would have washed out any emergent small – scale structures in the early Universe, notable amounts of relativistic *Dark Matter* are excluded. This requires either fairly massive particles as *Dark Matter* since accelerator physics exclude the existence of appropriate low mass candidates, or the *Dark Matter* particle must have been produced by a mechanism which prevents its thermalization with the rest of the Universe.

- It can be concluded from the observation of merging galaxy clusters like Abell520 or the Bullet Cluster that the observable effects on the kinematics of *Dark Matter* on the dynamics of celestial objects can not be explained sufficiently by modifications of the gravitational force.

- The relic density of a *Dark Matter* particle after freeze – out in the early Universe must yield the observed density of *Dark Matter*, Ω_{DM} of the CMB. In addition, the particle must be stable enough to explain the today's *Dark Matter* density. While a lesser relic density could be cured by the possibly that several species of *Dark Matter* particles exist, a relic density too large is in disagreement with the observed flatness of the Universe.

- The new physics related to *Dark Matter* must respect the observations of the photon to baryon abundance, η, and temperature T at the time of Big Bang Nucleosynthesis, as only a very limited amount of particle decays from the *Dark Matter* sector are allowed to maintain η and T. This is not the case for all theoretical scenarios.

1.4 Dark Matter Particle Candidates

In the conclusion of the last section, it has been shown that particles must satisfy several conditions to be viable *Dark Matter Candidates*: They must interact very weakly with baryons and electromagnetic radiation, their right relic density must be in agreement with the *Dark Matter* energy density and they must be non – relativistic to be allowed by the observed large scale structure of the Universe.

In this section, several theories providing candidates are discussed. It is shown that the unobserved fraction of the Baryons in the Universe, – the *baryonic Dark Matter*, is not sufficiently large enough to explain the rotational curves of galaxies, thus *non – baryonic Dark Matter* must be abound in our galaxy. As the next step, the neutrino as weakly interacting, non – baryonic particle cannot provide enough of the observed *Dark Matter* energy density Ω_{DM} without being in severe contradiction to the observed structure of the Universe. Since no Standard Model particles are left as candidates for the *Dark Matter*, motivated extensions like Supersymmetry, Extra Dimensions and Axions are scrutinized. Finally, the possibility of ultra – heavy *Dark Matter* candidates is explored.

1.4.1 Baryonic Dark Matter

The contribution of baryons to the total energy density of the Universe is about 4.5 percent, as derived from Big Bang Nucleosynthesis and observations of the anisotropies of the Cosmic Microwave Background. The contribution of detectable baryonic matter, stars and gas in galaxies and is only about $^1/_8$. It should be stressed that *baryonic Dark Matter* cannot substitute *non – baryonic Dark Matter* on the CMB and LSS scales, but it is important to determine its contribution on the galactic scale. So question arises where the non – luminous part of the baryonic matter is located.

It is proposed that *baryonic Dark Matter* is located in diffuse non – luminous molecular clouds or in massive objects like small black holes, white dwarfs or brown dwarfs named MAssive Compact Halo Objects (MACHO) [Tu99]. In order to explain the rotational velocities exhibited by galaxies, these objects should populate the halo of the galaxy in large numbers. The gravitational microlensing allows the detection of a MACHO when it passes in front of or nearly in front of a star and enhances the luminosity of the background star during the transit.

Several groups have searched for MACHOs by looking for the microlensing effect on background stars. These groups have ruled out dark matter being explained by MACHOs with mass in the range 10^{-8} to 100 solar masses. The MACHO collaboration claims to have found enough microlensing to predict the existence of many MACHOs with mass of about 0.5 solar masses sufficient to explain about 20 percent of the dark matter in our galaxy [Al00]. This result suggested that MACHOs could be white dwarfs or red dwarfs.

However, red and white dwarfs are not completely dark. The faint light emitted by them can was searched for with the Hubble Space Telescope (HST). Observations using the NICMOS instrument of the HST showed that less than one percent of the halo mass in our galaxy is composed of red dwarfs [Gr96, Na00]. The EROS2 collaboration does not confirm the signal claims by the MACHO group as they observed one microlensing event while expecting 39 [Ti07]. Furthermore, the sensitivity of the EROS2 experiment in comparison to the MACHO survey was higher by a factor of two.

Therefore, the rotational curves of the galaxies cannot be explained by MACHOs. This amplifies the impact of the evidence celestial dynamics provide to the hypothesis of *non – baryonic Dark Matter*. In particular, as the predominant part of *Dark Matter* in our galaxy must be non – baryonic in the absence of MACHOs, the chance to detect it in direct or indirect searches is enhanced.

1.4.2 Neutrinos as Dark Matter

At the first look, the Standard Model of Particle Physics provides us with an candidate for *Dark Matter*, the neutrino. Today, it is established that the neutrino has a mass. Since the late sixties, the observed neutrino flux from the sun was too low by a factor of three compared to the predicted flux from the standard solar model [Cl98]. The experiments SAGE and GALLEX confirmed the observed neutrino flux deficit for ν – capture on Ga probing also the ν's from the pp – cycle in the sun [Ga99, Cr99]. The experiments Super Kamiokande, SNO and KamLAND [Fu98, Ah02, Ar05] were able to detect both solar and atmospheric neutrinos and observed neutrino flavor oscillations, thus solving the solar neutrino deficit puzzle. These experiments allow the determination of the (squared) mass – differences between the physical eigenstates, but not the absolute mass. The absolute mass of the neutrino can be retrieved from the measurement of the lowered endpoint of the electron energy spectrum close of the β – decay or from the measurement of life – time of the neutrino – less double β – decay.

Today, the most stringent bound on the sum of mass of all three neutrino species comes from cosmology. As a relativistic particle, the neutrino freely streams through the Universe, inhibiting the growth of primordial small scale perturbations. Thus the neutrino mass should be imprinted in the power spectra of perturbations seen in large scale structures and the cosmic microwave background. A combined analysis of all available cosmological sources yield a upper limit of 0.17 eV for the neutrino mass [Se06].

From this value a upper limit of $\Omega_\nu < 0.04\ \Omega_{\text{total}}$ for the contribution of neutrino masses to the total energy density of the Universe can be given. By this limit, the ordinary Standard Model neutrino is ruled out as significant contribution to *Dark Matter*.

1.4.3 Supersymmetric Dark Matter

Supersymmetry (SUSY) is a generalization of the space – time symmetries found in quantum field theory that allows the transformation of fermions into bosons, and vice versa. As a logical consequence, for each particle of the Standard Model has a supersymmetric partner, which is denoted by putting a tilde on top of the symbol of the SM particle, e.g. for the electron neutrino ν_e a supersymmetric partner $\tilde{\nu}_e$ exists. To keep the SUSY theory anomaly free, an additional Higgs – Doublet has to be introduced, H_u and H_d. For each Higgs – Doublet, a spin $^1/_2$ superpartner $\tilde{H}_{u/d}$ is associated. The existence of such a non trivial extension of the Poincaré symmetry of ordinary quantum field theory is highly constrained by theoretical principles [Ha75, Co67].

Supersymmetry provides a framework for the unification of particle physics and gravity [Ni84, We00], possibly allowing an explanation of the *gauge hierarchy* of the electroweak scale to the Planck energy scale [Wi81]. While the electroweak symmetry breaking scale is characterized by the standard model Higgs vacuum expectation value of 246 GeV, the Planck energy scale is determined by the Planck mass $M_P \approx 10^{19}$ GeV. If supersymmetry were an exact symmetry of nature, the Standard Model (SM) particles and their supersymmetric partner would be degenerate in mass. Since no supersymmetric particles have been observed, supersymmetry must be broken. If the supersymmetry breaking mechanism is *soft* and the corresponding supersymmetry – breaking mass is in the range of a few TeV, the stability of the gauge hierarchy can maintained [†] Although no experimental results require new physics at the TeV – scale, it is expected on the grounds of three theoretical arguments:

- An explanation of the gauge hierarchy which is stable with respect to quantum corrections [Su84].
- The unification of the three gauge couplings at the GUT scale $\Lambda_{\mathrm{GUT}} \approx 10^{15}$ GeV which is not possible in the standard model.
- The existence of dark matter which is unexplainable within the Standard Model of particle physics [Be05a].

It seems straightforward to attribute *Dark Matter* to the existence of a neutral stable *thermal relic* particle, i.e. a particle which was in thermal equilibrium with all other particles in the early Universe for temperatures above its mass. Coincidently, such a particle which could yield the observed density of dark matter if its mass and interaction rate were governed by new physics at the TeV – scale.

In the *canonical* scenario of supersymmetry, a stable lightest supersymmetric particle (LSP) exists [Ha85a, Ni84, Ch88]. For most typical choices of model parameters, the lightest neutralino is the LSP. The stability of the LSP is ensured by the conservation of R – parity. R – parity is a multiplicative quantum

[†] In this context, soft symmetry – breaking terms are non – supersymmetric terms in the Lagrangian which are linear, quadratic or cubic in the fields, with some restrictions elaborated in ref. [Gi82, Ha90, Ja99].

number distinguishing SM particles from SUSY particles. R – parity or another mechanism which keeps the LSP stable is needed to explain the observed stability of the proton. Searches for exotic isotopes demand that a stable LSP must be electrically neutral.

The supersymmetric partner of the neutrino, the sneutrino, $\tilde{\nu}$, and the neutralino χ, a superposition of bino, photino and higgsino fields are natural candidates. The large annihilation cross – sections force the sneutrino mass to exceed several hundred GeV to satisfy the constraints of *Dark Matter* energy density. From a theoretical point of view, the sneutrino mass is uncomfortably heavy for the LSP in light of naturalness arguments. Moreover, the outcome of several WIMP searches rules out the ordinary sneutrino to be primary component of the *Dark Matter* halo in our galaxy. However, in models with gauge – mediated SUSY breaking, the lightest neutrino could still make a good WIMP [Di96].

Thus the most widely studied WIMP candidate is the lightest neutralino. Calculations show that the lightest neutralino will have the correct thermal relic density in several distinct regions of parameter space [Ba03, Bo03, El03a, El03b].

It should be noted that the thermal relic density can be modified by coannihilation. In such a scenario, the decay of the next lightest supersymmetric particle (NLSP) can reduce the relic density of the LSP. Since the cross – section for interactions between the NLSP and the neutralino χ is generally much larger than the cross – section for the $\chi - \chi$ self interaction, the LSP is kept longer in thermal equilibrium. Thus the LSP will decouple later with a reduced relic density.

The richness of SUSY models allow for further supersymmetric dark matter candidates, which are virtually impossible to detect. These particles include the gravitino, the spin $^3/_2$ superpartner of the graviton[Bo98], and the axino, the spin $^1/2$ superpartner of the axion [Co01]. In models assuming gauge – mediated supersymmetry breaking (GMSB)[Di97], the LSP is the supersymmetric partner of the graviton, the gravitino, a weakly interacting fermion which mass can be as low as a keV [‡]. A gravitino with a mass on the TeV scale is in contradiction with cosmological constraints, as a stable heavy gravitino produces too a relic dark matter density which is too large. On the other hand, an unstable gravitino interferes with nucleosynthesis, as the decay radiation from the gravitino would break up all nuclei [Mo93].

[‡]It can be shown, assuming no dilution of the gravitino during the early phase of the Universe, that cosmology requires a gravitino mass of $m_{\tilde{g}_{3/2}} \lesssim 2h^2\text{keV}$. In this formula, h is the Hubble constant in units of 100 $^{\text{km}}/_{\text{sMpc}}$

1.4.4 Extra Dimensions

Although the space – time we observe appears to consist of three space and one time dimension, it is not inconceivable that further dimensions reveal themselves at higher energy scales. The concept of extra dimensions received great popularity after the idea of Kaluza and Klein in 1921, who tried to unify electromagnetism with gravity by identifying the extra components of the metric tensor with the usual gauge fields [Ka21, Kl26]. The original theory was plagued by internal inconsistencies and was abandoned until the advent of supergravity in the late 1970s.

Later on it has been realized that a possible solution to the hierarchy problem could be achieved by exploiting the geometry of space – time. If, as in many extra – dimensional models, the ordinary $(3 + 1)$ dimensional space – time is a *brane* embedded in a $(3 + \delta + 1)$ dimensional *bulk* space – time, the hierarchy problem can be addressed by compactifying the extra dimensions. This allows that the fundamental Planck scale can be lowered to an energy near the electroweak scale, a scenario which has been introduced by Arkani – Hamed, Dimopoulos and Dvali (ADD) [Ar98]. Alternatively, this is achievable by the introduction of large curvature extra dimensions (warped extra dimensions) as has been suggested by Randall and Sundrum (RS) [Ra99]. Furthermore, there is a scenario called universal extra dimensions (UED) which introduces flat extra dimensions much smaller that those found in the ADD framework. In the two other scenarios the only field able to propagate through the bulk dimension is the gravitational field; in the universal extra dimension framework, all fields are allowed to freely propagate through the extra dimensions because the extra dimensions are small enough to avoid contradictions between theory and experiment. Additionally, there is phenomenological motivation to allow Standard Model (SM) fields to propagate in the bulk. Among the features the theory of universal extra dimensions are [Se03][§]:

- A motivation for three families of SM fields from anomaly cancellation.
- Dynamical electroweak symmetry breaking.
- The prevention of rapid proton decay.
- A viable dark matter candidate.

Additional motivation for the study of theories with extra dimensions comes from *string theory* and *M – theory*, which may be the best candidates for a consistent theory for quantum gravity and for the unification of all interactions. Such theories seem to require seven additional extra dimensions at least.

A general feature of extra – dimensional theories is that upon compactification of the extra dimensions, the fields propagating in the bulk have their momentum quantized in units of $p^2_{\text{bulk}} \approx \frac{1}{R^2}$. In the case of a single extra dimension, precision electroweak measurements put a constraint on the inverse radius of the extra dimension in UED models as low as $R^{-1} \gtrsim 300$ GeV [Ap01].

[§]For the rest of this section, only the theory of extra dimensions is considered.

If the fermion fields are constrained to the *brane*, as proposed in the ADD and RS frameworks, the constraint on the compactification scale is much stronger, demanding $R^{-1} \gtrsim$ several TeV [Ch02a].

For each bulk field, a set of Fourier expanded modes emerge, which are called Kaluza – Klein (KK) states. On our ordinary $(3+1)$ dimensional world brane, these KK states of the standard model particles appear as a tower of states with masses $m_{\mathrm{KKn}} = \frac{n}{R}$, where n labels the mode number and R is the dimension of the compactified extra dimension. Each of this KK states shares all the quantum numbers of the corresponding SM particle. The existence of a viable dark matter candidate is a consequence of momentum conservation in the compactified dimensions. This leads to the conservation of the KK number which cannot stabilize the lightest KK state. If the possibility to generate chiral fermions in the zeroth KK mode is required, like it is for SM particles, then the extra dimensions must be modeled out by an orbifold such as ${}^{S}/_{Z_2}$ in the case of one extra dimension. This orbifolding results in the violation of KK number, but can leave a remnant of this symmetry called KK – parity. Since all odd – level KK particles carry charge of this symmetry, the first excited KK state is stable. This stabilizes the lightest Kaluza – Klein (LKP) particle in a way quite analogous to the way the LSP which is stable due to R – parity conserving supersymmetry.

In the context of UED, the LKP is most likely to be associated with the first excitation of the hypercharge gauge boson [Ch02b], commonly this state is referred to as $B^{(1)}$. A calculation of the $B^{(1)}$ relic density yields that if the LKP is to account for the observed dark matter density Ω_{DM}, it mass should lie in the range of 400 – 1200 GeV [Se03]. The results for the LKP relic density calculation can vary depending on the spectrum of the other first level KK states. Unlike in the case of supersymmetry, the density of KK matter is *increased* through coannihilations with other KK particles. This results from the fact, that the interaction between the $B^{(1)}$ LKP and the next lightest Kaluza – Klein particle (NLKP) are comparable with the $B^{(1)}$ self – interaction while in the case of SUSY particles the interaction between LSP and NLSP are much larger than the LSP self – interaction. For the KK particles, decoupling in the presence of coannihilations happens at the same time as in the case of no coannihilations, the LKP density is later increased as the NLKP decays to the LKP.

The branching ratios for the $B^{(1)}$ annihilation is rather insensitive to the particle mass. The deeper reason for this is given in the bosonic nature of the LKP which implies that its annihilation is not chirally suppressed, allowing it to decay efficiently to fermion pairs. A large fraction of the LKP annihilation channels produce charged lepton pairs, as its annihilation cross – section is proportional to the hypercharge of the final state. This fact can be used to discern the nature of *Dark Matter* in indirect detection experiments as the secondary radiation from decays of fermionic LSPs differs from the radiation signature of bosonic LKPs.

1.4.5 Axions

The axion is the pseudo – Nambu – Goldstone boson of the Peccei – Quinn (PQ) solution to the strong CP problem [We78, Pe77a, Pe77b, Wi78]. Despite its assumed small mass, it is a viable *Dark Matter* candidate as several mechanisms have been proposed which allow the creation of cold axion populations which were never in thermal equilibrium with the rest of the Universe [Di83, Pr83, Ab83, Ya99, Na94].

The strong CP problem arises from the non – Abelian nature of the gauge symmetry of *Quantumchromodynamics* (QCD). As non – Abelian gauge potentials have disjoint sectors which cannot be transformed continuously into each other, there is no unique vacuum. Instead the vacuum configurations can be labeled uniquely by their integer topological winding number n. Thus the gauge invariant QCD vacuum state is given by a superposition of these configurations,

$$|\theta\rangle = \sum_n \exp(-i\theta n)|n\rangle. \tag{1.38}$$

The angle θ is a parameter describing the QCD vacuum state $|\theta\rangle$. The Adler – Bell – Jackiw anomaly breaks the classical chiral symmetry QCD exhibits in the massless quark limit [Ad69, Be69]. If quark masses are included, the physics of QCD is invariant under the following transformations:

$$q_i \to \exp(\frac{i\alpha_i\gamma_5}{2})q_i, \tag{1.39}$$

$$m_i \to \exp(-i\alpha_i)m_i, \tag{1.40}$$

$$\theta \to \theta - \sum_{i=1}^{N} \alpha_i. \tag{1.41}$$

The equation above shows the transformations of the quark fields q_i, the quark masses m_i and vacuum parameter θ. The phases are given by the α_i. Reshuffling the phases between the quark masses m_i and θ allow the construction of the invariant and thus observable quantity $\bar{\theta}$:

$$\bar{\theta} \equiv \theta - \arg\det \mathcal{M}, \tag{1.42}$$

where $\mathcal{M}$ is the quark mass matrix. The presence of θ in QCD violates the two discrete symmetries parity, **P**, and the combination of charge conjugation and parity, **CP**. But **CP** violation is not observed in strong interactions, i.e. the most easily observable effect of strong CP violation, a neutron electric dipole moment $|d_n|$ results in a upper limit of $|\bar{\theta}| \lesssim 10^{-9}$ [Ha99]. However, as CP violation in the standard model arises from complex quark masses, the natural value of θ is of order unity. Thus the closeness of $\bar{\theta}$ to zero constitutes the strong CP problem.

A light pseudo – Nambu – Goldstone boson, the axion a, arises in the Peccei – Quinn solution to this problem. In addition, the properties of the axion render it a viable particle candidate to explain *Dark Matter*. To illuminate the aptitude of the axion as a *Dark Matter* candidate, the theoretical range of its interaction strength and mass is shown.

It is convenient to define the axion decay constant f_a with the interaction Lagrangian of the axion given below:

$$\mathcal{L} = \left(\bar{\theta} - \frac{\phi_a}{f_a}\right) \frac{\alpha_s}{8\pi} F^{\mu\nu a} \tilde{F}^a_{\mu\nu}, \tag{1.43}$$

where ϕ_a is the axion field. Non – perturbative effects of QCD induce a potential for ϕ_a with a minimum at $\phi_a = \bar{\theta} f_a$, thus canceling $\bar{\theta}$ and solving the strong CP problem. The mass of the axion is inversely proportional to its decay constant f_a [Ra90]:

$$m_a = 0.62 \times \frac{10^{16}(\mathrm{eV})^2}{f_a}. \tag{1.44}$$

The original Peccei – Quinn axion model assumed that the axion decay constant f_a was on the order of the scale of electroweak symmetry breaking [We78, Pe77a, Pe77b, Wi78]. However, experiments exclude this model [Do78, Ba81a, Ba81b, Kr86].

The introduction of a new energy scale much larger than the electroweak scale can save the PQ idea. When the new energy scale where PQ symmetry is spontaneously broken is large enough, the mass of the axion can be pushed below all existing experimental limits. Two benchmark models for such extremely weak interacting axion models exist: In the Kim – Shifman – Vainshtein – Zakharov (KSVZ) or *hadronic* axion model, a new heavy quark which transforms as electroweak singulet is introduced additionally to an additional electroweak singulet scalar. While the ordinary fermions are PQ neutral, their interactions with the axion are mediated via the heavy quark field [Ki79, Sh80]. The Dine – Fischler – Srednicki – Zhitnitsky (DFSZ) model does not require additional quarks but two Higgs doublets and an additional singulet electroweak scalar. The scalar acquires a vacuum expectation value at the PQ symmetry breaking scale and couples to the fermions via its interactions with the two Higgs doublets [Zh80, Di83]. Both models contain at least one electroweak scalar boson which acquires a non – vanishing expectation value and breaks PQ symmetry. Such an invisible axion with a large decay constant $f_a \sim 10^{12}$ GeV provides a viable candidate for a *cold Dark Matter* particle [Di83, Pr83, Ab83, Tu86]. Higher f_a produce an axion energy density which exceeds Ω_{DM} and overcloses the Universe. The strength of the couplings of the axion to other particles are generally inversely proportional to f_a, but the exact strengths are model dependent.

1.4.6 Superheavy Dark Matter Candidates

Since partial wave unitarity of the S – matrix demands a maximum annihilation cross – section $\langle \sigma \mathrm{v} \rangle$ for a particle of a given mass m, *Dark Matter* particle candidates which went through the thermal freeze – out are limited in mass [Gr90].

Using the WMAP constraint on Ω_{DM}, the maximum mass of a dark matter particle which is a thermal relic of the early Universe is limited to $m_{\mathrm{DM}} \lesssim 120\mathrm{TeV}$ [¶]. There is still a possibility to evade this limit, and conceive super – heavy particles with masses $m_{\mathrm{DM}} > 10^{10}$ GeV if these particles were never in thermal equilibrium during freeze – out. If this is the case, then their relic abundance is not dependent on their annihilation cross – section but on their production cross – section. They have to be stable enough to contribute to the present day matter density, however.

Natural mass scales for these superheavy dark matter particles are the scale of inflation, (10^{11} GeV), or grand unified masses, (10^{16} GeV). The main motivation for superheavy dark matter particles has been the observation of cosmic rays at energies above the Greisen – Zatsepin – Kuzmin (GZK) [Gr66, Za66] cut – off by the AGASA experiment [Ta03]. Above the GZK cut – off at $\sim 5 \times 10^{10}$ GeV, protons interact resonantly with CMB photons with a center – of-mass energy nearly the mass of the Δ (1.232 GeV). The large cross – section for this reaction turns the Universe opaque to ultra – relativistic protons over cosmological distances ($\lesssim 50$ Mpc). The lack of known sources for ultra relativistic particles within this range spurred the development of exotic scenarios like the *Wimpzillas*.

Recent measurements of the ultra high energy cosmic ray spectrum confirm the GZK cut – off in contradiction to the AGASA result [Ab08]. Since the AUGER experiment does not observe cosmic rays above the GZK cut – off, it seems that the main motivation for superheavy dark matter has gone.

[¶] The reduction by a factor of ≈ 3 to the limit given in [Gr90] is due to the better constraints on Ω_{DM} from the WMAP experiment.

1.4.7 Conclusion

In previous sections the most promising theories for *Dark Matter* were investigated. As it has been shown, additional requirements for the candidates for *Dark Matter* emerged:

- As large amounts of *baryonic Dark Matter* can be excluded to abound the halo of our galaxy, the presence of *non – baryonic Dark Matter* is needed to explain the observed rotational velocities of our galaxy. This spurns the effort to look for direct or indirect signatures of *Dark Matter* in our galactic neighborhood.
- The neutrino as *hot Dark Matter* can be excluded to constitute the bulk of the required *Dark Matter* in the Universe due to problems with structure formation in the early Universe.
- Relics from the early Universe which could constitute *Superheavy Dark Matter* are in contradiction to the absence of cosmic rays above the GZK cut – off.

The remaining candidates are required to be *cold Dark Matter*. The most established candidates are medium mass ($\approx$ 1GeV $< m_\chi <\approx$ 100TeV) weakly interacting particles (WIMP), which are well motivated by supersymmetric extensions of the Standard Model or extra – dimensional theories and light $\approx 1\mu$eV $< m_a <\approx$ 1meV axions. If supersymmetry and axions are both realized in the Universe, the supersymmetric particle of the axion, the axino $\tilde{a}$ can emerge as an additional candidate for *cold Dark Matter* in some scenarios. Depending on the mechanism breaking supersymmetry, the gravitino, $\tilde{g}$ can emerge as candidate of *Dark Matter*. If this scenario is realized, the fact that the gravitino only interacts gravitationally will render the direct detection of *Dark Matter* nigh impossible.

Fig. 1.9 gives an overview of the expected masses and cross – sections with ordinary matter for the discussed well – motivated CDM particles.

It should be noted that the presented list of candidates is by no means complete, for example an alternative mechanism to supersymmetry which stabilizes the weak scale, the *little Higgs* models provide stable scalar particles which can provide the measured *Dark Matter* density, too [Bi03, Ch03].

Many other theories can provide candidates for *Dark Matter*, a review of non – baryonic candidates can be found in refs. [El00, Be00].

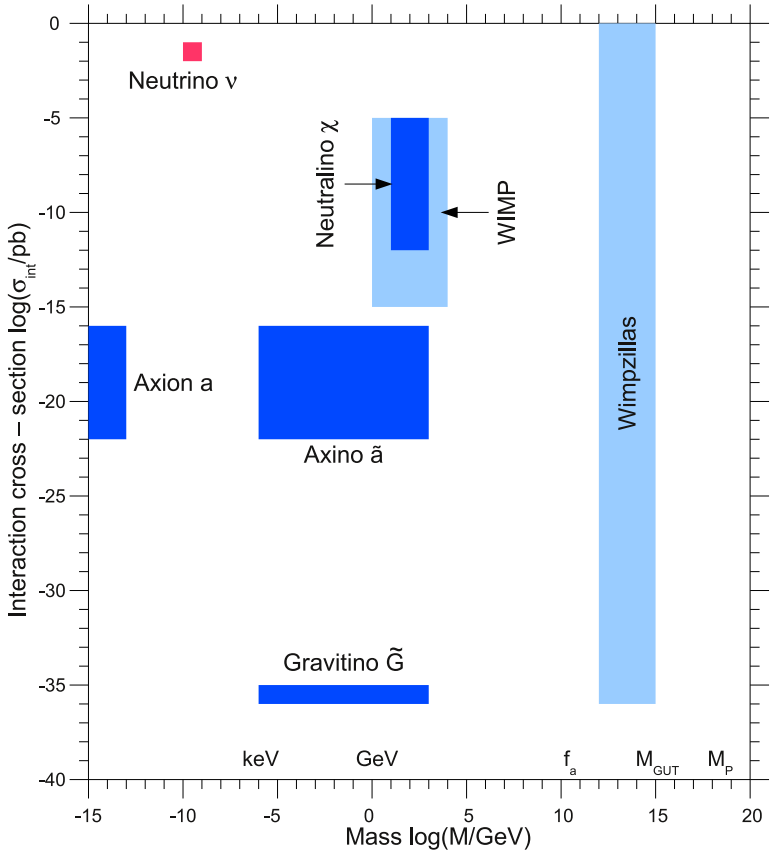

Figure 1.9: A schematic representation of some well motivated cold Dark Matter candidates. σ_{int} is the typical interaction strength in units of pb of particle with ordinary matter is shown. On the x – axis, the expected particle mass m_X in units of GeV is given. The area marked "WIMP" represents several mid mass candidates, e.g. the LKP from Kaluza – Klein scenarios. The neutrino is shown for comparison only, as it constitutes *hot* Dark Matter and is disfavored by structure formation arguments. The figure is drawn according to one found in Ref. [Ro04].

Chapter 2

Dark Matter Detection

The previous chapter presented some candidate particles for *Dark Matter*. In this chapter, general detection techniques for axions and WIMPs are presented. It is argued that the detection of particles beyond the Standard Model in collider experiments cannot resolve the question about the nature of the astronomically observed *Dark Matter* concludingly. In order to establish a firm link between a *Dark Matter* particle candidate and the observed effects of *Dark Matter* in the Universe, it must be shown that the particle is abundant in the Universe today. Both direct and indirect detection experiments looking for WIMP *Dark Matter* are addressed. A short summary of experiments looking for axions is given, too.

Observations indicate the presence of copious amounts of *Dark Matter* within galaxies and the halo of galaxies. As the distribution of *Dark Matter* in the galaxy is not known, it has to be modeled.

The most basic approach is to assume an isotropic and isothermal *Dark Matter* halo with a density profile $\rho(r) \propto r^{-2}$. In reality, observational constraints and numerical simulations indicate that *Dark Matter* halos deviate from the simple r^{-2} density profile and are anisotropic [Be98, Wi08].

Deep within the gravitational well of a galaxy, an overabundance of *Dark Matter* is expected. If the *Dark Matter* particle χ is a Majorana particle, two χ can annihilate and produce secondary particles with a total energy of two m_χ. The expected reaction rate depends on $\rho_\chi^2(\vec{x})$, thus regions of overdensity like the center of the galaxy should show an enhanced reaction rate. The search for the secondary particles of *Dark Matter* annihilation is labeled indirect detection. Indirect detection relies critically on the knowledge and modeling of the interactions of the secondary particles with the galactic environments, i.e. the gas distribution of the galaxy and the halo, the magnetic field and the interstellar radiation field.

For high – energetic γ – rays and neutrinos, the direction to the source can be identified relatively easy. The other channel for indirect *Dark Matter* detection are high – energetic positrons. Positrons and other charged cosmic rays diffuse through the galaxy and the halo as they interact with the local matter and the magnetic field. Thus they yield no information about the location of their origin.

In direct detection experiments one looks for the interaction of a WIMP with a suitable detector in a laboratory on earth.

In the isothermal, isotropic halo model, the mean velocity of the WIMPs is equal to the local circular velocity $v_c \approx 218 \pm 7$ $^{\mathrm{km}}/_{s}$ [Fe97]. For a laboratory on earth, this velocity has to be modified by the peculiar motion of the sun and the motion of earth around the sun. For these velocities, WIMPs will interact with ordinary matter through elastic scattering on nuclei. For WIMP type *Dark Matter*, direct detection experiments try to detect the recoil of an impinging dark matter particle on a nucleus in the detector.

This type of experiments needs a superb background reduction for the expected signature. For the sensitivity achieved in this field today, shielding from cosmic rays is mandatory, thus these experiments are located in underground laboratories. On top of that, radioactive contaminations of the experimental setup have to be avoided carefully and a reliable discrimination technique to distinguish natural radioactive background from the expected signal must be conceived.

2.1 Dark Matter Detection at Collider Experiments

If the *Dark Matter* particle has a mass in the range of a few tens of GeV up to roughly two TeV, the Large Hadron Collider (LHC) can produce such a particle. Unfortunately, it is impossible to determine the life – time of a produced neutral particle in a collider experiment if the life – time exceeds $\approx 10^{-8}$ s. Thus the LHC can provide only a *Dark Matter* particle candidate within a quite narrow mass range, since a collider experiment cannot probe the required stability of the particle [Ka08].

2.2 Indirect Detection of Dark Matter

The indirect detection of *Dark Matter* is the attempt to detect the signature of the annihilation of *Dark Matter* particles with the corresponding anti – particles. The annihilation rate is generally proportional to the density of WIMPs (ρ_χ) and anti – WIMPs ($\rho_{\bar{\chi}}$):

$$\sigma \propto \rho_\chi \rho_{\bar{\chi}}. \tag{2.1}$$

If sufficient over – densities of *Dark Matter* particles are located within our galaxy, a detectable flux of secondaries from WIMP annihilation can be detectable. The expected signal is highly dependent on the model of the *Dark Matter* halo density profile. Furthermore, the propagation of the produced secondaries through the galactic medium and the galactic magnetic field must be modeled, too.

The potential messengers heralding WIMP annihilation are anti – matter particles, synchrotron radiation of the produced charged secondaries, neutrinos and gamma rays. On top of the expected signal in each channel, ordinary physics happening in the galaxy provides a background.

High energetic positrons thermalize quickly due to inverse Compton – scattering off cosmic microwave background photons and synchrotron radiation in the galactic magnetic field. This restricts detectable flux to regions a few kpc nearby. Within this reach, the galactic center as most likely region of *Dark Matter* annihilation is located. Anti – protons are expected as well in *Dark Matter* annihilations and can travel much longer distances than positrons. During their passage of the interstellar medium they are expected to create additional secondary signals which should be observable if the anti – protons travel through regions outside the galactic plane.

The PAMELA satellite measured the ratio of positrons to electrons as well as the anti – proton to proton ratio up to energies of 100 GeV*. An anomalous positron excess has been detected while the measured $\bar{p}/p$ ratio is in agreement with standard secondary production models of cosmic ray propagation in the galactic medium [Bo09]. This asymmetry severely constraints *Dark Matter* models as they usually predict symmetric leptonic and hadronic secondary production. Standard astrophysics still offers many explanations for the positron excess, like nearby young pulsars or supernova remnants.

Dark Matter particle annihilation can proceed via the $\gamma\gamma$, γZ or γh decay channels, resulting in monoenergetic γ – rays. This monoenergetic lines are readily distinguishable from astrophysical sources and would serve as smoking gun evidence for *Dark Matter* annihilation. On top of these monoenergetic lines, the hadronic ($b\bar{b}$) and leptonic ($\mu\bar{\mu}$) decay channels will contribute continuous γ – ray spectra. It can be assumed that the γ-rays in the energy range of those produced in the annihilation process of *Dark Matter* propagate diffusionless. If detected, they reveal directly the line of sight to the region where *Dark Matter* annihilation commences. While no model for the diffusion of the γ-rays is needed, the dependency on the model for density profile of the *Dark Matter* persists.

Standard astrophysical processes are responsible for a large flux of high energetic γ – rays from the center of our galaxy which constitute a serious background [Za06]. The Fermi LAT satellite experiment searched eleven month for γ – lines from 30 GeV to 200 GeV obtained upper limits for γ – ray flux in the range of $0.6 - 4.5 \times 10^{-9}$ $^{\mathrm{cm}^2}/_{\mathrm{s}}$. Typical thermal WIMPs and standard *Dark Matter* halo models predict fluxes lower by one or more orders of magnitude [Ab10].

On top of the monoenergetic lines dwells a continuum of γ – rays from inverse Compton scattering on the galactic radiation field and synchrotron radiation from interactions with the galactic magnetic field. The synchrotron radiation

*This is the energy range of the published data in Ref. [Bo09]. The instrument is designed to detect e^+ in the energy range of 50 MeV to 300 GeV and $\bar{p}$ in the energy range of 80 MeV to 190 GeV.

is detectable by cosmic microwave background experiments [Ho07a]. The inverse Compton scattering of these leptons on photons of the cosmic microwave background or the starlight results in MeV to GeV γ – rays and is accessible by instruments like Fermi LAT.

Although the amount of neutrinos produced in *Dark Matter* annihilation in galactic or extra – galactic sources is too small to be detectable, WIMP *Dark Matter* annihilation in the center of the sun could potentially generate a detectable flux of monoenergetic high energy neutrinos via the $\nu\bar{\nu}$ channel or via decaying muons from the $\mu\bar{\mu}$ annihilation channel [Ba08]. The neutrino telescopes Antares[Co10] and IceCube [Ha09] placed upper limits on the muon flux from the sun which corresponds to the favored decay channel of Kaluza – Klein type WIMPs and on the χp spin dependent cross – section from the assumed WIMP capture rate in the sun.

2.3 Axion Searches

This section presents the various experimental methods used in the search for axions. As pseudoscalar particle, an axion can be produced by the interaction of two photons:

$$\gamma + \gamma \rightarrow a. \tag{2.2}$$

If one of the photons is a virtual one, this effect is known as the Primakoff effect [Pr51]. In an external electromagnetic field, this may result in the mixing of photons and axions by the Lagrangian:

$$\mathcal{L}_{a\gamma\gamma} = g_{a\gamma} a \vec{E} \cdot \vec{B}. \tag{2.3}$$

The coupling constant $g_{a\gamma}$ is defined as:

$$g_{a\gamma\gamma} = \frac{\alpha g_\gamma}{\pi f_a}, \tag{2.4}$$

with the electromagnetic fine structure constant α, the axion decay constant f_a and a constant g_γ which contains the dependence on the axion model. The conversion of an axion in a strong magnetic field due to the Primakoff effect and the subsequent detection of the resulting photon opens the field for the experimental search for the axion. This approach for axion detection was proposed by Sikivie in 1985 [Si85].
Three types of experiments are currently employed in the search for the axion: Photon regeneration experiments, axion helioscopes and resonator cavities.

Photon regeneration is best described by the catchy phrase shining light through walls experiments. This method does not rely on either astrophysical or cosmological sources. However the confirmation of the existence of a particle in the laboratory does not prove it is responsible for the effects of *Dark Matter* in the Universe. Such an experiment produces axions coherently by shining a LASER beam through a strong magnetic field and reconvert the produced axions in a collinear magnetic field on the other side of an optical barrier [Bi87]. Current limits from photon regeneration are a coupling strength $g_{a\gamma} < 2 \times 10^{-7}\ {}^{1}/_{\mathrm{GeV}}$ for masses $m_a < 5 \times 10^{-4}$eV. This limits are provided by the BFRT experiment [Ca93], the BMV experiment [Ro07] and the GammeV experiment [Ch08]. While not competitive in the moment, future upgrades of photon regeneration experiments are going to strengthen the limits dramatically [Si07b].

Axion helioscopes try to detect the axions produced in the core of the Sun by converting them back to photons in a strong magnetic field. In the core of the Sun, axions would be produced with a thermal spectrum of a mean energy of ≈ 4.2 keV. By pointing a volume permeated by a magnetic field into the direction of the sun, conversions of axions to photons are expected within this volume. The CAST collaboration uses a prototype LHC dipole magnet as the basis for their helioscope. This collaboration has produced the best limits on solar axions, $g_{a\gamma} < 0.88 \times 10^{-10}\ {}^{1}/_{\mathrm{GeV}}$ for masses $m_a < 10$ meV [An07]. The sensitivity for axions can be enhanced by filling helioscope with a gas of appropriate pressure [Bi89]. Employing this technique, the CAST experiment [Ar09a] and the SUMICO collaboration [In10] put limits on axions in the eV mass range, excluding parts of the axion model band.

The third technique is the resonant conversion of axions to radio – frequency photons in a microwave cavity permeated by a strong magnetic field. By tuning the cavity to the resonant condition, $h\nu = m_a c^2$, the abundance of axions in the galactic halo can be probed. The main problem the cavity experiments face is the fact that only one resonance frequency can be checked at a time. This turns the measurement of a broader range of axion masses in a time consuming process. Today's most sensitive microwave cavity experiment is the ADMX experiment, which could exclude axions as *Dark Matter* in the narrow mass band between $3.5 < m_a < 3.53$ μeV if realistic axion models are considered [As10]. A plot of the combined limits on axions from various experiments is shown in Fig. 2.1.

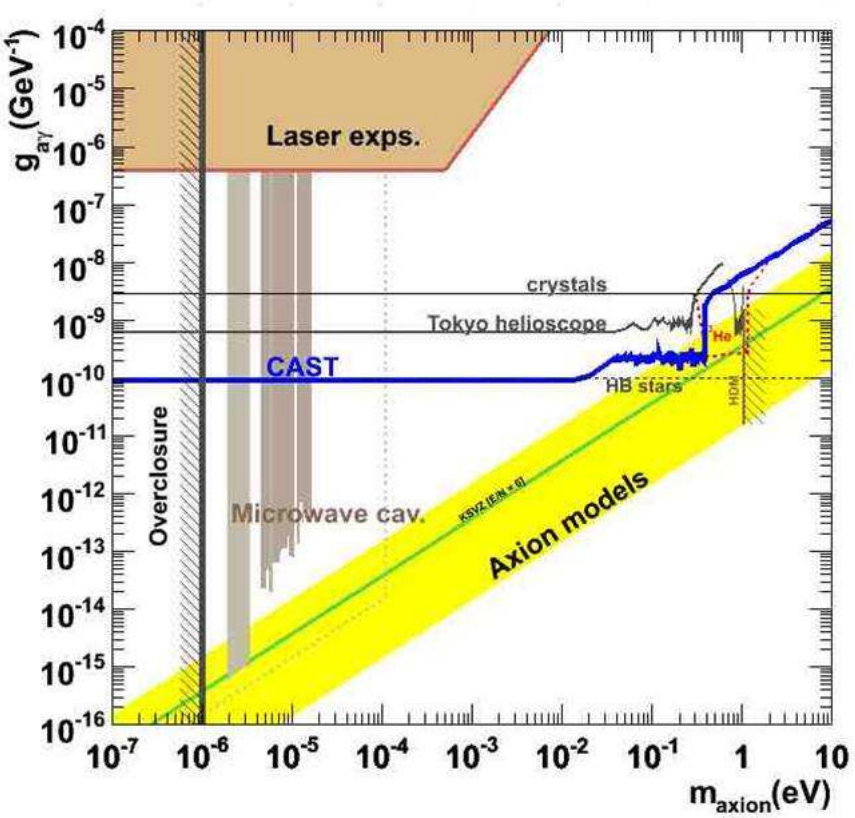

Figure 2.1: Exclusion plot on axions in the axion – photon coupling $g_{a\gamma}$ and the axion mass m_{axion}. Cavity, helioscope, LASER and underground detector experiments [Ah09a] are included. The brown line is the large scale structure formation *hot Dark Matter* (HDM) limit. The horizontal branch limit (HB) is derived from the cooling rate of HB stars [Ra06]. Overclosure arguments give a lower limit on m_{axion} [Pr83, Ab83, Di83]. The yellow band shows the theoretical range for KFVZ and DFSZ axions. This plot has been taken from Ref. [Ri09].

2.4 Direct Detection of Dark Matter

Direct detection of *Dark Matter* relies on the experimental detection of the rare interaction of a *Dark Matter* particle from the halo of our Galaxy with ordinary matter in a proper experimental setup. The interaction of WIMPs and ordinary nuclei can proceed via a spin – dependent (SD) or a spin – independent (SI) channel.

In the SD channel, the cross – section is proportional to the net angular momentum $\langle J \rangle$ of the protons and neutrons in the interacting nucleus. The matter is complicated further as the coupling of u and d quarks to the WIMPs are not expected to be exactly the same. Then the WIMP coupling to the proton and the neutron are expected to be different, too. The average effective angular momentum of a proton or a neutron in a given nucleus is an additional unknown which influences the WIMP – nucleus cross – section.

In the SI channel, coherent scattering of a WIMP on the nucleons of a nuclei result in $\sigma_{SI} \propto (Zf_p + (A - Z)f_n)^2$ for the WIMP – nucleus cross – section σ_{SI}. As the ratio of protons and neutrons differ between the nuclei, the average WIMP – nucleus cross – section depends on the target nucleus. Furthermore, the relative strength of the two channels is defined by the properties of the *Dark Matter* particle, too.

The direct detection approach is well suited for the detection of WIMP type *Dark Matter* particles in the mass range of a few tens to a few hundred GeV. For the velocities assumed for WIMPs in the galactic halo, the nuclear recoil is expected to be of the order of a few tens of keV. In this energy region, detectors are prone to a wide variety of background events induced by radioactivity of the experimental surroundings. Without a proper discrimination of the spurious events, the signal disappears in the much stronger background. Most modern experiments employ techniques which can discern nuclear recoils in the detector and signals due electrons and γs. Furthermore, it is possible to discriminate α – particles and protons from recoiling nuclei. This reduces the background from radioactivity to neutron induced nuclear recoils if the discrimination technique is applicable.

The DAMA/LIBRA experiment is located in the INFN laboratory Gran Sasso and operates ≈ 250 kg of highly radiopure NaI crystals read out by photomultiplier tubes (PMT). From a fit of the annual modulation of the observed count rate the presence of *Dark Matter* in the galactic halo with a confidence level of 8.2 σ is inferred [Be08a].

However, the straight forward WIMP interpretation of the modulation seen by DAMA/LIBRA is virtually excluded by the combination of the other direct *Dark Matter* searches.

The KIMS experiment runs 34.8 kg of scintillating CsI(Tl) crystals at the Yangyang Underground Laboratory in Korea read out by PMTs [Le07]. This experiment does not observe a modulation as seen in the DAMA/LIBRA experiment.

The COUPP experiment operates a bubble chamber of 1.5 kg superheated CF_3I at Fermi National Accelerator Laboratory (FNAL). The bubble chamber is examined photographically for bubbles due to interactions of impinging particles with the superheated liquid. The operation point of the bubble chamber can be tuned by its pressure and temperature such that only nuclear recoils provide the necessary energy loss for bubbles to form.

The results the COUPP experiment are in disagreement with a standard WIMP inferred from the modulation seen by the DAMA experiment [Be08b].

The TEXONO experiment operates ultra – low energy germanium semiconductor diodes (ULEG). This type of detectors is able to measure energies down to a threshold of 200 ± 10 eV with an efficiency of 50 percent. The low threshold is required to make the experiment competitive for the detection of low mass WIMPs. Parts of the DAMA – allowed region for the standard WIMP are excluded by the TEXONO experiment [Li09]. The bottleneck for further improvement are the very low masses of a few g of contemporary ULEGs.

The CoGeNext experiment operates a 500 g heavy p – type point contact germanium detector with a sub – keV threshold. The results are also excluding parts of the DAMA compatible standard WIMP parameter space [Aa08].

The following experiments allow the most stringent constraints on the medium mass WIMP type *Dark Matter*. The common method of these experiments is the simultaneous read – out of two independent signal channels of a detector. The ratio of the two signal strengths allows for the discrimination of various sources of energy deposition, i.e. it is possible to discern the energy deposition by a nuclear recoil from the energy deposition of an electron.

Liquid noble gas detectors like are three dimensional sensitive dual phase trajectory projection chambers (TPCs). Dual phase TPCs detect the direct scintillation light from an event in the liquid phase and the secondary proportional scintillation light in the gaseous phase from the ionization of the event driven in a high voltage field. The light is collected by photomultiplier tubes (PMT). The ratio of the primary and the secondary scintillation light allow the discrimination of nuclear recoils due to neutral particles from energy deposition of charged particles or γs. Three collaborations published exclusion limits on the *Dark Matter* – Nucleon cross – section, the XENON collaboration [An08] and the ZEPLIN – II collaboration [Al07] using a liquid xenon as target material and the WARP collaboration using liquid argon as target material [Be08c].

Another detector type consists of semi – conductor bolometers which are operated in such a way that the ionization and the heat deposited can be read out simultaneously. The required sensitivity of the bolometer demands operation temperatures close to absolute zero temperature. The discrimination between nuclear recoils and charged particles is possible in this case as the ionization yield, i.e. the amount of charged generated for a given heat deposition depends on the type of particle which deposited energy in the detector. Both silicium and germanium detectors of this type have been operated successfully.

The A^2 proportionality clearly favors the usage of germanium for the search for spin – independent WIMP – nucleon scattering. Both the CDMS collaboration [Ah09b] and the EDELWEISS collaboration [Ar09b] operated semi – conductor bolometers with different thermometer types successfully. In December 2009, the CDMS collaboration presented the most stringent limits on elastic, spin – independent WIMP – nucleus scattering.

If the cryogenic bolometer is made of an scintillating insulator, the scintillation light becomes detectable instead of the ionization. Thus the discrimination of the particle type becomes possible by light yield of a given event in the detector. If energy is deposited by a recoiling nucleus, the light is *quenched*; in comparison to an energy deposit by an electron or by a lighter particle, less scintillation light is produced in the crystal.

This technique allows the operation of a large variety of materials. The CRESST experiment operates a set of $CaWO_4$ bolometers at $\lesssim 30$ mk in the LNGS underground laboratory. The results of a successful commissioning run in 2008 can be found in Ref. [An09]. At the moment, the experiment is taking data with four times the number of detectors since mid 2009.

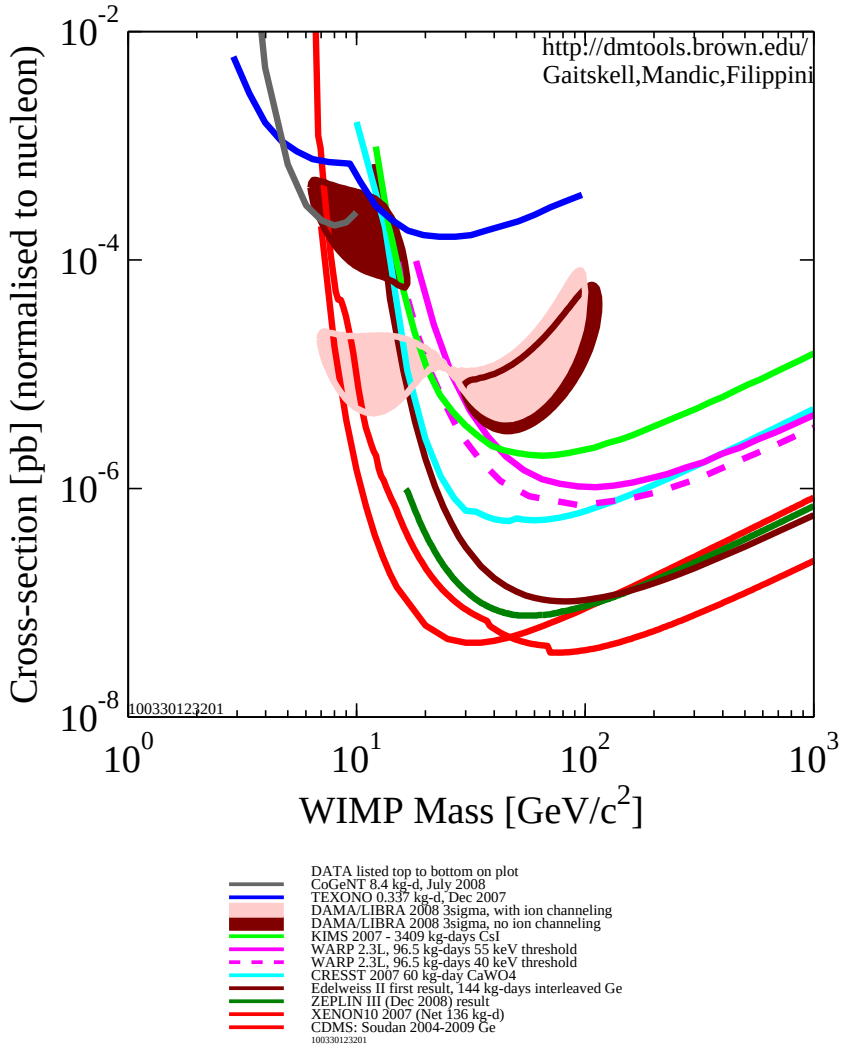

Figure 2.2: Spin – independent WIMP nucleon cross – section. The exclusion plots are based on the cited references given in Sec. 2.4. It has been generated via the DM exclusion plot generator available at *http://dmtools.berkeley.edu/limitplots/*.

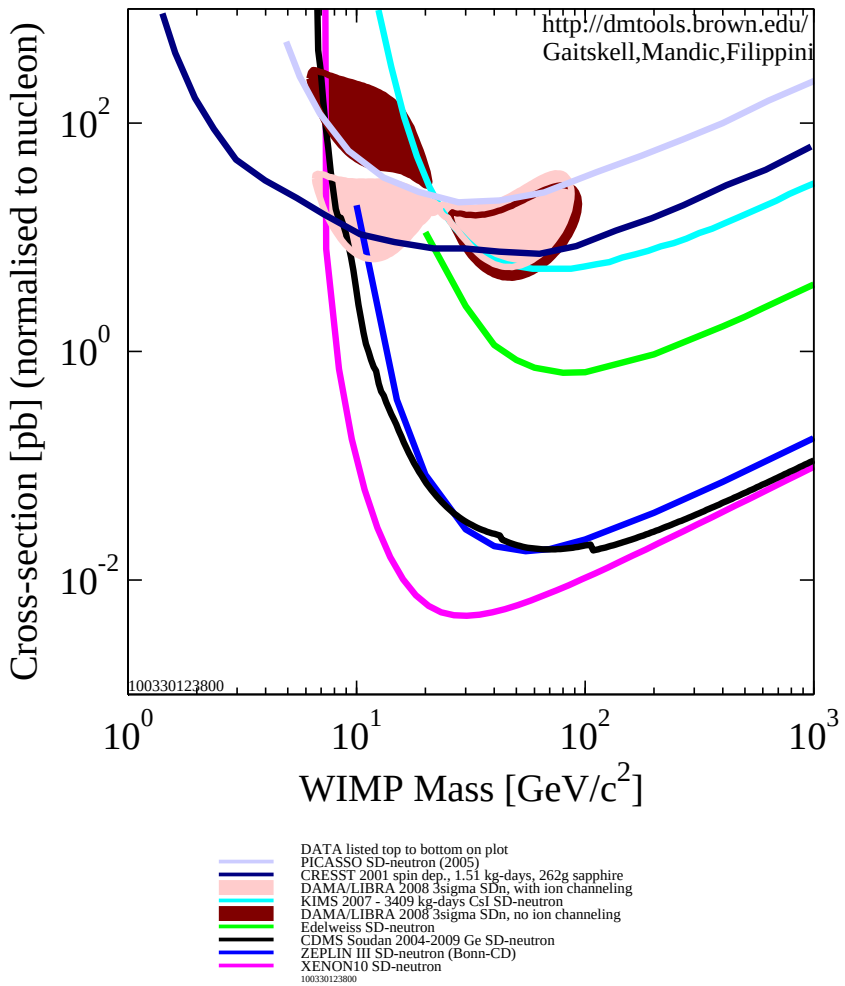

Figure 2.3: Spin – dependent WIMP neutron cross – section. The exclusion plots are based on the cited references given in Sec. 2.4. It has been generated via the DM exclusion plot generator available at *http://dmtools.berkeley.edu/limitplots/*.

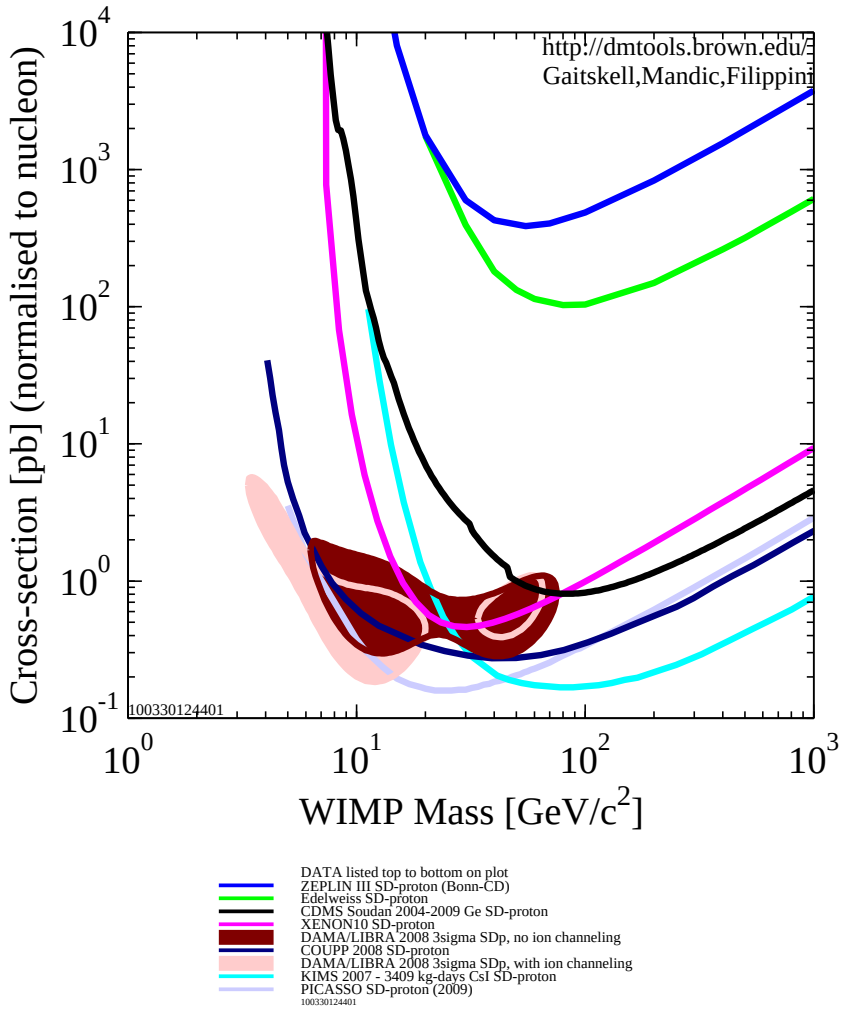

Figure 2.4: Spin – dependent WIMP proton cross – section. The exclusion plots are based on the cited references given in Sec. 2.4. It has been generated via the DM exclusion plot generator available at *http://dmtools.berkeley.edu/limitplots/*.

Chapter 3

Physics of neutron – nuclear interaction

The neutron – nuclear interactions result in possible background signals in direct *Dark Matter* detection experiments. In the section 3.1, a basic description of the underlying physics is presented. The richness of neutron – nuclear interactions on an energy scale ranging from thermal energies up to approximately 100 MeV seen for cosmogenic neutrons produced in muon showers requires the usage of specialized models for different energy ranges and reaction channels.

In a GEANT simulation, neutron – nuclear interactions are treated by four different implementations of physics processes which are driven by evaluated experimental data sets adopted from the ENDL databases:

- Elastic scattering of neutrons on nuclei, i.e. only kinetic energy is transferred to the scattered nucleus.
- Inelastic scattering of neutrons on nuclei, i.e. secondary particles are produced in the scattering reaction.
- Capture on the target nucleus, with a cascade of γs following the deexcitation of the nucleus.
- Induced fission, where the neutron induce the fragmentation of a heavy target nucleus into two lighter nuclei.

A quick overview of the implementation of the four reaction channels into GEANT4 is presented in the subsections 4.3.1 – 4.3.3 .

3.1 Basic Foundations of Neutron – Nuclear Interactions

The general theory of nuclear reactions is founded on the quantum – mechanical description of the scattering process. The fundamental equation of motion is the time dependent, multi – particle Schrödinger equation for the set of N nucleons of both the projectile and the target:

$$i\hbar\frac{\partial\Psi}{\partial t} = \mathcal{H}\Psi(t) \tag{3.1}$$

For a given Hamiltonian $\mathcal{H}$, the wave functions $\Psi(1,\ldots,N,t)$ solving the Schrödinger equation must obey the initial conditions and physical constraints of the experimental setup. In the limit $t \to \infty$, the wavefunction contains all information about the state of the system after the reaction. The result of a nuclear reaction depends not only on properties of the involved nuclei but also on the occurring interactions between those nuclei during the reaction process.

Since a nuclear reaction is not a stationary process, an adequate description of the projectile and the target must be given in the wave packet picture. In the initial state projectile and target are spatially separated and do not interact with each other. The dispersion of the wave – packet is assumed to be small on the time scale of the nuclear reaction itself and can be separated from the momentum change of the scattering process. Once the interaction zone is reached in configuration space, the state of the wave – packet changes*. This can lead to very complicated states within the interaction zone. As time progresses, the final state emerges as a wave – packet on the boundary of the interaction zone. Apart from the initial state wave package, all other reaction channels respecting the relevant conservation laws contribute to the final state, too.

A look at a typical plot of total cross – section versus kinetic energy of the projectile shows resonance like structures of vastly different widths Γ, called giant resonances, intermediate resonances and compound nucleus resonances. Using the uncertainty relation, the width of these resonances Γ can be related to the typical lifetime τ of the interacting system of the projectile and the target nucleus:

$$\Gamma \cdot \tau \simeq \hbar \tag{3.2}$$

$$\begin{aligned} \Gamma_R &= 1\ldots10\text{MeV}, \quad \tau_R = 10^{-21}\ldots10^{-22}s, \\ \Gamma_I &= 1\ldots10\text{keV}, \quad \tau_I = 10^{-18}\ldots10^{-19}s, \\ \Gamma_C &= 0.1\ldots1\text{eV}, \quad \tau_C = 10^{-14}\ldots10^{-15}s, \end{aligned}$$

While τ_R indicates a fast process since it is of the order of the time the projectile needs to traverse the diameter of the nucleus, the interaction time τ_C for

*The interaction zone is the region in which potentials of the various interactions between projectile and target are non negligible.

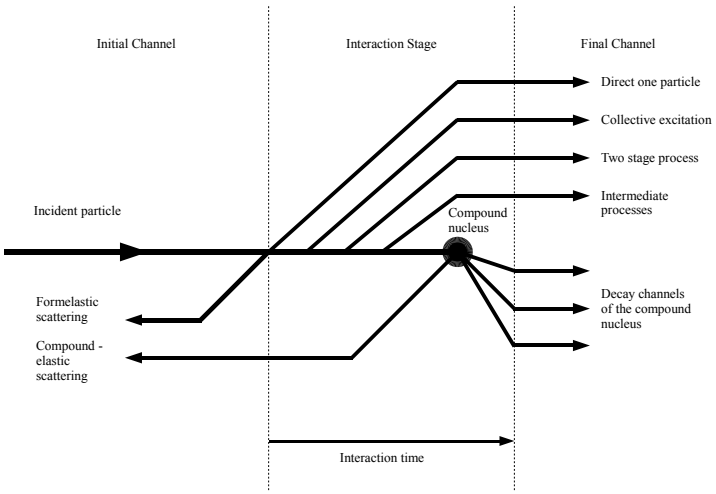

Figure 3.1: Schematic sketch of a general nuclear reaction.

compound nucleus resonances is about seven orders of magnitude longer. Broad giant resonances $\Gamma = \Gamma_R$ seen for high kinetic energies of the incident neutron, the optical model of nuclear interactions is a good description. The nucleus provides a potential well in which the incident particle can move freely and form stationary waves depending on its kinetic energy. In many cases, the shell model of the nucleus offers a good approach. The incident particle is partially absorbed or scattered while traversing a mean, complex valued one – particle potential V:

$$V(\mathbf{r}_a) = U(\mathbf{r}_a) + iW(\mathbf{r}_a) \tag{3.3}$$

After the definition of a suitable nuclear model describing the initial and final state and the separation of the specific interaction V_{ab}, the cross – section of a specific channel σ_{ab} can be calculated from matrix elements $< \Psi_f | V_{ab} | \Psi_i >$ for the direct quantum mechanical transition between initial and final state.

Narrow resonances $\Gamma = \Gamma C$ typically seen for incident energies in the few keV range are due to the formation of long – lived, highly excited compound nuclei which decay independently from its formation channel:

$$n + A \rightarrow C^* \rightarrow B + \sum b_i. \tag{3.4}$$

In the equation above, n denotes the neutron, A the target nucleus, $C^\star$ the compound nucleus, B the daughter nucleus and b_i the emitted secondary particles.

The excitation energy is statistically distributed on the many degrees of freedom of the compound nucleus, allowing the emission of a particle b_i only if it gained enough energy by statistical fluctuations. The quantum mechanical treatment of the reactions involving a compound nucleus requires a solution for a chain of transition probabilities between highly excited states of the compound

nucleus between the initial state Ψ_i and the final state Ψ_f. Such a calculation is impossible if wavefunctions of the intermediate states are unknown.

The statistical approach for the calculation of the scattering matrix by the Hausser – Feshbach theory becomes possible if the density of states of the compound nucleus allows for the simultaneous excitation of many states. This is the case if the width of the resonance Γ and the energy uncertainty in the initial channel ΔE_{in} is large against the energy spacing of the excited states of the compound nucleus ΔE_C. As the energy of the daughter nucleus rises, the number of final state grows exponentially. The calculation of single channels and the corresponding cross – sections becomes impractical if not impossible. In this case, the emission cross – section for a energy interval will be calculated by the complete statical theory of nuclear reactions, the Weisskopf – Ewing theory.

Intermediate processes exist between the extrema of direct reactions and compound nucleus reactions. Such reactions are considerably faster than compound nucleus reactions. A good approximation of such processes can be achieved by matrix elements with several intermediate states such as:

$$\sum_I < \Psi_f | V_{Ii} | \Psi_I >< \Psi_I | V_{iI} | \Psi_i > . \tag{3.5}$$

The capital letter I denotes an intermediate state. It should be kept in mind that a given nuclear reaction channel often show the characteristics of all three reaction mechanisms. A telling example for this situation is the compound – elastic reaction, where the incoming particle is absorbed and later remitted from the nucleus in its ground state without any emission of γs or other secondary particles.

Analogous to the classification of processes used in GEANT4, four distinct classes can be defined; elastic scattering, fission, inelastic scattering and capture reactions. Of these classes of interactions, elastic and inelastic scattering are the most relevant for the simulation of neutron background for dark matter experiments. A fission event will release several MeV, e.g. on average, an ^{235}U fission will release approximately 170 MeV in kinetic energy of the daughter nuclei, 4.8 MeV in kinetic energy of secondary neutrons and about eight MeV in prompt γ's [Mul80]. Thus an energy release into a direct *Dark Matter* detector events is by orders of magnitudes larger than the expected energies in WIMP – nucleus scattering.

Radiative capture reactions are discriminable from pure nuclear recoil background by the cascade of γs with a typical total energy in the range of a few MeV. However, for a high Z material like $CaWO_4$, the chance that all γs of such a cascade escape the detector is very low, allowing a clear identification of radiative capture events as discriminable background. As the cryogenic detector is slow ($\approx$ ms) in comparison to the nuclear reactions, the recoil and the detected gammas will be identified as the same event.

Chapter 4

Background simulations with GEANT4

In this chapter, an overview of neutron background simulations in GEANT4 is given and the strengths and shortcomings of GEANT4 with respect to the simulation of neutrons for the analysis of the background induced by them are discussed.

Almost all direct *Dark Matter* detection experiments rely on a unprecedented background reduction in the energetic region of interest where recoils due to *Dark Matter* particles are expected. As a result of this background reduction, the remaining background is comprised by only a few isolated events, and the familiar background subtraction technique proves pointless. In addition, the expected recoil energies are rather tiny, allowing all kinds of effects to distort the measured recoil energy. In the context of a simulation, this requires more than just statistical accuracy of the simulation, but accuracy on the single event basis*. Such a requirement is quite demanding for standard neutron propagation simulation tools, which were developed for either for higher energy or higher flux applications like FLUKA or MCNP [Ba07a, Fa05, Le06].

For the simulations presented in this work, GEANT4.9.1.3 was used which is a flexible monte – carlo simulation framework widely employed in physics. It relies on single particle tracking suited for few event statistics. As the source code is freely available, analysis of the underlying physics processes and their modification is possible within the framework.

*In this context, statistical accuracy implies that the simulation yields correct results for mean values from a large number of events after averaging, while accuracy on the single event basis requires that each reaction is treated properly in the light of the underlying physics, e.g. that energy and momentum conservation holds for every single event.

4.1 GEANT4: A Monte – Carlo Simulation Framework

The monte – carlo simulation package GEANT4 has been developed at CERN as a general simulation tool for the passage of particles through matter[Ag03, Al06]. The main focus of GEANT4 is the simulation of high energy collider experiments, but it is flexible enough to be employed for other experimental setups in particle physics as well. A legacy of its primal field of application is the tracking of particles along steps between their interactions with the surrounding material on a single event basis. This feature is well suited for the low level background simulation required in direct *Dark Matter* detection experiments.

All aspects of a particle physics simulation have been included in the framework and can be modified to suit the particular demands of the user:

- The geometry of the system,
- The materials involved,
- The fundamental particles of interest,
- The generation of primary events,
- The tracking of particles through materials and electromagnetic fields,
- The physics processes governing particle interactions,
- The response of sensitive detector components,
- The generation of event data,
- The storage of events and tracks,
- The visualization of the detector and particle trajectories, and
- The capture and analysis of simulation data at different levels of detail and refinement.

At the core of GEANT4 is an abundant set of physics models to handle the interactions of particles with matter across a very wide energy range. GEANT4 acts as a repository which incorporates a large part of all that is known about particle interactions, as data and expertise have been drawn from many sources. The framework is written in C++ and uses the object – oriented approach to allow for easy modification and extension of the code. The object – oriented methods help to manage complexity and limit dependencies by defining a uniform interface and common organizational principles for all physics models. By adhering to the object oriented paradigm, it allows a flexible way to handle specific physical problems:

For example, the objects which obtain the required cross sections via data files or computation are separated from the objects in which they are used or accessed. It is possible to overload both of these features if necessary. Similarly,

the computation of the final state of a reaction channel can be rerouted between alternative or complementary models on a flexible conditions, i.e. according to the energy range, the particle type, and the material. For the construction of a specific application the user chooses from these available options and implements code in user action classes supplied by the GEANT4 toolkit.

Within such a framework the functionality of models can be understood more intuitively. Additionally, the creation and addition of new models is a well – defined procedure that entails little or no modification to the existing code[†].

4.2 Physics Processes in GEANT4

Physics processes describe the particle interactions with the a particle found in a target material in GEANT4. These processes are derived from the actual physical models obtained from the experimentally observed physics or given by a theoretical model. Seven major categories of physics processes are provided by default:

- Electromagnetic,
- Hadronic,
- Decay,
- Photolepton – hadron,
- Optical,
- Parameterization,
- Transportation,

The object oriented design of GEANT4 makes the generalization and abstraction of physics processes a key issue. This approach ensures that new or modified processes can be created and assigned to a particle type. For the tracking of a given particle, each process has two important groups of methods, `GetPhysicalInteractionLength` (GPIL) and `DoIt`. The GPIL method gives the step length from the current space – time point to the next space – time point. This is done by the calculation of the probability of interaction based on the cross – section of the process. At the end of the step, the `DoIt` method implements the details of the interaction, changing the momentum, energy, direction and position of the particle as well as producing required secondary tracks.

[†]Several user guides are available at the following webpage: *http://geant4.web.cern.ch/geant4/support/userdocuments.shtml*. On this webpage, an installation guide, an application developer guide for simulations using the standard GEANT4 classes, an toolkit developer guide for the modification and extension of GEANT4 and a physics reference manual for the standard GEANT4 physics processes can be found.

4.2.1 Particles and Physics Processes Included in the Simulations

The particles which are considered in the neutron simulation include all particles which can be produced by the primary energies encountered in the simulation. For most simulations, the primary energy is below 20 MeV, which limits the number of producable particles to electrons, positrons, electron – neutrinos, $\bar{\nu}_e$, γs, protons, neutrons and various ions. For the simulation of high energy cosmogenic neutrons, additional particles have to be considered. Thus the heavier leptons and the zoo of heavy mesons and baryons is included into the particle list.

Electromagnetic interactions have been included for all charged particles encountered in the simulation. Standard vertex interactions and continuous interactions are included, e.g. the positron has a discrete annihilation process via `G4eplusAnihilation` and a continuous ionization process via `G4eIonisation`. An energy cutoff for $e^{\pm}$ and γs has been set to 250 eV, below this energy these particles deposit their total energy and are removed from the list of actively propagated particles.

Generally, the hadron particles have the following processes are attached to them: `G4LElastic` describing elastic scattering of hadrons via a parameterized approach, an appropriate `G4LEInelasticProcess` specialized for each hadron, and if charged, a multiple scattering process called `G4MultipleScattering` and an ionization process called `G4hLowEnergyIonisation`. The specific low energy processes for neutrons are investigated in the following section.

Decay processes are added for all unstable particles via the `G4Decay` process. Furthermore, decay processes for unstable nuclei which maybe produced by neutron capture or spallation have been included via `G4RadioactiveDecay` for all ions, i.e. all nuclei which are produced in the simulation.

For the high – energy regime above a few tens of MeV additional interaction processes are added for this energy range.

4.3 Implementation of Neutron Interaction in GEANT4

The neutron transport class library described in this section simulates the interactions of neutrons with kinetic energies from thermal energies up to about 20MeV. The upper limit is set by the comprehensive evaluated neutron scattering data libraries that the simulation is based on. The result is a set of secondary particles that can be passed on to the tracking sub – system for further geometric tracking within GEANT4.

The interactions of neutrons at low energies are split into four parts in analogy to the other hadronic processes in GEANT4. Elastic scattering, inelastic scattering, radiative capture, and fission are considered as separate models.

These models comply with the interface for use with the GEANT4 hadronic processes which enables their transparent use within the GEANT4 tool – kit.

All cross – section data are taken from the ENDF/B – VI [Ch06] evaluated data library. All inclusive cross – sections are treated as point – wise cross – sections for reasons of performance. For this purpose, the data from the evaluated data library have been processed, to explicitly include all neutron nuclear resonances in the form of point – like cross – sections rather than in the form of parameterizations. The resulting data have been transformed into a linearly interpolable format reducing the error due to linear interpolation between adjacent data points to the percent level. The inclusive cross – sections comply with the cross – sections data set interface of the GEANT4 hadronic design. When registered with the tool – kit at initialization, they are used to select the basic process. In the case of fission and inelastic scattering, point – wise semi – inclusive cross – sections are also used to select the active channel for an individual interaction.

4.3.1 Elastic Neutron Scattering

In the elastic neutron scattering, the incoming neutron scatters of the nuclear potential of the target nucleus without any internal excitations of either the neutron or the nucleus. For elastic scattering reactions, the momentum of recoil nucleus can adopt any angle to the incident direction and the recoil energy can take values between zero and a maximum energy given by:

$$E_{\mathrm{Rec}}^{\max} = 4\frac{m_n \cdot m_{\mathrm{t}}}{\left(m_n + m_{\mathrm{t}}\right)^2} E_n \tag{4.1}$$

In the formula above, m_n is the mass of the incident neutron, m_{t} denotes the mass of the target nucleus and E_n is the kinetic energy of the incident neutron.

The scattering amplitude $f(E_{\mathrm{inc}}, \theta)$ depends on the specific nuclear potential the target nucleus provides for the incident neutron.

All elastic neutron scattering event will be located in the same region in the scatterplot of light – yield versus total deposited energy where the nuclear recoils due to nucleus – WIMP interaction are expected. There is no possibility to discern experimentally if a given nuclear recoil resulted from elastic neutron scattering or WIMP – nucleus scattering.

The final state of elastic scattering is described by sampling the differential scattering cross-sections $\frac{d\sigma}{d\Omega}$. Two representations are supported for the normalized differential cross – section for elastic scattering. The first is a tabulation of the differential cross – section, as a function of the cosine of the scattering angle θ and the kinetic energy E of the incoming neutron.

$$\frac{d\sigma}{d\Omega} = \frac{d\sigma}{d\Omega}\left(\cos\theta, E\right). \tag{4.2}$$

In the second representation, the normalized cross-section are represented as a series of Legendre polynomials $P_\ell(\cos\theta)$, and the Legendre coefficients a_ℓ are tabulated as a function of the incoming energy of the neutron.

$$\frac{2\pi}{\sigma(E)}\frac{d\sigma}{d\Omega}(\cos\theta, E) = \sum_{\ell=0}^{n_\ell}\frac{2\ell+1}{2}a_\ell(E)P_\ell(\cos\theta) \tag{4.3}$$

In both cases, the kinematics of the elastic scattering can be calculated from the available data unambiguously. The momentum and the energy of both the scattered neutron and the recoiling nucleus will be distributed according to the input data files.

4.3.2 Inelastic Neutron Scattering

During an inelastic neutron scattering, the internal energy of the target nucleus is changed. The nucleus then de – excites via emission of γs or hadrons like neutrons, protons, αs and heavier fragments.

For low neutron energies, the de – Broglie wavelength of the incident neutron is on the scale of the size of the target nucleus. In this case, the neutron interacts with the target nucleus as a whole. For low energies the formation of a compound nucleus is most probable. From this compound nucleus a hadron can evaporate and any remaining internal excitation energy is emitted via γs. As the de – Broglie wavelength shortens with rising energy, the probability of an direct interaction of the incident neutron to interact with a single nucleon or an α – particle within the target nucleus increases. In such a direct interaction, both the neutron and other target constituent can be emitted. With rising incident energies, the nucleus tends to act as spectator to the reaction, albeit γs can be emitted from the final state nucleus if it is left in an excited state.

Since the total kinetic energy is not a fixed quantity in an inelastic scattering reaction, the kinematic is more difficile than in the case of elastic scattering. While it is obvious that the maximum recoil of the daughter nucleus depends in this case on the Q – value of the reaction as well as on the kinetic Energy E^n_{kin} of the incident neutron, an important feature of an endothermic reaction is the possible reduction of the allowed range of scattering angles. Reactions of the (α, xn) type are a viable source of ambient neutrons, especially as this reactions on the light nuclei ^{13}C and ^{17}O show relatively large cross – sections and low thresholds.

If charged secondaries are produced, inelastic reactions are easily discriminable from WIMP – nucleus scatterings. However, (n, n') reactions will result in an excited recoil nucleus. As the cascade of de – excitation γs from the daughter nucleus can escape the detector, the discrimination of a such events is not perfect. The size of this indiscriminable fraction depends critically on the used detector, i.e. the opacity of the detector material for γs of the given energy, the size of the detector and the detector sensitivity to discern a nuclear

recoil from a nuclear recoil plus a γ.

For inelastic scattering, the currently supported final states are ($nA \rightarrow$) $n\gamma$s (discrete and continuum), np, nD, nT, n^3He, $n\alpha$, $nD2\alpha$, $nT2\alpha$, $n2p$, $n2\alpha$, $np\alpha$, $n3\alpha$, $2n$, $2np$, $2nD$, $2n\alpha$, $2n2\alpha$, nX, $3n$, $3np$, $3n\alpha$, $4n$, p, pD, $p\alpha$, $2pD$, $D\alpha$, $D2\alpha$, DT, T, $T2\alpha$, ^3He, α, 2α, and 3α.

For a given isotope, not all of the listed channels above are found in the ENDF/B data bases or even physically viable. In Tab. B.1 the available isotopes per reaction channel in are listed for the neutron data set $G4NDL3.12$. The photon distributions are described as in the case of radiative capture described in the next subsection. The possibility to describe the angular and energy distributions of the final state particles as in the case of fission is maintained, except that normally only the arbitrary tabulation of secondary energies is applicable. In addition, the possibility to describe the energy angular correlations explicitly is supported, in analogy with the ENDF/B data formats. In this case, the production cross-section for reaction product n can be written as

$$\sigma_n\left(E, E', \cos(\theta)\right) = \sigma(E) Y_n(E) p\left(E, E', \cos(\theta)\right). \tag{4.4}$$

Here $Y_n(E)$ is the product multiplicity, $\sigma(E)$ is the inelastic cross-section, and $p(E, E', \cos(\theta))$ is the distribution probability. Using the equation above, azimuthal symmetry is tacitly assumed. For the distribution probability the following representations are supported:

- Isotropic emission of the reaction products.
- Discrete two-body kinematics.
- N – body phase – space distribution; in this case the angular dependence is constructed from the tabulated values for the number of particles and their total mass are used.
- Continuum energy – angle distributions; in this case, the expansion in terms of Legendre polynomials, tabulation in both the incoming neutron energy, and the secondary energy, and the Kalbach – Mann systematic is available for description of the angular dependence.
- Continuum angle – energy distributions in the laboratory system; in this case, only the tabulated form of angular dependence in incoming neutron energy, product energy, and product angle is implemented.

4.3.3 Radiative Capture

A capture of a neutron by a nucleus leads to the formation of the isotope with $(A+1, Z)$ in an excited state. The mass of the newly formed nucleus is not equal to the sum of the masses of the neutron and the target nucleus plus the kinetic energies of those particles. The energy excess is called the Q – value of the capture reaction:

$$E^{n}_{\mathrm{kin}} + E^{N(A,Z)}_{\mathrm{kin}} + m_n + m_{N(A,Z)} = E^{N(A+1,Z)}_{\mathrm{kin}} + m_{N(A+1,Z)} + Q \qquad (4.5)$$

In the equation above, the superscript n denotes the contributions of the neutron and $N\,(A, Z)$ denotes the contributions of the nucleus with baryon number A and charge Z. Momentum conservation of the reaction ensures that the kinetic energy of the emergent nucleus is small compared to the Q – value of the radiative capture. Thus the emergent nucleus must be in an excited state and evolves into a defined state of the daughter nucleus while emitting prompt γs. In turn, the emergent nucleus deexcites to the ground level by the emission of a cascade of γs.

In a first approximation, the kinetic energy carried by the daughter nucleus is obtained by multiplying the ratio of neutron mass to target nucleus mass with the kinetic energy of the incoming neutron, assuming that the excess kinetic energy is transferred into internal excitations of the compound nucleus:

$$E_{\mathrm{Rec}} = E_n \frac{m_n}{m_{\mathrm{t}}}. \qquad (4.6)$$

This nucleus will emit the deexcitation γs which will change the detected recoil energy. In the worst case, all deexcitation γs are emitted anti – parallel to the momentum of the nucleus and all γs fail to deposit sufficient energy to allow discrimination.

For light nuclei, the cross – section of radiative capture rapidly falls for energies above above a few keV, i.e. for oxygen, the cross – section of radiative capture for one MeV neutrons is computed to be about 3×10^{-8} barn, for calcium a value of 2 mb is expected. For tungsten, a cross – section of 100 mb is measured for one MeV incident neutron while the expected recoil energy in this case is about 7.2 keV. At one MeV incident kinetic energies, the total cross – sections are at least a factor 100 higher than the radiative capture cross – section.

As long as the nuclear recoil energy is below the detection threshold of the experiment, radiative capture does not contribute to the experimental background, even if the γ cascade completely escapes the detector.

The final state of radiative capture is described by either photon multiplicities, or photon production cross – sections, and the discrete and continuous contributions to the γ energy spectra, along with the angular distributions of the emitted γs. For the description of the γ multiplicity there are two supported data representations. It can either be tabulated as a function of the energy of the incoming neutron for each discrete photon as well as the eventual continuum contribution, or the full known transition probability array is used to determine the γ yields. If γ production cross – sections are used, only a tabulated form is supported. The photon energies E_γ are associated to the multiplicities or the cross – sections for all discrete γ emissions. For the continuum contribution, the normalized emission probability f is resolved into a weighted sum of normalized distributions g.

$$f\left(E \rightarrow E_\gamma\right) = \sum_i p_i(E) g_i(E \rightarrow E_\gamma) \tag{4.7}$$

The weights p_i are tabulated as a function of the energy E of the incoming neutron. For each neutron energy, the distributions g are tabulated as a function of the photon energy. As in the ENDF/B data formats, several interpolation laws are used to minimize the amount of data, and optimize the descriptive power. All data are derived from the ENDF/B evaluated data libraries. The techniques used to describe and sample the angular distributions are identical to the case of elastic scattering, but either a tabulation or a set of Legendre coefficients for each γ energy and continuum distribution is given.

In versions before GEANT4.9 the number of decay γs and their energies did not obey the experimental values in each case a neutron capture reaction was invoked. Furthermore, in some cases the sum of all γ energies did not match the Q – value of the neutron capture reaction. In more recent GEANT4 version this error has been fixed.

The influence on the neutron background results presented in Ch. 5 is negligible as the deposited energies in capture reactions is on the order of several MeV which is too high to induce neutron recoil background events with energies in the relevant region of interest between 10 and 40 keV. Compton scattering of the deexcitation γs results in total energy deposits which can be clearly distinguished from nuclear recoil only events. Even if all deexcitation γs escape the detector crystal without any energy deposition, the capture cross – sections at the necessary neutron energies are too tiny for radiative capture reactions to compete with elastic and inelastic scatterings.

4.3.4 Neutron Induced Fission

In this section the process who fission of nuclei is handled in GEANT4 is presented. While detector materials are generally not fissile, the treatment of fission is GEANT4 is included here for completeness of GEANT4 neutron physics. However, the construction of neutron spectra from impurities of spontaneous fissile materials like ^{238}U and ^{232}Th are important for neutron background simulations. Spontaneous fission of ^{238}U is the primary source for ambient neutron background in the MeV range, neither spontaneous nor neutron induced fission provide a background for direct *Dark Matter* searches. This can be easily seen as a fission event will provide about 180MeV of energy.

Neutron induced fission is possible for heavy nuclei like uranium and thorium. In such a case, the neutron is absorbed by the target nucleus and the resulting excited compound nucleus can decay into two medium mass nuclei plus additional neutrons. Additionally, the excited compound nucleus can evaporate neutrons before the actual fission of the nucleus. If the neutron is evaporated from an intermediate compound nucleus and this nucleus is still capable to undergo fission afterwards, these reaction channels are called higher chance fission channels.

For neutron induced fission, GEANT4 takes first to fourth chance fission into account. First chance fission is the fission from the ground state of the mother nucleus, while the higher order fission processes are fission processes of the excited states of the mother nucleus. Neutron yields are tabulated as a function of both the incoming and outgoing neutron energy. The neutron angular distributions are either tabulated, or represented in terms of an expansion in Legendre polynomials, similar to the angular distributions for neutron elastic scattering. If no data are available on the angular distribution, isotropic emission in the center of mass system of the collision is assumed. Six different possibilities are implemented for the representation of the fission neutron energy distributions. The energy distribution of the fission neutrons $f(E \to E')$ can be tabulated as a normalized function of the incoming and outgoing neutron energy, using the ENDF/B interpolation schemes to minimize data volume and maximize precision. The energy distribution can also be represented as a general evaporation spectrum,

$$f(E \to E') = f\left(\frac{E'}{\Theta(E)}\right). \tag{4.8}$$

Here E is the energy of the incoming neutron, E' is the energy of a fission neutron, and $\Theta(E)$ is effective temperature used to characterize the secondary neutron energy distribution. Both the effective temperature and the functional behavior of the energy distribution are taken from tabulations.

Alternatively energy distribution can be represented as a Maxwell spectrum,

$$f(E \to E') \propto \sqrt{E'}\exp(\frac{E'}{\Theta(E)}), \tag{4.9}$$

or a evaporation spectrum

$$f(E \to E') \propto E'\exp(\frac{E'}{\Theta(E)}). \tag{4.10}$$

In both these cases, the temperature is tabulated as a function of the incoming neutron energy.

For the energy dependent Watt spectrum, the energy distribution is represented by the following equation:

$$f(E \to E') \propto \exp(\frac{-E'}{a(E)})\sinh(\sqrt{b(E)E'}). \tag{4.11}$$

Fission photons are described in an analog way to capture photons, if evaluated data are available. In the absence of evaluated data, the measured nuclear excitation levels and transition probabilities are used, if available.

4.4 Analysis of the G4NeutronHP Class

The high precision neutron models discussed in the previous section depend on an evaluated neutron data library (G4NDL) for cross sections, angular distributions and final state information. It is important to keep in mind that the library is not complete as data for several elements are missing. The main materials used in the CRESST – II experimental setup are found in the data – base, but not for each isotope, but for the natural abundancy. This is the case for the three elements the detector modules are made off, oxygen, calcium and tungsten:

For neutron capture, elastic neutron scattering and inelastic neutron scattering , cross – sections for ^{16}O, ^{17}O are given, but ^{18}O data is missing. For calcium and tungsten a cross – section for the natural abundancy of isotopes is given. No final state state channel is given for neutron capture on ^{17}O.

A test simulation of neutron scattering on a small cubic $CaWO_4$ (4×4×4 cm) target using a beam of one MeV neutrons is set up to analyze the physical properties of the elastic and the inelastic neutron scattering. A number of 200000 primary neutrons has been started in each run of the simulation. The isotopic composition shown in Tab. 4.1 is used for the $CaWO_4$ detector material in the simulation. The rarer oxygen and calcium isotopes have been excluded to keep the analysis of the results simple. The primary energy of the incoming neutrons has been set to one MeV; the fixed energy allows for an easier interpretation of the result and it is expected that the major contribution to the relevant background within an energy range of less than 50 keV is caused by neutrons below this energy.

In the test simulation, each `G4Step` along a particle track within the detector volume is checked for the occurrence of an elastic or an inelastic neutron scattering event. If such an event happens, the energy and momentum of the incident neutron and of each secondary particle is stored. Histograms for the energy balance and scatterplots for the angular – energy relation for each detected nucleus are generated for incident neutrons within one percent of the primary neutron energy. This constraint allows an easier interpretation of the gathered data.

Isotope	Percentage
^{16}O	100 %
^{40}Ca	97.89 %
^{44}Ca	2.11 %
^{180}W	0.13 %
^{182}W	26.3 %
^{183}W	14.3 %
^{184}W	30.67 %
^{186}W	28.6 %

Table 4.1: Isotopic composition used in the neutron scattering physics test simulations.

4.4.1 Testing the `G4NeutronHPElastic` class

In this section the implementation of the `G4NeutronHPElastic` class is tested for energy conservation and energy – angular dependence using the G4NDL3.12 data – base as input.

Fig. 4.1 presents the dependence of the energy of the recoiling nucleus and its scattering angle in the laboratory system. The energy – angular dependence of all three nuclear species is the one which is expected, the visible broadening for oxygen recoils can be explained by the acceptance of reduced energy scattering events; as the maximum energy transfer to an oxygen recoil is 22.15 %, the maximum allowed reduction in incoming energy of 10 keV translates to a recoil variation in the order of 2.2 keV for oxygen. As the maximum recoil for calcium and tungsten nuclei is small the broadening is reduced.

The usage of a combined cross – section data file for the natural abundant mixture of calcium and tungsten results in the emergence of recoils for a single isotope only; in the case of calcium, only ^{40}Ca nuclei are produced, in the case of tungsten, only ^{183}W nuclei are found in the elastic scattering reactions. This is a result of the fact that the masses of the recoiling nuclei which are created as secondary particles by the `G4NeutronHPElastic` class are specified in the final state data of G4NDL, which contain a fixed value only.

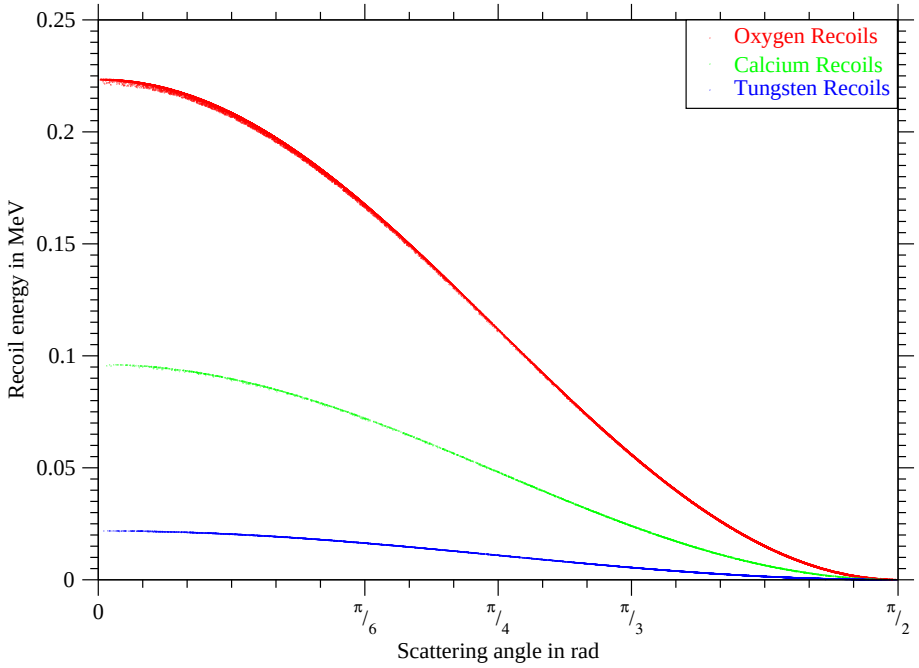

Figure 4.1: Angle – recoil energy using `G4NeutronHPElastic` neutron scattering on $CaWO_4$. Only scatterings of incident neutrons with a kinetic energy of 1 ± 0.01 MeV have been shown.

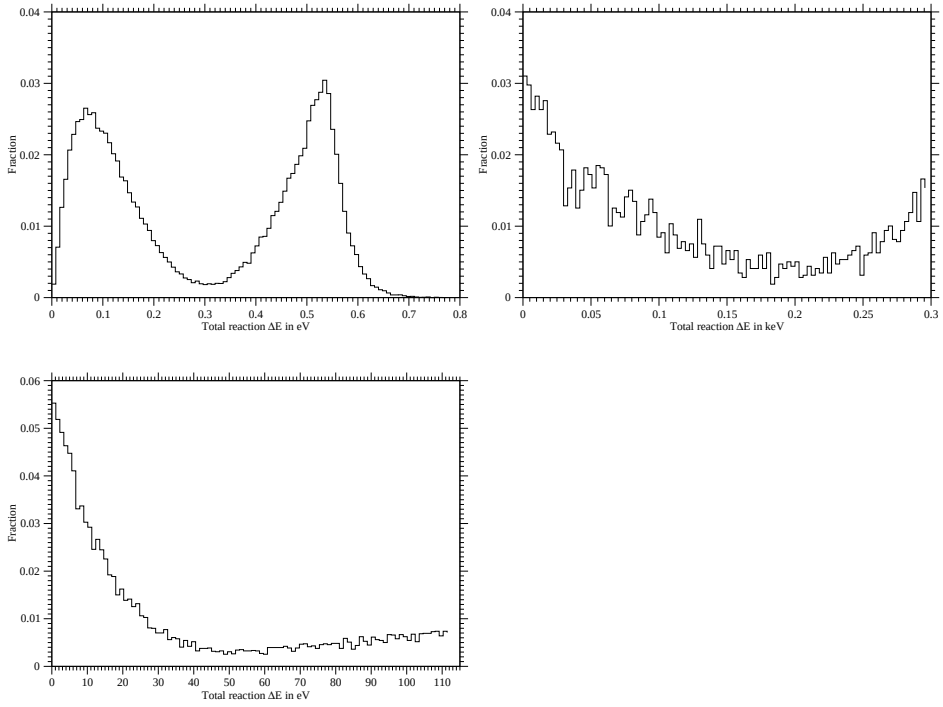

Figure 4.2: Δ E for O, Ca and W using the `G4NeutronHPElastic` class. The top left histogram shows the distribution of the total reaction ΔE for elastic recoils of O, the top right one for Ca. The histogram below is given for W recoils.

Fig. 4.2 shows the distributions of the total energy mismatch found for the three different nuclear species, i.e. the difference of energy of the incoming neutron to one of the scattered neutron plus the recoiling nucleus. Recoils on O show a total reaction energy mismatch of less than 0.7 eV out of a total of one MeV. For Ca recoils the ΔE is less than 300 eV and for W recoils it is less than 115 eV. On this level, energy conservation is sufficient for the required accuracy of the CRESST – II background simulations. Summing up the results of the test of the implementation of elastic scattering using the `G4NeutronHPElastic`, the following conclusion can be drawn:

- The correct correlation between recoil energy and scattering angle is given, i.e. simulations on the single recoil basis yield correct recoil energies.
- Energy conservation is respected on a sufficient level for simulations of nuclear recoil background in the 10 – 100 keV region.
- If the elastic scattering data is given for the natural abundant composition of an element, the quality of the observed energy conservation degrades.
- Elastic scattering data given for the natural abundant composition of an element forces that all secondary nuclei produced in the elastic scattering are of a single isotope only.

4.4.2 Testing the `G4NeutronHPInelastic` class

This subsection contains the results of the test of the implementation of the `G4NeutronHPInelastic` class. Serious issues arise with the implementation as neither energy conservation nor energy – angular correlation is respected by the `G4NeutronHPInelastic` class.

Inelastic neutron scatterings on oxygen are not not feasible for neutrons with an kinetic energy of one MeV. In the case of calcium, only the rare isotope ^{43}Ca has excitation levels below one MeV, the resulting two events are not analyzed. These events list ^{40}Ca as recoiling nucleus, which is physically forbidden. The problem is caused by the usage of one data file for the natural abundant mixture of all isotopes. The tungsten isotopes have a lot of levels which can be excited by neutrons of an kinetic energy of one MeV, approximately 8000 events are registered in the simulation of 200000 primary neutrons. The scatterplot presented in Fig. 4.3 shows the distribution of the tungsten events by isotope with respect to recoil angle and recoil energy in the laboratory frame. Unphysical recoil angles larger than 90 degrees in the laboratory system are present in large numbers. As the momentum of the deexcitation γs is tiny in comparison to the momentum of the recoil nucleus, such a situation cannot occur kinematically.

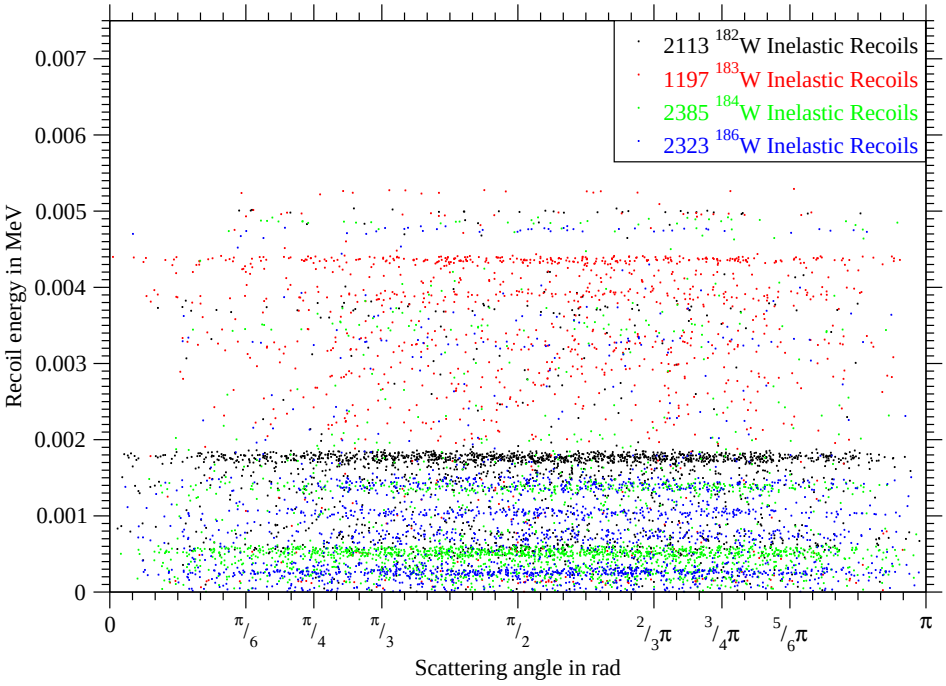

Figure 4.3: Angle – recoil energy using `G4NeutronHPInelastic` neutron scattering on $CaWO_4$. Only scatterings of incident neutrons with a kinetic energy of 1 ± 0.01 MeV have been shown.

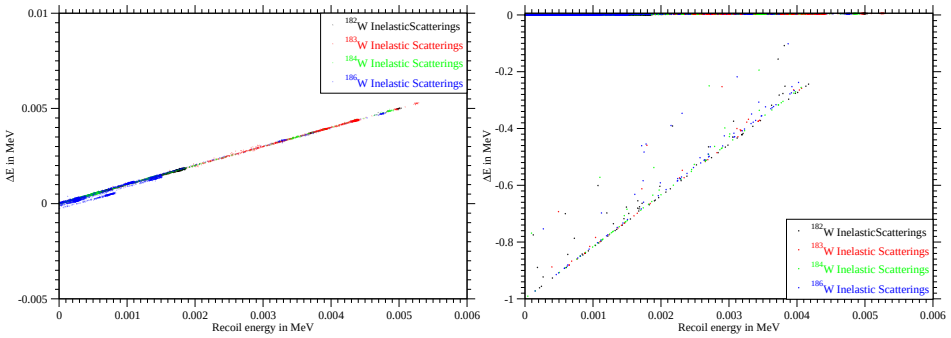

Figure 4.4: Recoil energy versus total reaction ΔE using `G4NeutronHPInelastic` neutron scattering. The left scatterplot shows the low ΔE part, where ΔE is proportional to the recoil energy. Positive ΔE indicates that the total kinetic energy of the secondary particles plus scattered neutron is larger than the kinetic energy of the incoming neutron. The right scatterplot shows the ΔE region, where the negative ΔE reveals the loss of energy in the final channel compared to the initial channel.

Furthermore, the recoil energies are about a third of the average recoil energy expected. Additionally, the experimentally observed dependence of the inelastic scattering recoil energy on the scattering angle is not reproduced. This is problematic if the recoil energy is below a detector threshold while the high energy part of the scatterings may induce valid background events if the deexcitation γs escape the detector crystal.

At least the `G4NeutronHPInelastic` class produces all tungsten isotopes, but the single scattering data – file approach leads to unphysical events as the randomly chosen nucleus is of an isotope which does not provide the resonance implied by the mixed cross – section data. While some excitation levels of the tungsten isotopes are indicated by the concentration of events for fixed specific energies, many events seem to be randomly distributed in the energy – angle plane. A single datafile containing the weighted cross – sections and angular information and the information on the excitation level is given for each isotope separately. The combination of these two data – sources results in unphysical scattering events.

Fig. 4.4 shows the mismatch between kinetic energy in the initial and the final channel of the inelastic scattering according to `G4NeutronHPInelastic`. While the bulk of events shows only a ΔE of a few keV, the proportionality between recoil energy and energy mismatch indicates that the recoil energy is simply added to the total energy of the reaction.

Some events show a large negative ΔE, i.e the kinetic energy of the incoming neutron is larger than the sum of energies of the scattered neutron, the recoiling nucleus and the produced deexcitation γs. In this cases, the `G4NeutronHPInelastic` class fails to produce the γs.

In the case of high energy inelastic scatterings involving several hadronic secondary particles, additional problems occurs as no recoil nucleus is produced in the final channel. Energy and momentum conservation is badly violated in this case, too.

The following conclusion can be drawn from the results of the simulation using the `G4NeutronHPInelastic` class:

- The experimentally observed relation between recoil energy and scattering angle is not given in the `G4NeutronHPInelastic` class, it appears as an average recoil energy is calculated.
- Unphysical scattering angles occur.
- The recoil energy according to the `G4NeutronHPInelastic` class is lower than the expected average.
- Several issues occur for high energy inelastic scatterings, in many cases no recoil nucleus is produced in this case.

The shortcomings of the `G4NeutronHPInelastic` class require a correction of the code.

4.5 Construction of the `CaWO4NeutronHPInelastic` Class

The spotted errors of the `G4NeutronHPInelastic` class must be corrected to improve the quality of the inelastic scattering in GEANT4. For this task, a new class called `CaWO4NeutronHPInelastic` based upon `G4NeutronHPInelastic` has been constructed. The used approach is presented in the following section.

The data describing the inelastic neutron scattering processes are still taken from the unmodified G4NDL3.12 data base. This implies that the correctness and completeness of the given G4NDL3.12 data is taken for granted. In reality, it is obvious that the inelastic neutron scattering data of G4NDL3.12 would profit from an overhaul and the implementation of isotope – wise data for the tungsten isotopes, for example. Some small errors are are also spotted in the excitation level data of calcium, where the original data base included some typos.

As in the case of `G4NeutronHPElastic`, the mean free path of a material fro a passing neutron for a particular inelastic scattering reaction channel determines when the main method of `CaWO4NeutronHPElastic` is called. Within this method, the data of the produced secondary particles obtained from the G4NDL3.12 is given in the laboratory frame of reference.

For simplicity, it is assumed that the final channel contains only the scattered neutron n' and the recoiling nucleus which may have been excited in the scattering:

In this case, the kinetic energy of the recoil has to be calculated from this data. For (n, n'_i) reactions, the excitation level is chosen with respect to the particular cross – sections of the various excitation levels for the given incident energy. In the center – of – mass frame (CMS) and in the non – relativistic limit, the reaction can be calculated from the given momentum $\vec{p}_{n'}$ and kinetic energy $T_{n'}$ of the scattered neutron n' by considering momentum and energy conservation:

$$\begin{aligned} \vec{p}_{n'} + \vec{p}_{\mathrm{Rec}} &= 0, \\ E_{\mathrm{inital}} = T_{\mathrm{Rec}} + T_{n'} + E_{\mathrm{ex}} & \end{aligned} \tag{4.12}$$

E_{ex} denotes the energy of any internal excitations of the recoiling nucleus. Since the outgoing momentum $\vec{p}_{n'}$ is constructed from the angular data given for the reaction, the kinetic energy of the recoiling nucleus can be calculated from the momentum[‡] :

$$T_{\mathrm{Rec}} = \frac{\vec{p}^{\,2}_{\mathrm{Rec}}}{2m_{\mathrm{Rec}}} = \frac{\vec{p}^{\,2}_{n'}}{2m_{n'}} = T_{n'}\frac{m_{n'}}{m_{\mathrm{Rec}}} \tag{4.13}$$

In the `CaWO4NeutronHPInelastic` class, the momentum of the recoiling nucleus is calculated in the CMS using the invariant mass to include relativistic

[‡] $T_{n'}$ has to be modified as it has not been calculated in a way such that T_{Rec} is considered

effects. The invariant mass – square s^2 can be calculated from the mass of the incident neutron m_n and the mass $m_\mathrm{t}$of the target particle:

$$s^2 = (m_n + m_\mathrm{t})^2 \tag{4.14}$$

In addition, the length of three – momentum vector in the CMS can be calculated, as the invariant mass s, the mass of the recoil nucleus m_rec, its excitation energy E_ex and the mass of emitted particle m_em are known. The modulus of the final state particle momenta $\vec{p}_f$ can be calculated using the formula below:

$$|\vec{p}_f| = \frac{1}{2s}\sqrt{\left[s^2 - (m_\mathrm{em} - (m_\mathrm{rec} + E_\mathrm{ex}))^2\right]\left[s^2 - (m_\mathrm{em} + (m_\mathrm{rec} + E_\mathrm{ex}))^2\right]} \tag{4.15}$$

As mentioned above, the direction of the momentum vector of the scattered neutron in the laboratory system is calculated from the data files. Assuming that the angular distribution is adequate, it is used to determine the final direction of the neutron and the recoiling nucleus. With both the direction of the scattered neutron and the modulus of $\vec{p}_f$, the resulting neutron momentum and recoil nucleus momentum can be reconstructed.

In the next step, the deexcitation γs are constructed. Since the half lives τ_i of the excited levels are around a few ten to a few hundred ps, it can be safely assumed that the neutron n' is emitted long before electromagnetic deexcitation via γs occur. Thus the momentum of the scattered neutron n' and the recoiling nucleus are set without interference of any the dexcitation γs. The properties of the deexcitation γs can be given by the G4NDL data base directly or can be calculated from the list of suitable excitation levels.

The excitation energy of the recoiling nucleus is emitted through a cascade of suitable γs in the example presented here. For each emitted γ, momentum conservation is applied to the γ – emission in the rest system of the recoiling nucleus. The obtained momenta of the particles are then transformed back to the laboratory frame of reference.

Rerunning the simulation using the `CaWO4NeutronHPClass` instead of the `G4NeutronHPClass` shows the improvements made. Fig. 4.5 shows the recoil energy – scattering angle scatterplot obtained using `CaWO4NeutronHPClass`. The spurious recoil scattering angles above 90 degrees are gone. The concentration of events along clearly visible lines indicate the different excitation levels of the various isotopes. The brown dots show the elastic scattering events giving the limit as the transferred energy in the inelastic scattering approaches zero. As the excitation energy transferred to the recoiling nucleus increases, the maximum kinetic energy of the recoiling nucleus is reduced. As expected for endothermic reactions, a maximum recoil angle is visible and leads to the effect that two recoil energies are possible for each recoil angle.

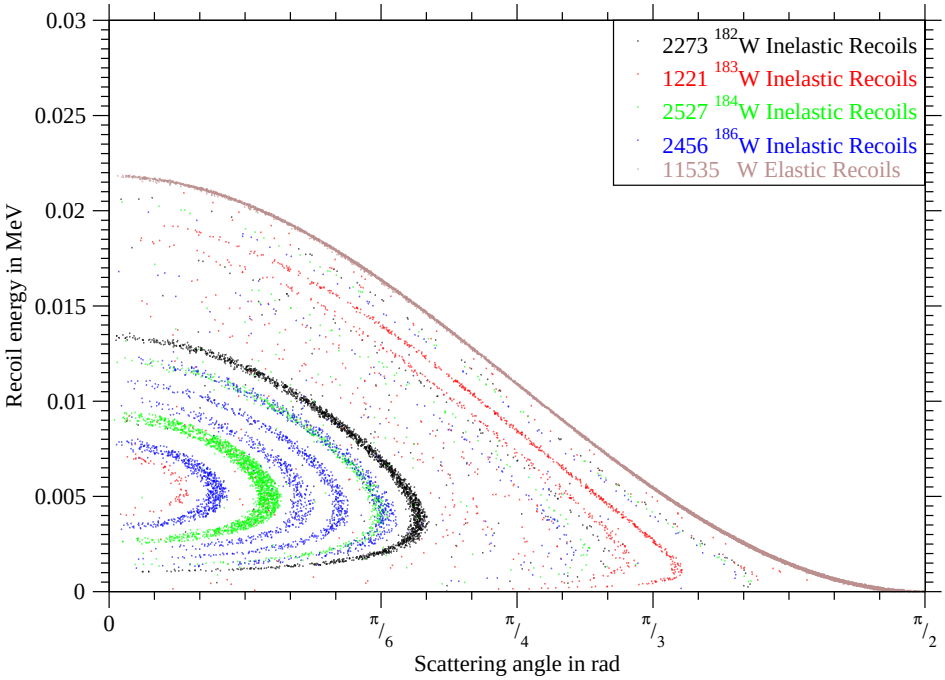

Figure 4.5: Angle – recoil energy relation for neutron scattering on $CaWO_4$ using `CaWO4NeutronHPInelastic`. In the scatterplot only inelastic scattering events with an incoming kinetic energy of 1 ± 0.01 MeV are shown. In the legend the total number of events is given for each isotope, for comparison sake the elastic scattering events are plotted, too. The excitation levels are clearly visible. A large number of events between the bands are seen, too.

For each isotope, the boomerang shaped concentration should indicate inelastic scattering on an excitation level. However, there are spurious echo structures located by other isotopes inside the true distribution which are the result of selecting the wrong excitation level fro the wrong isotope, this effect is a result of the usage of the mixed data file containing the inelastic scattering on the excitation levels of all tungsten isotopes in the same file, e.g. an inelastic scattering on ^{186}W has a chance to occur on an excitation level of ^{183}W, too.

Fig. 4.6 shows the deviation from energy conservation in dependence of the recoil energy. The deviation for the bulk of events is reduced from the of the `G4NeutronHPInelastic` class by a factor of 1000 to the level of a few eV.

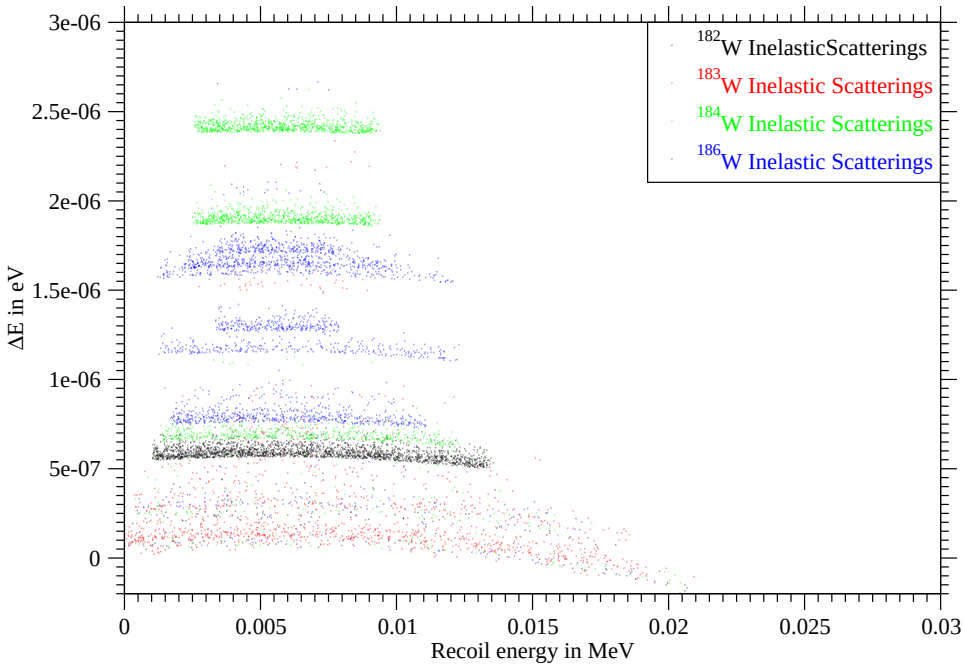

Figure 4.6: ΔE for inelastic scattering on $CaWO_4$ using `CaWO4NeutronHPInelastic`. The deviation from energy conservation in the inelastic scattering events shown as scatterplot in the recoil energy – ΔE plane. A handful of unphysical events with vast excess energies in the order of 700 – 1000 keV is not shown in this plot.

4.6 Some Remarks about the `CaWO4NeutronHPInelastic` Class

For the purposes of single event low energy neutron scattering simulation, the improved `CaWO4NeutronHPInelastic` class solves some of the more prominent issues of inelastic neutron scattering with regard to the simulation of the CRESST – II experiment.

- Energy conservation is now respected to a very high degree.
- The energy – angular correlation of the scattered recoil nuclei is now enforced to behave as it is experimentally observed.
- The production of the recoil nucleus is now enforced for inelastic scattering channels with more than one secondary hadron.

It should be stressed that the simulation of inelastic neutron scattering still has some issues, but these can be considered a minor nuisance for the neutron simulation of the CRESST – II experiment employing $CaWO_4$ detectors.

- For several elements, isotope data are still missing or only given for the natural abundance. This can result in unphysical reactions and secondary particles.
- The number produced γs from the final state data of G4NDL3.12 is determined statistically, allowing for an energy mismatch as too many γs or the wrong γs are produced.
- For hadronic multi – secondary inelastic scatterings, energy conservation is still problematic as it is determined statistically, rendering it non – sense in some cases.
- Sometimes these reaction channels come up with unexpected secondary particles.

The important low energy inelastic scatterings of the (n, n') type which are the most important for the neutron background simulation show a slightly wrong recoil energy and a γ cascade containing unphysical γs sometimes. The appearance of charged secondaries allows an easy discrimination of such inelastic scatterings in the CRESST – II experiment. Thus the mentioned shortfalls of the `CaWO4NeutronHPInelastic` class are acceptable as it is shown in Ch. 6 that inelastic neutron scattering contributes only in negligible amounts the relevant background for the CRESST – II experiment.

Chapter 5

Neutron Background for the CRESST – II Experiment

In this chapter, the experimental setup and the physics of the considered neutron sources relevant of the CRESST – II (**C**ryogenic **R**are **E**vent **S**earch using **S**uperconducting **T**hermometers) experiment are presented.

An overview of the CRESST – II experiment is given in the next Sec. 5.1, followed by an description of the geometrical setup of the experiment. The various neutron backgrounds of the experiment are reviewed in Sec. 5.3. The possibility of escaping γs in low energy inelastic neutron scatterings is discussed. The ambient neutrons from radioactive impurities in the rock and concrete of the experimental site are investigated. Another source of neutrons are (α, n) reactions on suitable nuclei, the most prominent nucleus is ^{13}C but natural αs can produce neutrons even on medium nuclei like copper. The fourth subsection deals with the cosmogenic neutron due to muon induced nuclear spallation in the surrounding area of the experiment.

5.1 Introduction to the CRESST – II experiment

The CRESST – II experiment is a direct detection Dark Matter experiment operating scintillating $CaWO_4$ crystals at Millikelvin temperatures. The objective of the experiment is the detection of WIMP – nucleus scattering by measuring the energy deposition in the detector crystal by the nuclear recoil.

For such a measurement, the apparatus has to be be decoupled from ambient vibrations and must be cooled down to low temperatures to allow operation of the superconducting phase thermometers for the signal readout and to reduce heat capacity of the detector crystals. A dilution cryostat provides the temperature to operate the detectors about 15 mK. The current setup of the cold – box allows for the installation of up to 33 detector modules. Around the coldbox an inner shield made out of high – purity copper and an outer shield made out of lead absorb electromagnetic radiation from the environment of the experiment. The radon box around these shield is a compartment which is flushed by nitrogen to eliminate radon contamination of surfaces close to the detectors. Outside the radon box, a muon veto is installed to detect the passage of muons through the critical volume around the detectors. The outmost shield is a neutron shield made from polyethylene. The experiment is located in hall A of the LN Gran Sasso underground laboratory near L'Aquila in Italy. This underground facility is shielded by about 3650 meters of water equivalent (m.w.e.) of rock against cosmic rays.

A detector module consists of crystal and two superconducting phase transition thermometers (SPT), one for the detection of the energy deposited in phonons directly on the detector crystal and the other one separated from the detector crystal which is coupled to an absorber made out of Si. This thermometer detects the scintillation light produced in the crystal. Each detector crystal is a cylinder made out of 300 g $CaWO_4$ with a diameter and a height of 4 cm each. Both thermometers are read out simultaneously; the non – thermal phonons produced in the wake of a nuclear recoil in the detector are absorbed in a thin tungsten film which operates as calorimeter in the transition to the superconducting phase while the disturbance of the electronic structure of the scintillator results in scintillation light which is collected by an absorber which is read out by a superconducting phase calorimeter, too. As the amount of produced scintillation light per unit deposited energy, the *lightyield*, depends on the particle which deposits energy in the detector, a discrimination of background events by particle type is possible.

Thus the simultaneous readout of both the phonon signal and the scintillation light signal allows for an easy discrimination of background signals induced by electrons and γs from nuclear recoils. Assuming the *Dark Matter* particle to be a WIMP, it should scatter of the nuclei in the detector, i.e. a recoiling nucleus heralds the scattering of a WIMP in the detector. In this case the remaining background for WIMP scatterings consists of nuclear recoils due to neutrons.

5.2 The Geometrical Setup in the Simulation

The geometrical setup of the CRESST experiment was included with high accuracy into the simulation. In Fig. 5.1 a sketch of the CRESST experimental setup is shown. Care was taken to model the closest parts to the detector crystals as accurate as possible.

The heart of the setup are the 33 cylindrical detector crystal made of $CaWO_4$. These crystals have a diameter of four cm and a height of four cm, weighting 300 g. The detectors are encased in an optical reflective plastic foil and a cylindrical holder made out of copper, which form a module. The actual SPTs which detect the phonon signal and the light signal are omitted as the masses are negligible and direct hits in the SPTs result in large signals which can be filtered out. These modules are located in a larger supporting structure, the carousel made from copper. The exact geometrical form and the measures of the copper modules and the carousel were taken from the CAD drawings of the CRESST-II experiment. Some minor parts were changed while trying to keep the amount of material close to the detectors in agreement with the drawings as detailed as possible. As example to illustrate the included simplifications, the springs on which the lower part of the carousel rests were replaced by tubes of the same mass. Furthermore, the wires from the modules to the readout squids located in the cryostat were omitted.

The setup of the cryostat contains the cylindrical coldbox where the carousel is located, the coldfinger which connects the coldbox to the cryostat above, and the cryostat itself. In the simulation, the cryostat consists of the various thermal shields and vacuum vessels, the small and complicated parts within the dilution unit itself and the SQUIDS are omitted. This is justified as these parts do not provide a large mass. The cryoliquid filling level for the simulations was taken to be 12.5 % of the maximum filling. The usage of a mean cryoliquid filling level simplified the simulation.

Around the coldbox a copper shield of at least 17.5 cm thickness is located, surrounded by a lead shield of a thickness of 22.5 cm, at least. Outside these two shields, the radon box is located. The radon box is a volume flushed permanently by nitrogen to prevent the influx of radon contaminated air from the laboratory around the inner shields.

The outmost shielding is the neutron shielding made out of 55 cm polyethylene (PE) surrounding the inner shielding on the sides. On the floor, the thickness of PE neutron shield is reduced by the steel wagon carrying the two halves of the inner lead and copper shields. The thickness of the PE inside the wagon is reduced to 20 cm. Around the upper part of the cryostat a PE tube of 36 cm thickness and 111 cm height is located. A cylindrical socket of 60 cm thickness and 21 cm height rests below the PE tube around the cryostat.

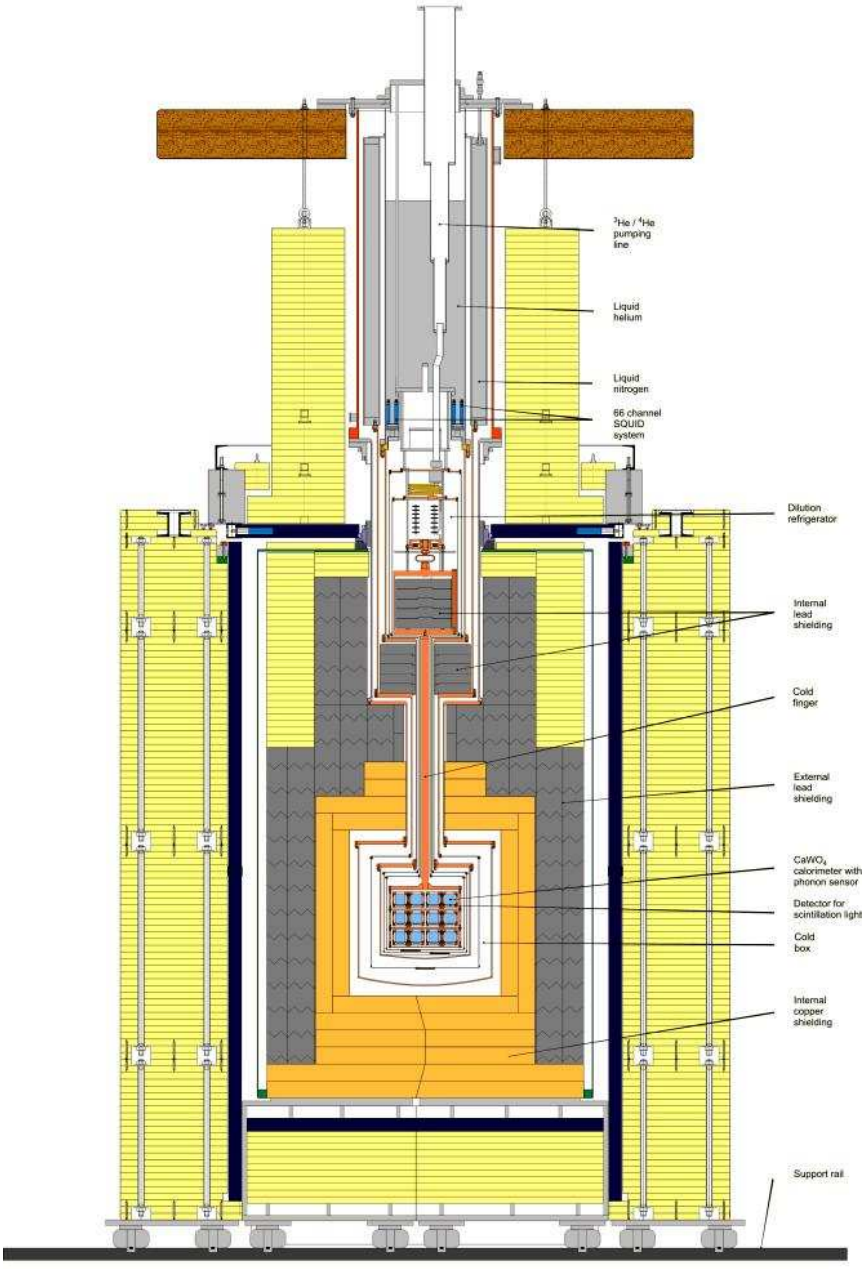

Figure 5.1: This figure shows the experimental setup of the CRESST – II experiment. This sketch is taken from *http://www.cresst.de/facility.php*

5.3 The Neutron Background in the CRESST – II Experiment

In this section the neutron background and its impact on the CRESST – II experiment is analyzed and discussed. The aim of the simulation is the analysis of the neutron sources in order to reduce the number of neutron induced events in the energetic region of interest of WIMP – nucleus scatterings. Throughout this work, a neutron is considered *dangerous* if it or its secondary products can induce a nuclear recoil within a selected energy window. Experimentally, the detection threshold of the detectors in the phonon channel is much better than the separation threshold where electromagnetic events and nuclear recoil events become discernable. This threshold is unique for each detector module, the lowest separation thresholds found at 8 keV while average modules show a threshold around 12 – 15 keV . In the following sections, the energetic region of interest (ROI) is bound by a lower threshold of 10 keV. Consequently, a neutron is required to have a minimum kinetic energy to deposit enough energy above the threshold in a single scattering. The maximum recoil energy in elastic scattering can be derived from kinematics:

$$E_{\mathrm{rec}}^{\mathrm{max}} = E_{\mathrm{inc}} \frac{4 m_n m_{\mathrm{t}}}{(m_n + m_{\mathrm{t}})^2} \tag{5.1}$$

In this equation $E_{\mathrm{rec}}^{\mathrm{max}}$ is the maximum recoil energy, E_{inc} is the energy of the incident neutron and m_n and m_{t} are the masses of the neutron and the target nucleus, respectively. For several relevant isotopes used in direct *Dark Matter* searches, the minimum kinetic energy of an incoming neutron to deposit 10 keV in a single scattering is shown in Tab. 5.1 . For most cases of low energy inelastic endothermal neutron scattering, Eq. 5.1 provides a good approximation and a strict upper bound for the recoil energy. The spectral shape of the neutrons at the location of the detector modules combined with the nuclear cross – sections determines the fractions of the recoiling nuclei.

Nucleus	Maximum energy transfer	Kinetic energy of the neutron in keV
^{16}O	0.22145	45.16
^{40}Ca	0.09518	105.06
^{70}Ge	0.05554	180.03
^{72}Ge	0.05404	185.03
^{74}Ge	0.05262	190.03
^{132}Xe	0.02984	335.02
^{182}W	0.02174	460.01
^{184}W	0.02150	465.01
^{186}W	0.02128	470.01

Table 5.1: The maximum energy transfer factor for elastic scattering of neutrons on various nuclei and the required minimum kinetic energy for an incident neutron to induce a 10 keV recoil.

5.3.1 Influence of Inelastic Scattering Processes $(n, n'\gamma_i)$ for the Neutron Background

On the first glance, such processes appear to expose a self – discriminating signature as each nuclear recoil is accompanied by at least one γ from the de – excitation of the recoiling nucleus. In the case of the CRESST – II experiment, the mean free path for γs with energies above about a MeV becomes comparable to the size of the employed detector modules.

If the γ manages to escape the detector with little or no energy deposition via Compton scattering, the resulting signature may allow misidentification with an ordinary nuclear recoil event. While the mean free path of least energetic de – excitation γs of tungsten is too short to escape the crystal, the direct de – excitation γs of the higher excitation levels have a free mean path on par with the dimensions of the crystal. This can be seen in Tab. 5.2 and Fig. 5.2. For neutrons in the MeV range, the cross – section of the inelastic $(n, n'\gamma)$ reaction on tungsten is in the range of 20 % – 30 % of the total cross – section.

The total attenuation of the γs is included in the simulation as part of GEANT4 physics for photons, thus this part of the contribution to the background events by inelastic scatterings is treated correctly. In Sec. 4.5 the correction of the nuclear recoil physics for inelastic scattering has been presented and is included in the forthcoming simulations.

Inelastic scattering provide a possibility to populate the lightyield versus deposited energy plot with events between the nuclear recoil band and the electromagnetic band. If the γ is absorbed completely, characteristic bands for each inelastic nuclear level are formed in a scatterplot of the deposited energy in the phonon channel and the lightyield, i.e. the ratio of energy deposited seen in the light channel and the phonon channel.

In most cases, the incomplete absorption of the de – excitation γ result

Isotope	Energy γ keV	Total attenuation in $CaWO_4$ in $^{cm^2}/_g$	Mean free path in cm
^{182}W	100.1	2.90	0.058
	229.3	0.41	0.41
	351.0	0.191	0.87
	1035.7	0.0637	2.62
	1221.4	0.0603	2.76
^{183}W	46.5	4.81	0.035
^{184}W	111.2	2.23	0.075
^{186}W	122.5	1.66	0.095

Table 5.2: Total Attenuation and mean free path in $CaWO_4$ for the de – excitation γs of the first excited states of tungsten. In the case of ^{182}W the effect of the γ energy on the mean free path is shown. The lowest energy level is given for each tungsten isotope, the transition energies are taken from Ref. [Si10]. The total attenuation is obtained using the XCOM Photon Cross Section Database [Be05b].

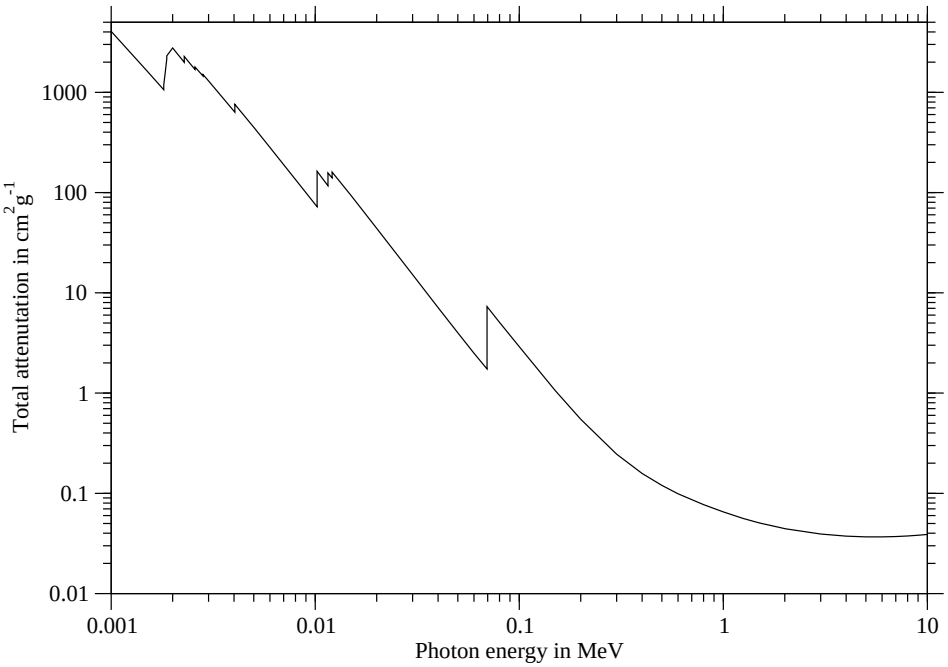

Figure 5.2: Total attenuation including coherent scattering of photons in $CaWO_4$. The data points for this plot have been generated with the help of XCOM Photon Cross Sections Database [Be05b]. It can be found at *http://physics.nist.gov/PhysRefData/Xcom/html/xcom1.html*.

in an event in the γ band, as the maximum transferred energy in Compton scattering for the de – excitation γs considered here is in the order of 50 – 80 percent. Thus the resulting lightyield of the Compton scattering and the nuclear recoil is practically the lightyield of the recoiling electron. If the energy transfer in the Compton scattering is exceptionally low, a very low energetic event with a lightyield comparable to an α or a nuclear recoil can be mimicked as the calorimeters which measure the scintillation light and the non – thermal phonons of the scattering are too slow to separate the recoil from the Compton scattering by timing.

It is shown that the contribution of inelastic neutron scatterings to the background in the region of interest (ROI) defined by an energy deposition in the range between 10 and 40 keV is negligible for the simulated sources presented in the next sections.

5.4 Ambient Neutrons from the LNGS Cavity

The neutron flux within the LNGS underground laboratory has been measured by several groups, but the results show a considerable variance. In Tab. 5.3 several measurements in the Gran Sasso underground laboratory are quoted. These measurements employed different detector concepts and were conducted at different places in the underground laboratory. The quoted measurements do not allow a reliable reconstruction of the shape of the neutron background as the energy bins are generally too large. The quoted measurements employed different methods which may result in different total fluxes. The location of the measurement in the LNGS is important for the measured spectrum as the amount of U and Th within the concrete and water content of the concrete dictate the total strength and the form of the neutron background spectrum.

In order to obtain a spectrum of the neutron flux which is in reliable agreement with the measurements and the measured activity in the surrounding of the experimental hall, Wulandari did a monte – carlo simulation taking the radiochemical composition of the concrete and the rock surrounding the experimental site into account [Wu04]. The primary neutrons were either from spontaneous fission of U and Th within the concrete and rock or from (α, n) reactions of αs from he decay chains of U and Th on lighter elements within rock and concrete. Different amounts of water content in the rock and the concrete were simulated by Wulandari.

The simulation and the spectrum obtained by Belli *et al.* [Be89b] from experimental measurements in the LNGS underground laboratory agree quite well for energies above one MeV if concrete with a water content of 8 percent is assumed as the material where the neutrons are produced.

The spectral data shown in Tab. 5.4 and Tab. 5.5 agree fairly well above one MeV while showing excess flux below this energy compared to the work of Belli *et al.*.

<table>
<tr><td rowspan="2">Energy range in MeV</td><td colspan="6">Neutron flux in 10^{-6}cm^{-2}s^{-1}</td></tr>
<tr><td>[Be89b]</td><td>[Ar99]</td><td>[Al89]</td><td>[Be85]</td><td>[Ri88]</td><td>[Cr95]</td></tr>
<tr><td>10^{-3} – 1</td><td rowspan="2">0.54(1)</td><td></td><td rowspan="2"></td><td rowspan="2"></td><td rowspan="6">2.56(27)</td><td rowspan="2"></td></tr>
<tr><td>1 – 2.5</td><td>0.14(12)</td></tr>
<tr><td>2.5 – 5</td><td>0.27(14)</td><td>0.13(4)</td><td rowspan="4">0.78(3)</td><td rowspan="4">3.0(8)</td><td rowspan="4">0.09(6)</td></tr>
<tr><td>5 – 10</td><td>0.05(1)</td><td>0.15(4)</td></tr>
<tr><td>10 – 15</td><td>0.6(2) $\times 10^{-3}$</td><td>0.4(4) $\times 10^{-3}$</td></tr>
<tr><td>15 – 25</td><td>0.5(3) $\times 10^{-6}$</td><td></td></tr>
</table>

Table 5.3: Compilation of several measurements of the ambient neutron background cited in Ref. [Wu04]. Ref. [Ar99] was measured in hall A where the CRESST experiment is located of the LN Gran Sasso, all other measurements were conducted in hall C.

Energy in MeV	Integrated flux in $^{n}/_{\mathrm{cm^2 s}}$
0.5 – 1.0	2.2×10^{-7}
1.0 – 1.5	1.2×10^{-7}
1.5 – 2.0	1.0×10^{-7}
2.0 – 2.5	1.2×10^{-7}
2.5 – 3.0	7.4×10^{-8}
3.0 – 3.5	4.3×10^{-8}
3.5 – 4.0	2.1×10^{-8}
4.0 – 4.5	2.9×10^{-8}
4.5 – 5.0	1.7×10^{-8}
5.0 – 5.5	1.5×10^{-8}
5.5 – 6.0	8.7×10^{-9}
6.0 – 6.5	7.8×10^{-9}
6.5 – 7.0	1.7×10^{-8}
7.0 – 7.5	1.5×10^{-9}
7.5 – 8.0	1.2×10^{-9}
8.0 – 8.5	5.4×10^{-11}

Table 5.4: Simulated ambient neutron flux at the hall A at the LNGS laboratory taken from Ref. [Wu04]. In this table, the integrated neutron flux in 500 keV bins from 500 keV up to 8.5 MeV is listed. The total ambient neutron flux above 500 keV is about 7.952×10^{-7} $^{n}/_{\mathrm{cm^2 s}}$.

In this work, the data of Tab. 5.4 shown in Fig. 5.3 will be used as the input spectrum for the simulation of the ambient neutron background. Neutrons of energies below 500 keV induce tungsten recoils below ten keV and were excluded from the first set of simulations as they are stopped nearly completely in the neutron shielding. In a first simulation of the ambient neutron background presented in Sec. 6.1, the neutron spectrum above 500 keV shown in Tab. 5.4 has been employed as primary spectrum. While restricting the spectrum to a maximum of 8.5 MeV, most of the relevant cosmogenic neutron contribution is neglected. This is done on purpose as this part is included in the measurement at the LN Gran Sasso but was not included in the simulation of Wulandari.

Energy interval in MeV	Integrated flux in 10^{-6} $^{n}/_{\mathrm{cm^2 s}}$
less than 0.5×10^{-8}	0.53 ± 0.36
0.5×10^{-8} – 10^{-3}	1.77 ± 0.45
10^{-3} – 1.0	0.87 ± 0.32
1.0 – 2.5	0.35 ± 0.12
2.5 – 5.0	0.18 ± 0.05
5.0 – 10.0	0.05 ± 0.02

Table 5.5: Simulated ambient neutron flux at the LNGS laboratory taken from Ref. [Wu04]. The table contains the fluxes for the given bins adopted from Tab. 5.3 with statistical errors.

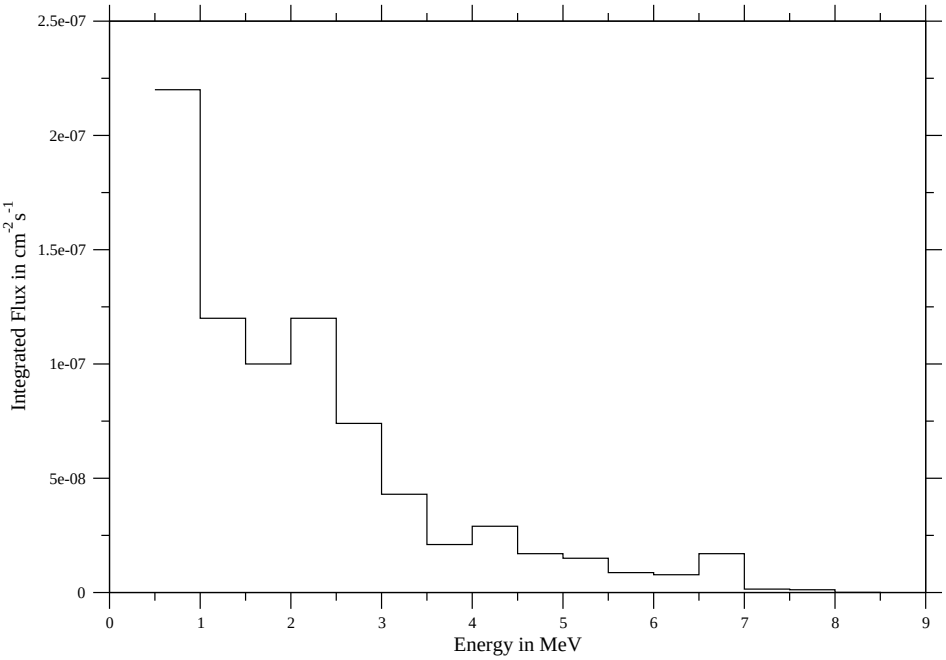

Figure 5.3: Primary ambient neutron spectrum as used in the simulation. The integrated flux given is the flux per 500 keV bin.

The neutron background below 500 keV cannot produce tungsten nuclear recoils of more than 10 keV, but it can induce oxygen recoils. A simulation of the low energy ambient neutrons has been conducted presented in Sec. 6.1.1. The integral flux for this simulation is taken as the difference between the value given in Tab. 5.5 for the bin 1 keV and 1 MeV and the bin between 500 keV and 1 MeV given in Tab. 5.4. The spectrum is assumed to show a linear slope which is determined by the flux per keV for the bin below one keV in Tab. 5.5 and the one from 500 – 1000 keV given in Tab. 5.4.

For a large part of the simulated data of the ambient neutron flux, a slightly harder neutron spectrum was used. In this case, the energy bins of Tab. 5.4 were shifted 300 keV upwards. As a considerable time was required for the accumulation of this simulation data, it was compared to the simulation using the correct spectrum. No significant effect on either the rate or the energetic distribution of the background events was noted. As considerable time was used to gain the data with the harder spectrum, it was decided to use it in the analysis, too.

5.5 Neutrons Production by (α, n) Reactions in PE and Copper

Several isotopes of light elements allow the production of neutrons by α particles. In this section, the potential of such reactions for selected materials used in the construction of the CRESST – II experiment is investigated. The incident α – particles are provided by ubiquitous contaminations of uranium, thorium and the daughter isotopes of their decay chains. These chains and the energies of naturally occurring α – particles can be deduced from figs. 5.4, 5.5 and 5.6.

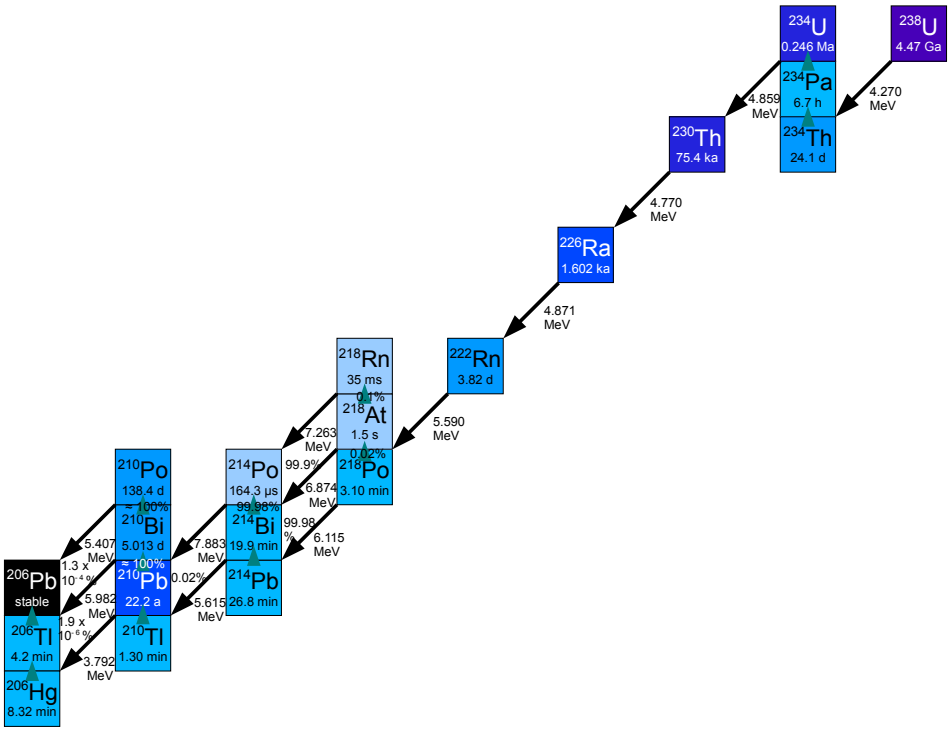

Figure 5.4: The Uranium – Radium decay chain. Diagonal arrows indicate α – decays, small green arrows denote β – decays. Branching ratios are given on the left side of the arrow depicting the α – decay or on top of the arrow of the β – decay. The Q – value of the α decay are given, β – endpoint energies are omitted. As the half – life of a given isotope increases, the background color changes from light blue to dark blue.

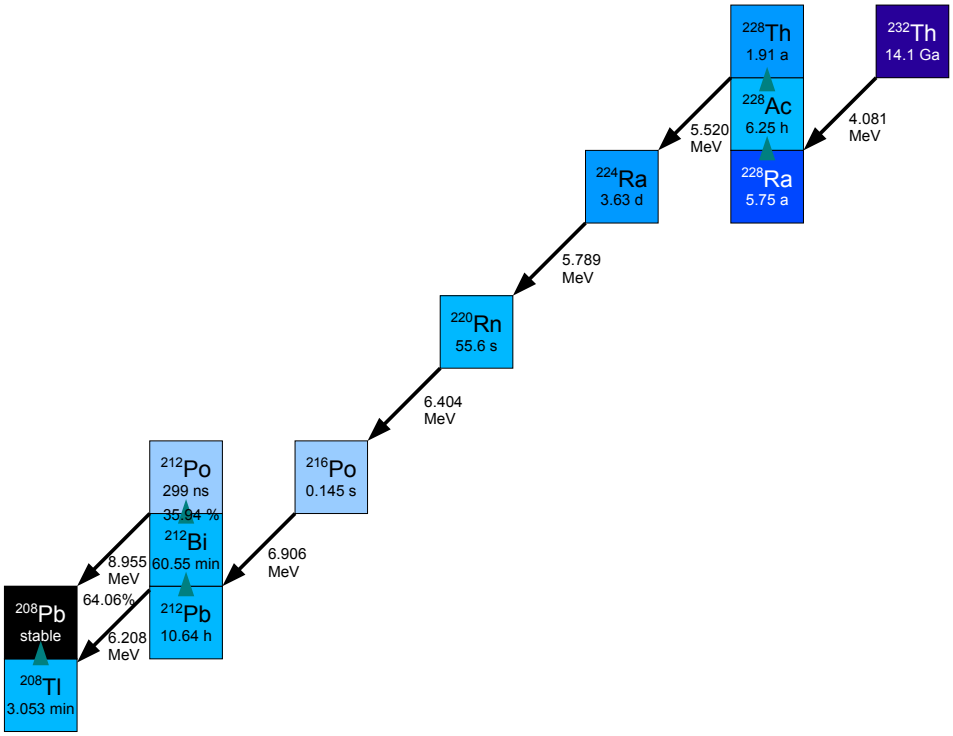

Figure 5.5: The Neptunium decay chain. In this figure, the chain from isotope ^{232}Th downwards is shown. Diagonal arrows indicate α – decays, the small green arrows show β – decays. Branching ratios are given on the left side of the arrow of the associated α – decay. The branching ratio of β – decays is found on top the associated arrow. The Q – value of the α decay are given, β – endpoint energies are omitted. As the half – life of a given isotope increases, the background color darkens.

For the purpose of neutron shielding hydrogen – rich compounds are most effective, as the momentum transfer of the neutron to a proton is maximal as their masses are similar. This is the reason for the large neutron stopping power of hydrogen – rich materials like water or polyethylene ($(CH_2)_n$). Both materials have roughly the same density ($\approx 1\ ^{g}/_{cm^3}$), but polyethylene (PE) has the advantage to be solid at room temperature, thus a neutron shielding around a given detector setup is easier to build and maintain with PE than with water. Unfortunately, both materials contain isotopes which allow (α, n) – reactions for rather low incident α energies.

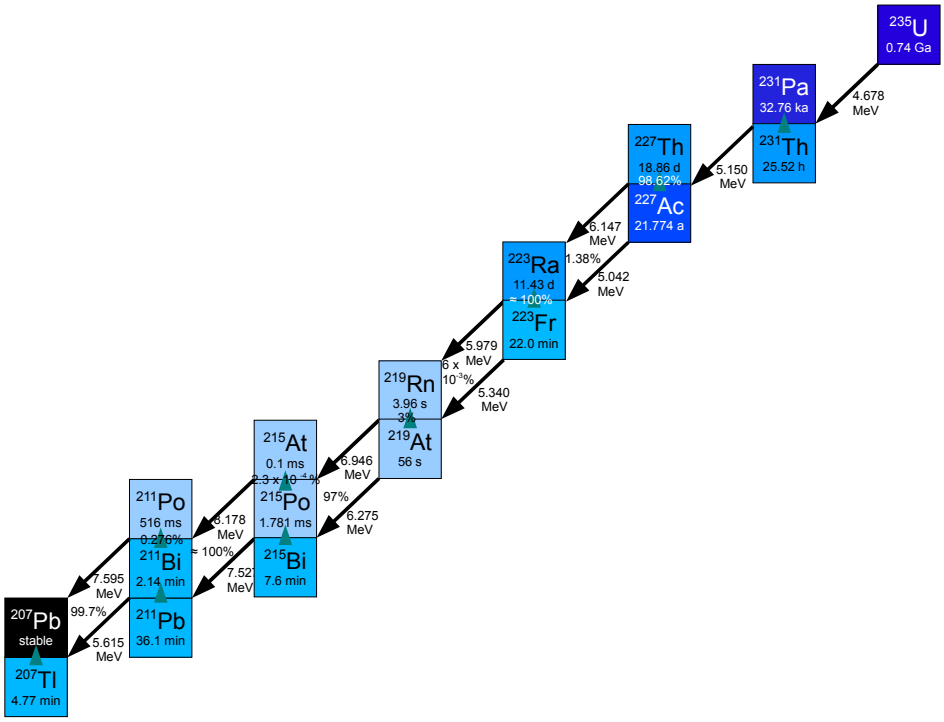

Figure 5.6: The Actinium decay chain. In this figure, the chain down from the isotope ^{235}U is shown. Diagonal arrows indicate α – decays, the small green arrows denote β – decays. Branching ratios are given on the top left to the arrow depicting the α – decay or on top of the arrow of the β – decay. The Q – value of the α decay are given, β – endpoint energies are omitted. Isotope with longer half – lives are noted by darker background color.

The small deuterium (0.012% nat. ab.) content found in both materials can be neglected since the kinematic threshold for the break – up reaction of deuterium for an α particle is 6.645 MeV in the laboratory system as shown in Tab. 5.6 and the low natural abundancy of deuterium. Taking the energy – loss of an α – particle in matter into account, the potential rate for the D(α, n)αp reaction is severely limited as the α has to interact with a deuterium nucleus before its energy drops below the reaction threshold. For the most energetic naturally occurring αs of about 8 MeV, the energy loss in PE is about 55 – 60 $^{\mathrm{keV}}/_{\mu\mathrm{m}}$, thus it has to react along a track of $\approx$ 20 μm. The energy loss in water is about ten percent smaller than the energy loss in PE. In the case of water, the isotopes ^{17}O (0.04% nat. ab.) and ^{18}O (0.2% nat. ab.) provide viable targets for neutron production; the kinematic thresholds can be found in Tab. 5.6. In PE, traces of ^{13}C (1.1% nat. ab.) allow neutron production via the (α, n) reaction.

The Coloumb barrier limits the potential for α – particles to induce a (α, n) – reaction. As the nuclear force is limited to short distances, the α – particle is required to run up the Coulomb potential of the nucleus to reach the volume where the tunneling probability through the Coulomb barrier is large enough that the nuclear force between α – particle and nucleus can induce the reaction with a non – negligible rate. If the kinetic energy of the α – particle is not sufficient to propel it close enough to the nucleus, the reaction cannot happen. For the energy range of α particles encountered here, the kinetic energy is rapidly lost by an α along its track, severly limiting its chance to penetrate the Coulomb potenial sufficently along its track through the target material.

For a rough estimate, the required energy of a α – particle to come close enough to a nucleus that the nuclear force between particle and nucleus can induce a reaction can be calculated classically. The energy needed to bring a α – particle from infinity to the distance of 10 fm to a nucleus with Z protons, neglecting the effects the atomic shell of the nucleus exerts on the approaching particle*:

$$W \approx \frac{-1}{4\pi\epsilon_0} \int_{\infty}^{10\mathrm{fm}} \frac{2 \times Z_{\mathrm{nuc}}}{r^2} dr \approx 280\,\mathrm{keV} \times \mathrm{Z_{nuc}}.$$

A more realistic calculation has to take the screening effects of the detailed charge distribution of the atomic shell, a realistic nuclear potential and quantum mechanics into account. For many lighter nuclei, tables of experimental cross – section data motivated by studies of stellar nucleosynthesis are available, eliminating the necessity of detailed calculations of the reaction threshold.

*10 fm is a generous estimate on the size of a heavy nucleus, using the empirical formula for the nuclear radius: $r \approx r_0 A^{1/3}$, $r_0 \approx 1.2$ – 1.5 fm [Bl52]. This distance is about twelve times the radius of a proton, and about four times the distance where the Coulomb force starts to exceed the nuclear force between two protons.

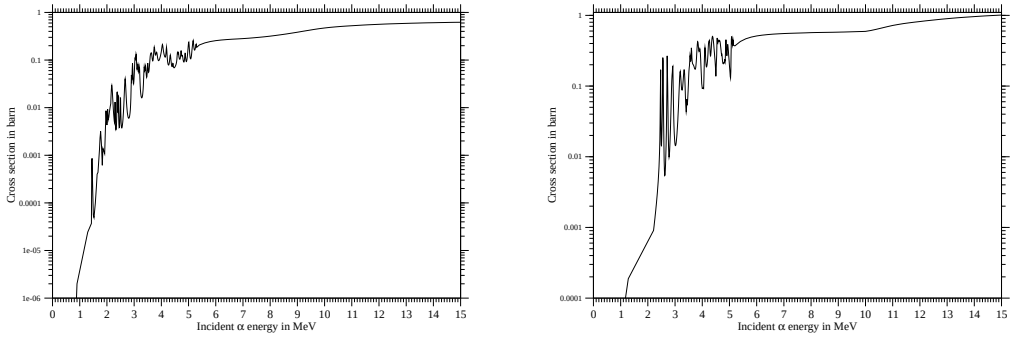

Figure 5.7: Combined cross – sections of the (α, xn) reactions on ^{17}O (left) and ^{18}O. The data for the figure are taken from the JENDL – 3.3 database found at *http://www.nndc.bnl.gov/sigma/*.

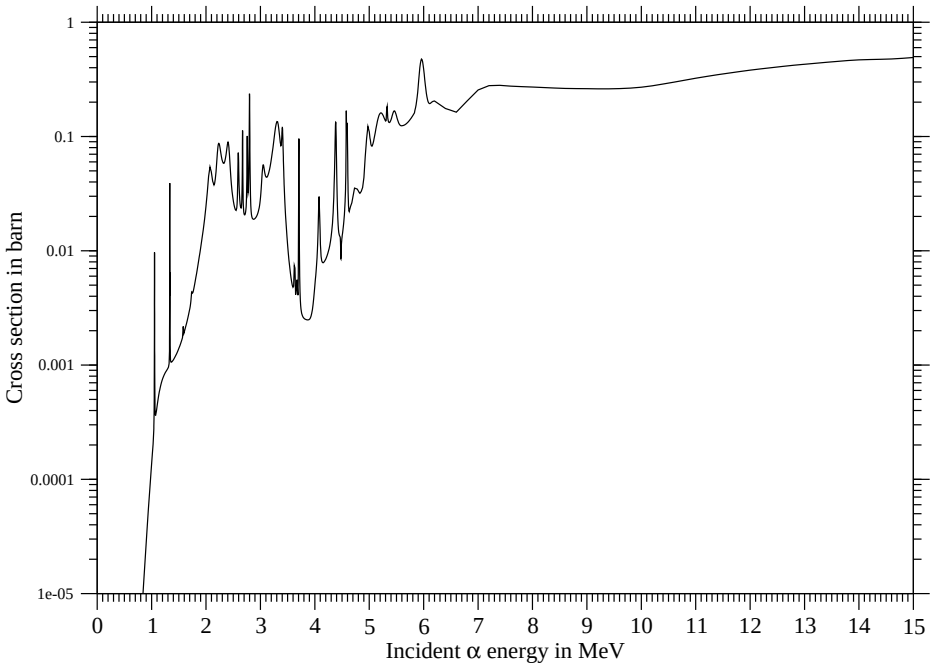

Figure 5.8: Combined cross – section of the various (α, xn) reactions on ^{13}C. The data for the figure are taken from the JENDL – 3.3 database found at *http://www.nndc.bnl.gov/sigma/*.

From the JENDL – AN2005 database[†] a non zero cross – section for ^{17}O is given for a minimum energy of 1.294 MeV. In the ^{18}O (α, n) cross – section data, the lowest cross – section with a value of 1.88×10^{-4} barn is given for an energy of 1.28075 MeV by JENDL – AN2005. These values are about 60 percent of the value obtained from the rough estimate given above. A noticeable cross – section of the order of 0.1 barn is reached for incident energies above 3 MeV. Assuming natural abundance in the oxygen isotopes, 0.243 percent of all oxygen atoms are (α, n) targets for α – particles with a kinetic energy above 1.3 MeV. The exact spectral shapes of the cross – sections on the oxygen isotopes can be seen in Fig. 5.7.

Polyethylene contains a good target for the (α, n) – reaction, the carbon isotope ^{13}C. The JENDL – AN2005 gives a minimum incident energy of 0.7931 MeV for the exothermic reaction $^{13}\mathrm{C}\,(\alpha, \mathrm{n})^{16}\,\mathrm{O}$. If natural abundance in the carbon isotopes is assumed, the fraction of ^{13}C nuclei is 1.07 percent. In Fig. 5.8, the spectral shape of the combined (α, xn) cross – sections of ^{13}C is shown.

[†]The JENDL – AN2005 database can be found at the website of the Japanese Atomic Energy Agency(JAEA) at: *http://wwwndc.jaea.go.jp/jendl/jendl.html*.

5.5.1 (α, n) Neutron Production on $CaWO_4$ in the CRESST – II experiment

Another interesting material to look for (α, n) – reaction is the material from which the detectors themselves are made. Neutrons produced in the detectors have an enhanced probability to hit surrounding detector modules due to their proximity and the lack of shielding between them. In the case of the CRESST-II experiment, the detectors are made from $CaWO_4$. Apart from the production of neutrons by spontaneous fission of uranium and thorium, (α, n) reactions could occur in this material, too. The oxygen isotopes ^{17}O and ^{18}O have been addressed in the previous paragraph, the situation for the calcium and tungsten isotopes has to be addressed now.

For the tungsten isotopes, the Q – values for the (α, n) reaction exceed the energies of α – particles from the natural occurring decay chains. In addition, the size of the coulomb barrier for these nuclei with Z equal 74 renders them insensitive to (α, n) reactions for natural occurring α particles.

In the case of calcium, a few rare isotopes are susceptible for (α, n) – reactions. ^{43}Ca, ^{46}Ca and ^{48}Ca have no or only a tiny nuclear threshold, making

Target	Nat. Abundance in percent	Q – Value in MeV	Threshold in MeV
D	0.0115	-2.2245645(8)	6.64541000(239)
^{12}C	98.93	-8.50201(49)	11337.858(653)
^{13}C	1.07	2.21561*	0.0
^{16}O	99.757	-12.13484(29)	15171.49(363)
^{17}O	0.038	0.58672(11)	0.0
^{18}O	0.205	-0.69615(62)	0.850953(758)
^{40}Ca	96.941	-11.172(7)	12.291(8)
^{42}Ca	0.647	-5.1877(10)	5.6826(11)
^{43}Ca	0.135	0.0684(8)	0.0
^{44}Ca	2.086	-2.1825(8)	2.3812(9)
^{46}Ca	0.004	-0.2227(22)	0.2421(23)
^{48}Ca	0.187	-0.133(4)	0.144(4)
^{180}W	0.12	-11.63(5)	11.89(5)
^{182}W	26.50	-11.0845(10)	11.3284(10)
^{183}W	14.31	-9.014(12)	9.2111(12)
^{184}W	30.64	-10.1355(12)	10.3560(12)
^{186}W	28.43	-9.1706(14)	9.3679(14)

Table 5.6: Q – values and reaction thresholds for (α, n) – reactions on natural occurring isotopes of hydrogen, carbon, oxygen, calcium and tungsten. The reaction thresholds do not consider the coulomb barrier the α – particle has to penetrate. The natural abundances of isotopes are taken from *Karlruher Nuklidkarte (2006)*. The quoted data are obtained with the Q – value calculation program QCalc found at the Brookhaven National Laboratory website at: *http://www.nndc.bnl.gov/qcalc/*.
* For the reaction $^{13}C\,(\alpha, n)\,^{16}O$ no uncertainty was given.

these nuclei potential targets for high energy αs. Unfortunately, no evaluated experimental data for (α, n) reactions on calcium isotopes can be found in the JENDL – AN2005 database. The necessary kinetic energy for an α particle to pass the Coulomb barrier of the calcium nucleus can be calculated to be 6.75 MeV[‡]. Since the α – particle can tunnel through the remaining peak of the Coulomb barrier, a non vanishing probability for a reaction exists which decreases exponentially for lower energies.

In Ref. [He89], estimated thick target yields for various elements for six and eight MeV α – particles are given. For calcium, a neutron yield between one and two times 10^{-7} neutrons per α are given for six MeV α – particles. A yield between five and seven times 10^{-6} is presented for eight MeV α – particles. These values have to be adjusted to the isotopic abundance of the reacting nuclei. From Tab 5.6, the total abundance of exothermic reacting isotopes in natural abundant calcium is taken as 0.326 %, thus reducing the contribution to the total neutron background drastically. As example, an activity of 1 Bq of appropriate αs of six MeV in calcium yields three to six neutrons per year.

Concerning the radio – impurities in the detectors, the CRESST experiment is in the comfortable position that it can identify α – particles with a superior sensitivity. The assumption that the daughter nuclei in the decay chains of ^{232}Th, ^{235}U and ^{238}U are in equilibrium can be dropped if the concentration of the bottle neck isotopes ^{226}Ra, ^{228}Ra and ^{227}Ac can be measured directly.

The analysis of the α decay background in the two detector modules of CRESST Run 30 revealed no significant overabundances of daughter nuclei of the decay chains. The α – decay count rates and the associated level of contamination showed a large variance between the analyzed modules. The module named *Zora* showed a higher level of contaminations, the observed α – decay rate of 3.6×10^{-5} Bq around the energy of the decay of ^{238}U, 4678 keV. This rate corresponds to a contamination of ^{238}U in the detector crystal of 9.71 ppt. The count rate observed for the long – living ^{230}Th isotope of 1.75 mBq amounts to contamination level of 7.8×10^{-15}. The final bottleneck in the uranium – radium chain, ^{226}Ra with a half – life of 1602 a, can be estimated to have an abundance of less than 9.65×10^{-16}. Since the decay energy of ^{234}U of 4859 keV is quite close to the decay energy of ^{226}Ra of 4871 keV, both decays cannot be disentangled. Assuming the equilibrium concentration of ^{234}U of 7.8 10^{-15} from the known concentration of ^{238}U, the activity sustained by ^{226}Ra is only lowered by six percent in this case. The concentration of ^{226}Ra is then reduced to about 9×10^{-16}. The last isotope in this chain which needs to be examined is ^{210} Po. As a daughter isotope of the persistent ^{210}Pb it can be found if significant lead contaminations are present in the crystal. From the visible peak in the spectrum of α decays, a activity of 0.22 mBq is inferred, this amounts to a contamination of 9×10^{-21}. As the activities of the isotopes from the uranium – radium decay chain differ, the assumption that the concentrations of daughter nuclei is in equilibrium must be dropped.

[‡]This value for the Coulomb barrier has been calculated with a code found at *http://wnsl.physics.yale.edu/cbarrier.htm*.

The contamination from ^{232}Th is obtained from its activity to be 0.28 ppb. An activity from the contamination of ^{235}U could not been detected, but α – decays of its daughter nuclei ^{231}Pa (1.1 ppt) and ^{227}Th ($\approx 3 \times 10^{-21}$) and ^{223}Ra ($3.4 \times 10^{-21}$) allow for the determination of contaminations from this decay chain.

In total, about 27000 α decays above 6 MeV have been detected with the *Zora* module in 67.7 days. Applying a α – neutron conversion rate given in Ref. [He89] of $1 - 2 \times 10^{-7}$ for neutrons of six MeV, a neutron production rate per module on calcium nuclei of less than 5×10^{-5} $^{n}/_{\mathrm{d}}$ can be estimated for modules of a comparable contamination level of the *Zora* module. The contribution of (α, n) reactions on the suitable oxygen isotopes in one module is below 4×10^{-6} $^{n}/_{d}$ from if a flat cross – section of 0.4 barn and a mean range of an α in $CaWO_4$ of 0.2 μm is assumed not considering the energy loss across this part.

As the number of produced neutrons is estimated to be below 3.1×10^{-4} $^{n}/_{\mathrm{kgd}}$ for 10 operational modules out of 17 installed modules, this source will not be considered for the simulation. A look at the results of Ch. 6 justify this decision, as the production rate above is about an order of magnitude less than the total nuclear recoil background within the ROI of 10 – 40 keV.

5.5.2 Neutron Production on Polyethylene in the CRESST – II Experiment

In order to estimate the radioactive contamination of the bulk polyethylene (PE) a chemical analysis of the used PE has been conducted at the chemical laboratory at the INFN LNGS laboratory on August, the $23^{\text{rd}}, 2007$ [Ba07b]. One sample was taken from sawdust from bulk PE used for the construction of the neutron shielding which was stored at the CRESST – II experimental site for two years, the other sample was taken from granular PE which had arrived at the laboratory site recently. An inductively coupled plasma – mass spectrometry (ICP – MS) at the chemical laboratory of the LN Gran Sasso was conducted on both samples using a commercial ICP – MS Agilent Technologies model 7500a device. Both samples were checked for a variety of radioactive isotopes as can be seen in Tab. 5.7. The error given in the tabulated values ranges between 30 – 40 % according to the report of the analysis. The sawdust bulk PE sample is by an order of magnitude dirtier than the granular sample, but this can also be attributed to dust and working abrasive contamination on the sawdust sample. However, the concentration of uranium and thorium contamination in the PE are taken as a worst case scenario for impurities found in the shielding PE.

The neutron spectrum produced by radioactive impurities in a specified material via (α, n) reactions and spontaneous fission can be obtained with the SOURCES 4A code [Wi99]. SOURCES4A calculates the neutron spectrum in a given material according to the user specified radioactive impurities.

The target material and the radioactive impurities must be defined by the user, the code can evaluate the equilibrium concentrations of the daughter nu-

Isotope	Bulk PE sample	Granular PE sample
	Concentration in ppb	
^{39}K	5300	360
^{88}Sr	200	2.6
^{133}Cs	0.46	0.025
^{147}Sm	0.7	< 0.1
^{208}Pb	210	130
^{209}Bi	6	0.18
^{232}Th	1.3	0.05
^{238}U	0.5	0.03

Table 5.7: Radioactive impurities found in polyethylene (PE) samples from the CRESST neutron shielding. Two samples were analyzed using the ICM – PS technique at the chemical laboratory of the LNGS on August, $23^{\text{rd}}, 2007$ using an ICP – MS Agilent Technologies model 7500a. One sample was 0.59 g sawdust from a bulk piece of PE stored in the LNGS underground laboratory for two years, the other sample was 2.58 g from granular PE freshly brought to the underground laboratory. The error on the concentration values is estimated by the laboratory to be within 30 – 40 %.

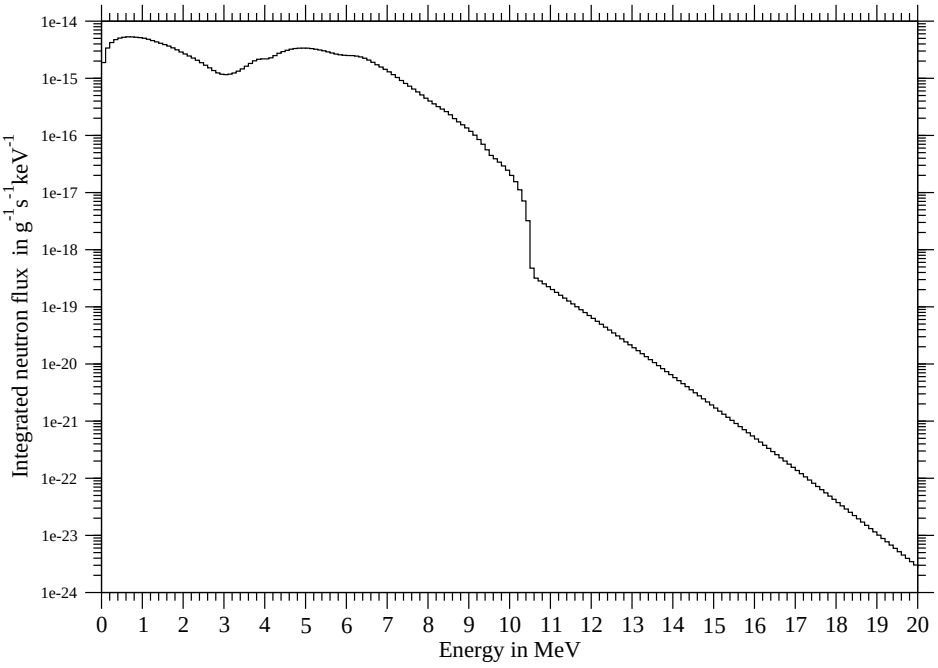

Figure 5.9: Neutron fluxes induced by (α, n) reactions and s.f. of uranium and thorium in the PE neutron shielding.

clei independently. The α – decay spectra of the impurities and the daughter nuclei are then propagated through the target material and the resulting neutron spectra are calculated. The resulting neutron spectra by energy and flux are given as tables in the output file of the SOURCES code. Minor features have been added to the obtained SOURCES4A spectrum above ten MeV; for energies above ten MeV, the neutron spectrum has been extrapolated up to the maximum energy of the relevant (α, n) – reaction if it is above ten MeV. Additionally, a Maxwellian spontaneous fission spectrum is added for the given contaminations of spontaneous fissile isotopes up to energies of 20 MeV.

As the input spectrum for the simulation, the larger contamination values of the sawdust sample will be adopted for the simulations presented in this work. The modified neutron spectrum obtained by SOURCES for this contamination in bulk PE is shown in Fig. 5.9.

The influence of additional neutrons produced by αs on the surface of the PE shielding from Rn contamination in the air of the laboratory will be ignored. The measurements of the radon activity in the air in the LNGS laboratory disagree, while a published value of about 160 $^{\mathrm{Bq}}/_{\mathrm{m}^3}$ before installation of a new ventilation system and about 22.5 $^{\mathrm{Bq}}/_{\mathrm{m}^3}$ after installation of the ventilation system

has been published [Ba97]; on the other hand, measurements in 2006 claimed values of about 180 $^{\mathrm{Bq}}/_{\mathrm{m}^3}$ [Ki06]. As the half – life of most radon isotopes is rather short, the influence of the circulation of the air within the experimental halls becomes a very important factor for the effective radon activity at the PE shielding. Thus a measurement of the radon activity at several crucial points in the ventilation of the CRESST – II experiment and at several benchmark points of the PE shielding is needed. An educated guess of the neutron flux due to Rn on the surface of the PE shielding is found in App. C.3.

5.5.3 Neutron Production on Copper in the CRESST – II Experiment

One peculiarity of the radioactive contaminations in the copper shielding is given by the fact that (α, n) reactions on copper nuclei are possible if α – particles with kinetic energy exceeding the reaction thresholds of 6.183 MeV (^{65}Cu), respectively 7.978 MeV (^{63}Cu) are provided to the copper bulk. For lead, this reaction channels are closed as both the Coulomb barrier of the Pb nuclei and the nuclear reaction thresholds are well above the energies which can be provided by natural occurring α emitters. In Tab 5.8, suitable α – sources are presented. A fraction of 39.1 percent of total intensity of the six α – decays of the Np – decay chain is provided by α – decays with energies well above the (α, n) threshold of ^{65}Cu. The 5.8 percent of equilibrium alpha intensity in the ^{212}Po decay can produce neutrons on ^{63}Cu, too. The Ac decay chain in equilibrium provides 29 percent in suitable αs with energies above the (α, n) threshold on ^{65}Cu but no α with enough energy to produce neutrons on ^{63}Cu. Only 12.5 percent of the equilibrium α flux of U – Ra can induce neutron production on ^{65}Cu. Thus ^{232}Th contaminations and its daughter isotopes in the Np chain are the most dangerous concerning (α, n) production.

The neutron production rates on copper are given, the α – decay of ^{212}Po of the ^{232}Th decay chain exhibits the largest neutron production rate of 1.2×10^{-6} $^{n}/_{\alpha}$ on ^{65}Cu and of 3.7×10^{-6} $^{n}/_{\alpha}$ on ^{63}Cu [St64]. The expected neutron flux can be calculated with extensions of the mentioned SOURCES4A code [Ca04, Le06]. A spectrum of the expected neutron flux from thorium contaminations in bulk copper including the contributions from (α, n) reactions has been presented in Ref. [Pa07]. In bulk copper, the total neutron flux induced by one ppb ^{232}Th in secular equilibrium is about 8.385×10^{-12} $^{n}/_{\mathrm{scm}^3}$ with a mean energy of 0.79 MeV only.

Nucleus	Threshold or E_α in MeV	Decay Chain	Relative Flux
^{65}Cu	6.183		
^{212}Bi	6.208	Np	64.06 %
^{219}At	6.275	Ac	6×10^{-3} %
^{220}Rn	6.406	Np	100 %
^{218}At	6.874	U – Ra	0.02 %
^{216}Po	6.906	Np	100 %
^{219}Rn	6.950	Ac	$\approx$ 100 %
^{218}Rn	7.263	U – Ra	2×10^{-5} %
^{215}Po	7.521	Ac	$\approx$ 100 %
^{211}Po	7.595	Ac	0.278 %
^{214}Po	7.883	U – Ra	99.98 %
^{63}Cu	7.978		
^{212}Po	8.955	Np	35.94 %

Table 5.8: Potential α – sources for neutron production via (α, n) reactions on copper.

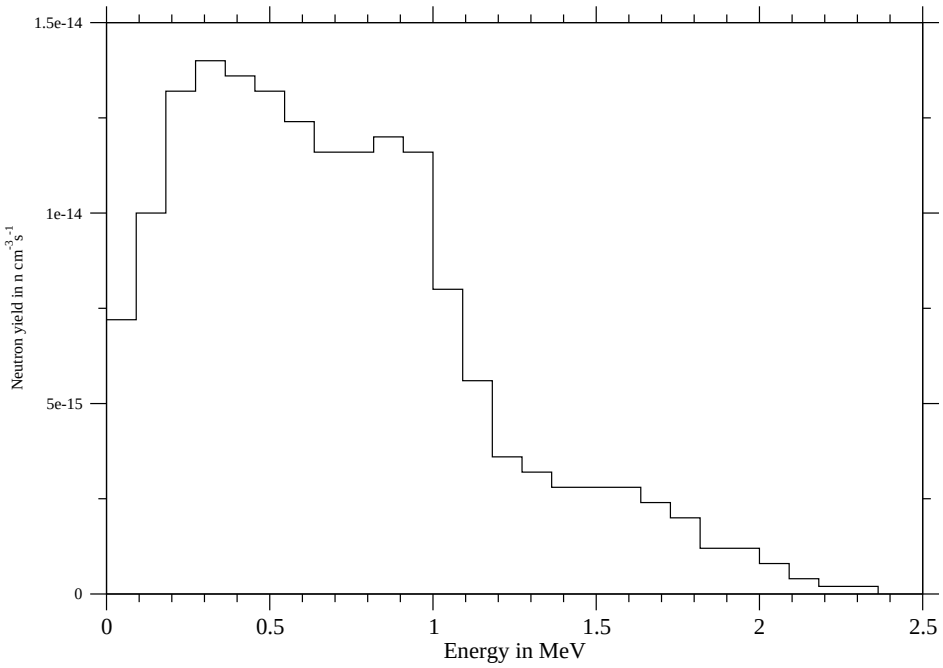

Figure 5.10: Neutron Spectrum produced by 20 ppt Th in bulk copper. The tail of the s.f. neutrons has been cut above 2.3 MeV. This spectrum has been adopted from a the spectrum presented in Ref. [Pa07].

5.6 Neutrons Production by Spontaneous Fission of ^{238}U and ^{232}Th

For natural occurring isotopes, both ^{238}U and ^{232}Th can undergo spontaneous fission and are both available in non negligible amounts in virtually all materials. The neutron spectrum from the various nuclei capable of spontaneous fission can be obtained with the help of the SOURCES 4A code mentioned before [Wi99]. In SOURCES4A the contributions from spontaneous fission of the appropriate nuclei in the decay chain are calculated separately to the generated spectrum of neutrons produced by (α, n) reactions.

In Tab. 5.9 the neutron yields of spontaneous fissile isotopes found in decay chains of ^{238}U and ^{232}Th are compared. Compared to neutron flux from ^{238}U, the sum of all other contributions about four orders of magnitude smaller assuming that the uranium contamination is not enriched. The relative s.f. neutron yield of ^{235}U is two percent of the ^{238}U neutron yield, the low natural abundancy of ^{235}U diminishes the influence of ^{235}U even further. A contamination of ^{232}Th is required to be a million times larger to result in the same s.f. neutron flux than a contamination of ^{238}U as the s.f. branching ratio in ^{232}Th decays is much smaller than the one encountered in the heavier ^{238}U nucleus. The primary neutron spectra used in the simulations in Sec. 6.3 will consider all contributions.

Isotope	Flux in $^{n}/_{\mathrm{gs}}$	Mean Energy in MeV
^{238}U	1.353×10^{-2}	1.688
^{234}U	2.691×10^{-7}	1.889
^{230}Th	1.282×10^{-8}	1.708
^{235}U	2.153×10^{-6}	1.890
^{231}Pa	3.310×10^{-9}	1.925
^{232}Th	1.225×10^{-8}	1.587

Table 5.9: Neutron fluxes from the spontaneous fission isotopes in the Ra (^{238}U, ^{234}U and ^{230}Th), the Ac (^{235}U and ^{231}Pa) and the Np (^{232}Th) decay chain. The flux is given in neutrons per gram and second, the average energy $\bar{E}$ is given in units of MeV. The fluxes are standardized to one g of natural occurring uranium containing 99.28% ^{238}U and 0.72% ^{235}U. The concentration of the daughter isotopes is the equilibrium concentration of the decay chains. In the case of thorium, the flux is standardized to a gram of thorium instead of uranium. The fluxes are obtained from the SOURCES 4A code [Wi99].

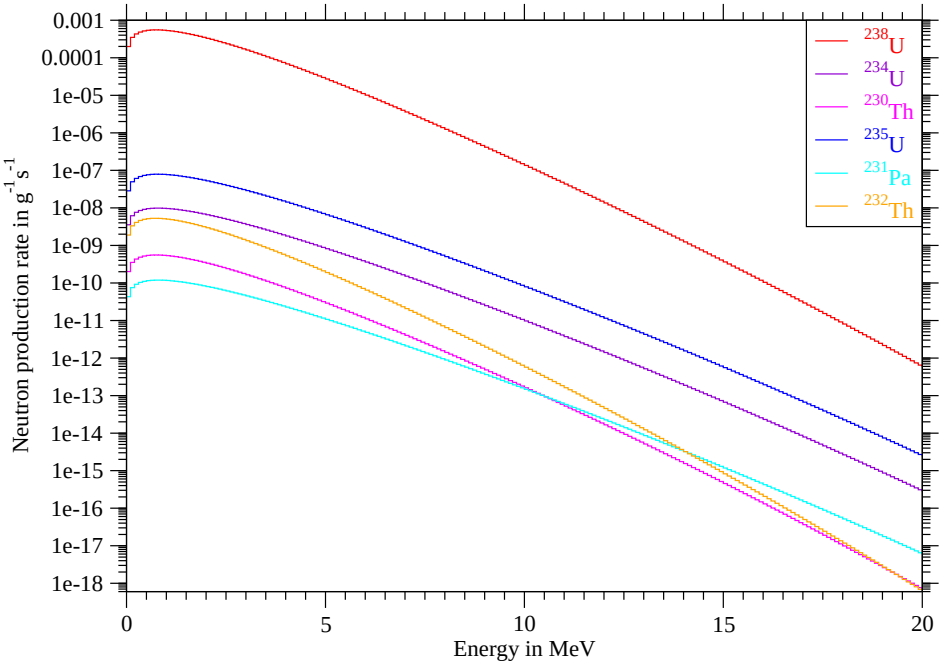

Figure 5.11: Spontaneous fission neutron flux spectrum obtained from the SOURCES 4A code for energies below 10 MeV. Above 10 MeV the spectrum is extended according to a Maxwellian distribution for fission neutrons. The intensity of the flux is given for a sample of one gram of natural abundant uranium (99.28% ^{238}U and 0.72% ^{235}U) and the related daughter nuclei capable of spontaneous fission with decay equilibrium concentrations and for one gram of natural abundant thorium (100% ^{232}Th) combined.

As the SOURCES4A code calculates the spontaneous fission spectrum of eligible nuclei separately, the neutron energy spectra for the various nuclei considering the natural abundancies in uranium and the secular equilibrium concentrations of daughter isotopes have been extracted. These spectra reach up to 10 MeV in neutron energy and the given fluxes are the integrated fluxes averaged over an energy range of 100 keV. Interest in the behavior of the rare high energy neutrons demand an extension of the primary neutron spectrum up to an energy of 20 MeV. This is achieved by adding the tail of a Maxwellian energy distribution to the spectra obtained from the output of SOURCES4A. Fig. 5.11 shows the partial spontaneous fission neutron flux from ^{238}U, ^{232}Th, ^{235}U and their spontaneous fissile daughter nuclei for secular equilibrium contaminations.

Element	Concentration in ppb
K	< 10000
Ni	< 30
Rb	< 5
Cd	60
In	< 5
Sm	< 5
Pt	< 20
Th	< 0.2
U	< 0.2

Table 5.10: Impurities found in lead samples from the CRESST EM shielding. A sample was analyzed using the ICM – PS technique at the chemical laboratory of the LNGS on August, $22^{\text{nd}}, 2008$. The weight of the sample was 0.7485 g, it was cleansed in an ultrasound bath at 70° C . The achieved accuracy for this measurement is about 20 – 30%. Note that some elements have a very poor detection limit as the carrier gas and the matrix elements can chemically form oxides or double charge ions whose mass to charge ratio overlaps with that of the considered elements.

The uranium and thorium contaminations in the lead from which the gamma shield of the CRESST experiment have been measured by an ICP – MS analysis at the chemical laboratory at the INFN LNGS laboratory on August, the $22^{\text{nd}}, 2008$ [Ro09]. The results of the analysis can be found in Tab. 5.10. Virtually all contaminations are below the sensitivity limit of the chemical analysis. For uranium and thorium, both contamination levels are each below 200 ppt within an experimental error of then chemical analysis of 20 – 30 %.

No measurement of the contaminations of the copper from the innermost γ – shield have been made. As copper is generally known to be producable in very high purity, one tenth of the upper limit on the concentration in the lead sample is assumed to be the upper limit for the uranium and thorium contaminations in the copper.

A comparison to the results of the UKDM Collaboration measurements gathered on the ILIAS webpage on radiopurity of the uranium and thorium contaminations shows that a level of contamination of less than 20 ppt for each uranium and thorium has been measured before[§].

[§]ILIAS is a project of Integrated Infrastructure Initiative (I3) type supported by the European Commissions 6th Framework Programme (FP6), it aims to bring together Europes leading Astroparticle – Physics infrastructures. It maintains a ILIAS database on radiopurity which is accessible at: *http://radiopurity.in2p3.fr/search.php?Material=copper.*

5.7 Cosmogenic Neutrons

In this section the expected diffuse neutron background due to cosmogenic induced neutrons found in the LN Gran Sasso underground lab is addressed. This type of background has much higher energies than the neutrons from sources presented in the previous sections. The shielding power of PE drops for higher neutron energies which is a result of the decreasing neutron cross – sections for energies above a few MeV. Additionally, high energy neutrons produce copious amounts of secondary neutrons by spallation and inelastic (n, xn) scatterings on heavy nuclei. The cosmogenic neutrons are secondary particles produced by the ubiquitous high energy muon flux ($\bar{E} \approx 270$GeV at the LN Gran Sasso). At this energies, the muons – nuclei interaction results in a shower of secondary particles. The neutrons among these secondaries are produced by three distinct processes:

- Through muon – induced spallation of nuclei, where the interaction between muon and nucleus via a virtual photon leads to the production of secondary particles. Among the hadronic particles and γs which are produced in the wake of the deep inelastic scattering, neutrons can be produced directly in the interaction or can be evaporated by the neutron – rich fragments.
- Neutrons are part of the hadronic part of the cascade developing in the wake of the initial muon interaction. High energy neutrons are produced in π^- interactions on the protons of a target nucleus. Low energy neutrons are evaporated from excited nuclei hit by neutrons of the cascade. The contribution of protons to the neutron production is suppressed as protons lose energy by ionization rapidly.
- High energy γs in the electromagnetic part of the cascade can produce additional neutrons via photo – disintegration of a hit nucleus.

Compared to the neutrons produced by the sources presented before, cosmogenic neutrons from muon induced reactions have a much harder energy spectrum extending to much higher energies.

An active muon veto will deal with most of the muon induced background, as tracks of charged particles in the muon – induced shower passing the veto can be identified and associated events in the detectors can be vetoed. The numerous background events which are in coincidence with with a high energy deposition in the muon veto can be detected easily ¶. Neutrons propagating perpendicular to the shower can pass the veto unnoticed, however. The influence of this *diffuse* muon induced neutron background has to be investigated by simulations. The true efficency of the muon veto for the CRESST – II experiment can only be solved by a top – down simulation starting with muons, which is not part of this work, however.

¶In the CRESST – II experiment, the rate of events in the detectors within the ROI (10 – 40 keV) and coincident hits in the muon veto is $\approx 0.1\ ^1/_{\mathrm{kgd}}$ [Pf10].

A thorough analysis of the impact of a neutron veto on the EDELWEISS experiment can be found in Ref. [Ho07b], where the muon veto around the experiment reduces the background rate induced by muons of kinetic energies from 20 GeV to 200 GeV by a factor of 680 ± 183 for a low energy muon veto trigger level of two MeV. For a trigger level of five MeV used for the CRESST – II muon veto the suppression factor is on the order of ≈ 140, as shown in Fig. 6.7. in Ref. [Ho07b]. According to Horn's analysis of muon induced neutrons for the EDELWEISS experiment, the average angle between muons and the neutrons with energies above a 100 MeV is tiny. High energy neutrons with a scattering angle larger than 45° are suppressed by at least an order of magnitude compared to neutron in forward direction. On the other hand, neutrons up to 100 MeV are emitted virtually isotropically as they result from de – excitations of Δs and Giant Dipole Resonances in the hit nuclei. Furthermore, it has been shown in simulation that high energy neutrons can travel large distances from the track of the muon [Ag99]. This can lead to a substantial contribution of stray neutrons produced at quite a distance to the muon veto which may pass the veto unnoticed.

As the muon generator in the work of Horn is centered on the immediate region around the experimental setup, the amount of stray cosmogenic neutrons maybe underestimated, since 35 percent of all started muons hit the muon veto directly according to Tab. 6.2. in Ref. [Ho07b]. As 53 percent of the started events deposit more than two MeV in the veto, the efficiency of the veto is exaggerated for ambient muon induced neutrons not aligned with the muon induced shower.

The used energy spectrum of the cosmogenic neutrons in this work is the mean ambient cosmogenic neutron spectrum expected from the muon flux and the surround rock for the LNGS laboratory. This spectrum does not consider the neutron production on the support structure of the experiment or the parts of the experiment located inside the veto. Since neutrons propagating within the muonic shower can be vetoed by detecting of the charged constituents of the shower, it is assumed in this work that their contribution to the remaining neutron induced background is small.

In this work, the simulation of cosmogenic neutrons uses neutrons as primary particles with an appropriate energy spectrum. This spectrum was obtained by Demetyev based upon measurements of the muon spectrum at LNGS laboratory [De99]. The angular direction of the primary muons has been provided by the LVD experiment [LVD94]. The spectral shape of the primary muon spectrum is given by

$$\frac{dN}{dE} = \text{const.} \times \left[\mathrm{E} + (\gamma - 1) \cdot \bar{\mathrm{E}}\right]^{-\gamma+1}, \tag{5.2}$$

in the formula above, $\gamma = 2.70$ is the exponent of the atmospheric muon spectrum and $\bar{E}$ is the mean energy of the muons at a the depth of the LN Gran Sasso of 3650 m.w.e. . The energy transfer of the muon to the hadronic cascade was calculated by Bezrukov and Bugaev [Be81] and a total reaction probability of inelastic muon – nucleus interaction in the rock of $9.45 \times 10^{-6}\ {}^{1}/_{\mathrm{ga}}$ was used

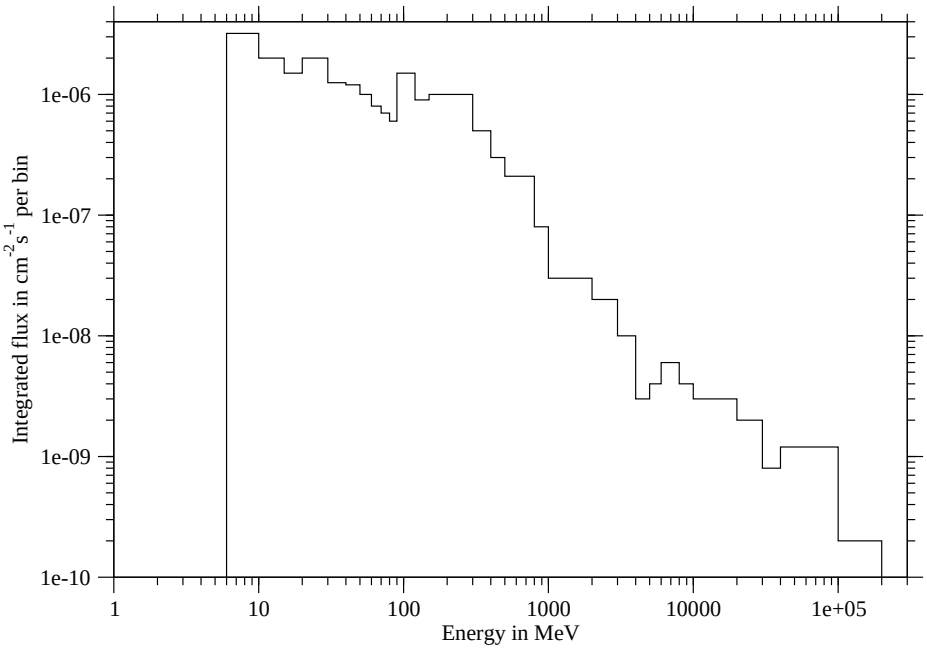

Figure 5.12: Energy spectrum of muon induced neutrons. The solid line is the neutron spectrum according to Demetyev[De99]. The spectrum is cut below 6 MeV and the negligible contributions to the neutron flux above 200 GeV are omitted. The total integrated muon induced neutron flux is 1.9824×10^{-2} $^{1}/_{\mathrm{cm^2 a}}$.

for the normalization of the neutron spectrum. The general shape of Demetyev's spectrum has been confirmed by independent simulations by Wulandari [Wu04] using the MUSUN muon simulation code. The resulting spectrum is used as input spectrum for the simulation and is shown in Fig. 5.12.

The spectrum is cut below 6 MeV and above 200 GeV. The lower cut is motivated by the fact that the flux at low energies is dominated by the contributions to the neutron flux from ambient radioactivity. The flux above the upper threshold is negligible for the simulation. A overlap in the region between six MeV and 8.5 MeV between the cosmogenic neutron spectrum and the ambient neutron spectrum exits, however the additional flux from the cosmogenic spectrum is insignificant to the ambient neutron flux in this region. The contribution of the cosmogenic part is negligible as it is less than one percent of the ambient flux in this energetic range.

Chapter 6

Simulation of the Neutron Background

In this section, a series of simulations of the various neutron backgrounds discussed in the previous section is presented. This simulation is divided into four parts along the major neutron sources described in the previous sections:

- First, the background of the ambient neutron background found in the LN Gran Sasso.
- Second, α – induced neutrons from the PE shielding.
- Third, the spontaneous fission neutrons from uranium and thorium contaminations in the lead and copper shielding of the experiment.
- The cosmogenic neutrons produced by muons in the ambient rock of the LNGS provide are the source for the last simulation run.

Care has been taken to keep most information of the collected data of a nuclear recoil event available for further processing, e.g. deposited energies are stored by the particle type responsible for each of them. Furthermore, starting energy, location and momentum of the primary neutron are collected. The global time, energy, charge and baryon number of the first particle hitting the detector in an event is stored for each detector module, too. Two counters contain the number of observed elastic and inelastic neutron – nucleon scatterings in the detector module.

The data collected during the simulation of a distinct experimental setup and a neutron source with a defined energy spectrum and starting location is generally found in several files as the simulation has been distributed into a number of runs on the available computers found at the local area network the Arbeitsbereich I, Subatomare Physik at the Physikalisches Institut at the Eberhard – Karls Universität at Tübingen. All simulation runs used the same version of GEANT4.9.1.3 with a modified version of the *G4NeutronHPInelastic* process presented in Sec. 4.5 .

In the analysis the data of several data files is processed at the same time. In a first step, the raw physical data records of an event from the output of the simulation is converted in detector output by application of the detector parameters which contain the general light output of a detector module, the various quenching factors and further parameters describing the light detector resolution. The status of the light detector and the phonon detector of the module can be defined, too. If required, these parameters can be specified for each detector separately. In the analysis of the neutron sources in the next sections, the default set of parameters is found in Tab. 6.1.

The first of these parameters is the lightyield, i.e. the conversion factor of deposited energy to energy in photons. The quenching factors of the various hadronic particles describe the attenuation of the light output of the given particles compared to electrons and γs. These values are treated as constants in energy throughout the analysis presented in the following sections. Such a simplification may not be justified for the analysis of the low energy experimental data, as the overlap between nuclear recoils and electromagnetic events depends critically on the energy dependent quenching factors and the lightyield. In the simulation the absence of ambient electromagnetic background allows the extraction of the nuclear background does not depend as critically on the energy dependencies of the parameters. The used quenching factors for the heavy nuclei are taken from Tab. A.2. Proton and the α quenching factors are slightly lower than the values found in Tab. A.2. This difference in the proton and the α quenching does not compromise the discrimination of electromagnetic, proton, α and nuclear recoil events in the simulation. A_0 and A_1 are the powers series coefficients of the deposited energy parameterization of the FWHM of the light detector. These two parameters are of interest for the construction of probability maps only.

Parameter	Value
Lightyield	0.05
Q_{O}	10
Q_{Ca}	17.9
Q_{W}	35
Q_p	1.75
Q_α	5.0
A_0	0.95 $\mathrm{keV_{ee}}$
A_1	0.24 $^{\mathrm{keV_{ee}}}/_{\mathrm{keV_{ee}}}$

Table 6.1: Default parameter set used in the simulation of Ch. 6. The lightyield is the total amount of energy which is converted by an electron or γ induced event into photons. The Qs are the quenching factors of the various hadronic particles which can deposit light in the detectors. A_0 and A_1 describe the FWHM of the light detector signal for a given electron – equivalent energy deposited in the phonon channel.

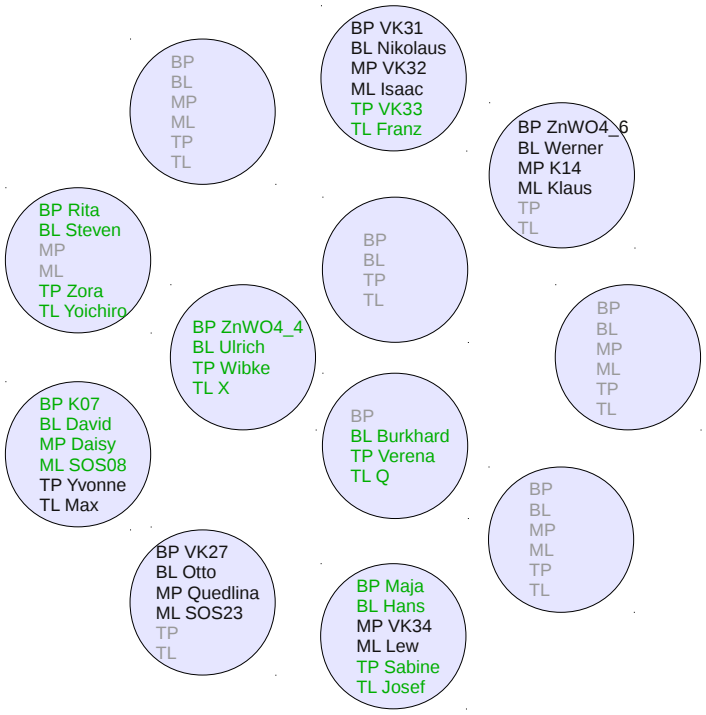

Figure 6.1: Detector positions for the simulation of the CRESST – II experiment presented in this work. The position of light (L) and phonon (P) detectors on the top (T), bottom (B) or middle (M) position in the towers of the carousel are shown. Channels of modules with *operational* phonon and light detectors are colored green, *installed* modules exhibiting non operational channels are colored black and positions without installed modules are depicted grey.

For the comparison of the analysis of simulations with the experimental results, three different sets of detectors are used. If required, other configurations can be investigated easily. Fig. 6.1 shows both the setup and configuration of the detector modules in Run 32 of the CRESST – II experiment. A minimum energy deposition of 5 keV is required for the detection of a hit in the simulation. The discrimination of nuclear recoils from electromagnetic events requires a higher threshold in energy; unless noted explicitly, an optimistic threshold in the deposited energy of 10 keV is assumed. The upper boundary for the analysis window of 40 keV is chosen as the energy of expected WIMP – induced nuclear recoils decreases exponentially. A lightyield above 0.25 cannot be induced by a nuclear recoil alone and is removed from the determination of the background event rate. If not mentioned otherwise, the region of interest (ROI) in the deposited energy – lightyield scatterplots is defined by an energy deposition between 10 and 40 keV and a lightyield below 0.25. The exact procedure of the definition of the various event classes and the technical terms used can be found in App. A .

6.1 Transport Simulation of the Ambient Neutron Background

In this section, the neutron background for the CRESST – II experiment from the ambient neutron flux observed in the LN Gran Sasso underground lab is discussed. Apart from the actual setup with the polyethylene (PE) neutron shielding in place, a control simulation where the PE shield is removed is done to allow a comparison with the observed background rates prior to the installation of the neutron shield. The comparison between both simulations runs gives an estimate for the quality of the neutron shield around the experiment and can test how well the input flux in the simulation matches the observed flux.

This subset of simulations demands the largest share of simulation time as 18.69 million primary neutrons are required for the simulation of 10 kga exposure for the ambient neutrons above 500 keV. The computing time needed on an AMD Phenom II 810 processor for the processing of one million primary neutrons is about nine to ten hours.

The used spectrum is the ambient neutron spectrum between 500 keV and 8.5 MeV presented in Tab. 5.4 and Fig. 5.3. A total number of 8.95 billion primary neutrons have been started, which is equivalent to an exposure of 4788.5 kga. The required computing time for such an exposure is about 81000 – 90000 hours which was distributed to the various computers available in the Arbeitsbereich I, Subatomare Physik at the Physikalisches Institut at the Eberhard – Karls Universität at Tübingen.

The simulated neutrons induced 2680 detector hits in one of the 33 detectors of the simulation setup in 1897 events, resulting in a mean multiplicity of 1.41. This translates to a total detector hit rate induced by ambient neutrons *before* any constraints of $1.53(5) \times 10^{-3}$ cts $\mathrm{kg}^{-1}\mathrm{d}^{-1}$ for a confidence level of 90 %. The distribution of the multiplicities of these events are shown in Tab. 6.2.

Multiplicity	Events with given multiplicity
1	1354
2	373
3	122
4	30
5	14
6	4

Table 6.2: Detector multiplicities observed from the simulation of ambient neutrons above 500 keV primary energy. All 33 modules and the full geometry including all shieldings were considered and no constraints were applied to the data set from the simulation. A total number of 2680 detector hits in 1897 events were registered in the simulation of 4788.5 kga exposure.

The effective background is reduced from the raw number given above by the application of four constraints:

- The number of active detectors can be varied. This allows the reduction of the multiplicity if more active detector modules are operated and may reveal possible geometric effects on the background rate. Three setups will be considered; all 33 detector modules, 17 installed detector modules and the ten operational detectors of the current CRESST run. The position of the detectors in the setups can be deduced from Fig. 6.1. Multiple events can be eliminated from the set of valid background events.
- A threshold on the energy deposition and the definition of a region of interest for the energy deposition will yield a background rate comparable with the experimental observation.
- A constraint on the lightyield will allow the separation of events were a nuclear recoil and a γ deposit energy in the detector simultaneously. In most cases, such events do not constitute a background to the nuclear recoil band in the experiment and have to be subtracted from the set of background events.
- A separation of the simulation data by the recoiling nucleus can be done. If a separation of the nuclear recoil band by the different species can be achieved in the experiment, the effective background can be reduced.

Multiple hits in the detectors can be subtracted from the ensemble of detector hits as the interaction of WIMPs with the detector material cannot compete with the expected rate of neutron double scatterings. However, as nuclear neutron – nucleus cross – sections are much larger than WIMP – nucleus cross – sections a significant number of multiple hits induced by neutrons is expected. The fraction of multiple hit events to single hit events increases with the number of detectors, which is seen in Tab. 6.3 which contains the observed multiplicities using the three additional constraints:

- At least one detector hit shows a deposited energy of 10 – 40 keV.
- Each hit of the event has to deposit at least 5 keV.
- Both phonon and light detector channels are flagged as operational in the analysis.

For the remaining events, the ratio of multiple hit events to single events is reduced for the *full* setup of 33 detectors from 28.6 % to 23.0 %. The set of events obtained from the 17 *installed* detectors reveals a fraction of 11.9 % of multiple detector hit events. For the *operational* set of ten detectors, events with multiple detector hits constitute 8.0 % of all events passing the constraints.

Multiplicity	Operational (10)		Installed (17)		All (33)	
	Events	%	Events	%	Events	%
1	69	92.0	119	88.1	194	77.0
2	5	7.5	14	10.4	42	16.7
3	1	0.5	1	0.7	14	5.6
4			1	0.7	2	0.8

Table 6.3: Detector multiplicities observed from the simulation of ambient neutrons above 500 keV primary energy. Applied constraints and detector sets are defined in App. A.

As the number of available detectors is reduced, the number of multiple hit events decreases faster than the number of single detector hits. Setting a threshold to the deposited energy converts *physical* multiple hit events to *observed* single hits. In the case of ambient neutrons, the low statistics due to the small overall number of events leaves quite an uncertainty for the obtained fraction of multiple events.

In the next step, the remaining events are separated by the calculated lightyield, removing events with a lightyield above 0.25 which are induced by low – energy electromagnetic background and inelastic neutron scattering events where the energy deposited by the γ dwarfs the nuclear recoil. As input parameters for the calculation of the lightyield of an event, it is required to specify the nuclear quenching factors Q_i, the inverse of the relative lightyield of a nuclear recoil event to an electromagnetic event. Proceeding along the line outlined in Sec. A.3, the lightyield of each event is obtained. The average quenching factors presented in Tab. A.2 are used as input parameters for this calculation:

- The quenching factor of oxygen is taken to be $Q_{\mathrm{O}} = 10.0$.
- The quenching factor of calcium is taken to be $Q_{\mathrm{Ca}} = 17.9$.
- The quenching factor of tungsten is given by $Q_{\mathrm{W}} = 35.0$.
- The quenching factors of other particles are irrelevant in this context as they do not contribute to the background in the region of interest in the simulation.

The calculated resulting lightyield is below the one expected from the nuclear quenching factor given above. This is a consequence of the fact that the quenching factor of electromagnetic particles is set to unity. However, the energy deposited in the phonon channel is reduced by the energy radiated in the scintillation light channel. The amount of deposited energy depends on the intrinsic lightyield of the detector crystal L_{crystal} [*] .

[*]The e.m. intrinsic lightyield L_{crystal} is a quantity which can vary greatly between different crystals. It is on the order of a few percent, generally about 1.5 %. For the presented analysis an excellent value of 5 % percent has been assumed.

The total energy deposited into the scintillation light channel and into the phonon channel can be calculated from the sum of the contributions of the different particles involved:

$$E_{\text{photon}} = \sum_i \frac{E_{\text{dep i}} L_{\text{crystal}}}{Q_i},$$
$$E_{\text{phonon}} = \sum_i E_{\text{dep i}} \left(1 - \frac{L_{\text{crystal}}}{Q_i}\right)$$

The ratio of E_{photon} to E_{phonon} divided by the intrinsic lightyield of the crystal L_{crystal} can be used to discriminate e.m. events from nuclear recoils:

$$\text{LY}_{\text{event}} = \frac{E_{\text{photon}}}{E_{\text{phonon}}} \frac{1}{L_{\text{crystal}}}$$

In a real experiment, the energy depositions in the light and the phonon channels must be calibrated. In this case, the resulting lightyield from response of the light channel of a γ or β – source and the heat seen in the phonon channel is defined as unity for each tested energy. The small percentage of missing energy in the phonon channel is neglected in this approach. The resulting *calculated* lightyield can be related to the calibrated LY_{cal} by a factor:

$$\text{LY}_{\text{cal}} = \text{LY}_{\text{event}} \frac{1}{1 - L_{\text{crystal}}}$$

The rescaling factor has to be applied to the nuclear recoil events, decreasing their lightyields. For sensible choices of quenching factors and intrinsic lightyields, the classification of events into the various recoil bands is robust, the results presented throughout this chapter do not depend significantly on the choice of parameters.

The events are separated into three classes according to their *calculated* lightyield[†] :

- *Oxygen Recoils* are all recoils which show a *calculated* lightyield between 0.08 and 0.125. This translates to a quenching factor of the detector hit between 8 and 12.5.
- *Calcium Recoils* are all recoils which show a *calculated* lightyield between 0.04 and 0.08. This translates to a quenching factor of the detector hit between 12.5 and 25.
- *Tungsten Recoils* are all recoils which show a *calculated* lightyield between 0.02 and 0.04. This translates to a quenching factor of the detector hit between 25 and 50.

[†]The calculated lightyield is obtained by application of the mean quenching factor of the nucleus to its deposited energy in the simulation. At this point, the resolution of the photon detector is assumed to be perfect.

Multiplicity	Events with given multiplicity		
	Operational	Installed	All
	Nuclear Recoils		
1	68	117	190
2	5	14	42
3	1	1	12
4		1	2
	Oxygen in ROI – Nuc. Rec.		
1	62	103	170
2	4	12	37
3	1	1	12
4		1	2
	Calcium Recoil ROI – Nuc. Rec.		
1	6	14	20
2	1	2	7
3			2
	Tungsten Recoil in ROI – Nuc. Rec.		
1	0	0	0
2	0	0	0
3	0	0	1

Table 6.4: Detector multiplicities observed from the simulation of ambient neutrons above 500 keV primary energy.

For events with higher multiplicities, the event class is determined by the lightyield of any detector hit in the energetic region of interest allowing a double detector hit event to be found in multiple classes. Other detector hits just need to deposit more than 5 keV with any lightyield. The comparison between Tab. 6.4 and Tab. 6.3 reveals that the high lightyield fraction of events exhibiting a lightyield above 0.25 is very tiny. Is is an indication that almost all neutrons passing to the surroundings of the detector modules are moderated to energies incapable of producing γs in inelastic scatterings. For the setup of the 10 *operational* detectors, only a single event is removed out of 69. For the 17 installed detectors, two events out of 119 are removed. And for the full setup of 33 detectors, four single hit events out of 194 are removed. Furthermore, two triple hit events out of 14 rejected since at least one detector hit exhibits a lightyield above 0.25. Thus the background in the ROI due to ambient neutrons is found almost exclusively in the nuclear recoil band.

The significance of the distribution of events in the three different nuclear recoil classes is limited as a low number of background events is observed. Using the *operational* ten detector setup, the distribution of events in the nuclear recoil band is determined. For single detector hits, events have a likelihood of 91^{+5}_{-7} % to be found in the oxygen recoil band and 9^{+7}_{-5} % to be located in the calcium recoil band (90 % C.L.). Single detector hit tungsten recoils have not been observed in the simulation run due to insufficient statistics, an upper limit of 3.3 % can be inferred with 90 % C.L. .

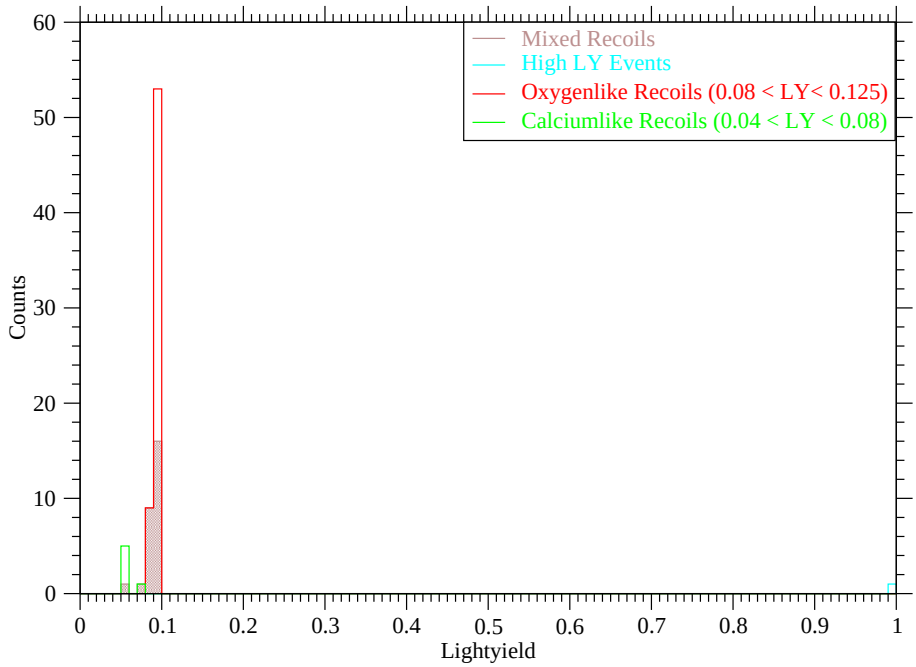

Figure 6.2: Histogram of the *calculated* lightyield of all single detector hits by ambient neutrons obtained from the simulations of the ten detector setup with energy deposition between 10 – 40 keV.

Double detector hit events which show a detector hit in the oxygen recoil band in the region of interest provide 80^{+19}_{-34} percent (90 % C.L.) of all double detector hit events. On this confidence level, the result for double detector hits showing a hit in the energetic ROI in the calcium band is 20^{+34}_{-19} % and the upper limit for double detector hits within the tungsten recoil band is 32 %. The distribution of the single detector hit event *calculated* lightyields of these events presented in Tab. 6.4 can be seen in Fig. 6.2.

Of the 68 observed nuclear recoil events, 27 are in fact a combination of multiple nuclear recoils on different nuclei. These events populate the region between the quenching factors of recoils on a single nuclear species. In the region of interest between 10 and 40 keV, the effect of the mixed nuclear recoils on the observed *calculated* lightyields for background events from ambient neutrons is tiny. For events with lower deposited energies this effect becomes more pronounced, as the number of mixed nuclear recoils in comparison to the number of single species nuclear recoils increases. As a result, at low energies the mixed nuclear recoils events widen the observed lightyield distributions and bend the oxygen band to a slightly lower and the tungsten band to a higher mean lightyield than expected from single nuclear species recoils at higher energies.

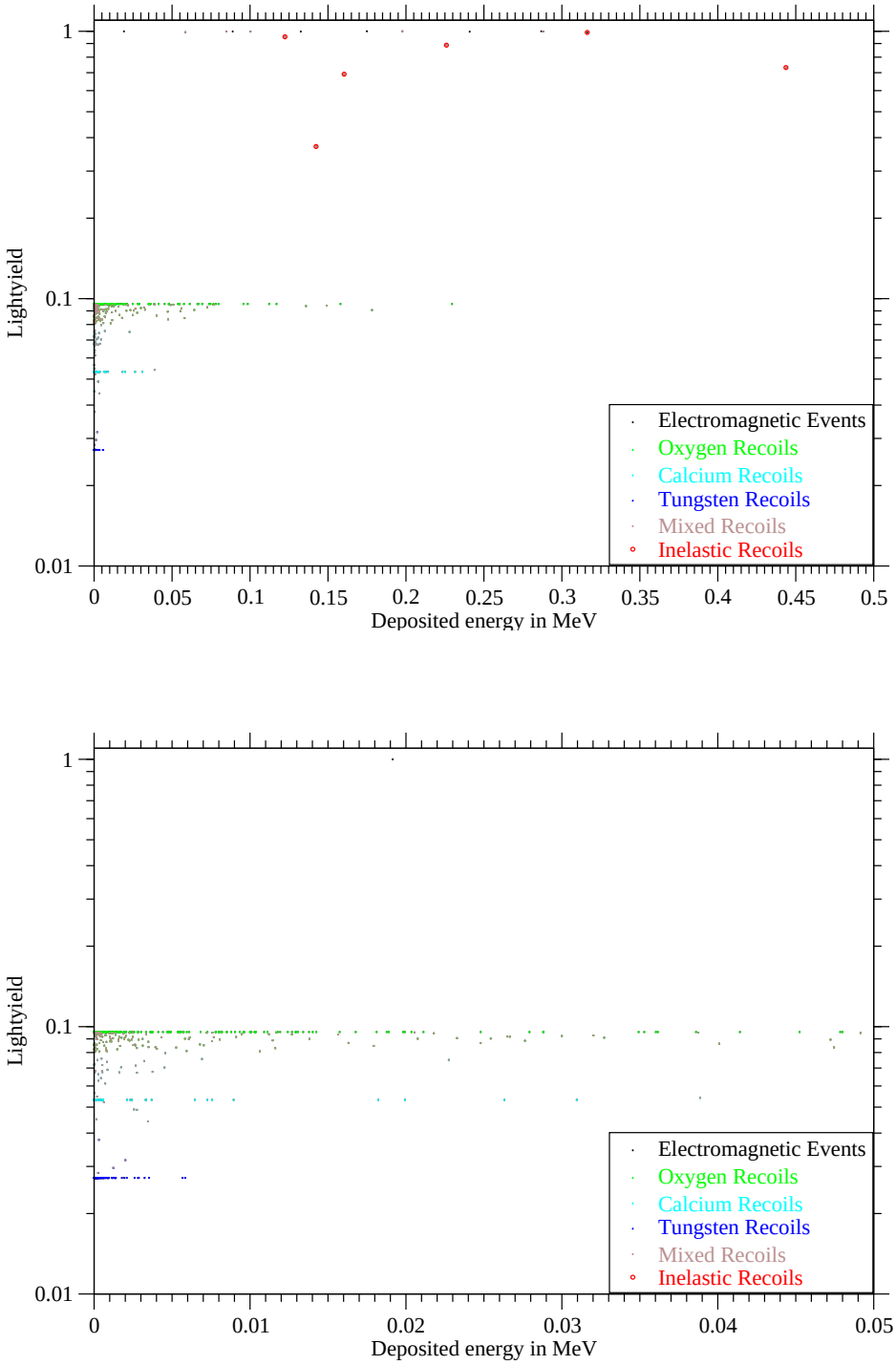

Figure 6.3: Single detector hits for the *operational* detectors by ambient neutrons excluding detector resolution effects. The bottom plot shows the low energy region of the plot above.

The type and position in the deposited energy – lightyield scatterplot is shown in Fig. 6.3. From the two scatterplots shown in the figure, a number of interesting things can be learnt.

The maximum energy of single detector hit nuclear recoils is limited to energies below approximately 250 keV, with the bulk of events located at very low energies below 50 keV and most events are even outside the ROI below its lower threshold of ten keV. The observed maximum energies of the three nuclear species indicates that the kinetic energy of the neutrons impinging on the detectors must be lower than one MeV. Six events seen in the sample below 500 keV exhibit a large lightyield, which identifies them as inelastic scatterings along the $(n, n_i'\gamma)$ reaction channels. As inferred from the distribution of lightyields within the ROI, events with intermediate lightyields populate the area between the lines along the single species nuclear lightyields. For lower energies, the fraction of such events increases considerably.

The histogram shown in Fig. 6.4 visualizes the background distribution with respect to the deposited energy.

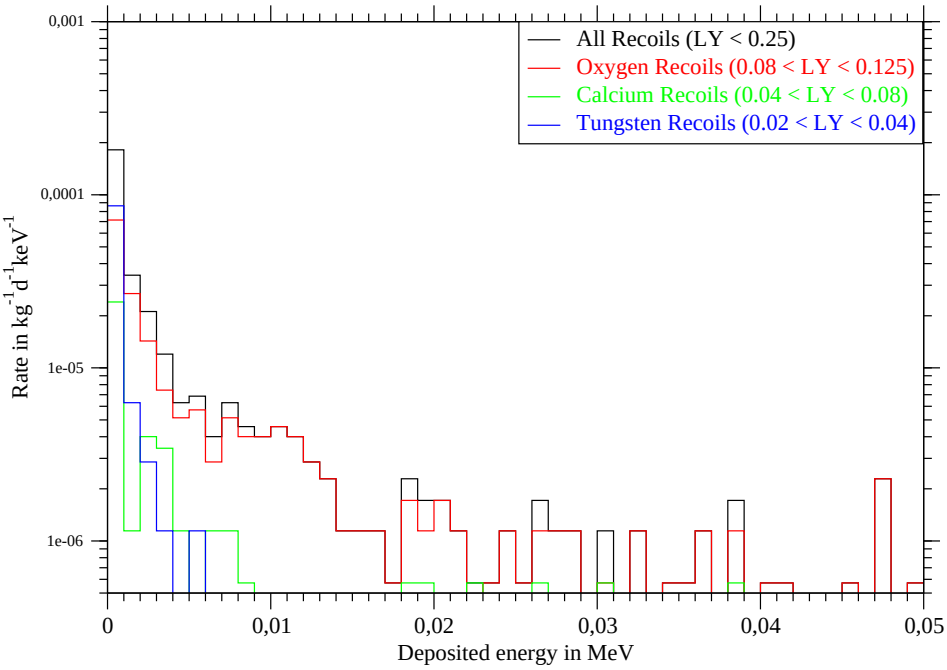

Figure 6.4: Background rates calculated from all single detector hits for the ten detector setup for energies up to 50 keV. In this case, no minimum energy deposition was required for a valid event.

Hit type	Counts	Rate in cts $kg^{-1}d^{-1}$
	Operational Setup (10 Det.)	
All nuclear recoils	$68^{+15.2}_{-13.0}$	$\mathbf{1.29^{+0.29}_{-0.25} \times 10^{-4}}$
Oxygen recoils	$62^{+14.6}_{-12.4}$	$1.18^{+0.28}_{-0.24} \times 10^{-4}$
Calcium recoils	$6^{+5.84}_{-3.39}$	$1.14^{+1.12}_{-0.66} \times 10^{-5}$
Tungsten recoils	$0^{+2.30}$	$< 4.39 \times 10^{-6}$
	Installed Setup (17 Det.)	
All nuclear recoils	$118^{+19.5}_{-17.3}$	$1.31^{+0.22}_{-0.19} \times 10^{-4}$
Oxygen recoils	$103^{+18.3}_{-16.1}$	$1.14^{+0.20}_{-0.18} \times 10^{-4}$
Calcium recoils	$14^{+7.9}_{-5.5}$	$1.55^{+0.88}_{-0.61} \times 10^{-5}$
Tungsten recoils	$0^{+2.30}$	$< 2.58 \times 10^{-6}$
	Full Setup (33 Det.)	
All nuclear recoils	$191^{+24.3}_{-22.2}$	$1.09^{+0.14}_{-0.13} \times 10^{-4}$
Oxygen recoils	$170^{+23.1}_{-20.9}$	$9.73^{+1.32}_{-1.20} \times 10^{-5}$
Calcium recoils	$20^{+9.1}_{-6.7}$	$1.14^{+0.52}_{-0.38} \times 10^{-5}$
Tungsten recoils	$0^{+2.30}$	$< 1.32 \times 10^{-6}$

Table 6.5: The single detector hit neutron induced nuclear recoil events in the region of 10 – 40 keV induced by ambient neutrons. The setups and the definition of the recoil types is outlined in App. A. The confidence level used is 90 % and is calculated in Poissonian statistics.

A summary of the single hit background rates according to the simulation for the three setups by recoil types can be found in Tab. 6.5. A self shielding effect of neighboring detector modules is noticed, since the table indicates that the background is reduced slightly (16 %) as the detector setup is enlarged from ten to 33 active detectors. This effect can be understood as the chance of multiple scattering events rises with the number of nearby detector modules.

As the statistical errors still encompass the mean background rates of the three sets of detector modules, this effect has to be addressed in the sections where neutron sources with much larger sets of events are discussed.

From the simulation of the ambient neutron background, several conclusions can be drawn:

- After application of constraints to the lightyield, the energy deposition and the multiplicity of hit detectors, the resulting background rate of $1.29^{+0.29}_{-0.25} \times 10^{-4}\ {}^{\mathrm{cts}}/_{\mathrm{kgd}}$ is still about a factor 800 too low to be in agreement with the observed background rate in Run 32 of the CRESST – II experiment.
- For a setup of ten *operational* detectors, 8.1 % of all nuclear recoil events exhibit multiple detector hits. This number rises as more detectors are included in the analysis. In contrast, preliminary analysis of the experimental Run 32 resulted in zero multiple detector hits for a sample of about 50 single detector hits.
- Using multiple detector hits to veto events, a self shielding effect of additional detector modules is vaguely observable, but still within the 90 % confidence limit. The mean background rate decreases by 16 % as the number of operational detector modules is increased from ten to 33.
- Inelastic scatterings and high lightyield detector hits are rare. The amount of produced secondary particles reaching the detectors is not significant.
- Nuclear recoil events in the region of interest are mainly found in the oxygen recoil band ($\approx$ 90 % of all events).

6.1.1 The Ambient Neutron Background below 500 keV

As explained in Sec. 5.3, no tungsten recoils above ten keV are kinematically possible for incident neutron energies below 460 keV. Initially, the main question for the simulation presented here was the prediction of the rate of tungsten recoils seen in the CRESST experiment. In Tab. 5.4 and Tab. 5.5 a value of 0.82 is found for the ratio of the ambient neutron flux in the bin 1 – 500 keV to the flux given above this energy. In order to reduce the computing time needed for the simulation of the ambient neutron background with its excessive amount of primary neutrons, it was decided to exclude the low energy neutrons from the simulation of the ambient neutron background.

During the analysis the interest in the low energy neutrons has been revived, especially when it became obvious that a clear separation of nuclear recoils in the low energy region between 10 and 40 keV was not achievable and further questions about events in the oxygen recoil band arose. As the energy transfer from a neutron to a oxygen nucleus is about an order of magnitude larger than the energy transfer to a tungsten nucleus, neutrons with energies as low as 46 keV can induce oxygen recoils above a detector threshold of ten keV. There are two possible reasons why the simulation of these low energy neutrons could be interesting:

- If the detector resolution in the experiment does not allow the discrimination of oxygen recoils from tungsten recoils, oxygen recoils contribute fully to the *Dark Matter* background.
- If the nuclear recoils due to *Dark Matter* particles are expected on oxygen rather than tungsten.

Another run of the ambient neutron simulation was set up in which the missing low energy part of the ambient neutron spectrum was simulated. A total flux of $6.5 \times 10^{-7}\ {}^{\mathrm{cts}}/_{\mathrm{cm^2 s}}$ was assumed between 1 to 500 keV, with a linear slope fitting the fluxes deduced from tabs. 5.4 and 5.5 at 1 keV and 500 keV. About 15.28 million primary neutrons were required for the simulation of 10 kga exposure. A total of 7.2 billion primary low energy neutrons were processed in total which amount to a simulated exposure of 4712.8 kga, matching the exposure simulated for the ambient neutron flux above 500 keV. Tab. 6.6 shows the multiplicities of detector hits, obtained for the constraints outlined in App. A.

Multiplicity	Number of events		
	Operational (10)	Installed (17)	All detectors (33)
1	2	2	3
2			0
3			1

Table 6.6: Detector multiplicities observed from the simulation of low energy ambient neutrons below 500 keV primary energy. The applied constraints and the definition of the used detector sets are unchanged and found in App. A.

As expected, all events are located in the oxygen recoil band. The event rate due to low energy ambient neutrons compared to the event rate induced by ambient neutrons with energies above 500 keV is tiny, for the *operational* detector setup the ratio is 2 : 68, in the case of the *installed* detector setup, a ratio of 2 : 118 is observed and for the *full* detector setup, three events are added to the 191 by the low energy ambient neutron background. Inclusion of the low energy neutron contribution to the background rate in the ROI between 10 – 40 raises the background rate to $1.33^{+0.29}_{-0.25} \times 10^{-4}$ cts kg^{-1}d^{-1} for the ten detector module setup. For the full setup of 33 detectors, the combined ambient background rate is $1.11^{+0.14}_{-0.13} \times 10^{-4}$ cts kg^{-1}d^{-1}. Form this simulation additional conclusions can be drawn:

- The background events induced by ambient low energy neutrons are on the level of about two percent of the background events induced by the ambient neutron background above 500 keV.
- As there have been only a few of events obtained in the simulation, no analysis of their distribution is possible.
- The additional contribution to the neutron background rate does not change the discrepancy by a factor of 600 between the simulated background due to ambient neutrons and the observed one of about 0.078 cts kg^{-1}d^{-1} in the real experiment.
- To explain a background rate of 0.08 kg^{-1}d^{-1} of CRESST – II Run 32 with an external neutron source, such a source is required to provide about 660 Bq in neutrons according to the observed rate of background events in the ROI per primary neutron in the combined simulations of Sec. 6.1 and 6.1.1 with the spectral shape employed for the simulations. For example, assuming an ^{241}Am – Be source to be sufficiently similar to the ambient input spectrum, the needed total activity of such a source in α particles is about 12.4 MBq using a standard conversion factor of 6.6×10^{-5} $^{n}/_{\alpha}$ [Gi85]. The required activity 1200 times over the legal limit for unmonitored sources excludes the hypothesis that a weak source accidently placed somewhere around the experimental setup is responsible for the observed nuclear recoil background in run 32.

6.1.2 Simulation of Ambient Neutrons without PE shielding

In this subsection a simulation of the ambient neutron background for the setup without polyethylene shielding is presented. The background rates previously predicted by the simulation in this section are about a factor 800 too low compared to the rates seen in the current CRESST – II setup [Pf10]. To test the simulation, the CRESST – II setup without the polyethylene (PE) shielding was set up. Thus a comparison of the simulated neutron rate to the observed neutron rate of the runs conducted before the PE neutron shielding was placed and an estimate of the effectiveness of the neutron shield of the CRESST setup can be gained. In the absence of the outer PE shield, it is assumed that the ambient neutron background dominates all other considered neutron sources by at least an order of magnitude [Wu04].

The input spectrum for the simulation is the same as presented in Sec. 5.4 for the part above 500 keV incident energy while the low energy part from 1 – 500 keV is taken from subsection 6.1.1. The starting area of the primary neutrons was reduced to 24.54 m^2 as the absence of the polyethylene shield allowed for a reduction in the size of the box engulfing the experimental setup. For the simulation of about ten years of experimental run time, 60 million neutrons with energies above 500 keV had to be started and 49.2 million neutrons with an energy between 1 and 500 keV.

An investigation in the influence of detector choice for double detector hit event rates has been performed on the simulation of the CRESST – II setup without PE shielding. Two extreme setups where chosen to determine the effect of the detector module geometry on the observed multiplicity: The first setup minimizes the distance between the two analyzed modules, the two neighboring detectors in tower 9 of the carousel on the lower and the middle position are selected for the analysis. The second setup maximizes the distance between two modules, the module in the lower position of tower 9 and the module in the upper position in tower 4 are selected in this case. A third investigation combined any two detector modules and calculated the average number of single and double detector hits.

For this simulation, an energetic region of interest of 12 – 40 keV has been chosen in accordance to Ref. [An05]. The selection criterion for multiplicity two required one module to show a detector hit in the region of interest and the other module to show a hit above 12 keV. Each detector hit was required to show a lightyield of less than 0.5 . The resulting number of detector hits and of nuclear recoil background rates are presented in Tab. 6.7 . Neighboring detectors show a smaller background for single hits, but a larger background of double events. For comparison, the mean number of detector hits for events of multiplicity one (1565) and two (19) are given for all possible pairs of the 33 available detectors. The rates for single detector hit events is quite fixed, double detector hits show a variance of a factor of about 3.7 . To obtain the 90 % C.L. boundaries for the pairs, the standard deviation is calculated assuming a Gaussian distribution.

Multi – plicity	Nearby Modules	Rate cts $kg^{-1}d^{-1}$	Far Modules	Rate cts $kg^{-1}d^{-1}$	Avg.	Rate cts $kg^{-1}d^{-1}$
1	1510	$0.713^{+0.031}_{-0.029}$	1566	$0.734^{+0.032}_{-0.030}$	1565	$0.733^{+0.037}_{-0.036}$
2	44		12		19	

Table 6.7: Detector multiplicities observed from the simulation of ambient neutrons in the absence of the polyethylene shielding of the CRESST experiment.

16 nuclear recoils translating into a background of $0.87^{+0.45}_{-0.33}$ cts $kg^{-1}d^{-1}$ (90 % C.L.) in the ROI between 12 and 40 keV have been reported for the CRESST experiment with two detector modules prior the installation of the neutron shield, the radon box and the muon veto for a net exposure of 20.5 kgd [An05] [‡]. A simulation of a simplified CRESST setup has been presented in Ref. [Wu04], found a background of 0.5 – 0.6 cts $kg^{-1}d^{-1}$ in the energy range of 12 – 40 keV.

While the background rate of $0.713^{+0.031}_{-0.029}$ cts $kg^{-1}d^{-1}$ obtained in this section is higher than the one found in Ref. [Wu04], it agrees quite well with the experimental one. Five lessons can be learnt from the simulation of the unshielded setup:

- The used neutron spectrum and the employed neutron physics in the simulation yield a background event rate which is consistent with the one seen in the experiment. This is an evidence that the discrepancy of the simulation of the shielded experiment is not caused by erroneous neutron – nuclear physics in the modified GEANT4 used for the simulations.
- The discrepancy of about 20 % between Wuladari's simulation employing a simplified setup versus a more detailed simulation presented in this emphasizes the importance of detailed experimental geometries versus *toy* geometries.
- In the simulation, the PE shield in combination with the larger number of operational detector modules reduces the background rate induced by ambient neutrons by a factor of about 5500 in the energetic region between 12 and 40 keV.
- An leakage of the simulated PE shielding of 10 – 15 % is required to explain the observed rate in run 32 of the CRESST – II experiment. Such a leakage requires large visible holes which are not detected in the used PE shielding.
- The geometrical distance between detector modules influences the double detector hits strongly. The double detector rate for the detector carousel in the CRESST – II experiment varies by a factor of 3.7 between neighboring detector modules and those in maximum distance.

[‡] In the quoted reference, a value of 0.87 ± 0.22 kgd is given. Poissonian statistics at a C.L. of 90 % have been applied as the number of counts is so low.

6.2 Simulation of (α, n) and S.F. Neutrons Produced in the PE Shielding

In this section, the simulation of the neutron background due to (α, n) reactions and spontaneous fission of impurities in the polyethylene neutron shielding is presented.

In Sec 5.5.2, a spectrum produced with the SOURCES4A code according to the impurities found in bulk polyethylene (PE) as listed in Tab. 5.7 has been presented. In this simulation the higher contaminations observed in the bulk PE sample of 1.3 ppb of Th and 0.5 ppb of U distributed uniformly within the PE elements of the shielding have been employed. Such a contamination results in 13500 neutrons produced per year with a resulting energy spectrum shown in Fig. 5.9. In this case, the total neutron production rate within the PE shielding is $4.3 \times 10^{-4}\ {}^{n}/_{s}$. The contribution of the radon induced (α, n) reactions is not considered in this simulation as it is at least an order of magnitude less.

135 million primary neutrons resulted in 12645 detector hits in 9025 events, the unconstrained multiplicity structure with an average multiplicity of 1.40 is shown in Tab. 6.8. The simulated exposure of 100000 kga needed about 1300 h of computation time on a Intel Core i5 CPU 750 clocked at 2.67 GHz.

The analysis of the data is identical to procedure described throughout Sec. 6.1, the basic constraints are reiterated here: At least one detector hit in the range of 10 – 40 keV and a general threshold of five keV for a detector hit are required. Three sets of operational detectors are defined; the first set is defined by the ten operational detectors of CRESST – II Run 32, the second encompasses the seventeen installed detectors of Run 32 and the third one uses all possible 33 modules which fit into the carousel. The position of the detector modules within the carousel is presented in Fig. 6.1.

Multiplicity	Number of events
1	6416
2	1842
3	567
4	148
5	36
6	12
7	4

Table 6.8: Detector multiplicities observed from the simulation of neutrons produced in the PE shielding. All 33 modules were considered for the table above. No constraints were applied to the data set. A total number of 12645 detector hits were registered in 9025 events the simulation of 100000 kga exposure.

Multiplicity	Operational		Installed		All	
	Events	%	Events	%	Events	%
1	422	90.2	653	85.9	1148	76.5
2	46	9.8	102	13.4	293	19.5
3			5	0.7	49	3.3
4					9	0.6
5					2	0.1

Table 6.9: Detector multiplicities and relative fractions observed from the simulation of neutrons produced in the PE shielding. The applied constraints on energy and lightyield plus the definition of the used detector sets are outlined in App. A .

The multiplicities of the events fulfilling the constraints given above are shown in Tab. 6.9. The fraction of events with different multiplicities depends on the number of detector modules considered in the analysis. For example, the fraction of double detector hits rises from 9.8 % for the *operational* detector setup to 13.4 % for the *installed* setup to 19.5 % if all detector modules are considered. Furthermore, the maximum multiplicity of events rises with the number of active detector modules. As shown in the case of the ambient neutrons, the background in the ROI is only a small subset of the total number of these detector hits. The bulk of detector hits is found at recoil energies below ten keV.

After calculation of the lightyield, the separation of the nuclear recoils events from the high lightyield events is the next step as the latter events cannot be distinguished experimentally from electromagnetic background from ambient γ and β sources. For compatibility of the experimental and the simulated background, the high lightyield events are isolated from the set of valid events. Further separation of the remaining events into three different nuclear recoil bands yields additional information about the background events. The relevant constraints given in App. A are reiterated here:

The energy range is restricted to a region of interest (ROI) between ten to 40 keV. No other detector module is allowed to show an energy deposition above a threshold of five keV. A *calculated* lightyield of less than 0.25 is required for the detector hit within the ROI. The remaining nuclear recoil events are separated into three distinct bands centering around the mean lightyield of the nuclear species encountered in $CaWO_4$.

The application of these additional constraints reduces the amount of detector hits from 422 to 418 for the setup with ten operational detectors. Four single detector hit events exhibited a lightyield which puts them above the nuclear recoil region in the deposited energy – lightyield plot. Of the double detector hit events, four events contained a detector hit with a lightyield above 0.25, too. The vast majority of 99 % of all events deposit their energy in the nuclear recoil bands within the ROI.

Multiplicity	Number of events		
	Operational	Installed	All
	Nuclear Recoils		
1	418	646	1127
2	46	99	288
3		5	49
4			9
5			2
	Oxygen in ROI – Nuc. Rec.		
1	367	569	994
2	42	90	259
3		5	43
4			9
5			2
	Calcium Recoil ROI – Nuc. Rec.		
1	43	66	120
2	4	11	36
3			8
	Tungsten Recoil in ROI – Nuc. Rec.		
1	8	11	13
2	2	2	4
3			1
4			1

Table 6.10: Detector multiplicities observed from the simulation of (α, n) neutrons produced in the PE shielding. The applied constraints and the definition of the used detector sets are outlined in App. A.

Tab. 6.10 shows the distribution of those events into the three nuclear recoil sub – bands. The fraction of multiple detector hit events is similar to the numbers found for the ambient neutrons. For the constraints outlined in App. A the analysis of the *operational* setup results in 9.9 percent multiple detector hit events. A fraction of 13.9 percent of multiple detector hit events is found for the *operational* detector set of ten detectors. If all 33 detectors are active, 23.6 percent of all events show energy deposition in more than one detector module.

Statistically, the increase seen in multiple hit event fraction for the different detector setups between ambient neutron source and neutrons produced in the PE is not significant. Since the observed multiplicity is more sensitive to the high energy tail of the energy spectrum at the location of the detectors, the consistence of the multiplicities found for the two neutron sources imply that the effective spectra at the location of the detectors and secondary production in the surrounding material of the detectors is similar for both ambient neutrons and neutrons produced in the PE.

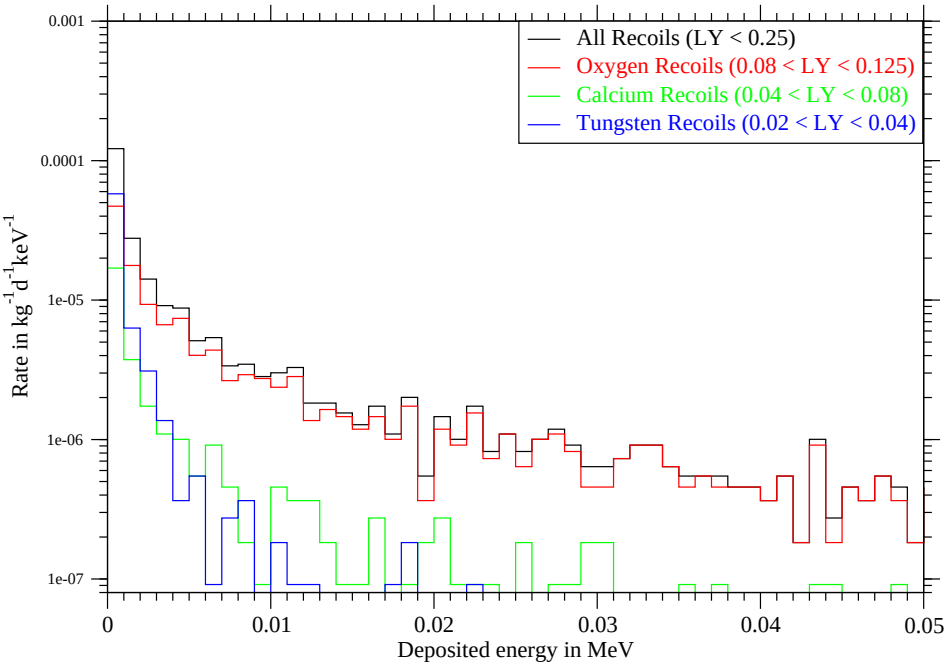

Figure 6.5: Histogram single detector nuclear recoil events up to 50 keV induced by neutrons from the PE shielding for ten operational detectors. Primary neutrons are provided by (α, n) and s.f. reactions in the PE shielding.

The expected background rates for single detector hit events can be found in Tab. 6.11 while the histogram of the deposited energy of the nuclear recoil events can be seen in Fig. 6.5. The histogram shows the steady decline of the nuclear recoil background event rate by a factor of seven between 10 and 40 keV. Nuclear recoils are mostly located within the oxygen band.

It should be noted that the background rates presented in Tab. 6.11 do not include the uncertainty in the contamination level of the PE. The chemical analysis claims an error on the order of 30 – 40 %. If this uncertainty is considered, the background rate for the *operational* setup of the CRESST – II Run 32 within 90 % C.L. becomes $3.81^{+1.90}_{-1.32} \times 10^{-5}$ cts kg^{-1}d^{-1}.

Only a third of the background events rate seen for ambient neutrons is provided by neutrons from the PE, which are about 14 times more efficient in inducing a background event. This is a consequence of the reduced average amount of shielding and starting locations closer to the detectors of the primary neutrons from this source.

Hit type	Events	Rate in cts $kg^{-1}d^{-1}$
	Operational Setup (10 Det.)	
All nuclear recoils	$418^{+35.2}_{-33.1}$	$\mathbf{3.81^{+0.32}_{-0.30} \times 10^{-5}}$
Oxygen recoils	$367^{+33.1}_{-30.9}$	$3.35^{+0.30}_{-0.28} \times 10^{-5}$
Calcium recoils	$43^{+12.5}_{-10.2}$	$3.92^{+1.13}_{-0.93} \times 10^{-6}$
Tungsten recoils	$8^{+6.4}_{-4.0}$	$7.30^{+5.89}_{-3.67} \times 10^{-7}$
	Installed Setup (17 Det.)	
All nuclear recoils	$646^{+43.4}_{-41.2}$	$3.47^{+0.23}_{-0.22} \times 10^{-5}$
Oxygen recoils	$569^{+40.8}_{-38.7}$	$3.05^{+0.22}_{-0.21} \times 10^{-5}$
Calcium recoils	$66^{+15.0}_{-12.8}$	$3.54^{+0.81}_{-0.69} \times 10^{-6}$
Tungsten recoils	$11^{+7.2}_{-4.8}$	$5.91^{+3.87}_{-2.59} \times 10^{-7}$
	Full Setup (33 Det.)	
All nuclear recoils	$1127^{+56.9}_{-54.7}$	$3.08^{+0.16}_{-0.15} \times 10^{-5}$
Oxygen recoils	$994^{+53.4}_{-51.3}$	$2.72^{+0.15}_{-0.14} \times 10^{-5}$
Calcium recoils	$120^{+19.6}_{-17.4}$	$3.29^{+0.54}_{-0.48} \times 10^{-6}$
Tungsten recoils	$13^{+7.7}_{-5.3}$	$3.56^{+2.10}_{-1.45} \times 10^{-7}$

Table 6.11: The single detector hit nuclear recoil events between of 10 – 40 keV induced by neutrons from the PE shielding. App. A explains the used constraints. The systematic uncertainty in the chemical analysis of the PE of 30 – 40 % is not included in the 90 % C.L. Poissonian errors given.

Fig. 6.6 shows the distribution of single detector hit events in deposited phonon energy and lightyield of the *operational* detector setup of ten detectors for all deposited energies. As the full range of recoil energies is shown in these plots, the constraints are changed accordingly. Different sets of single detector hit events result for extended energy range and the limited ROI constraints. The four high lightyield events removed between the sets of Tab. 6.9 and Tab. 6.10 are accompanied by subthreshold hits.
Such events are converted to multi detector hit events and excluded from the set of events presented in Fig. 6.6 . Recoils in the oxygen band are found up to 300 keV, the calcium and the tungsten band extend to an endpoint of 100 keV and 25 keV, respectively. Thus the inducing neutron spectrum ends at energies $\approx$ 1300 keV revealing the strong moderation of the primary neutron spectrum.

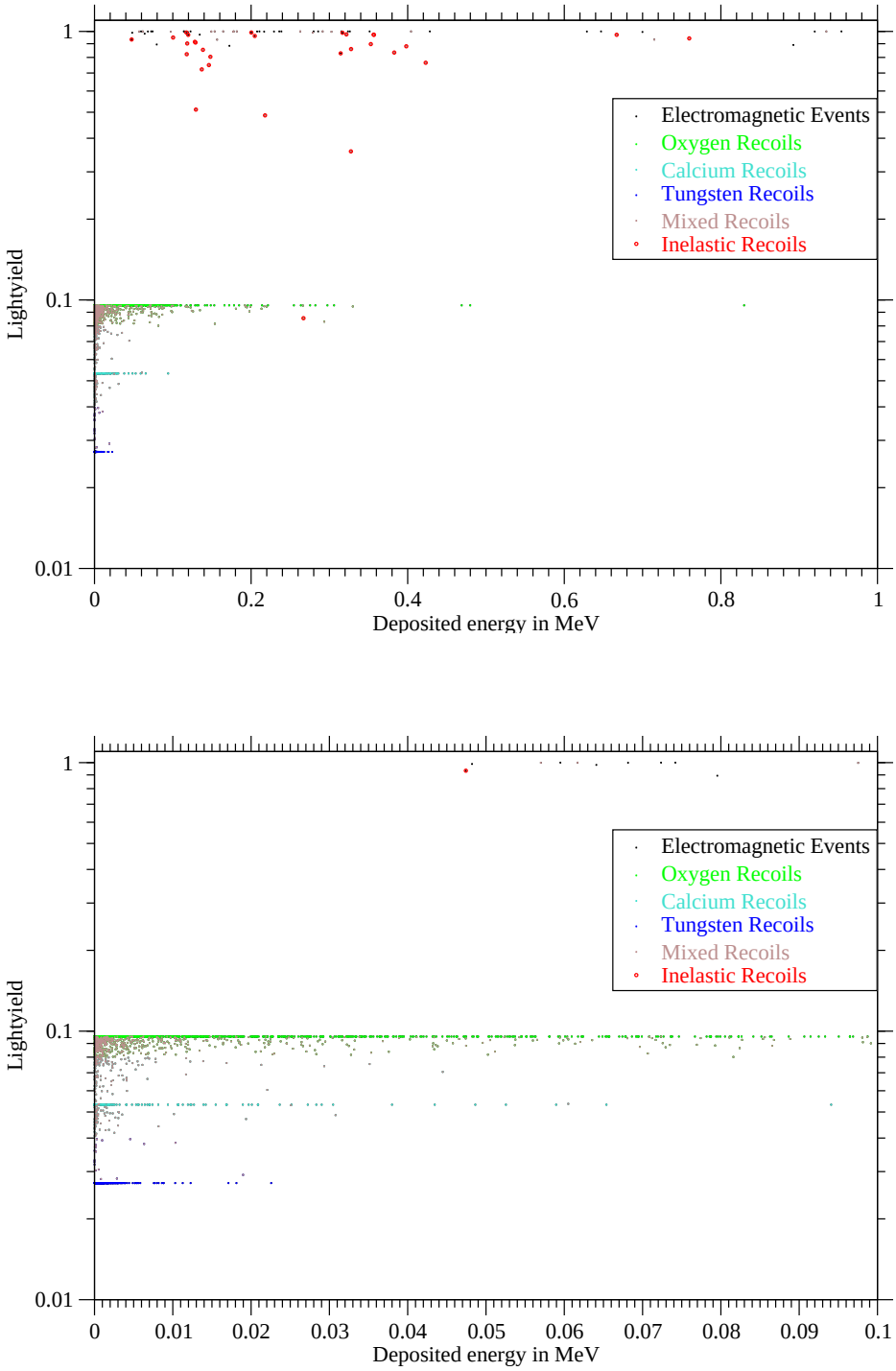

Figure 6.6: Scatterplots of single detector hit events for the *operational* ten detector setup. The primary neutrons were produced by (α, n) – reactions and s.f. in the PE shielding.

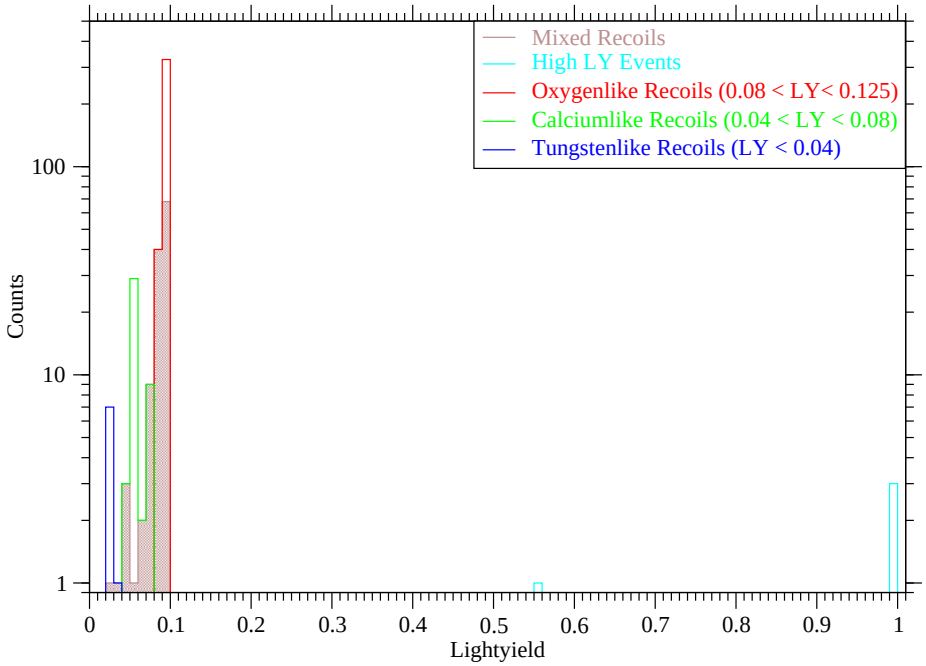

Figure 6.7: Histogram of single detector hit events by different lightyields. The events are required to exhibit a total energy deposition between 10 and 40 keV. The primary neutron source for the presented sample are (α, n) and s.f. reactions in the PE shielding.

The distribution of the lightyields and the number of single detector hit events with their mixed recoil contribution is shown in Fig. 6.7 for deposited energies within the ROI. Analysis of the distribution of single and double detector hits within the nuclear recoil bands yield the following result:

For single detector hit events, $87.8^{+1.2}_{-2.5}$ % of all events are found in the oxygen recoil band ($0.08 < \mathrm{LY_{calc}} < 0.125$), $10.3^{+2.6}_{-2.2}$ % are located in the calcium recoil band ($0.04 < \mathrm{LY_{calc}} < 0.08$) and about $1.9^{+1.5}_{-1.0}$ % have been placed in the tungsten recoil band.

For the double detector hit events, the distribution extracted from the simulation is $87.5^{+5.0}_{-8.5}$ % for oxygen recoils, $8.3^{+8.9}_{-5.3}$ % for calcium recoils and $4.2^{+7.9}_{-3.4}$ % for tungsten recoils. The numbers are given with a 90 % C.L. on the analysis of the set containing 10 operational detectors. The results of the analysis of the other detector sets are well within the 90 % C.L. interval, the low number of events yield much larger errors.

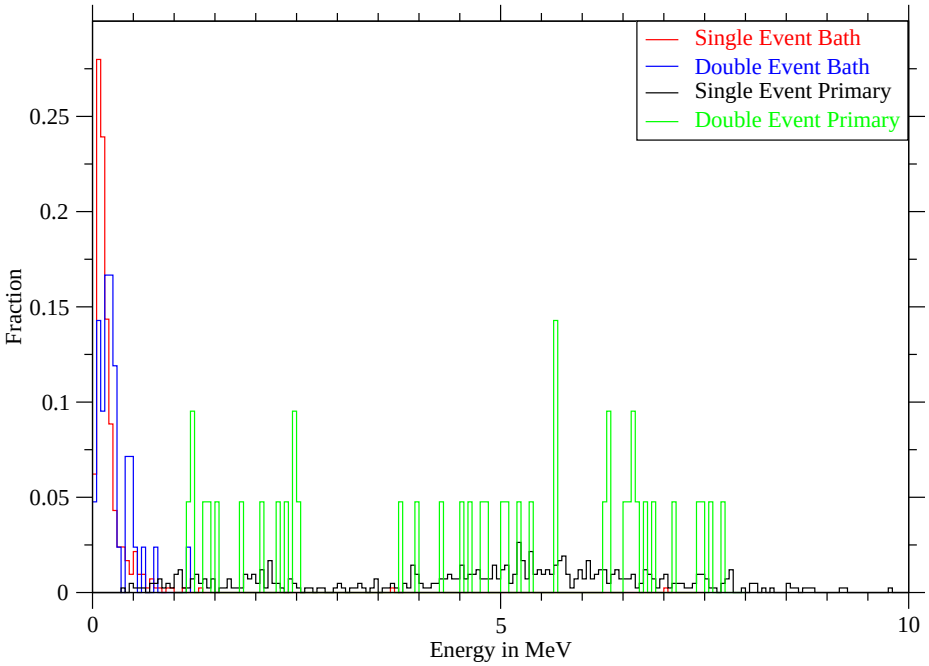

Figure 6.8: Spectrum of the fraction of events to by kinetic energy of the primary neutrons from the PE shielding and the kinetic energy of the *bath* neutrons impinging on the actual detector. The *operational* detector setup of the CRESST – II run 32 have been used to extract nuclear recoil events which deposited an energy between 10 – 40 keV.

For the recoils in the energetic ROI, the primary neutron energies and the neutron *bath* energies, i.e. the kinetic energies of the neutrons responsible for the event, are analyzed. Fig. 6.8 reveals that neutrons responsible for detector hits conforming to all constraints have been moderated in the setup because their primary energy spectrum is not in agreement with their energy spectrum passing into the detector modules. This is not a selection effect on the primary neutron energy, since the primary energy of neutrons which induced a hit in the ROI is similar to the input spectrum, but the neutron *bath* around the detectors is restricted to energies below 500 keV with only a handful of events found at excess energies. For the double detector hits, both *bath* and primary spectrum are shown, too. The low number of events prevent a meaningful analysis of the primary spectrum, but for the double detector hit event *bath* a general shift to higher energies than in the case of the single detector hit event *bath* is visible.

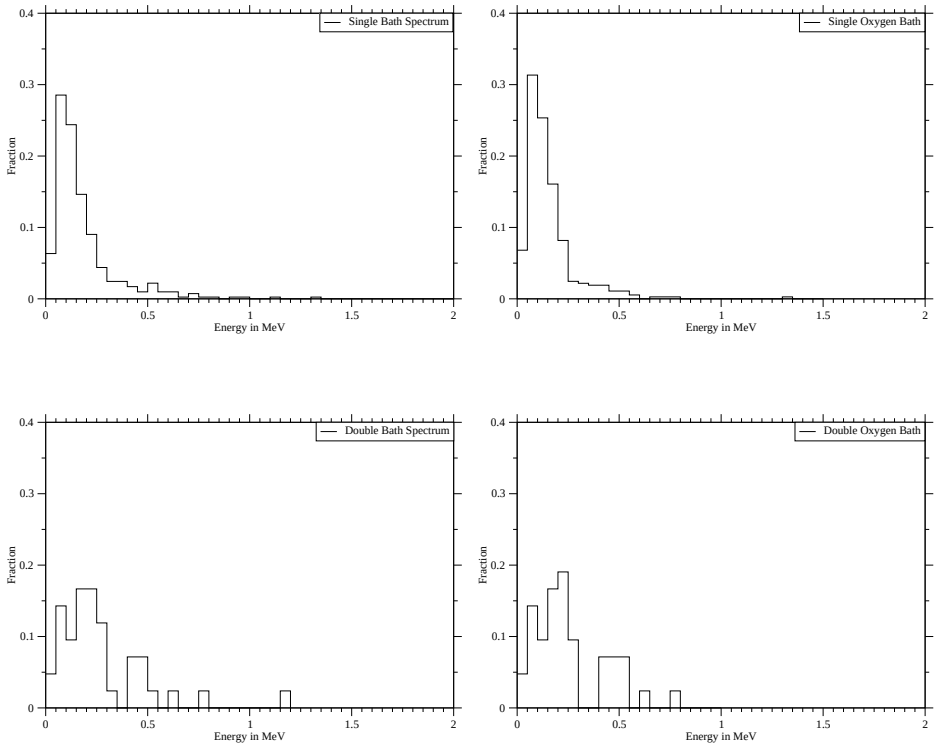

Figure 6.9: Histograms of the distribution of the kinetic energy of incoming neutrons per 50 keV bin for all nuclear recoils and oxygen band recoils in particular. The spectra for single detector hit events and double detector hit events are shown. The neutrons are started from the PE shielding according to the parameters specified in Sec. 5.5 . The *operational* detector setup of the CRESST – II run 32 have been used to extract nuclear recoil events which deposited an energy between 10 – 40 keV.

The difference in the neutron *bath* energies for oxygen single and and double detector hit events in comparison to all detector hits is shown in Fig. 6.9. The oxygen band detector hits dominate the all nuclear detector hit distribution as they contribute about 90 % of the background hit events in the ROI of 10 – 40 keV. Single detector hits in the ROI are much more probable to have been induced by neutron *bath* energies below 150 keV, about 30 % are induced by neutrons with incoming energies of 50 – 100 keV. In comparison to single detector hits double detector hits are only half as likely to be induced by such low energy *bath* neutrons. Above 200 keV, double detector hits are more likely to be induced, especially around the resonance in ^{16}O at 430 keV. While a single scattering on this resonance may result in a hit outside the ROI, its huge cross – section ensures that it appears coincident in many multiple detector hit events. The general shift towards higher energies in multiple scatterings is logical as at least the threshold energy has to be deposited in each detector hit. For low energies, the reduced neutron energy diminishes the fraction of secondary scattering events above threshold greatly.

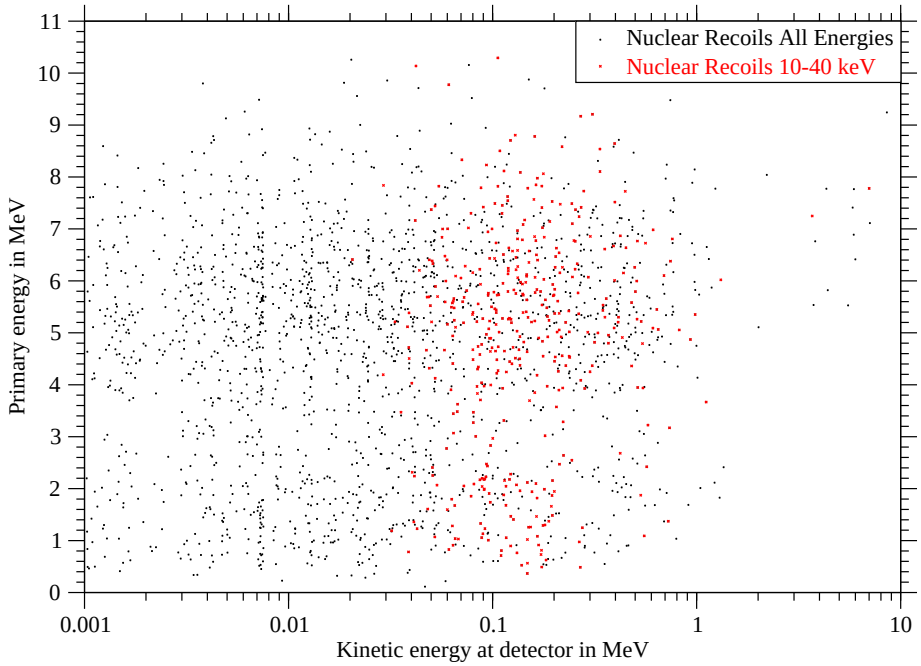

Figure 6.10: Scatterplot of the incident energies at the detectors and the primary starting energy of neutrons responsible for single detector hits in the ROI of 10 – 40 keV and above 5 keV threshold and for all energies. The neutrons originate from (α, n) reactions in the PE shielding. In both cases a *calculated* lightyield of less than 0.25 is required. The analyzed detectors are the ten operational detectors of the CRESST – II run 32.

The distribution of incident energies at the detectors shown in Fig. 6.10 suggests that for a single detector hit within the ROI of 10 – 40 keV, the needed neutron kinetic energy at the location of the detectors is almost completely in the range between 50 keV and 500 keV. If the requirement to deposit energy in the ROI is dropped, the *bath* spectrum of neutrons around the detectors is extended down to energies below a keV while additional detector hits of neutrons above about 500 keV are rare. The distribution of primary energies follows the input spectrum for most energies, at the lowest energies the contribution is considerably suppressed.

Summarizing the results of the presented analysis of the simulation of the (α, n) neutrons produced by impurities within the PE shielding, the following conclusions can be drawn:

- The total background event rate in the nuclear recoil band for the *operational* setup of the CRESST – II Run 32 is about $3.81^{+1.90}_{-1.32} \times 10^{-5}$ cts $\mathrm{kg}^{-1}\mathrm{d}^{-1}$. This is about a factor of 2000 lower than the observed background in Run 32. A contamination of U and Th three orders of magnitude larger than the measured samples does not seem plausible. A neutron source at an average position of the simulation has to provide 0.9 $\mathrm{Bq_n}$ of neutrons to sustain the observed background rate of 0.078 cts $\mathrm{kg}^{-1}\mathrm{d}^{-1}$ of Run 32. For a location featuring average shielding, an Am – Be source of 0.1 μg ^{241}Am and an activity of 12 $\mathrm{kBq_\alpha}$ provides such neutron flux.

- The neutrons responsible for single detector hits within the ROI of 10 – 40 keV have a quite limited range of energies when entering the geometrical volume of the detector modules. Their energies are bound by a lower boundary of 50 keV and an upper boundary of 500 keV.

- Less than one percent of all events depositing energy in the ROI exhibit a LY larger than 0.25 according to the simulation respecting the constraints outlined in App. A . The vast majority of those events are γs produced in the vicinity of the detector modules.

- The *bath* spectrum of a single detector hits is shifted drastically to low energies compared to the primary neutron energy spectrum. The *bath* spectrum of the double detector hits contains additional features at energies about 500 keV due to the position of a strong elastic neutron scattering resonance in ^{16}O, it is generally harder than the single detector hit *bath* spectrum because of the scattering kinematics and the detector thresholds.

6.3 Neutrons Produced in the Lead and the Copper Shielding

In this section the impact of the neutrons from the natural neutron producing processes in the lead and copper shielding of the setup of the CRESST – II experiment is examined. In Sec. 5.6, a measurement of the uranium and thorium impurities in the lead shielding has been presented, resulting in an upper limit of 0.2 ppb of each U and Th with a considerable error of 30 – 40 percent. For the copper, no measurement of the material used in the CRESST experiment has been performed. An value of 20 ppt of U and Th is assumed for the simulations. The proximity to the detector modules offsets the smaller number of primary neutrons compared to the sources investigated before.

In both locations, spontaneous fission of uranium and thorium nuclei is expected. Additionally, neutrons from (α, n) – reactions of α particles produced by the decay of nuclei of thorium, uranium and their daughter nuclei in the copper shielding are simulated. In Fig. 5.11, the contributions to the total spontaneous fission neutron flux from ^{238}U, ^{232}Th, ^{235}U and their spontaneous fissile daughter nuclei in equilibrium contribution has been shown. The most relevant contribution to the total neutron flux is from ^{238}U, the sum of the contributions of all other isotopes is on the per mill level.

It is shown in Sec. 6.3.1 that s.f. neutrons from the lead shielding are the second strongest contributor to the total background rate. Reactions of the (α, n) type are forbidden since the Q – values of the reactions are higher than the available energies of α – particles from the decay chains of Th and U.

The same effect is observed for the neutron flux due to the assumed contamination of 20 ppt of each U and Th in the copper. In this case, only 116.7 neutrons are expected per year, but its contribution to the complete nuclear recoil background seen in the detectors is about one third of the contribution due to spontaneous fissions in the lead. On top of this neutrons are the neutrons produced by the (α, n) reaction in copper. Fig. 5.10 shows the energy spectrum of the additional (α, n) neutrons. In the case of U, the neutron production rates can be safely neglected. Assuming a 20 ppt contamination Th in copper along with the associated daughter nuclei in equilibrium concentration, eight additional neutrons per year are expected. This number is small compared to the 116.7 neutrons from spontaneous fission. Neglecting absorption effects, the resulting increase of the effectiveness to induce background events of s.f. neutrons started in copper compared to s.f. neutrons started in the lead is enhanced by a factor of seven due to the geometrical proximity to the detectors.

The low number of neutrons produced per year and the high chance of nuclear recoils in the detector allow for rather quick simulations for the sources presented in the next two subsections. For both the simulation of s.f. neutrons from the lead shielding and the copper shielding a time of about eight hours for a million of primary neutrons is required on a Intel Core i5 CPU 750 running at 2.67 GHz.

6.3.1 Simulation of the Spontaneous Fission Neutrons from the Lead Shielding

In this subsection, the nuclear recoil background generated by the neutron from the impurities in the lead shielding is presented. As in the case of the ambient neutron background, the constraints outlined in App. A are applied throughout this section.

A homogeneous distribution of the U and Th contaminations in the bulk of the lead shield has been assumed. Production of neutrons via (α, n) reactions on lead are not possible for naturally occurring α particles, leaving spontaneous fission of ^{238}U and other spontaneous fissile nuclei as the primary neutron source. The energy spectrum is the spectrum of spontaneous fission neutrons shown in Fig. 5.11 scaled to the appropriate concentration of 200 ppt U and Th with the contributions of the equilibrium concentrations of daughter isotopes capable of spontaneous fission. The neutron flux generated by spontaneous fissile isotopes of 2580 ^{1}/a for the given contaminations of U and Th in the lead is small compared to the neutron flux generated by other sources at other places of the detector, but its contribution to the nuclear recoil background rate is enhanced by the proximity of the source to the detectors. The momentum direction of primary neutrons is isotropically distributed. The geometrical setup is the same as the one described in Sec. 5.2.

A total number of 25.8 million primary neutrons have been simulated, resulting in 233509 hits in the 33 detector modules with multiplicities shown in Tab. 6.12. In total, 165293 separate events occurred in the simulation. The resulting mean multiplicity observed in these events is 1.41 which has been observed for both investigated sources before. The simulated exposure in the simulation presented here is 100000 kgd.

Multiplicity	Number of events
1	116453
2	34507
3	10216
4	2985
5	786
6	254
7	71
8	11
9	7
10	2
11	0
12	1

Table 6.12: Detector multiplicities observed from the simulation of s.f. neutrons produced in the lead shielding. All 33 modules were considered for the table above. No constraints were applied to the data set. A total number of 165293 events were registered in the simulation of 100000 kga exposure.

Multiplicity	Operational		Installed		All	
	Events	%	Events	%	Events	%
1	9090	91.7	14062	85.5	22850	75.0
2	779	7.9	2111	12.8	6053	19.9
3	48	0.5	248	1.5	1294	4.2
4	1	0.01	18	0.11	234	0.8
5			4	0.02	44	0.1
6					9	0.03

Table 6.13: Detector multiplicities observed from the simulation of s.f. neutrons in the lead shielding. The applied constraints and the definition of the used detector sets are outlined in App. A.

In the energetic region of interest between ten and 40 keV 40048 hits in 30354 events were counted in all 33 detector modules. A summary of the observed multiplicities for the three different detector setups is given in Tab. 6.13. The fraction of multiple detector hit events is similar to the numbers found for the ambient neutrons and the neutrons produced in the PE. For the constraints outlined in App. A the analysis of the *operational* setup results in 8.3 percent multiple detector hit events. For the *installed* detectors, a fraction of 14.4 percent multiple detector hit events are found. If all 33 detectors are active, 25.0 percent of all events show an energy deposition in more than one detector module. While a lower multiple hit fraction the *operational* detector setup between ambient neutron source and neutrons produced in the PE is statistically not significant.

Tab. 6.14 contains the remaining events after separation by *calculated* lightyield and removal of events outside the nuclear recoil bands. The number of removed high lightyield events is tiny compared to the number of nuclear recoils. For the ten detectors of the *operational* set, 148 events out of 9090 single detector hits in the ROI between 10 – 40 keV are not located in the nuclear recoil band. This results in a fraction of high lightyield events of 1.6 percent. For the seventeen detectors of the *installed* set, the same fraction of 1.6 percent is obtained. For the *full* detector set, the fraction is slightly higher, 1.8 percent of all single detector hit events in the ROI are not found in the nuclear recoil band. For double detector hit events, the fraction of removed high lightyield events is similar. The fraction of removed events is 0.8 percent in the case of the *operational* detectors, 1.3 percent for the *installed* detectors and 1.4 percent for the *full* detector setup.

Multiplicity	Number of events		
	Operational	Installed	All
	Nuclear Recoils		
1	8942	13832	22435
2	772	2084	5967
3	48	243	1276
4	1	18	231
5		4	44
6			9
	Oxygen in ROI – Nuc. Rec.		
1	7930	12288	19924
2	687	1880	5416
3	46	223	1178
4	1	18	214
5		4	41
6			9
	Calcium Recoil ROI – Nuc. Rec.		
1	887	1365	2189
2	105	279	745
3	4	32	205
4		4	63
3			13
3			3
	Tungsten Recoil in ROI – Nuc. Rec.		
1	125	179	321
2	18	36	87
3	1	9	28
4			9

Table 6.14: Detector multiplicities observed from the simulation of s.f. neutrons from the lead shielding, the constraints are given in App. A.

The distribution of events within the three recoil bands does not diverge from the results seen in the simulation of the ambient and the polyethylene shielding neutron background. Single detector hit events in the oxygen band ($0.08 < \mathrm{LY_{calc}} < 0.125$) contribute $88.87^{+0.48}_{-0.50}$ % of all events; $9.92^{+0.51}_{-0.49}$ % of the events are found in the calcium recoil band ($0.04 < \mathrm{LY_{calc}} < 0.08$) and about $1.40^{+0.22}_{-0.20}$ % of all events are placed in the tungsten recoil band. For the double detector hit events, the distribution seen in the simulation is $84.93^{+1.83}_{-2.00}$ % for oxygen recoils, $13.19^{+2.04}_{-1.87}$ % for calcium recoils and $1.88^{+1.03}_{-0.74}$ % for tungsten recoils. The numbers are given with a 90 % C.L. on the analysis of the set containing 10 operational detectors. The relative ratio of single detector hit nuclear recoil events in the three different bands is in agreement with the ratios obtained for the nuclear recoil background induced by ambient neutrons and those produced in the PE shielding. For the double detector hit events, the ratios presented here are well within the error bars of the ratios found for the previous two sources.

Hit type	Counts	Rate in cts $kg^{-1}d^{-1}$
	Operational Setup (10 Det.)	
All nuclear recoils	$8942^{+157.4}_{-155.2}$	$\mathbf{8.16^{+0.14}_{-0.14} \times 10^{-4}}$
Oxygen recoils	$7930^{+148.1}_{-145.9}$	$7.24^{+0.14}_{-0.13} \times 10^{-4}$
Calcium recoils	$887^{+50.6}_{-48.4}$	$8.09^{+0.46}_{-0.44} \times 10^{-5}$
Tungsten recoils	$125^{+20.0}_{-17.8}$	$1.14^{+0.18}_{-0.16} \times 10^{-5}$
	Installed Setup (17 Det.)	
All nuclear recoils	$13832^{+195.4}_{-193.2}$	$7.42^{+0.10}_{-0.10} \times 10^{-4}$
Oxygen recoils	$12288^{+183.9}_{-181.8}$	$6.60^{+0.10}_{-0.10} \times 10^{-4}$
Calcium recoils	$1365^{+62.4}_{-60.2}$	$7.33^{+0.33}_{-0.32} \times 10^{-5}$
Tungsten recoils	$179^{+23.6}_{-21.4}$	$9.61^{+1.27}_{-1.15} \times 10^{-6}$
	Full Setup (33 Det.)	
All nuclear recoils	$22435^{+248.4}_{-246.3}$	$6.14^{+0.07}_{-0.07} \times 10^{-4}$
Oxygen recoils	$19924^{+233.8}_{-231.6}$	$5.45^{+0.06}_{-0.06} \times 10^{-4}$
Calcium recoils	$2189^{+15.6}_{-13.4}$	$5.99^{+0.22}_{-0.20} \times 10^{-5}$
Tungsten recoils	$321^{+31.1}_{-28.9}$	$8.79^{+0.85}_{-0.79} \times 10^{-6}$

Table 6.15: The neutron induced nuclear recoil events in the region of 10 – 40 keV induced by s.f. neutrons from the lead shielding. App. A contains a description of the used detector sets and the applied constraints.

A table summarizing the single detector hit background rates in the nuclear recoil band according to the remaining events can be found in Tab. 6.15, the error is given on a C.L. of 90 %. The proximity to the detector modules and the missing moderation of the PE allows for a much higher background rate per primary neutron in comparison to the sources investigated earlier. The total nuclear background rate shown in Tab. 6.15 of $8.16 \pm 0.14 \times 10^{-4}$ cts $kg^{-1}d^{-1}$ scales with the contamination of spontaneous fissile isotopes.

As the used contamination level of 200 ppt is obtained from the upper limit of the chemical analysis, the error of the chemical analysis of 30 % has to be taken into account, too. Including this uncertainty, the adjusted total background rate due to neutrons from spontaneous fission in the lead shielding is $8.16^{+2.62}_{-2.57} \times 10^{-4}$ cts $kg^{-1}d^{-1}$.

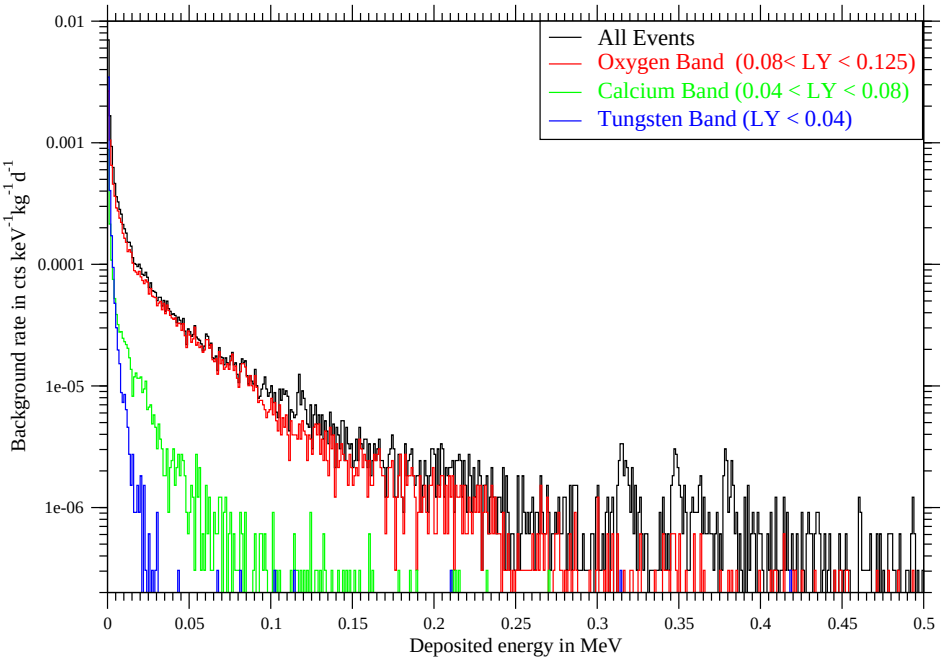

Figure 6.11: Histogram of the spontaneous fission induced nuclear recoil events between 0 – 500 keV. Only single detector hit events are included. The applied constraints are described in App. A. As the black histogram contains single detector hits of all lightyields, the inelastic tungsten scatterings at 100 keV and in the region around 350 keV are clearly visible.

In Fig. 6.11, a histogram of the background rates in the low energy region up to 500 keV extending the data presented in Tab. 6.15 is shown. The background rate drops sharply at about 350 keV in the oxygen band, at about 150 keV in the calcium band and about 35 keV in the tungsten band. For elastic recoils these endpoints points in the recoil spectra translate to an maximum neutron *bath* energy of about 1.6 MeV.

In Fig. 6.12, a scatterplot of the background events is presented in the deposited energy – lightyield plane, for the low energy region up to 50 keV and for energies up to 800 keV which includes all single detector hit events in the nuclear recoil region. Twelve ineleastic scattering events are found in the nuclear recoil region below 50 keV. In six cases, the γ escaped the detector as *calculated* lightyield matches the input nuclear lightyield of Ca and W. The other six inelastic events are inelastic scatterings on keV where the γ deposited a fraction of its energy in the detector crystal.

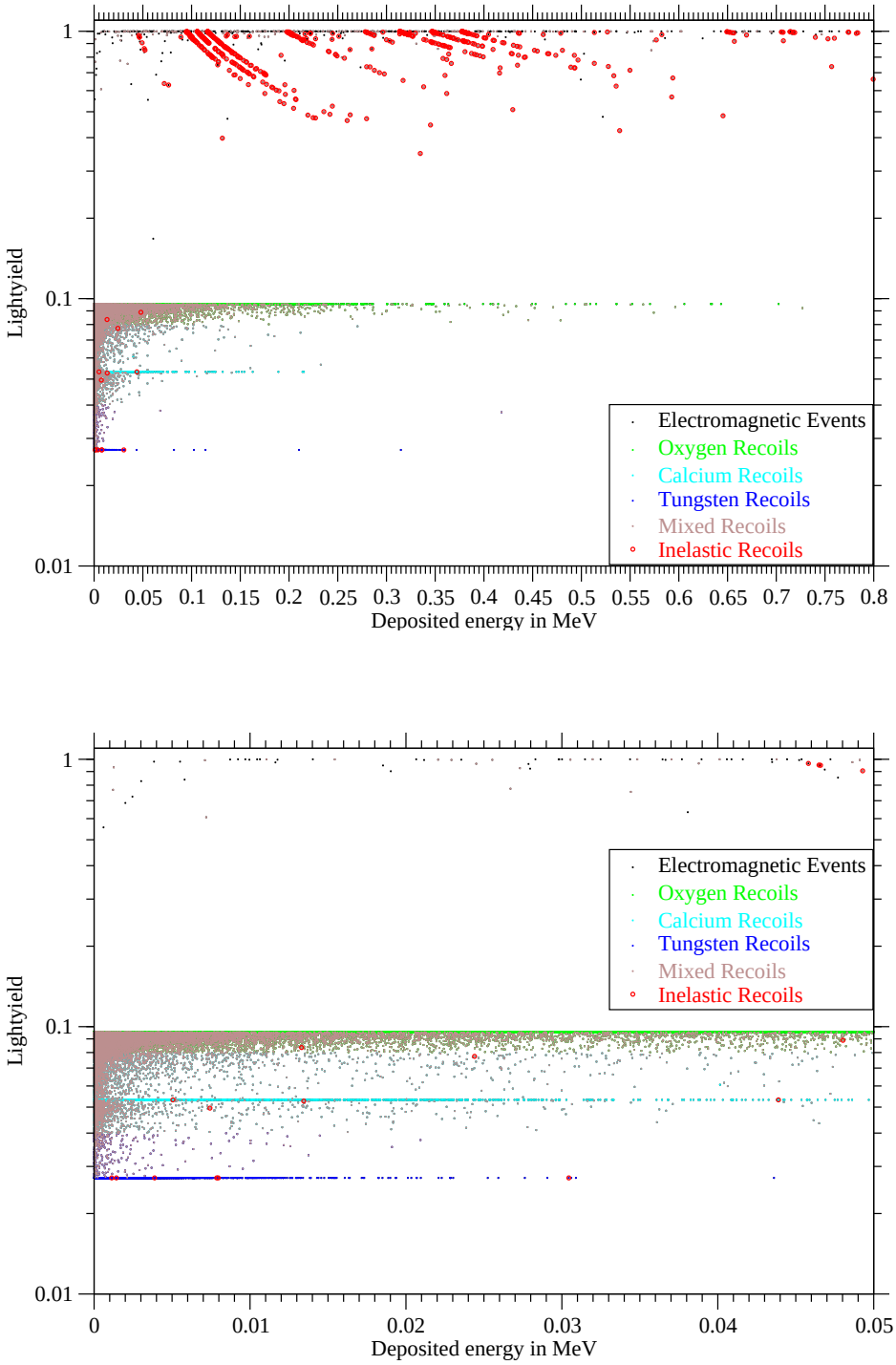

Figure 6.12: Deposited energy – lightyield scatterplot of single detector hit nuclear recoils induced by s.f. neutrons produced in the lead shielding.

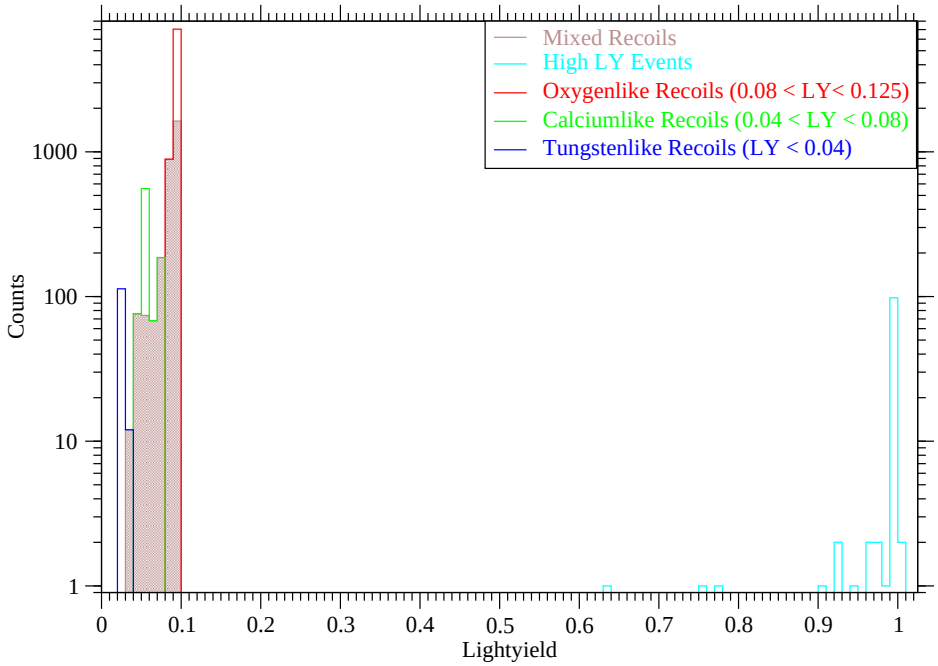

Figure 6.13: Histogram of the *calculated* lightyield of all single detector hits for the ten detector setup with energy deposition between 10 – 40 keV by different hit characteristics.

The distribution of the *calculated* lightyields of the single detector hit events in the ROI between 10 – 40 keV is presented in Fig. 6.13. Out of 7930 *oxygen recoil* events, about 7040 show the *calculated* lightyield expected for an oxygen – only recoil event. 2517 multiple recoil single detector hits provide about a third of all oxygen recoil events. In total, 887 events are found in the calcium recoil band with a lightyield between 0.04 and 0.08. About half of these events, 483, are calcium – only recoils, the rest are events where several different nuclei are hit in the same detector module. Nearly 90 % out of 125 total events in the tungsten lightyield band are tungsten – only recoils. The remaining twelve recoils are combinations of tungsten recoils with calcium or oxygen recoils in the same detector module.

High lightyield events are registered in 112 cases in which stray ambient γs hit a detector module. In 36 cases, energy deposition by nuclear recoils was also detected on top of a dominant energy deposition by electrons or γs. Three of those events show a lightyield between 0.6 and 0.8 which allows potential misidentification with low energy αs if the finite resolution of the light detectors in the real experiment is taken into account.

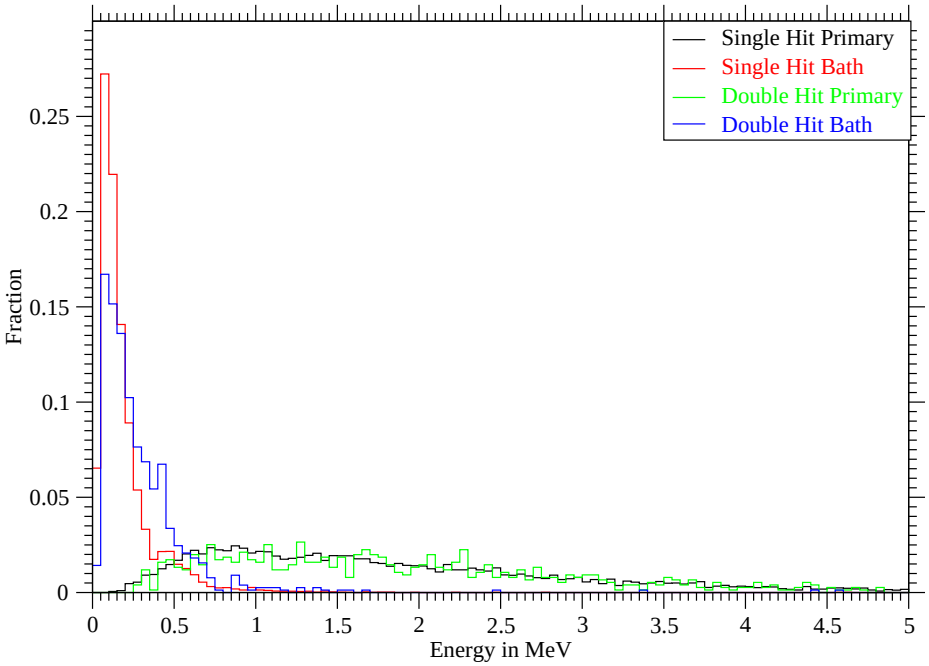

Figure 6.14: Histograms of the primary s.f. neutron energy and the *bath* energy, i.e. the kinetic energy of the first particle which hit the detector module if it is a neutron. Histograms are shown for single and double detector events.

Fig. 6.14 shows the relative fraction of single and double detector hits within the ROI for the primary energies and the *bath* energies. The *bath* spectrum is the kinetic energy spectrum of the neutrons inducing a nuclear recoil in the ROI at the location of the detector modules; this spectrum differs drastically from the primary neutron spectrum. This is a result of the moderation the primary neutrons experience on their way to the detector modules.

About 80 percent of all single detector hit events in the ROI are induced by neutrons with kinetic energies below 250 keV, more than half of the single detector hits are even the result of impinging neutrons with less than 150 keV. The spectrum of detector incident neutron energies is shifted a bit to higher energies for the double detector hits, as the chance to deposit enough energy above threshold in both detector modules decreases with lower neutron energy. The fraction of neutrons with energies above 250 keV is about twice as large as in the case of the single detector hits. The peak in the double bath spectrum at the bin from 400 – 500 keV is the result of a resonance in the elastic oxygen – neutron elastic scattering at 435 keV which increases the total cross – section for neutrons on $CaWO_4$ by a factor of three.

Fig. 6.15 illustrates the energy distribution of *bath* neutrons contributing to the single and double detector nuclear recoil hit event classes within the ROI of 10 – 40 keV by nuclear recoil bands. A closer look at Fig. 6.14 reveals that 60 percent of all single detector hits are induced by neutrons with incoming energies of less than 150 keV, while only 35 percent of the double detector hit events are induced by neutrons of such low energies. As in the case of the (α, n) – neutrons from the PE, the overall softness of the neutron *bath* spectrum around the detectors responsible for detector hits in the ROI stresses the influence the moderation of neutrons in the lead and copper γ – shields excerts for the spectral shape of the nuclear recoil background observed in the energetic region of interest.
Since about 90 % of all nuclear recoil events are located in the oxygen recoil band, the distribution of incoming neutron energies at the place of the detectors for oxygen lightyield recoils is quite similar to the distribution shown by all nuclear recoil events. The increased fraction for *bath* neutrons in the bins below 100 keV seen in the top plots of Fig. 6.15 for recoils in the oxygen band is the result of the larger energy transfer of oxygen recoils with respect to calcium and tungsten recoils.

The plots for single and double detector hits with a hit in the ROI for the calcium recoil band show a diffrent neutron *bath* spectrum shifted to higher energies. This shift can be understood as the maximum energy transfer of neutrons scattering is lower on calcium than on oxygen. While most single detector hits in the calcium recoil band are induced by *bath* neutrons in the energetic region between 100 and 400 keV, a visible contribution of about 15 % is induced by neutrons in the energy range of 450 – 750 keV.

Recoils in the tungsten band are induced by *bath* neutrons following a spectrum shown in the bottom plots of Fig. 6.15. The kinetic energies of about 80 % of the *bath* neutrons are larger than 500 keV as the energy transfer in neutron tungsten scattering is even smaller.

The neutron *bath* energies for single and double detector hits in the oxygen band are significantly different, the number of single detector hits in the ROI are induced by low energy neutrons is much higher as the neutron in a double detector hit event has to deposit at least the threshold energy in both detector modules. For detector hit events in the calcium band, single and double detector hit event spectra the difference is not as pronounced. Since only 18 double detector hit events showing a hit simultaneously in the energetic ROI of 10 – 40 keV and in the tungsten recoil band have been detected in the simulation, no meaningful comparsion can be made for this case.

Two main aspects shape the *bath* neutron spectra of Fig. 6.15 for detector hit events between 10 and 40 keV in the nuclear recoil bands; on the one hand, the kinematics of the elastic scattering dicate the distribution of recoil energies in each band for a fixed incoming neutron energy and on the other hand, the spectrum of all available neutron energies determine the amount of scatterings at a given energy.

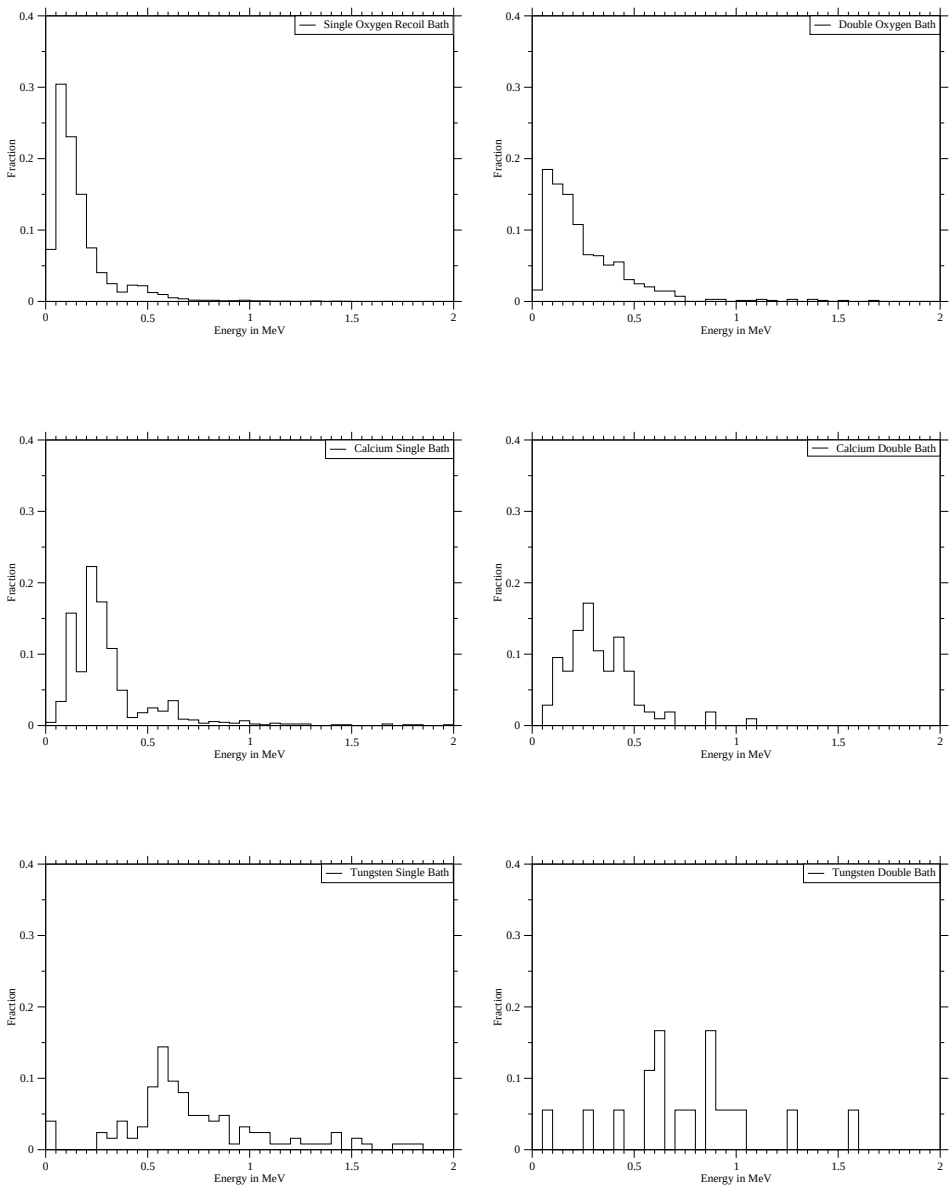

Figure 6.15: Histograms of the bath energy of single and double detector hits of all nuclear recoils and of the oxygen band nuclear recoils in particluar found for the ten detector setup in Tab. 6.15.

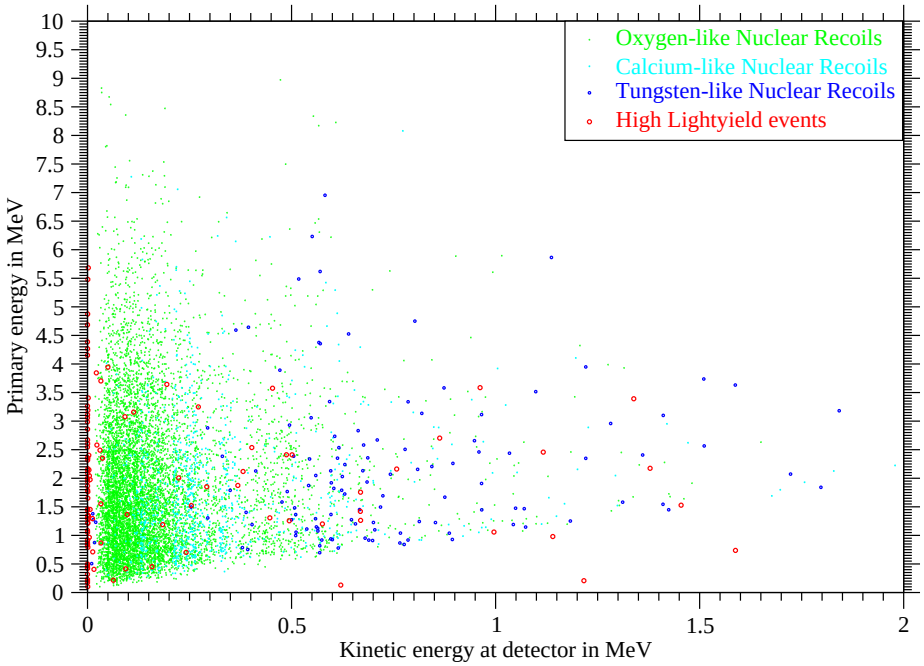

Figure 6.16: Scatterplot for single detector hit events of the primary neutron energy and the *bath* energy, the kinetic energy of the first particle which hit the detector module if it is a neutron. The shown events are required to be single detector hit events only. The primary neutron have been started within the volume of the lead shielding.

The scatterplot seen in Fig. 6.16 visualizes the relation of primary neutron energy and kinetic energy of the first particle which hits the detector in a single detector hit event. In the case that the first hitting particle is a neutron, this energy is also called the neutron *bath* energy. As in the case of the (α, n) neutrons from the PE shielding, the neutrons responsible for single detector hits in the ROI are moderated to low energies by the lead and copper shieldings. The *calculated* lightyield of the events allows further characterization.

The concentration of high lightyield events with ultra low *bath* energy can be explained by two processes. On the one hand, deexcitation γs from the capture of a low energy neutron in a detector module show such a signature. On the other hand, if the *bath* energy is exactly zero, i.e. no neutron hit the detector, a stray γ has hit the detector. The events where the first particle hitting the detector has more energy than the primary neutron, a neutron capture occured outside the detector modules and a deexcitation gamma is registered by a detector module.

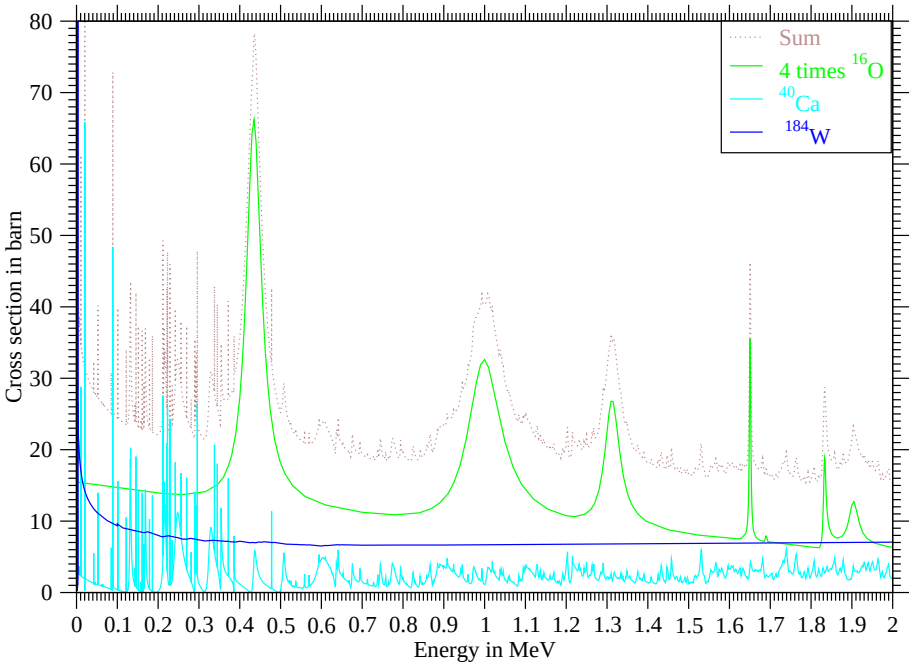

Figure 6.17: Total neutron cross – section for neutrons for selected isotopes of the elements found in $CaWO_4$. The total cross – section of ^{16}O has been quadrupled to account for the stoichiometry of $CaWO_4$.

The main contribution to the *bath* spectrum responsible for oxygen recoils decays exponentially with energy exhibiting a cut – off at very low energies since a minimum of 10 keV has to be deposited in the detector. Multiple nuclear recoils in the same detector module with a *calculated* lightyield in the oxygen recoil band provide the population of *bath* neutrons below the required energy of 45 keV necessary for a recoil above the threshold energy of 10 keV.

A faint clustering at *bath* energies between 400 and 500 keV can be attributed to the enhanced cross – section due to the neutron – ^{16}O resonance at 435 keV which can be seen in Fig. 6.17 showing the total neutron nuclear cross – section for $CaWO_4$. The position of narrow resonances enhancing the cross – sections in Ca can be guessed, too. The resonances for tungsten are positioned below 3 keV incident neutron energy, thus they cannot deposit within the energetic ROI. The majority of tungsten recoils are located at energies above 500 keV, which is a result of the kinematics of neutron scattering on tungsten. The few tungsten recoils below the threshold of 440 keV are the result of multi scattering in a single detector module. The few tungsten recoils below 50 keV are completely stopped in the detector module.

The simulation of neutrons produced by spontaneous fission in the lead shielding of the experiment results in the following conclusions:

- The resulting background rate in the lead shield s.f. neutron simulation of $8.16^{+2.62}_{-2.57} \times 10^{-4}$ cts kg^{-1}d^{-1} is roughly a factor 80 too low to explain the observed background rate of 0.078 cts kg^{-1}d^{-1} in CRESST – II Run 32 alone. It is not plausible that the bulk contamination in the lead shielding deviates by such a margin from the analyzed sample presented in Tab. 5.10 .

- The neutron spectrum responsible for hits in the region of interest is moderated effectively to lower energies by the lead and copper shielding.

- The neutron induced background for single detector hit events is found mostly at energies below 300 keV, only one percent of the background found between 10 and 40 keV is found at energies above 300 keV.

- The double detector hit energy spectrum extends to slightly higher energies, a resonance in the ^{16}O – n system at 435 keV kinetic neutron energy explains the cumulation of double detector hit events with that incoming energy.

- For detector hits in a given ROI, the effective *bath* neutron spectra are visibly different.

- A majority of 88.7 % of all nuclear recoil events within the ROI are found in the oxygen recoil band, a fraction of 9.9 % of all events are in the calcium recoil and 1.4 % are in the tungsten recoil band. This partition does not differ significantly from the partition found in the case of (α, n) neutrons in the PE. This implies that the shape of the resulting *bath* spectrum from both sources is very similar.

- The distribution within the nuclear recoil lightyield bands does not differ significantly between single and double detector hit events. A small increase in observed in the fraction of events with a hit in ROI and in the calcium band, their fraction raises from 9.9 to 13.2 precent for double detector hit events.

- Mixed recoil events have to be considered for the positioning of the constraints on specific nuclear recoils in the deposited energy lightyield scatterplot. Mixed recoils shift the observed mean lightyield in the oxygen band to lower lightyields; in the calcium recoil band, the deviation around the mean value is broadened and in the tungsten recoil band mixed recoils shift the average lightyield to higher values. For the *calculated* lightyields the shift is about one percent in the region between 5 – 20 keV for single detector hit events and increases for lower energies where mixed recoils are more abundant.

6.3.2 Simulation of the Spontaneous Fission and (α, n) Neutrons produced in the Copper Shielding

This subsection contains the results gained from the simulation of the nuclear recoils seen in the detectors due to spontaneous fission neutrons from U and Th contaminations in the copper shielding of the CRESST setup.

The used simulation setup is the same as for the simulation used for the other sources, it can be found in Sec. 5.2. The starting locations of the primary neutrons were placed homogeneously distributed within the volume of the copper shielding. The copper parts of the detector carousel and the cryostat are excluded as starting locations. A total flux of 116.7 neutrons per year is expected to be produced in the 13.59 t of the copper shielding, if 20 ppt of uranium contamination is assumed.

For the simulation of the s.f. contribution to the neutron produced in the copper shielding, 1.66 million primary neutrons are started homogeneously distributed within the volume of the copper shielding amounting to an exposure of the detector modules of 142245 kga.

On top of this primary neutrons, the contribution of 8.06 neutrons produced per year by (α, n) reactions of on copper as detailed in Sec. 5.5.3 with the spectrum shown in Fig. 5.10 is included. In total 114650 primary neutrons produced by (α, n) reactions in copper are simulated. The starting direction of the primary neutrons of both sources is isotropically distributed.

Tab. 6.16 shows the multiplicities of all simulated events which had energy deposited in at least one detector module. All detector modules are considered, no further constraint is applied to the events. In total 94595 detectors where hit in 66549 separate events, resulting in a mean multiplicity of 1.42.

Multiplicity	Number of events
1	46736
2	13932
3	4200
4	1196
5	351
6	95
7	29
8	7
9	3

Table 6.16: Detector multiplicities observed from the simulation of neutrons produced in the copper shielding. All 33 modules were considered for the table above. No constraints were applied to the data set. A total number of 66549 events with detector hits were counted in the simulation of 142245 kga exposure.

Multiplicity	Operational		Installed		All	
	Events	%	Events	%	Events	%
1	4563	89.4	7025	83.6	11020	71.0
2	506	9.9	1192	14.2	3440	22.2
3	33	0.6	169	2.0	859	5.5
4			18	0.2	168	1.1
5					34	0.2
6					3	0.02
7					2	0.01
8					1	0.01

Table 6.17: Detector multiplicities observed from the simulation of neutrons produced in the copper shielding. The definition of the valid detector events classes and the applied constraints are given in App. A.

Tab. 6.17 shows the multiplicities after application of the basic constraints of the three detector sets and the energetic ROI of 10 – 40 keV. The resulting fraction of multiple detector hits is 10.6 % for the *operational* ten detector module setup, 16.4 % if the seventeen *installed* modules are considered and 29.0 % if all 33 detector modules are considered. The fraction of multiple detector hit events is significantly larger than the fraction obtained in the simulation of the s.f. neutrons in lead. In the case of the ten detector setup, the fraction of multiple scatterings is increased by nearly 28 %, for other setups the fraction is about 15 % larger.

The fraction of multiple detector hit events within the three nuclear recoil bands for the neutron sources in the copper shielding can be extracted from Tab. 6.18. For the *operational* detector setup, $85.35^{+0.72}_{-0.74}$ percent of all single detector hit events are found in the oxygen recoil band, $11.93^{+0.77}_{-0.74}$ percent are located in the calcium band and the tungsten band contains $2.72^{+0.43}_{-0.38}$ percent of all single detector hit events. In the case of double detector hit events for the *operational* detector modules, the following fractions are obtained; $81.49^{+2.17}_{-2.39}$ percent are found within the oxygen recoil band, $14.58^{+2.51}_{-2.28}$ reside in the calcium recoil band and $3.93^{+1.63}_{-1.26}$ percent of all events populate the tungsten recoil band. The given errors are given by the minimum and maximum fractions which can be obtained by varying the numbers of each nuclear recoil class independently at a 90 % C.L. .

The increased occurrence of calcium and tungsten recoils for both single and double detector hit events is an indication for an neutron *bath* spectrum extending to higher energies than in the case of the sources examined before.

Multiplicity	Number of detector hits		
	Operational	Installed	All
	Nuclear Recoils		
1	4519	6954	10895
2	499	1179	3406
3	33	168	851
4		18	168
5			33
6			3
7			2
8			1
	Oxygen in ROI – Nuc. Rec.		
1	3857	5927	9276
2	436	1040	2971
3	29	152	740
4		18	157
5			30
6			3
7			2
8			1
	Calcium Recoil ROI – Nuc. Rec.		
1	539	812	1293
2	78	181	520
3	9	35	172
4		4	38
5			14
6			1
7			1
8			1
	Tungsten Recoil in ROI – Nuc. Rec.		
1	123	215	326
2	21	40	111
3	1	7	50
4			5
5			2

Table 6.18: Simulated detector multiplicities observed in the various nuclear recoil bands. The primary neutrons are s.f. and (α, n) neutrons produced in the copper shielding. The definitions of the valid detector events classes and the applied constraints are given in App. A.

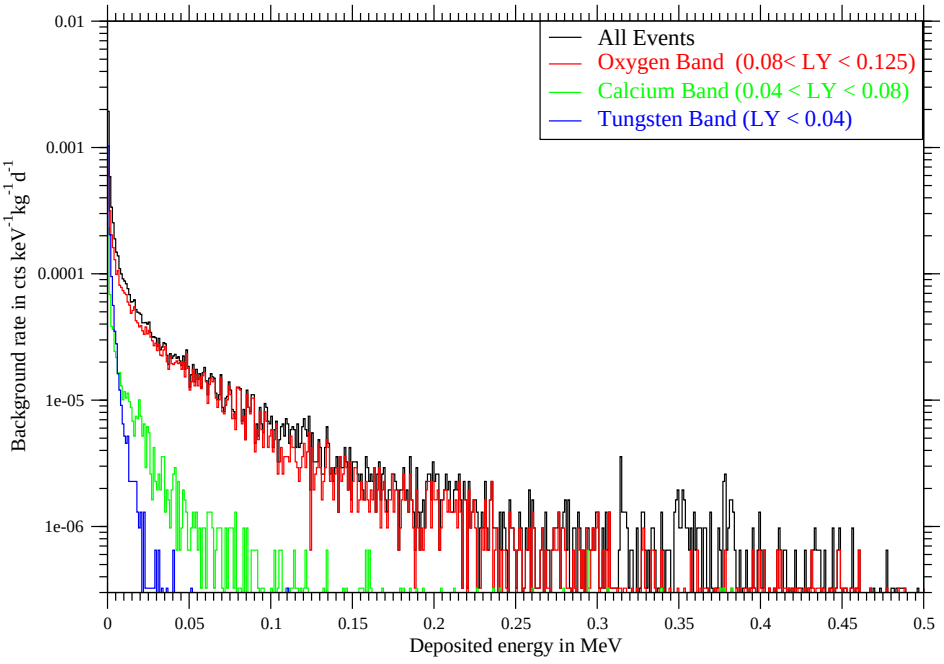

Figure 6.18: Histogram of the nuclear recoil events below 500 keV due to neutrons from the spontaneous fission neutrons and (α, n) from the copper shielding.

A comparison between Tab. 6.17 and Tab. 6.18 reveals that about one percent of all events are removed since they show a lightyield above the oxygen recoil band. The fraction of removed high lightyield events is in agreement with the result of the simulation of the s.f. neutrons in the lead shielding.

Fig. 6.18 shows the nuclear recoil background rates per $\mathrm{kg}^{-1}\mathrm{d}^{-1}\mathrm{keV}^{-1}$ for single detector hit events of different *calculated* lightyield shown in Tab. 6.19. The background declines from 0.002 $\mathrm{kg}^{-1}\mathrm{d}^{-1}\mathrm{keV}^{-1}$ at deposited energies below 1 *keV* to 1.0×10^{-6} at deposited energies of 250 keV. Three regions with distinct slopes can be identified, the steepest slope is observed below 10 keV where tungsten and calcium recoils become important. For higher energies, oxygen recoils are the dominant background. Around 300 – 400 keV inelastic tungsten scattering contribute a visible contribution above the nuclear recoil lightyield region. The bulk of the oxygen recoils is limited by an energy of approximately 300 keV, the energy spectrum of the calcium recoils ends about 120 keV and the tungsten recoils are found mostly below an energy of 30 keV. This indicates that the major fraction of all single detector hit events are induced by a neutron *bath* spectrum up to about 1.3 MeV.

The nuclear background rate shown in Tab. 6.19 of $2.90 \pm 0.14 \times 10^{-4}$ cts kg^{-1}d^{-1} is proportional to the contamination of spontaneous fissile isotopes. If the copper contains more than 20 ppt of ^{238}U, the induced background event rate rises.

To obtain a rate of 0.08 cts kg^{-1}d^{-1} as seen in Run 32 of the CRESST – II experiment, the ^{238}U contamination in the copper shielding is required to exceed 5.5 ppb. This level of contamination is a order of magnitude too high to be plausible. Even if the contamination is of such a magnitude, a background rate of multiple detector hit events of 8.42×10^{-3} cts kg^{-1}d^{-1} is expected according to Tab. 6.18. For example, if 57 single detector hit events in the ROI of 10 – 40 keV are seen , about five events with higher multiplicity are expected according to the simulation. In the experiment, not a single double detector hit event has been detected for the 57 detector hits seen [Pr11]. The abscence of the multiple detector hit events is a puzzeling feature of the data obtained in Run 32.

Fig. 6.20 shows the distribution of the single detector hit events in the deposited energy – *calculated* lightyield plane. Six events with lightyields between 0.1 and 0.5 are observed below 200 keV. Four of those events are associated with an inelastic neutron scattering on tungsten, one is a multi nuclei single detctor module hit with is accompanied by energy deposition of a stray γ and the last event is a detector hit by an α produced in the perimeter of the detector modules.

The highest deposited energies seen in the nuclear recoil lightyield bands are oxygen recoils of about 850 keV energy deposition. Calcium and Tungsten recoil spectra show lower endpoints of 380 keV and 110 keV, respectively.

The comparison of the *bath* spectra of the neutrons from the lead and from the copper shielding presented in Fig. 6.19 indicates that the neutrons started in the copper shielding are less moderated as the ones started in the lead shielding since the *bath* spectrum shows larger contributions at higher energies.

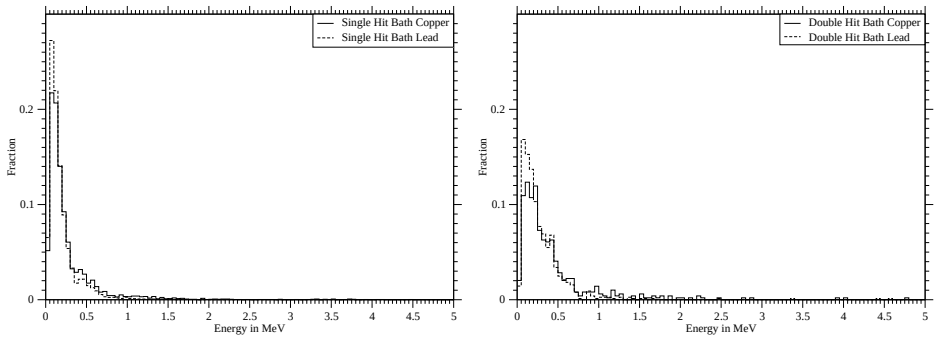

Figure 6.19: Histogram of the fractions of the neutron bath energies for single and double detector hit events for the neutrons produced in the lead shielding and the copper shielding.

Hit type	Counts	Rate in cts $kg^{-1}d^{-1}$
	Operational Setup (10 Det.)	
All nuclear recoils	4519^{+112}_{-110}	$\mathbf{2.90^{+0.07}_{-0.07} \times 10^{-4}}$
Oxygen recoils	3857^{+104}_{-102}	$2.47^{+0.07}_{-0.07} \times 10^{-4}$
Calcium recoils	$539^{+39.8}_{-37.6}$	$3.46^{+0.26}_{-0.24} \times 10^{-5}$
Tungsten recoils	$123^{+19.9}_{-17.7}$	$7.89^{+1.27}_{-1.13} \times 10^{-6}$
	Installed Setup (17 Det.)	
All nuclear recoils	6954^{+139}_{-137}	$2.62^{+0.05}_{-0.05} \times 10^{-4}$
Oxygen recoils	5927^{+128}_{-126}	$2.24^{+0.05}_{-0.05} \times 10^{-4}$
Calcium recoils	$812^{+48.5}_{-46.3}$	$3.06^{+0.18}_{-0.17} \times 10^{-5}$
Tungsten recoils	$215^{+25.7}_{-23.5}$	$8.11^{+0.97}_{-0.88} \times 10^{-6}$
	Full Setup (33 Det.)	
All nuclear recoils	10695^{+172}_{-170}	$2.05^{+0.03}_{-0.03} \times 10^{-4}$
Oxygen recoils	9276^{+160}_{-158}	$1.79^{+0.03}_{-0.03} \times 10^{-4}$
Calcium recoils	$1293^{+60.7}_{-58.6}$	$2.49^{+0.12}_{-0.11} \times 10^{-5}$
Tungsten recoils	$326^{+31.3}_{-29.1}$	$6.27^{+0.60}_{-0.56} \times 10^{-6}$

Table 6.19: The neutron induced nuclear recoil events in the region of 10 – 40 keV induced by s.f. and (α, n) neutrons from the copper shielding. The total number of started neutrons is 1774650. Per year, 124.8 primary neutrons are expected for a contamination of 20 ppt of uranium in the copper.
The definition of the applied constraints and a description of the setups is given in App. A. The total detector mass was 300 g of $CaWO_4$ for each detector module. The error given is at 90 % C.L. and calculated according to Poissonian statistics.

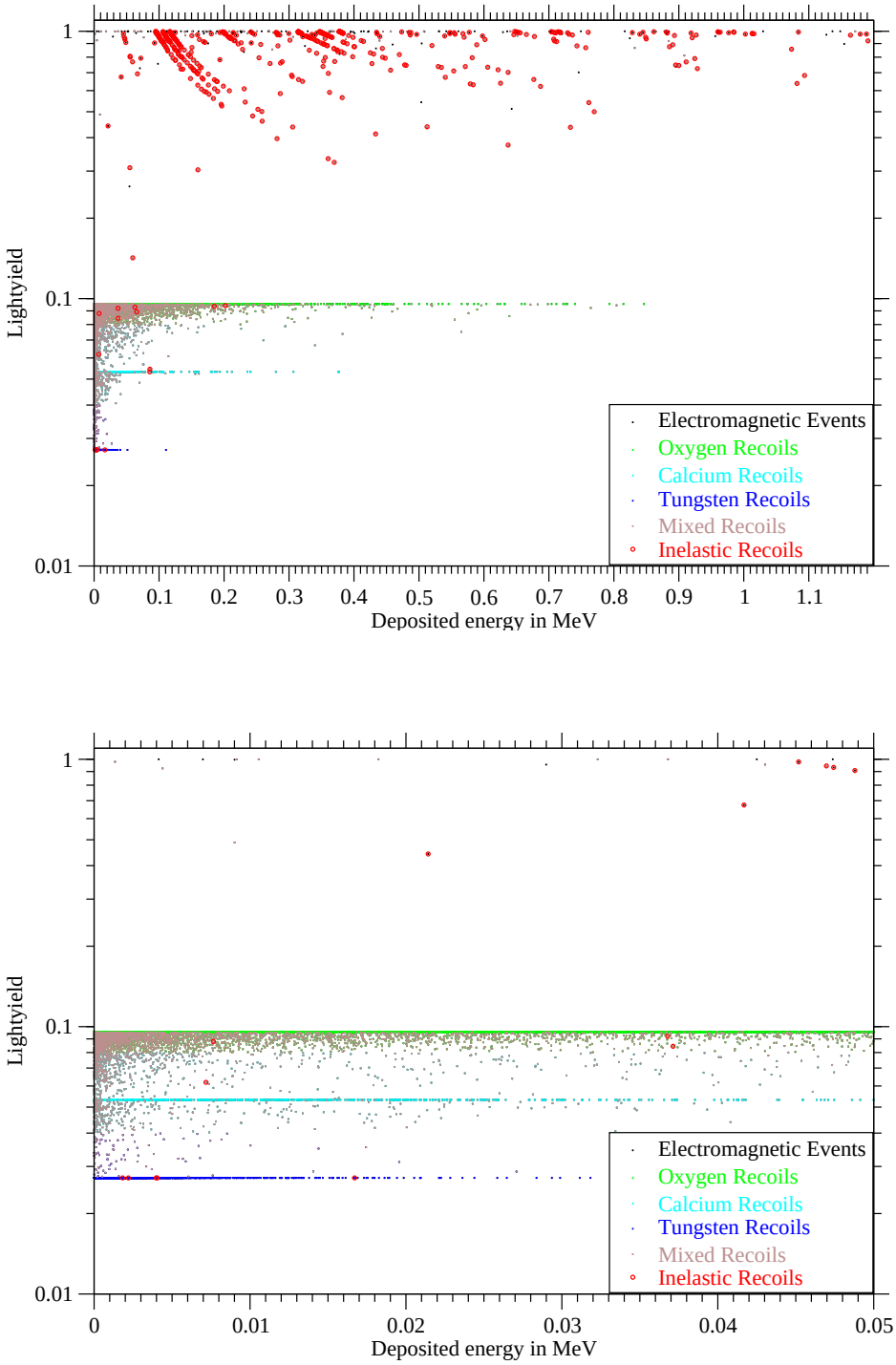

Figure 6.20: Deposited energy – lightyield scatterplot of single detector hit nuclear recoils induced by neutrons produced in the copper shielding.

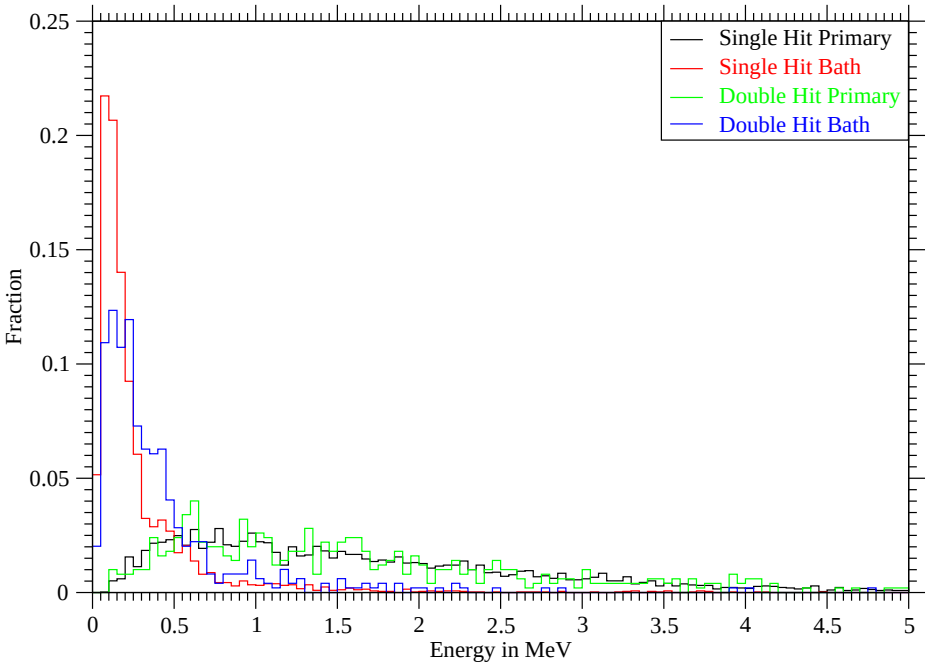

Figure 6.21: Histograms of the primary neutron energy and the *bath* energy, i.e. the kinetic energy of the first particle which hit the detector module if it is a neutron. Histograms are shown for single and double detector events. The primary neutrons are produced in the copper shielding by s.f. of ^{238}U and ^{232}Th and (α, n) reactions on Cu.

The primary neutron spectrum and the *bath* neutron spectrum in the case of neutrons produced mainly by (α, n) reactions in the copper are similar to such spectra shown for the neutrons produced within the PE or the lead shielding shown in figs. 6.14 and 6.8 . The majority of all neutrons responsible for detector hits between 10 and 40 keV are of energies below 500 keV. For the neutrons produced in the copper shielding, the ten percent most energetic neutrons causing single detector hits have energies above one MeV. In the case of the s.f. neutrons from the lead shielding, the most energetic ten percent of neutrons are found above 500 keV. In the case of double detector hits, the most energetic ten percent of *bath* neutrons have energies above 1.4 MeV instead of 700 keV found for the s.f. neutrons from the lead shielding. The distortion of the energy spectrum from the (α, n) neutrons is negligible, the main reason for the harder spectrum is the reduced moderation as the neutrons are produced much closer to the detectors.

The simulation of neutrons produced in the copper shielding by spontaneous fission and (α, n) reactions on the Cu results in thefollowing conclusions:

- As the exact contamination level of the copper is unknown, the background from neutrons produced in the copper shielding might be seriously underestimated. The obtained background rate of$2.90 \pm 0.07 \times 10^{-4}$ cts $\mathrm{kg}^{-1}\mathrm{d}^{-1}$ is a factor of 220 lower than the observed background. The required contamination level of 5 ppb of ^{238}U for a total background rate of 0.078 cts $\mathrm{kg}^{-1}\mathrm{d}^{-1}$ seems too high if compared to the contamination reported normally in copper.

- The neutron induced background for single detector hit events is found mostly at energies below 500 keV, only one percent of the background detector hits between 10 and 40 keV are found at energies above 500 keV.

- The high energy tail of the neutron *bath* is more prominent for neutrons produced in the copper shielding, as the most energetic ten percent are found above a threshold nearly twice as high as in the case of s.f. neutrons from the lead shielding. This observation is supported by the increased number of events located in the calcium and tungsten recoil bands between 10 and 40 keV, too. Since the primary neutron spectra for the neutrons from the lead shielding and the copper shielding are dominated by the s.f. neutron spectrum, this effect can be explained by the reduced moderation as the amount of material between neutron source and detectors is smaller for neutrons started in the copper shielding.

6.4 Simulation of Cosmogenic Neutrons

In this section, the resulting background from the simulation of cosmogenic neutrons is discussed. As pointed out in Sec. 5.7, the neutrons produced in the experimental setup and support structure are not considered, it is expected that at least a part of the charged particles in the wake of muon induced spallation are noticed by the muon veto. This is not the case for neutrons produced in the rock surrounding the experimental cavity, for which the spectrum given by Demetyev [De99] is assumed. The direction of the neutrons is determined according to the flux rates given for the roof, walls and floor of the experimental hall found in the thesis of Wulandari [Wu04]. The neutrons are started from the same starting area as the ambient neutrons are started, a box around the experimental setup which has a length and a width of 2.82 m each and a height of 5.19 m. 14765 neutrons are expected to pass into the volume encompassed by the specified starting area. No active muon veto has been included in the simulation of the cosmogenic neutron flux.

As the energy of the incoming neutrons in this simulation starts at six MeV and extends up to the GeV region, the physics list used in the simulation was expanded to model the neutron – nuclear interactions at the extended energy range and include the particles which can be produced at high energies. A much more detailed ab – initio simulation and analysis of the cosmogenic neutrons is to be found in the forthcoming work of M. Bauer [Ba11].

The 22427292 primary neutrons produced 245776 detector hits in 138469 events for an simulated exposure of 15189.6 kga. The mean multiplicity of 1.78 deviates significantly from the value obtained from the other sources of about 1.41. This is the result of a large number of high multiplicity events which are an indication for the formation of a secondary shower by the primary neutron.

The simulation of the diffuse cosmogenic neutron background results in a total detector hit rate induced by cosmogenic neutrons of $4.43^{+0.02}_{-0.02} \times 10^{-2}$ kgd with a C.L. of 90 % *before* application of any of the constraints presented in App. A . The required computing time for one million primary neutrons is about 60 h on a Intel Core i5 CPU 750 running at 2.67 GHz. The multiplicity structure of these events is presented in Tab. 6.20.

Multiplicity	Number of events
1	82647
2	32003
3	12976
4	5319
5	2281
6	1143
7	615
8	358
9	238
10	159
11	112
12	101
13	60
14	50
15	43
16	35
17	27
18	27
19	25
20	16
21	18
22	10
23	16
24	8
25	5
26	5
27	5
28	4
29	6
30	4
31	5
32	2
33	1

Table 6.20: Detector hit multiplicities induced by cosmogenic induced neutrons. The multiplicity, the number of events and number of detector hits for that multiplicity are presented. The total number of detector hits is 245776 in 138469 for an exposure of 15189.6 kga. Any hit with non – zero deposited energy in one of the 33 detectors is shown in the table above.

For the determination of a background rate in the simulation which is comparable to the experimental situation, the constraints as presented in the analysis of the previous neutron sources are applied to the set of detector hits. The two foremost constraints are the thresholds for a detector hit in the energetic region of interest and the threshold for a detector hit in another detector module used for the vetoing of multiple scattering in the experiment. Demanding at least one detector hit with an deposited energy between 10 – 40 keV and other hits to have to deposit at least 5 keV reduces the structure of the detector hits to the numbers shown in Tab. 6.21.

As in the previous cases, the number of multiple hits event rate raises with the number of active modules. For ten detectors, 18.3 % of all events showing a hit in the region of interest are multiple hits events; for the 17 detector setup, the fraction of multiple hit events is 26.7 % and for the full setup of 33 detectors the multiple hit event fraction is 40.2 %.

For cosmogenic neutrons the total fraction of multiple detector hit events is nearly twice the observed fraction for the other simulated neutron sources. Furthermore, events with much higher multiplicities are observed. The total contribution of very high multiplicity events is much larger than for the previously simulated neutron sources, this is an indication that the highest energy primary neutrons induce showers in the surrounding material around the detector modules.

In the next step, the additional constraint demanding a maximum permitted lightyield of 0.25 is applied to the data to remove non nuclear recoil detector hits in the energetic ROI. The constraint is not applied to detector hits which accompany another detector hit within the ROI.

Furthermore, the data sets are split into the three classes according to the expected lightyield of a given nuclear recoil, this clases are labeled oxygen ($0.08 < LY < 0.125$), calcium ($0.04 < LY < 0.08$) and tungsten ($LY < 0.04$). The distribution of the remaing events according to their multiplicity and location of the detector hits in the ROI is presented in tabs. 6.22 – 6.25 .

For the setup with ten *operational* detectors, 126 out of 8549 single detector hit events are rejected as their *calculated* lightyield is above 0.25. The resulting fraction of single detector hit events removed by the lighyield constraint for the cosmogenic neutrons for all three sets of detectors is 1.8 percent. The fraction of removed events is only slightly larger than the one obtained from the simulation of the other neutron sources. Seventy – two of the rejected single detector hit events are hits but electrons or γs only. In all cases, it can be concluded that the γ was produced outside the detector crystal as the nuclear recoil was due to elastic scattering. One case of inelastic scattering was detected, in this case no γ was detected by the detector. This event may have been an (n, xn) reaction or a (n, n_i') reaction where the deexcitation γ escaped the detector module.

Multiplicity	Number of events					
	Operational	%	Installed	%	All	%
1	8549	81.7	12579	73.3	18300	59.8
2	1454	13.9	3198	18.6	7407	24.2
3	300	2.9	843	4.9	2623	8.6
4	88	0.8	252	1.5	1015	3.3
5	39	0.4	117	0.7	462	1.5
6	18	0.2	66	0.4	260	0.8
7	8	0.08	38	0.2	145	0.5
8	7	0.07	21	0.1	101	0.3
9	4	0.04	16	0.09	52	0.2
10	2	0.02	11	0.06	49	0.2
11			9	0.05	36	0.1
12			5	0.02	19	0.06
13			7	0.04	29	0.09
14			2	0.01	14	0.05
15			3	0.02	18	0.06
16			1	0.01	12	0.04
17					10	0.03
18					8	0.03
19					7	0.02
20					7	0.02
21					4	0.01
22					1	0.003
23					4	0.01
24					7	0.02
25					0	0
26					4	0.01
27					1	0.003
28					2	0.007
29					1	0.003
30					1	0.003
31					0	0
32					0	0
33					1	0.003

Table 6.21: Detector multiplicities observed from the simulation of cosmogenic neutrons. The three presented setups are defined in App. A. The following constraints were used to identify the valid detector hit events:
Both light detector channel and phonon detector channel are operational, at least one detector hit with an deposited energy of 10 – 40 keV and each hit has to deposit at least 5 keV.

Nuclear Recoils

Multiplicity	Number of detector hits		
	Operational	Installed	All
1	8423	12399	18021
2	1437	3160	7321
3	295	837	2606
4	87	250	1007
5	37	116	455
6	18	64	259
7	8	36	142
8	7	21	100
9	4	16	52
10	2	11	49
11		9	35
12		5	19
13		7	26
14		2	15
15		3	16
16		1	12
17			10
18			8
19			7
20			7
21			4
22			1
23			4
24			7
25			0
26			4
27			1
28			2
29			1
30			1
31			0
32			0
33			1

Table 6.22: Detector multiplicities observed from the simulation of cosmogenic neutrons for all nuclear recoils. The definition of the valid detector events classes are outlined in App. A.

Oxygen Recoils in ROI – Nuclear Recoil

Multiplicity	Number of detector hits		
	Operational	Installed	All
1	7354	10810	15762
2	1279	2816	6500
3	264	746	2332
4	80	223	908
5	33	104	414
6	15	60	241
7	7	34	130
8	6	19	91
9	3	15	49
10	2	10	47
11		8	33
12		5	15
13		6	26
14		2	15
15		3	15
16		1	12
17			10
18			8
19			7
20			7
21			3
22			1
23			4
24			7
25			0
26			4
27			1
28			2
29			1
30			1
31			0
32			0
33			1

Table 6.23: Detector multiplicities observed from the simulation of cosmogenic neutrons for hits in the oxygen nuclear recoil band. The definition of the valid detector events classes are outlined in App. A.

Calcium Recoils ROI – Nuclear Recoil

Multiplicity	Number of detector hits		
	Operational	Installed	All
1	879	1321	1889
2	180	395	976
3	48	142	427
4	9	52	198
5	9	18	100
6	5	10	62
7	2	7	34
8	3	7	26
9		5	11
10		5	11
11		3	9
12		2	8
13		1	11
14			4
15			6
16			5
17			5
18			2
19			3
20			3
21			1
22			0
23			2
24			2
25			0
26			2

Table 6.24: Detector multiplicities observed from the simulation of cosmogenic neutrons for hits in the calcium nuclear recoil band.

The remaining number of events after application of the lightyield constraint are shown in Tab. 6.22 . Of all single detector hit events, $87.32^{+0.50}_{-0.52}$ % are in the oxygen recoil band, $10.44^{+0.53}_{-0.52}$ % in the calcium recoil band and $2.24^{+0.28}_{-0.26}$ % are found in the tungsten recoil band, according to tabs. 6.23 – 6.25 . For double detector hit events, $85.33^{+1.24}_{-1.33}$ percent are located in the oxygen recoil band, $12.06^{+1.37}_{-1.28}$ percent are found in the calcium recoil band and $2.61^{+0.77}_{-0.64}$ % are observed in the tungsten recoil band.

The distribution of the lightyields is in agreement with the ones obtained from the other simulations.

Tungsten Recoils in ROI – Nuclear Recoil

Multiplicity	Number of detector hits		
	Operational	Installed	All
1	190	268	369
2	39	99	202
3	8	37	95
4	4	9	49
5	2	6	21
6	0	3	11
7	0	5	8
8	0	1	6
9	1	0	4
10		0	2
11		1	5
12		0	6
13		1	1
14			2
15			1
16			1
17			0
18			1
19			1
20			1
21			0
22			0
23			0
24			0
25			0
26			1

Table 6.25: Detector multiplicities observed from the simulation of cosmogenic neutrons in the tungsten nuclear recoil band.

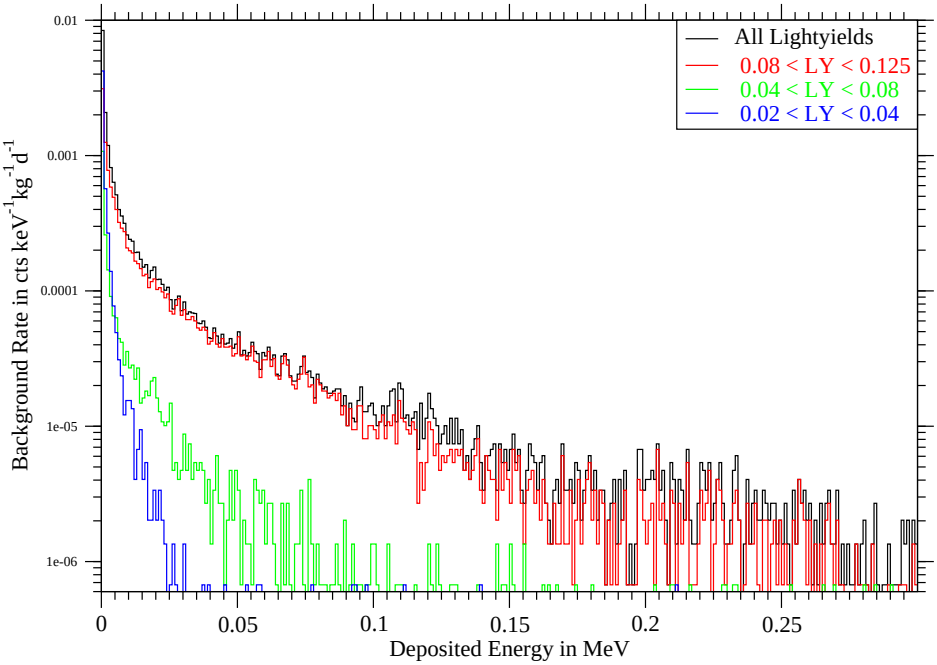

Figure 6.22: Histogram of nuclear recoil event rates for energies up to 300 keV due to neutrons from muon – induced neutrons. The black histogram contains all events, the red histogram denotes the oxygen – like detector hits with a lightyield between 0.08 and 0.125, the green histogram shows the calcium – like detector hits with a lightyield in the band 0.04 – 0.08 and the blue histogram gives the tungsten – like recoils with a lightyield of 0.02 – 0.04.

Fig. 6.22 shows the histogram of the nuclear recoil background rates for energies up to 300 keV for the *operational* detector setup. The recoils on oxygen and combinations of O – W and O – Ca recoils in the same detector constitute the majority of events. For energies above 30 keV elastic tungsten recoils are practically absent. Calcium recoils rarely surpass energies of 95 keV. Tab. 6.26 presents the rates observed in the three lightyield regions within 90 % confidence levels.

The distribution of single detector hit events in the deposited energy and lightyield plane is shown in Fig. 6.23 for the setup of 10 detectors. The maximum deposited energy for events in the oxygen recoil band is about 3 MeV, maximum deposited energies in the calcium and tungsten band are about one MeV. For energies below 100 keV, the fraction of multi recoil single detector events becomes more significant, bluring the distribution of events in the three recoil bands into a single blob. For events which deposited between 10 and 40 keV, the histogram of the *calculated* lightyields is shown in Fig. 6.25.

Hit type	Counts	Rate in cts $kg^{-1}d^{-1}$
	Operational Setup (10 Det.)	
All nuclear recoils	8423^{+152}_{-150}	$\mathbf{5.08^{+0.09}_{-0.09} \times 10^{-3}}$
Oxygen recoils	7354^{+142}_{-140}	$4.42^{+0.09}_{-0.08} \times 10^{-3}$
Calcium recoils	879^{+50}_{-48}	$5.28^{+0.30}_{-0.29} \times 10^{-4}$
Tungsten recoils	$190^{+24.2}_{-22.0}$	$1.14^{+0.15}_{-0.13} \times 10^{-4}$
	Installed Setup (17 Det.)	
All nuclear recoils	12399^{+184}_{-182}	$4.33^{+0.06}_{-0.06} \times 10^{-3}$
Oxygen recoils	10810^{+172}_{-170}	$3.78^{+0.06}_{-0.06} \times 10^{-3}$
Calcium recoils	1321^{+61}_{-59}	$4.62^{+0.21}_{-0.21} \times 10^{-4}$
Tungsten recoils	$268^{+28.4}_{-26.2}$	$9.38^{+1.00}_{-0.92} \times 10^{-5}$
	Full Setup (33 Det.)	
All nuclear recoils	18021^{+222}_{-220}	$3.24^{+0.04}_{-0.04} \times 10^{-3}$
Oxygen recoils	15762^{+208}_{-206}	$2.84^{+0.04}_{-0.04} \times 10^{-3}$
Calcium recoils	1889^{+73}_{-71}	$3.41^{+0.13}_{-0.13} \times 10^{-4}$
Tungsten recoils	$369^{+33.2}_{-31.0}$	$6.65^{+0.60}_{-0.56} \times 10^{-5}$

Table 6.26: The neutron induced nuclear recoil events in the region from 10 – 40 keV muon induced neutrons after application of constraints. The events are classified into the three different nuclear recoil categories which are given in App. A. The total number of started primary neutrons is 22427292. A total number of 14765 primary neutrons are required for the simulation of 10 kga of exposure. The total detector mass was 10 kg of $CaWO_4$. The error is calculated for Poissonian statistics with a C.L. of 90 %.

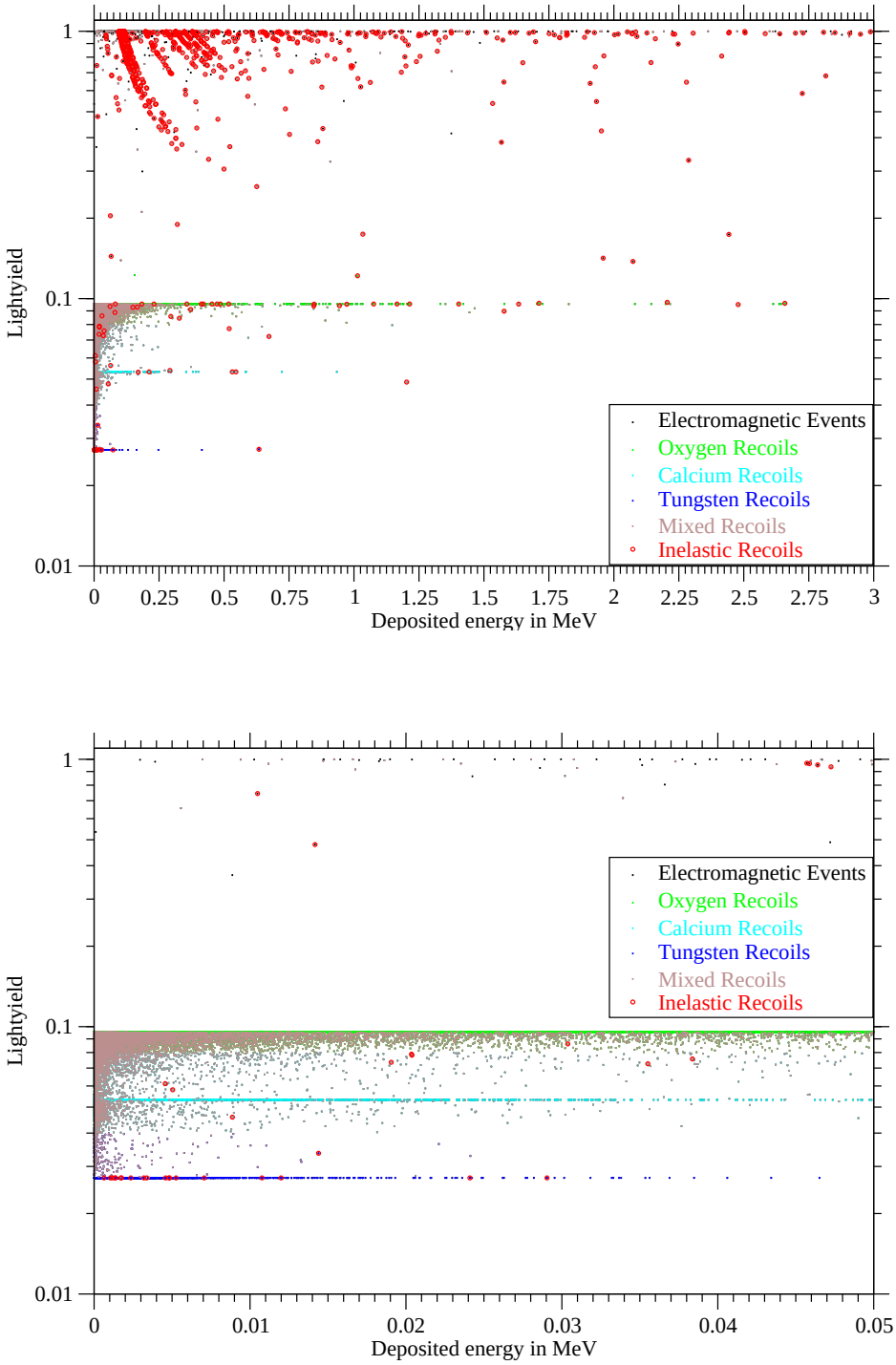

Figure 6.23: Scatterplot of the deposited energy and the lightyield for cosmogenic neutrons for deposited energies up to 3 MeV.

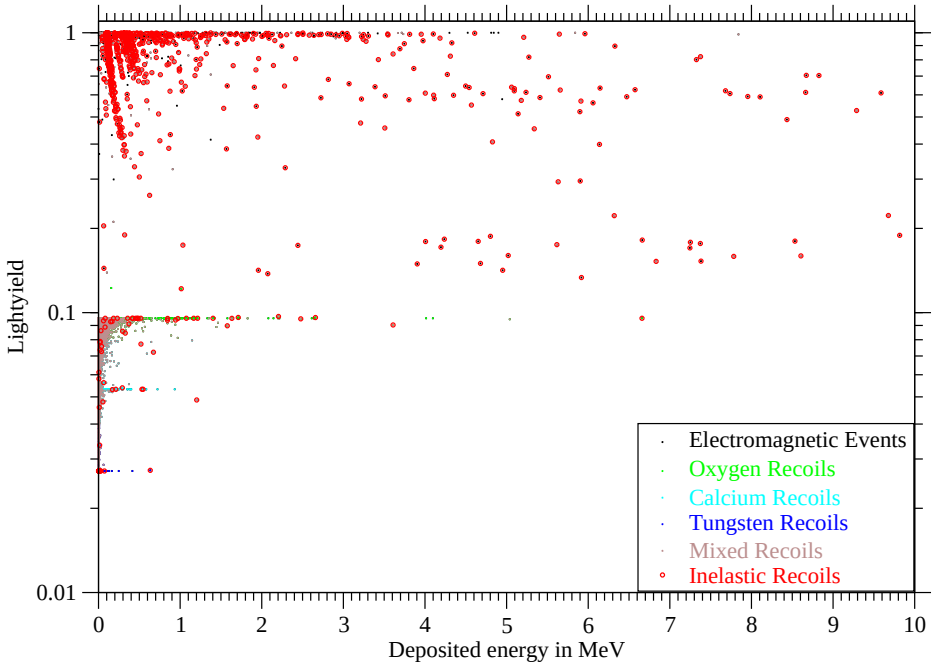

Figure 6.24: Scatterplot of the deposited energy and the lightyield for cosmogenic neutrons for deposited energies up to 10 MeV.

A sizeable number of inelastic scatterings with low lightyields can be located in the scatterplots. This events are neutron multiplication reactions of the (n, xn) – type which is much more prominent in heavy nuclei like tungsten than in light nuclei like oxygen or calcium. The required neutron energies for such reactions are quite high, in the case of tungsten the $(n, 2n)$ reaction threshold is in the order of seven to nine MeV depending on the tungsten isotope in question. Furthermore, the cross – section is about one barn for energies slightly above the threshold. The required reaction threshold in the abundant oxygen and calcium isotopes is about twice as high and the cross – sections are generally lower by two orders of magnitude. This look at the cross – sections for inelastic scattering explain the increased occurrence of low lightyield inelastic neutron scatterings on tungsten for the high energy cosmogenic neutron spectrum in comparison to the other neutron spectra contemplated.

For energies above 4 MeV two additional bands emerge visibly in the scatterplot shown in Fig. 6.24. These bands are the manifestation of (n, p) and (n, α) as they involve an inelastic neutron – nucleon scattering according to the simulation. Such reaction channels demand a flux of high energy neutrons at the location of the detector modules which have not been observed for the other neutron sources examined here.

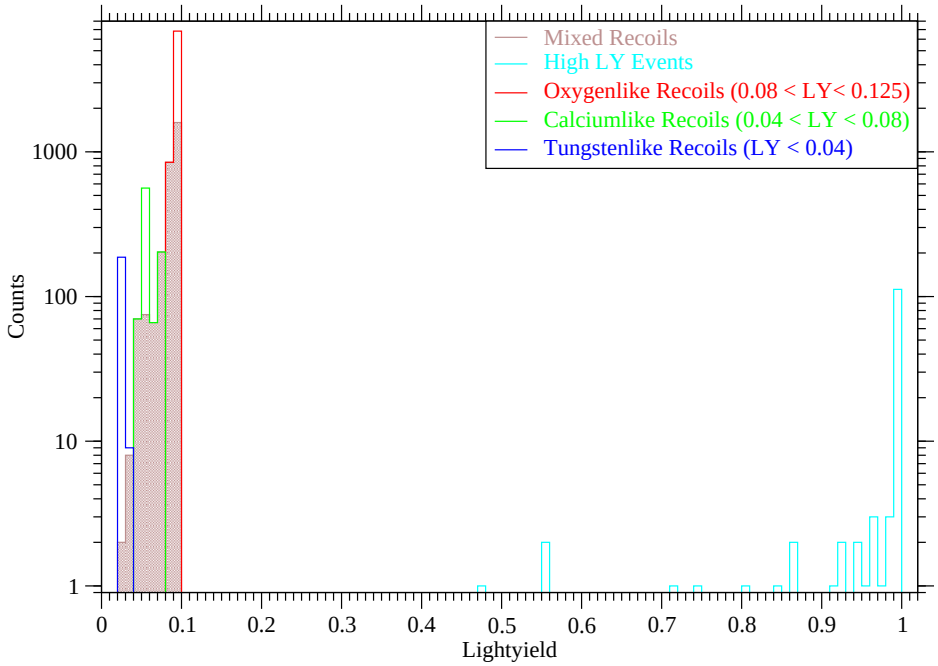

Figure 6.25: Histogram of the single detector hit events *calculated* lightyields between 10 and 40 keV. The neutron source for this plot are cosmogenic neutrons with the spectrum shown in Fig. 5.12 .

The distribution of lightyields shown in Fig. 6.25 includes 126 high lightyield events. In 77 of these events, all energy have been deposited by a γ or electron only. These particles have been produced in the experimental setup around the detectors. Two stray proton only recoils hitting a single detector module with a *calculated* lightyield of 0.55 have been detected within the energy range of 10 – 40 keV, too. No single detector hits of α particles have been found in energetic ROI in the simulation, however. In comparison to the total number of 8423 detector hits, the two proton hits are insignificant for background considerations.

The distribution in the nuclear recoil bands and the fraction of mixed recoil events is similar to the other simulated neutron sources. In the oxygen recoil band, 31.8 % of all events are mixed recoil events. 11.0 % of all oxygen recoils show a *calculated* lightyield in the range of 0.08 – 0.09. The calcium recoil band contains 45.9 % of mixed recoils, 37.6 % of the single detector hits are ouside the bin containing the lightyield expected from calcium only scatterings. The tungsten recoil band contains 5.1 % of mixed recoils, 4.6 percent of all events have a lightyield between 0.03 – 0.04.

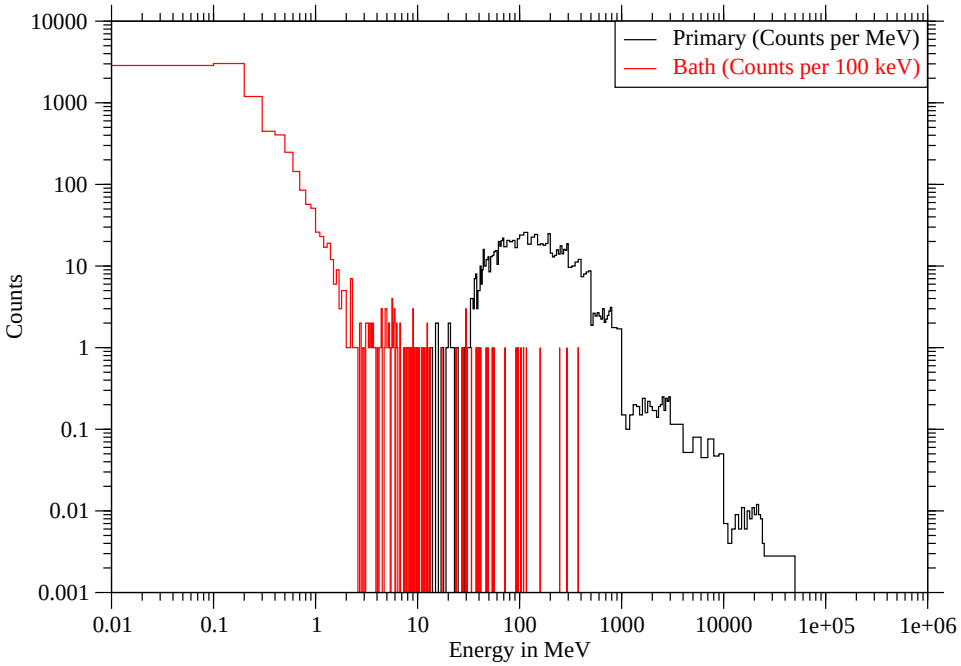

Figure 6.26: Energy spectrum of the primary neutrons and the neutrons depositing in the ROI, the *bath* neutrons. All detector modules of the CRESST – II run 32 have been used, the energetic ROI is located at 10 – 40 keV.

Fig. 6.26 presents the distribution of the *bath* neutrons responsible for single detector hit nuclear recoils in the ROI from 10 – 40 keV for all 33 detector modules. The primary spectrum follows the input spectrum with energies up to 50 TeV, with the main contribution found around a few 100 MeV. The steps seen in the primary spectrum are an artifact of the mechanism assigning a starting energy to the primary neutrons in the simulation. In this mechanism, an energy range is selected according to the integral neutron flux given by input spectrum. The exact starting energy is obtained by applying a flat random distribution within the selected bin. The bulk of neutron *bath* flux is found at energies below 10 MeV. Less than one percent is found between 100 – 300 MeV which deposit energies between 10 – 40 keV via diffractive scattering.

The *bath* spectrum is given by secondary neutrons of the primary neutrons which fits with the observed increase in mean multiplicity.

The following conclusions can be drawn from the simulation of the diffuse cosmogenic neutron background:

- For the assumed diffuse cosmogenic neutron flux of 198 $^{n}/_{\mathrm{m^2a}}$, a single detector hit nuclear recoil background rate for the *operational* detector module setup of $5.08^{+0.09}_{-0.09} \times 10^{-3}$ cts kg^{-1}d^{-1} is obtained. With this rate, the diffuse cosmogenic neutron background is the strongest background source investigated, its total strenght is still a factor 16 below the observed background.

- As the primary energies of the diffuse cosmogenic neutrons are much above the energies of the other sources presented, secondary neutron production occurs. For the highest primary energy, secondary particle cascades are generated which lead to detector hits in large numbers of detector modules. This results in a mean multiplicity of 1.71 for all detector hit events which is about 20 % higher than the mean multiplicity seen for the other neutron sources.

- Out of 8549 single detector hit events in the ROI, two have been induced by secondary protons produced outside the detector modules. At this ratio, the experimentally observed low – energy hits in the α particle lightyield band must originate from other sources.

6.5 Simulation of a Neutron Calibration of the CRESST Experiment

In this section the simulation of a neutron calibration of the CRESST experiment with an Am – Be neutron source is presented. Such a calibration offers the opportunity to analyze the detector response with a statistically sound number of neutron induced nuclear recoils. Furthermore, the larger set of nuclear recoil events allows an additional check for the validity of the simulations. The main aspect of this analysis is the comparison of the rate of observable neutron scatterings on oxygen in two detector modules of the experimental setup.

The experimental setup is the same as used for the previously presented simulations and can be found in Sec. 5.2 . The neutron source is located in a square of 5 cm $\times$ 5 cm attached to the radon box at the height of the center of the detector carousel in a distance of 86cm to the central axis of the experiment. The used generic primary neutron spectrum is shown in Fig. 6.27 . The actual spectral shape depends on the degradation of the α – particles within the volume of the sample which varies with the granularity of the mixture and size effects of the source. An independent measurement of the actual neutron spectrum in the calibration was not available. In total, 15 million primary neutrons have been started in the simulation of the calibration run.

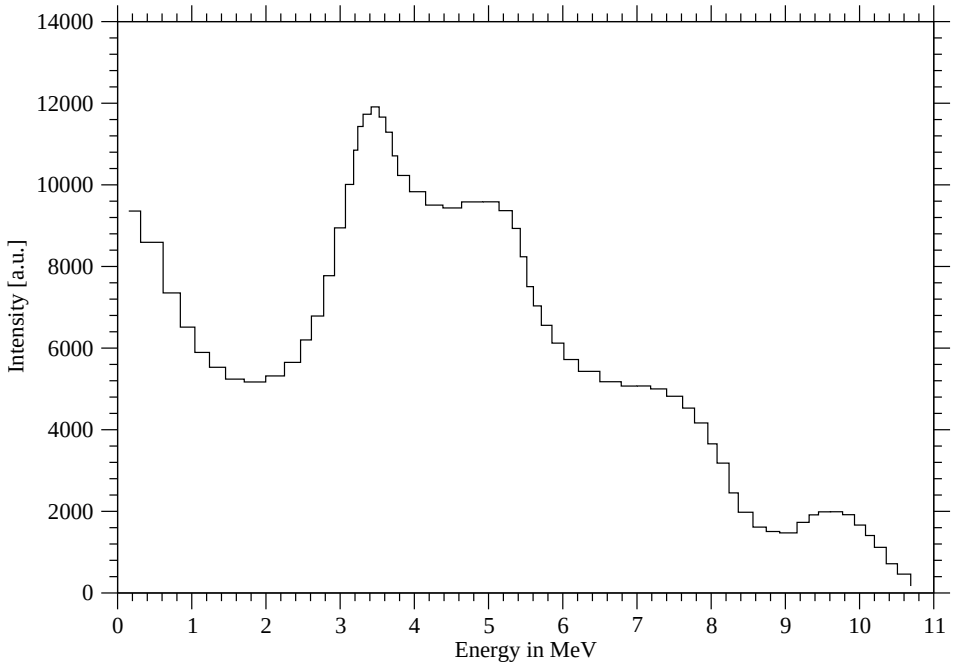

Figure 6.27: The neutron spectrum used in the simulation of the neutron calibration.

Multi – plicity	All events	Number of hits	Constrained events	Number of hits
1	38715	38715	5709	5709
2	6546	13092	199	398
3	1128	33849	7	21
4	183	732		
5	26	130		
6	3	18		
7	1	7		
8	1	8		

Table 6.27: Overview of the multiplicities in the simulation of the calibration run. The row labeled all events contains all detector hits observed in the eight analayzed detectors of the simulation. The constrained events remain after application of the contraints given below. The individual thresholds for each detector modules are found in Tab. 6.28 .

The presented simulation requires a different set of constraints to be comparable to Pfister's analysis of the neutron calibration of run 32 of the CRESST – II experiment found in Ch. 6 of Ref. [Pf10] . Pfister's analysis concluded that on average 4.6 % of all valid detector hits for an ensemble of eight detector modules are coincident with hits in other detectors of this ensemble. In his analysis, the fraction of coincident hits seen per detector varies between 2.1 % and 7.1 % while the total number of hits in the oxygen recoil region per module fluctuates from 160 to 301 [§].

It is important to stress that the analysis of the calibration run is subjected to different constraints than those used in the previous sections. A constrained event listed in Tab. 6.27 must pass the following constraints:

- The detector module must be found in Tab. 6.28 . Only hits in these eight detector modules operational during the calibration are accepted.
- The *calculated* lightyield is less than **0.25** in each detector module.
- Detector hits must be within a time widow of **20** ms.
- Only events with an energy deposition between the detector threshold as given in Tab. 6.28 and **500** keV are considered for the analysis.

Fig. 6.28 presents a histogram showing the energy distribution above 15 keV for single, double and triple detector hits according to the constraints outlined in this section. The agreement of the simulated energy distribution to the experimental one as shown in Fig. 6.3. of Ref. [Pf10] is quite good, however a deficit of energy deposits from 25 – 30 keV and between 40 – 70 keV can be explained as the scaling factor is a bit too large.

[§]Following the convention used in Ref. [Pf10] , fractions are computed on the number of the detector hits not the number of events consisting of a set of detector hits.

Name	Position	Threshold in keV	Multiple fraction in %
Daisy / SOS08	15	14.4	$7.0^{+3.8}_{-2.7}$
K07 / David	6	14.6	$5.6^{+4.2}_{-2.7}$
Maja / Hans	4	11.1	$2.3^{+2.6}_{-1.4}$
Rita / Steven	7	8.8	$2.1^{+2.6}_{-1.3}$
Sabine / Josef	22	12.5	$2.7^{+2.1}_{-1.3}$
VK33 / Franz	18	11.8	$5.1^{+3.0}_{-2.1}$
Verena / Burkhard / Q	30	12.9	$7.1^{+3.4}_{-2.3}$
Wibke / X	31	12.2	$5.2^{+3.4}_{-2.2}$

Table 6.28: The detector modules analyzed for the calibration run according to Tab. 6.2. of Ref. [Pf10] . Name, position number, the energy threshold for the module and the experimentally observed fraction of multiple detector hits within the 90 % oxygen recoil band using a 90 % Poissonian C.L. are given.

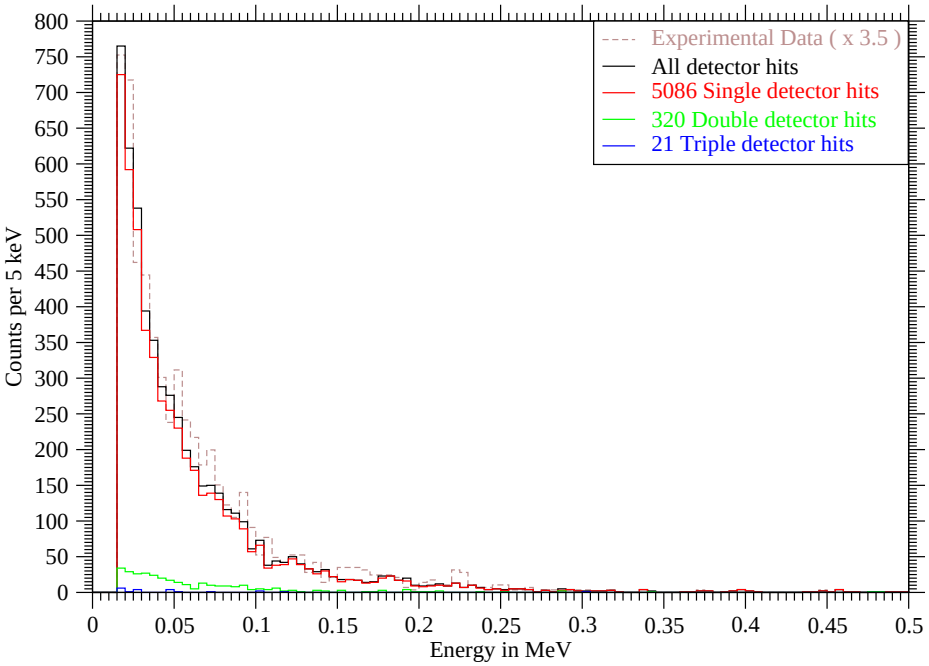

Figure 6.28: Histogram of the deposited energies seen in the simulation of the calibration run using 5 keV bins. The histogram of the experimental energy depositions is scaled up by a factor of 3.5 and taken from Fig. 6.3. of Ref. [Pf10] .

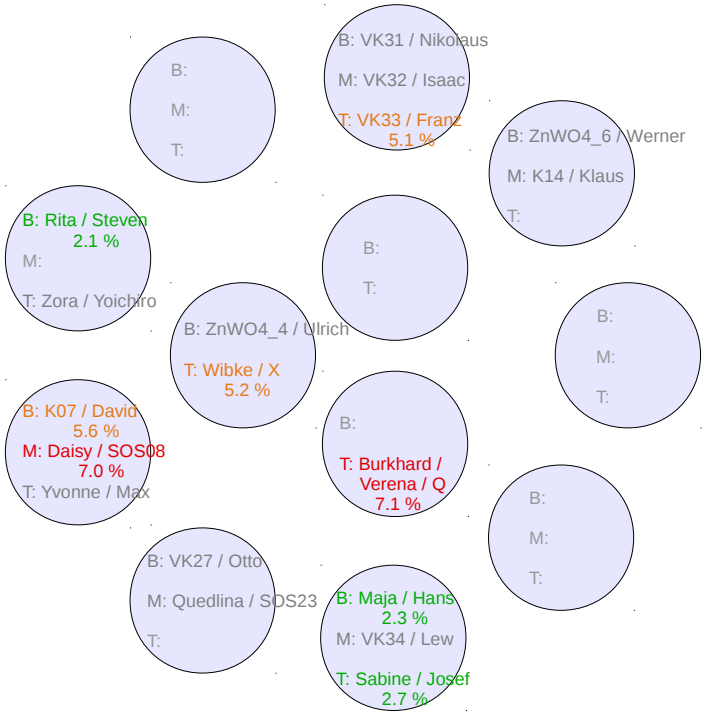

Figure 6.29: Sketch of the detector positions and the observed multiple hit fractions in the calibration run. B, M and T denotes the bottom, middle and top position in each tower of the carousel. Named modules not used in the analysis of the calibration run are colored grey.

The simulation yields an average percentage of double and triple detector hits of $6.8^{+0.8}_{-0.7}$ % (90 % C.L.) for nuclear recoils which is about 50 % higher than the experimentally observed fraction of $4.6^{+3.3}_{-3.3}$ % according to Tab. 6.2. of Ref. [Pf10] if the 90 % C.L. is calculated from the experimental fractions. The rate according to the simulation fits finely with the rate of 7 percent multiple hits seen experimentally in two detector modules and is about 25 percent higher than the observed fraction in three other modules. The other three modules show ratios of 2.1, 2.3 and 2.7 percent only, which is in clear disagreement to the simulation. The 90 % Poissonian confidence limits given in Tab. 6.28 show that the average fraction is at the fringe of the 5 % suitable interval for each of the high multiplicity and the low multiplicity modules. While the medium and high multiplicity detectors are within their appropiate confidence intervals, the low multiplicity modules are outside the lower 5 % confidence intervals of the other modules. Furthermore, the fractions are not caused by the geometrical setup of the detector modules as no pattern regarding the multiplicity and the position of detector modules as Fig. 6.29 reveals.

A reduction of the multiple hit fraction to 6.3 % is achieved if only recoils in the oxygen band are accepted, however, the experimental resolution is not suffiencent to discern oxygen from calcium recoil at the low energies where most recoils are located.

A higher fraction of multiple scattering events is expected to be found in the simulation as the detectors do not reject hits as it is done in the analysis of the experimental calibration run if the pulse shape differs from the standard pulse shape. For energies between 5 – 100 keV in the calibration run, most detector modules have efficiencies ϵ about 90 – 95 percent, the Wibke / X module has an efficency of 85 % and the Rita / Steven module has only an efficenty of 67 % due to noise on the light detector according to Tab. 6.1. of Ref. [Pf10] . Assuming the removed events to be induce by neutrons, the experimentally observed number of multiple detector hit events for two given detectors A and B are reduced by the product of their efficiencies $\epsilon_A \cdot \epsilon_B$ while the number of single detector hits in module A is scaled down by ϵ_A plus the number of events where both detectors are hit but one detector hit is rejected. Thus a higher fraction of multiple detector hits ($\approx \epsilon_{\mathrm{avg}}^{-1}$) is expected from the simulation as it does not take efficiencies into account. For a constant efficiency of each detector module, the apparent multiplicity rate has to be decreased by 5 – 10 percent to match the experimental situation. The situation is easily complicated if the efficiency varies during the run.

Tab. 6.29 uses the constraints outlined above on the simulated background for comparison, furthermore three different set of detector modules are shown to determine the effect of the number of operational detector modules:

- The ten operational detectors of run 32 as defined in Fig. 6.1.
- The eight detector modules presented in Tab. 6.28 as used in the calibration.
- Seven detector modules, which are given by the eight detector module setup without the module Rita / Steven.

The high statistic simulations of neutron source in the inner shields agree with multiple fraction observed from the simulated calibration run of about 7 %, supporting the hypothesis that the primary neutrons from these sources are sufficiently moderated to be blur the difference between the *bath* spectra. The simulation of ambient and PE neutrons do not provide enough statistics, the determined fractions are 5.1 % and 7.9 %, respectively. Cosmogenic neutrons provide a fraction of multiple detector hits of 13.1 % which is nearly twice the fraction extracted from the simulated calibration run.

As expected, the multiple fraction decreases with the number of evaluated detector modules; in the case of the calibration run, the fraction of multiple detector hits falls from 6.8 % for eight detector modules to 6.0 % for seven detector modules.

Source	Single det. hits	%	Double det. hits	%	Higher multi–plicities	%
	Neutrons from the PE shielding					
10	612	90.5	64	9.5	0	
8	515	**92.1**	44	**7.9**	0	
7	448	94.9	24	5.1	0	
	Neutrons from the Cu shielding					
10	7907	91.0	750	8.6	36	0.4
8	6519	**92.7**	492	**7.0**	21	**0.3**
7	5604	93.2	392	6.5	15	0.2
	S.f. neutrons from the Pb shielding					
10	12789	91.7	1076	7.7	89	0.6
8	10587	**93.2**	720	**6.3**	49	**0.4**
7	9078	94.5	500	5.2	24	0.2
	Ambient neutrons					
10	94	91.3	6	5.8	3	2.9
8	74	**94.9**	4	**5.1**	0	
7	61	93.8	4	6.2	0	
	Cosmogenic neutrons					
10	14002	84.7	2082	12.6	456	2.8
8	11726	**86.9**	1488	**11.0**	280	**2.1**
7	10222	88.7	1108	9.6	196	1.7
	Am – Be calibration					
10	6702	91.8	550	7.5	45	0.6
8	**5709**	**93.2**	**398**	**6.5**	**21**	**0.3**
7	5101	94.0	314	5.8	9	0.2

Table 6.29: Single nuclear scattering detector hits versus double scatter hits from selected neutron sources. It is important to notice that the fractions presented in this table count detector hits instead of detector hit events as in the other tables throughout this work. The specifications of the presented sources are found in Ch. 6. The Am – Be setup is presented in Sec. 6.5 which outlines the contraints on the detector modules, too. The threshold for the eight detectors is set as given in Tab. 6.28. The two additional modules Zora / Ulrich and $ZnWO_4$ / Ulrich are subject to an arbitary threshold of 15 keV, for the seven detector setup, the module Rita / Steven has been removed.

From the comparison of the result of the experimental calibration run with the simulation presented here, the following conclusions can be drawn:

- The simulated histogram shown in Fig. 6.28 of the energy deposition is in good agreement to the experimental one presented in Ref. [Pf10] .
- The incoming *bath* neutron spectrum at the location of the detector modules is moderated, 90 % all neutrons for both single and double detector recoils have energies below 725 keV. For the single detector hits, 50 % of the *bath* neutrons are found below 225 keV and half of the double detector hits are induced by neutrons of less than 340 keV. If the primary neutron spectrum is moderated stronger than assumed in the simulation, a lower multiple fraction is expected.
- The simulation results in a higher fraction ($6.8^{+0.08}_{-0.07}$ %) of multiple nuclear scatterings than experimentally observed average of ($4.6^{+3.3}_{-3.3}$ %). Both errors given mark the 90 % confidence interval. In the experimental calibration run, of the individual detectors show a huge variance from 2.1 to 7.1 % which seems independent of the actual detecor position. As multiple hit rate of the three modules showing the least multiple hits is out of the lower 5 % confidence interval of the other five modules, am experimental systematic effect is suspected.
- If the low lightyield events (LY < 0.08) are discarded from the simulation, the rate drops to 6.3 percent.
- As detector hits in the experiment must pass a test of the pulse shape with regard to a standard pulse, which is not applied in the simulation, the multiple hit fraction obtained from the simulation has to be reduced.
- Apart from the discussed recoil – only events, a considerable amount of nuclear scatterings accompanied by coincident γ detector hits in another detector have been reported for the calibration run [Sc10]. The simulation does not yield such a result. As the simulation processes only one neutron and its secondary particles at a time, a steady rate of thermalized neutrons around the detector modules maybe captured and produce extra γs in the real calibration. Inaccuaries of the GEANT4 simulation with respect to γ production in neutron capture and inelastic scattering processes are expected, too.

6.5.1 Simulation of Low Energy Neutrons inside the Cavity of the CRESST Experiment

In this subsection, the simulation of low – energy neutrons within the cavity holding the cold – box of the CRESST – II experiment is presented. There are two possibilities to achieve a significant difference in the ratio of single to double scatterings in the two measurements using different neutron sources:

- If the neutron energy spectrum has significant overlap with resonances in the cross – section of the target material, the chance to encounter multiple scatterings rises. This is especially dangerous for nearly unmoderated neutron spectra with sizable peak structures.
- In the presence of a threshold on the minimum accepted energy deposition, a significant part of suitable low energy neutrons will deposit energy below the threshold in a double scattering event. This situation is excarbated for high ratios $^{E_{\text{thres}}}/E_n$ and large energy transfers, i.e. low energy neutrons scattering on light nuclei like oxygen in $CaWO_4$.

As it has been shown in Fig. 6.17 presented in Sec. 6.3.1, oxygen resoncances are missing below 430 keV, the spikes in the cross – section of calcium do not contribute much leaving two broader resonances centered at 250 and 320 keV capable of a maximum calcium recoil of 24 keV and 30.5 keV. The elastic neutron tungsten cross – section can be assumed as constant at energies above 200 keV, the required incoming neutron energy for a maximum recoil above 8.8 keV on tungsten is 410 keV. Thus for low energy neutrons on $CaWO_4$, the incoming energy of the neutrons is of minor importance only. The most important contribution is given by elastic oxygen recoils. The recoil rate above threshold increases as the fraction of elastic recoils with deposited energies above the detector threshold increases.

If the energy transfer is sufficiently large, and the detector threshold is not negligible to the energy of the incident neutron, the chance that both detectors observes a signal above the threshold can be drastically reduced, e.g. a neutron with a kinetic energy of 80 keV can deposit about 17.4 keV at maximum, it must deposit at least 15 keV to be detected; its remaining kinetic energy of less than 65 keV is not sufficient to transfer an energy above the detector threshold of 15 keV in another detector.

To investigate the influence of the mentioned effect in low energy scatterings, a simulation was conducted which started neutrons with primary energies from zero to 100 keV on the inner surface of the cavity inside the copper shielding surrounding the cold – box of the cryostat in the CRESST – II experiment. The starting directions of the neutrons were isotropically distributed. For each energy, a sample of two million neutrons was started. The constraints and the selected detector sets are the same as the ones given for the analysis of the calibration run presented in the previous section.

Detector modules	Single det. hits	%	Double det. hits	%	Higher multi– plicities	%
	0 – 100 keV					
10	2493	98.8	30	1.2	0	
8	2183	**98.8**	26	**1.2**	0	
7	1592	99.4	10	0.6	0	
	0 – 200 keV					
10	8350	96.2	324	3.7	3	0.0
8	7065	**97.0**	216	**3.0**	0	
7	5732	97.6	142	2.4	0	
	0 – 300 keV					
10	13098	94.9	688	5.0	22	0.2
8	11042	**95.9**	456	**4.0**	15	**0.1**
7	9145	96.1	356	3.7	12	0.1
	0 – 400 keV					
10	16894	93.5	1132	6.3	51	0.3
8	14123	**94.6**	774	**5.2**	36	**0.2**
7	11893	95.3	562	4.5	24	0.2

Table 6.30: Simulated multiplicity of low energy neutrons for a flat neutron spectrum from zero keV to the shown energy. For each endpoint energy two million primary neutrons were started on the inner surface of the cavity holding the detector carousel. The constraints and the detector setups are described in Sec. 6.5 , the starting direction is distributed isotropically.

The results of the simulation shown in Tab. 6.30 confirms the hypothesis that low energy neutrons show a much smaller ratio of observed single scattering to double scattering. For the eight detector setup, only 1.2 % of all hits are accompanied by a hit in another detector module if the flat primary neutron spectrum ends at 100 keV. This fraction increases as the endpoint of the primary spectrum is pushed to higher energies; with an endpoint of 400 keV, 5.2 % of all detector hits are accompanied by hits in other modules. Furthermore, the event rate rises as the amount of recoils above threshold increases.

This subsection yields an important result regarding the rate of multiple detector hit events:

- If the neutron energy spectrum within the experimental cavity is sufficiently moderated, the amount of multiple detector hits is sharply reduced.

6.6 Conclusion: Impact of the Examined Neutron Sources

In this section, the results of the previous sections presenting the simulations of the neutron sources are compared and a conclusion of the combined results is drawn. A double conundrum emerges as the results of the simulation is tested against the experimental results:

- In the simulation, the total nuclear recoil background rate between 10 and 40 keV is a factor 15 lower than the observed one in run 32 of the CRESST – II experiment.
- The predicted fraction of multiple detector hits events of 16.67 % for the simulated sources is much higher than the one obtained from the experimental run 32. Experimentally, the missing double detector hit events are the feature most notable. The effect of reduced detector efficiencies and downtimes of modules has not been taken into account, but cannot explain the vast discrepancy.

The presented simulations yield a total single detector hit nuclear recoil background within the ROI between 10 – 40 keV for ten *operational* detectors of $6.33^{+0.29}_{-0.29} \times 10^{-3}$ cts kg^{-1}d^{-1}. According to Tab. 6.31, one nuclear recoil background event is expected per 158.2 kgd translating to a 90 % C.L. exclusion limit for medium mass WIMP – tungsten scattering of 6.5×10^{-7} pb per nucleon, about an order of magnitude below current best limits for spin – independent direct *Dark Matter* detection. Even for perfect resolution in the light detectors, an indiscriminable WIMP – tungsten scattering background of a single event per 7519 kgd exposure would remain, corresponding to an exclusion limit about of 2×10^{-9} pb at 90% C.L. for a WIMP of a mass of 60 GeV. In this case, a predicted sensitivity about one and a half order of magnitude below todays best published limits on medium mass WIMP searches would be achievable [Ah09b] .

High – energy cosmogenic neutrons and their secondary products in the experimental setup as presented in Sec. 6.4 provide 80 percent of the background rate. Sec. 6.3 revealed that neutrons from U and Th impurities in the inner Pb and Cu shieldings provide about one fifth of the total background event rate. Sec. 6.2 concluded that 0.6 % of the background events are induced by radioactive impurities in the PE shielding. Sec. 6.1 predicts a contribution of about 2 % induced by ambient neutrons from the surrounding rock and concrete of the experimental hall. Tab. 6.31 summarizes the contributions to single detector hit nuclear recoil background events between 10 to 40 keV by source and nuclear recoil band using the default constraints outlined in App. A .

Preliminary analyis of CRESST – II run 32 claims 57 single detector hit nuclear recoil events in the 90 % oxygen band for an exposure of 734 kgd [Pr11]. Using a Poissonian 90 % C.L. with equal lower and upper intervals, the background in the ROI of $0.078^{+0.19}_{-0.16}$ cts kg^{-1}d^{-1} disagrees by a factor of 9.4 – 16.1 compared to the result obtained from the simulation. Apart from the background rate, the question of the absent double detector hits persists on its own.

Source	All nuclear recoils Rate in cts $kg^{-1}d^{-1}$	%	Oxygen – like recoils Rate in cts $kg^{-1}d^{-1}$	%
Cosmogen.	$5.08^{+0.09}_{-0.09} \cdot 10^{-3}$	79.8	$4.42^{+0.09}_{-0.08} \cdot 10^{-3}$	79.6
S.f. in Pb	$8.16^{+2.62}_{-2.57} \cdot 10^{-4}$	13.0	$7.24^{+2.40}_{-1.79} \cdot 10^{-4}$	13.1
n from Cu	$2.90^{+0.07}_{-0.07} \cdot 10^{-4}$	4.6	$2.47^{+0.07}_{-0.07} \cdot 10^{-4}$	4.5
Ambient	$1.33^{+0.29}_{-0.25} \cdot 10^{-4}$	2.1	$1.22^{+0.28}_{-0.24} \cdot 10^{-4}$	2.2
n from PE	$3.81^{+1.90}_{-1.32} \cdot 10^{-5}$	0.6	$3.35^{+1.69}_{-0.96} \cdot 10^{-5}$	0.6
Total	$\mathbf{6.33^{+0.29}_{-0.29} \cdot 10^{-3}}$		$\mathbf{5.55^{+0.26}_{-0.20} \cdot 10^{-3}}$	

Source	Calcium – like recoils Rate in cts $kg^{-1}d^{-1}$	%	Tungsten – like recoils Rate in cts $kg^{-1}d^{-1}$	%
Cosmogen.	$5.28^{+0.30}_{-0.29} \cdot 10^{-4}$	80.1	$1.14^{+0.15}_{-0.13} \cdot 10^{-4}$	84.9
S.f. in Pb	$8.09^{+2.95}_{-1.87} \cdot 10^{-5}$	12.3	$1.14^{+0.54}_{-0.26} \cdot 10^{-5}$	8.6
n from Cu	$3.46^{+0.26}_{-0.24} \cdot 10^{-5}$	5.3	$7.89^{+1.27}_{-1.13} \cdot 10^{-6}$	5.9
Ambient	$1.14^{+1.12}_{-0.66} \cdot 10^{-5}$	1.7	$< 4.39 \cdot 10^{-6}$	< 3.3
n from PE	$3.92^{+2.86}_{-1.87} \cdot 10^{-6}$	0.6	$7.30^{+9.32}_{-4.92} \cdot 10^{-7}$	0.5
Total	$\mathbf{6.59^{+0.44}_{-0.38} \cdot 10^{-4}}$		$\mathbf{1.34^{+0.17}_{-0.13} \cdot 10^{-4}}$	

Table 6.31: Rates of neutron induced nuclear recoil between ten and 40 keV by different lightyields. The selected detector setup for the background rates is the ten detector *operational* detector setup. The given error is the 90 % C.L. Poissonian error. The contamination levels for lead are taken to be 0.2±0.06 ppb for both U and Th. In copper, a contamination of 20 ppt of both contaminants are assumed. S.f. neutrons and (α, n) neutrons are included. As this value is an estimate, no error for the concentration of the contaminants was assumed. For PE, 1.3 ppb of Th and 0.5 ppb U with an error of 40 % each.

The neutron physics used in the GEANT4 simulation works reliably which is supported by the result found in Subsec. 6.1.2 showing that the simulated nuclear recoil background rate is in agreement with the experimental background for the experimental setup without the PE shielding. The cross – section data used in the simulation agree with the values found in the available databases. The geometrical setup in the simulations agrees quite well with the actual one. A major error within the simulation code which reduces the nuclear recoil background for the full setup by an order of magnitude is not plausible.

Rescaling the flux of the considered sources to obtain the experimentally observed background rate is in contradiction to performed measurements. The necessary increase of the ambient neutron flux is impossible considering the experimentally measured neutron flux rates in LN Gran Sasso. Impurity concentration in the lead used in the simulated setup cannot be increased by a factor of 80 without getting into contradiction to the measured concentrations presented in Tab. 5.10 . The necessary increase in the PE impurity of is even more unrealistic in view of the measured contaminations of Tab. 5.7 . No measurements of the radiopurity of the Cu used for the CRESST – II copper shielding and the crystostat are available, and if the U and Th contamination in the copper shielding is increased from 20 ppt to 5 ppb the observed experimental background rate is matched. However, such a contamination is not plausible as it is about an order of magnitude higher than copper contamination levels published for other experiments. A flux of μ – induced neutrons of 15 times the flux given by refs. [Wu04, De99] contradicts the measured μ rates at LNGS, even if the suppression of neutron production on light to medium nuclei by a factor of three of GEANT4 and FLUKA in comparison to the experimental data of the NA55 experiment is assumed [Ch02c]. This would dimish the discrepancy between experimental background rate and simulated one to a factor of four. On the other hand, the inclusion of the effect fo a muon veto detecting the μ and its induced charged particle shower easily counteracts this effect as about half of the experimentally observed nuclear recoil hits are accompanied by a hit in the muon veto and removed accordingly. The background rate induced by stray cosmogenic neutrons is partially subjected to the μ veto if charged particles are hitting the veto. Obtaining the size of the effect of an active μ veto is out of scope of a simulation starting with neutrons as presented here, a top – down simulation starting with μs is required to address this question. The experimentally observed background which is coincident with a μ observed in the muon veto of 25 counts in 734 kgd is due to direct muon hits of the experimental setup, it cannot be compared directly to the background of the simulated diffuse cosmogenic neutron flux which is produced in the rock and concrete around the LNGS cavity.

As the required adjustments for the considered neutron sources are to large to be plausible, it is worthwhile to investigate the requirements on an additional generic neutron source to provide the necessary flux. In order to estimate the effect of a contamination not considered in the simulations, it is instructive to calculate the equivalent contaminations needed to produce the observed nuclear recoil background of 0.08 cts $kg^{-1}d^{-1}$. Tab. 6.32 presents the results.

Location	Equivalent for 0.08 cts $kg^{-1}d^{-1}$			
	Activity		$m_{^{241}Am}$	$m_{^{238}U}$
	Bq_n	$Bq_{\alpha\ ^{241}Am}$	g	g
Ambient	660	9.9 M	76.2 μ	48.2 k
PE shield	0.8	12.1 k	98.4 n	62.4
Pb shield	8 m	120	0.96 n	588 m
Cu shield	1.37 m	22	0.14 n	80 m

Table 6.32: Equivalent contaminations required for the background rates obtained in the simulations. It is assumed that the neutrons are produced from a contamination of an Am – Be source or ^{238}U. The α activity is the one of the given mass of ^{241}Am, neutron activity is valid for both amounts of elements. No further neutron production mechanisms are considered.

Some caveat about the values in the table above must be given:

- The effects of the difference between the energy spectrum of the equivalent source and the simulated one are not considered.
- Uniform dispersion of the source over the same volume as in the simulation.
- Secondary neutron production either by daughter nuclei or by αs on the local materials of the contamination is not included.

Two source types are considered in Tab. 6.32, a sealed Am – Be source which serves a example for neutron production by (α, n) reactions and ^{238}U which serves as example for spontaneous fissible (s.f.) isotopes. The required activity in neutrons drops drastically as the source is placed closer to the detector modules. Within the PE shielding, neutron activities on the mBq level are sufficient to explain a nuclear recoil background of 0.08 cts $kg^{-1}d^{-1}$. While the required uranium contaminations are too large to be reasonable, the amount of Am to explain the observed background rates is extremly tiny. The question in this situation is how a neutron source made of Am and Be could arrive into the experimental setup. In the absence of Be, ^{13}C is a substitute, but requires an α acitivity two to three orders of magnitude larger as the (α, n) cross – section is lower and ^{13}C has only 1.1 % isotopical abundance.

Contaminations of another actinide used as neutron source are even more sensitive. Only about 1.12 million atoms of the s.f. isotope ^{252}Cf dispersed into the volume of the copper shielding are sufficient to supply a neutron flux of 0.08 cts $kg^{-1}d^{-1}$. This is less than a millionth of the required amount of Am required. Furthermore, neutron production of ^{252}Cf does not require the availability of a suitable target as Am does. If not encapsulated, (α, n) reactions can be initated by the α decay of Cf isotopes on top of the enormous s.f. neutron rate. Even the slightest contaminations capable of providing neutrons close to the detector modules entail catastrophic consequences for the sensitivity of an experiment like the CRESST – II experiment.

Source	Fraction in % of given multiplicity		
	Single	Double	Higher
Ambient	92.0	7.5	0.5
n from PE	90.2	9.8	
S.f. from Pb	91.7	7.9	0.5
n from Cu	88.3	9.8	1.9
Cosmogenic	81.6	13.9	4.5

Table 6.33: Observed multiplicities in the presented background simulations considering ten *operational* detector modules for the CRESST – II experiment.

Apart from the correct rate of background events, a second challenges remains, as the ratio of observed multiplicities is smaller than the one inferred from the simulated sources, especially the experimental absence of double detector hit events is confusing. From the experimentally observed 57 single detector hits, between six and 8 double detector hit events are expected while none is observed. The mean kinetic energy of the neutron from a large cross–section (α, n) reaction is well above one MeV, thus a higher fraction of multiple detector hit events is expected from the tendency Tab. 6.33 reveals. Either an efficient moderation is available as the source is located at a distant place from the detectors; or the neutrons are produced at very low energies, via reactions with tiny cross – sections for high α energies on Cu close to the detectors, for example. This consideration contradicts the assumption that a source is hidden close to the detectors and relaxes the dangers of a source close to the detectors somewhat.

No double detector hits have been found so far while three triple detector hit events were detected in run 32, albeit these triple detector hits where found in the set of 17 *installed* detector modules, 9 of those modules did not allow lightyield discrimination [Pr11] ¶. Two of the three triple detector hits show a MeV sized energy deposit and a double hit in the nuclear recoil band each. The third one is composed out of three low energy nuclear recoils. These events are likely to be induced by the remnants of a μ induced shower evading detection by the μ veto.

For each triple hit event, a large number of double detector hit events is expected. For the cosmogenic neutrons, the most energetic neutron source simulated, the results of the simulation shown in Tab. 6.34 predict 2.3 double detector hit events per detector hit event with higher multiplicity for the *installed* detector modules. In the comparison of single to triple detector hit events, the experimentally observed ratio of 19 to one is twice the expected one obtained from the simulation of 9 to one for cosmogenic neutrons presented in Tab. 6.34; at a Poissonian 90 % C.L. , the chance of observing three or less triple detector hit events while expecting six is 8.5 %. This discrepancy indicates that the observed background events are not likely to be induced by cosmogenic

¶As the setup of the 17 *installed* detector modules yields a closer desciption of the analysed detectors in the experimental run 32, the results for this simulated setup are used for the analysis of the mutliplicities.

Source	Fraction in % of given multiplicity		
	Single	Double	Higher
Ambient	88.1	10.4	1.4
n from PE	85.9	13.4	0.7
S.f. from Pb	85.5	12.8	1.6
n from Cu	83.6	14.2	2.2
Cosmogenic	73.2	18.7	8.1

Table 6.34: Observed multiplicities in the presented background simulations considering the 17 *installed* detector modules for the CRESST – II experiment.

neutrons. 11 double detector hit events are expected from the simulation while none is observed experimentally. The simulated multiplicity distribution of the neutrons produced in the copper shielding predicts 1.2 triple events for 57 single events; statistically, a probability of about 20 % to observe at least three triple detector hit events is given. The chance of observing no double detector hits event while expecting seven of them is less than 0.01 % in Poissonian statistics for neutrons from the copper shielding.

Generally, a natural neutron source capable of producing a high amount of triple detector hits but producing less double detector hits than triple detector hits is not possible, even the case of cosmogenic neutrons shows a higher fraction double detector hits than those of all higher multiplicities combined. As the chance that a number of particles deposit energy above threshold in two detectors is larger than the chance that three detectors observe energy deposits above threshold.

Disregarding the three triple events for a moment, the missing double detector hit event rate is hardly explainable by the investigated sources. For the *installed* 17 detectors available for partial detection of detector hits and the simulated sources, Tab. 6.34 shows an increased fractions between 10 and 19 % of all events should be double detector hit events, being in significant disagreement to the zero observed events in the experiment.

On the other hand, the simulation of the Am – Be calibration in Sec. 6.5 predicts a rate of double oxygen detector hit background events in agreement with observed double detector hit background event rate according to Ref. [Pf10], showing that a reliable prediction of the multiplicities can be obtained by the simulation for the calibration run. Thus the missing double detector hit events are not likely to be just an artifact of the simulation.

Subsec. 6.5.1 has shown that only an ultra soft *bath* neutron energy spectrum ending below 300 keV can reproduce the experimentally observed abscence of double detector hits above threshold. The endpoint of the background event energy spectrum is not dicated by the neutron nuclear cross – section, but by the kinematics of scattering. The fraction of energy depositions above the detection threshold in the oxygen band dicates the amount of observed double detector hits since oxygen recoils provide the bulk of background events. Ad-

Single detector hit events

Source	Fraction in nuclear recoil band in %		
	Oxygen	Calcium	Tungsten
	$0.08 < \mathrm{LY} < 0.125$	$0.04 < \mathrm{LY} < 0.08$	$\mathrm{LY} < 0.04$
Ambient	91^{+5}_{-7}	9^{+7}_{-4}	< 3.3
n from PE	$87.8^{+2.2}_{-2.5}$	$10.3^{+2.6}_{-2.2}$	$1.9^{+1.5}_{-1.0}$
s.f. from Pb	$88.68^{+0.48}_{-0.50}$	$9.92^{+0.51}_{-0.49}$	$1.40^{+0.22}_{-0.20}$
n from Cu	$85.35^{+0.71}_{-0.74}$	$11.93^{+0.77}_{-0.74}$	$2.72^{+0.43}_{-0.38}$
Cosmogenic	$87.32^{+0.50}_{-0.52}$	$10.44^{+0.53}_{-0.52}$	$2.24^{+0.28}_{-0.26}$

Double detector hit events

Source	Fraction in nuclear recoil band in %		
	Oxygen	Calcium	Tungsten
	$0.08 < \mathrm{LY} < 0.125$	$0.04 < \mathrm{LY} < 0.08$	$\mathrm{LY} < 0.04$
Ambient	80^{+19}_{-34}	20^{+34}_{-19}	< 32
n from PE	$87.5^{+2.2}_{-2.5}$	$8.3^{+8.9}_{-5.3}$	$4.2^{+7.8}_{-3.4}$
s.f. from Pb	$84.93^{+1.83}_{-2.00}$	$13.19^{+2.04}_{-1.87}$	$1.88^{+1.03}_{-0.74}$
n from Cu	$81.49^{+2.17}_{-2.39}$	$14.58^{+2.51}_{-2.28}$	$3.93^{+1.63}_{-1.26}$
Cosmogenic	$85.33^{+1.24}_{-1.33}$	$12.06^{+1.37}_{-1.28}$	$2.61^{+0.77}_{-0.64}$

Table 6.35: The observed fractions in percent for single and double detector hit events seen in the three nuclear recoil bands. The given error is obtained by taking the maximum error found in the 90 % C.L. variation of a single parameter.

ditionally, the number of nuclear recoils in the calcium and the tungsten band for neutron energies below one MeV is suppressed by kinematics as the fraction below threshold is larger than the one for oxygen recoils. As the distribution of the background events into the nuclear recoil bands is not known since it is not possible to clearly seperate the nuclear recoil bands at the low energies of the ROI, no answer can be given if the experimentally LY distribution is in agreement with the one obtained from the simulation.

The moderation needed to convert the neutron spectrum of a standard contamination to the needed low energies is only attainable for a source located outside the PE shielding. As it has been shown in Tab. 6.32, such a source is required to be quite active and it becomes hard to explain how it could have been placed accidentally at its position.

It has been shown for most of the simulated sources that the effective neutron energy *bath* spectrum for detector hits is well below one MeV. The lightyield distribution of nuclear recoils due to nucleus – WIMP interactions is distinct from the lightyield distribution of neutron induced nuclear recoils. For background events in the ROI, Tab. 6.35 predicts about 90 % oxygen recoils for single detector hits and a slightly reduced fraction of 85 % for double detector hits with a hit in the oxygen recoil band within the energetic ROI. For the 57 experimentally observed single detector hit events, about six events are expected to be found in the calcium recoil band and one event should be materialize in the tungsten recoil band. Due to the insuffient light detector resolution in the experimental run, the lightyield distribution in the different nuclear recoil bands cannot be distentangled.

Chapter 7

Conclusion

In the last esction of the previous chapter, the overall impact of the examined neutron sources has been presented. For the applied constraints, both the total background rate and the fraction of double detector hit events are in clear discrepancy to the experimental result.

A rescaling of the investigated neutron sources to match the simulated background to the observed one is impossible as it breaks the primary neutron fluxes calculated on measured contaminations levels and spectra as has been shown in the discussion of Sec. 6.6. The missing overall background event rate could be increased to the observed level if some unknown hidden neutron sources within the experimental setup are revealed, however.

In addition to the missing background event rate, the fraction of multiple detector hit events allows another independent check on the neutron induced background hypothesis. The experimental absence of any double detector hit events is in clear disagreement to result of the simulation which predicts a double detector hit event fraction between 7.5 – 13.9 % according to the different sources. On top of the double detector hit fracion, higher multiplicity hit events can contribute in the range of 0.5 – 4.5 % of the total amount of detected events. Under the assumption that the majority of the experimentally observed events are induced by neutrons, about four to seven double detector events are expected for the observed number of single detector hit events. The expected numbers are in disagreement with the experimental zero result, as the probability for observing less than one double detector hit event is < 1.9 % and < 0.01 %, respectively. Starting from the observed triple detector hit events, a similar disagreement between the simulated results and the experiment are found.

The combination of the missing background event rate and the absence of double detector hits allows the conclusion the it is unlikely that the experimentally observed background is induced by neutrons only.

Appendix A

Definition of Event Classes for the CRESST – II Background Simulation

In this section, the classification of events used in the sections of chapter 5 is reviewed. Unless noted otherwise, the following constraints have be used to select events from the raw data set:

- At least one detector hit shows a deposited energy of 10 – 40 keV.
- Each registered detector hit of the event has to deposit at least 5 keV in the detector crystal.

Events which fulfill both constraints are labeled by the multiplicity of detector hits. Three different detector setups are used, the positions of the detector modules of these setups can seen in Fig. 6.1:

- The *operational* detector setup. This setup contains the ten detectors of the Run 32 of CRESST – II experiment which both a working light and phonon detector.
- The *installed* detector setup. This setup encompasses 17 detectors of the Run 32 of the CRESST – II experiment which show either a working light or phonon detector.
- The *full* detector setup. This setup uses the full number of 33 installable detector modules in the carousel of the CRESST – II experiment.

For the setups presented above, additional constraints are applied regarding the calculated lightyield. A first constraint on the events checks if the *calculated* lightyield is less than 0.25 *. This removes low – energy electromagnetic background and inelastic scattering events in which the electromagnetic component masks the contribution of the nuclear recoil. For this calculation of the lightyield, the fixed nuclear quenching factors presented below are assumed:

- The quenching factor of oxygen is taken to be $Q_{\mathrm{O}} = 10.0$.
- The assigned quenching factor of calcium is $Q_{\mathrm{Ca}} = 17.9$.
- The quenching factor of tungsten is given by $Q_{\mathrm{W}} = 35.0$.
- The quenching factor of protons is assumed to be $Q_p = 1.75$.
- The adopted quenching factor of α – particles is $Q_\alpha = 5$.
- The quenching factors of deuterium, tritium and ^{3}He are assessed to be $Q_{\mathrm{D}} = 2.5$, $Q_{\mathrm{T}} = 3$ and $Q_{^3\mathrm{He}} = 4.33$. These values are of no real interest as these secondaries are extremely rare in the conducted simulations.

Three classes of events are distinguished according to their *calculated* lightyield:

- *Oxygen Recoils* are all recoils which show a *calculated* lightyield between 0.08 and 0.125. This translates to a quenching factor of the detector hit between 8 and 12.5.
- *Calcium Recoils* are all recoils which show a *calculated* lightyield between 0.04 and 0.08. This translates to a quenching factor of the detector hit between 12.5 and 25.
- *Tungsten Recoils* are all recoils which show a *calculated* lightyield between 0.02 and 0.04. This translates to a quenching factor of the detector hit between 25 and 50.

In the presentation of the various neutron background simulations, additional technical terms are often used.

- The default region of interest (ROI) in the deposited energy – lightyield scatterplot is the window defined by an energy deposition between 10 and 40 keV and a lightyield of less than 0.25.
- Unless noted otherwise, the *calculated* lightyield is used in the histograms and scatterplots presented for the simulated neutron sources. It does not include any variance in the lightyield induced by the limited lightdetector resolution seen in the experiment. The resulting lightyield is always lower than the generic lightyield used for the recoiling nucleus, this feature is induced by the rescaling of the electromagnetic lightyield to exactly unity.

*The calculated lightyield is obtained by application of the mean quenching factor of the nucleus to its deposited energy in the simulation. At this point, the resolution of the photon – detector is assumed to be perfect.

- *Mixed* events are events in which at least two different species of nuclei deposited energy within a single detector module.
- *Inelastic* events are counted by the simulation of the experimental setup. Whenever a neutron induces a scattering reaction on a nucleus in a detector crystal, a counter for either elastic or inelastic scattering is incremented by one for the given event. The values of both counters are conveyed to the output data of the simulation for further use.
- *High lightyield* events exhibit a *calculated* lightyield of more than 0.5.

A.1 Modeling the Quenching of Scintillation Light for Recoiling Nuclei

To achieve comparability of the energy deposition in the simulation and the actual experiment, the quenching must be taken into account. The term quenching is used for the splitting of the deposited energy into the available detection channels of the employed detector. In the case of the CRESST – II experiment, a part of the deposited energy is converted to scintillation light while the rest is deployed in lattice vibrations. If a particle deposits energy in the crystal, the ratio between scintillation light signal to phonon signal varies. Generally, the crystal by the peculiarities of its electronic and phononic band structure and the mechanism of scintillation in the crystal govern the detected energy distribution between the various detection channels. Additionally, the characteristics of the detector devices for the scintillation light and the phonons determine the observed ratio of scintillation light to phonon signal. External parameters like temperature, pressure and the density of crystal defects can influence the scintillation mechanism, changing the ratio of deposited energy seen in the detection channels. But also for fixed external parameters of the crystal, the light to phonon ratio depends on several parameters.

The most important of these parameters is the charge – mass ratio of the depositing particle, which allows the determination of the type of particle which deposited its kinetic energy in the detector.

Usually, the quenching factor of impinging electrons and gamma rays is set to unity.

A.2 The Scintillator $CaWO_4$

The CRESST experiment and the scattering experiment at the MLL in Munich are using cryogenic particle detectors made of Calciumtungstate ($CaWO_4$). Calciumtungstate crystallizes in the tetragonal system, space group $I4_1/a(100)$. The structure of calcium tungstate crystal may be viewed as composed of tungstate $W0_4^{2-}$ anions bonded to calcium Ca^{2+} cations ionically. The metallic sites are found on planes separated by a distance of $c/4$ from each other and perpendicular to the c – axis. Each calcium atom shares corners with eight

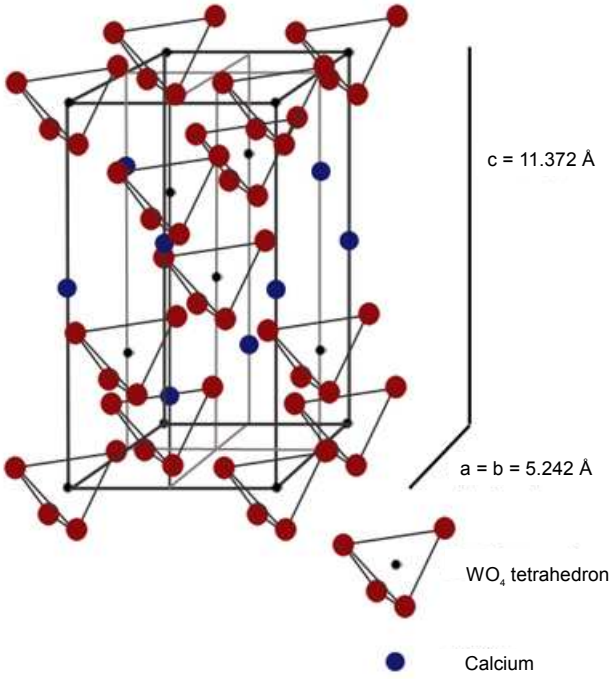

Figure A.1: The structure of $CaWO_4$.

adjacent WO_4 tetrahedra. Each tungsten is bound primarily covalent to four oxygen atoms to form a tetrahedron slightly squashed ($\approx$ 7 %) along the c – axis. The local site symmetry of both calcium and tungsten sites is the $S4$ point symmetry. The oxygen sites have only trivial point symmetry and the crystal has an inversion center. The $CaWO_4$ crystal has the scheelite structure depicted in Fig. A.1, the lattice parameters and other physical properties are shown in Tab. A.1.

$CaWO_4$ is an intrinsic scintillator with high light yield and high thermal quenching temperature[†]. It is accepted that the scintillation light emission is

[†]Thermal quenching describes the fact that the scintillation light emission intensity decreases as the probability of nonradiative transitions in the crystal rises with temperature.

Physical Property	Value
Lattice Parameters	$a = 5.2429$ Å , $c = 11.3737$ Å
Density	5.9 – 6.12 gcm^{-3}, avg. 6.01 gcm^{-3}
Molecular Weight	287.93 g
Thermal Conductivity	4 Wm^{-1}K^{-1}
Melting Point	1580 °C
Optical Properties	$n_w = 1.918 - 1.920$, $n_e = 1.934 - 1.937$

Table A.1: Physical properties of $CaWO_4$. The value for the lattice parameters a and c at a temperature of 300 K and a pressure of one atm are taken from Ref. [Ha85b].

due to electronic transitions of the charge transfer type between oxygen and tungsten within the anion complex WO_4^{2-}, which is interpreted in the excited state as a self – trapped molecular exciton [Tr74, Gr75, Ni00, Mi02b, Na98]. The scintillation light yield is measured down to 20 mK and is found to be constant below 10 K [Mi07]. At temperatures above 200 K, the light yield is suppressed by thermal quenching, decreasing the light yield with raising temperature. Between 200 K and 20 K, only a small increase in light yield is observed and below 10 K, the light yield remains constant. A rise in lightyield is often encountered in undoped solid – state scintillators. At low temperatures, transitions from and to defect states in the electronic structure of the crystal are effectively frozen out. Both dark transitions from random excited crystal defects and scintillation light from delibarate doped defects are thus reduced at low temperatures. Intrinsic scintillation transitions are enhanced as competing de – excitation channels are closed.

A.3 Modeling the Quenching in the Analysis of the Simulations

In this chapter, the treatment of the quenching effect in the simulation is explained. The suppression in scintillation light yield received from energy deposit of a species of particles compared to another is called the quenching factor. Commonly, the standard light yield is defined as the amount of scintillation light received from an electron or a γ:

$$Q_i = \frac{L_i}{L_{\text{e.m.}}} \tag{A.1}$$

Scintillation is a process in which a material converts energy deposited by passing particles into optical photons. A generic connection between energy loss ${}^{dE}/_{dx}$ and scintillation light yield ${}^{dL}/_{dx}$ is given by *Birks law* [Bi67]:

$$\frac{dL}{dx} = \frac{a\frac{dE}{dx}}{1 + b\frac{dE}{dx}} \tag{A.2}$$

Birks law describes two physical processes. Firstly, the light output is proportional with a to the ionization long the path of the ionizing particle given by its energy loss. Secondly, the scintillation mechanism can become saturated, the degree of this saturation is given by b.

The experimentally obtained quenching factors are presented in Tab. A.2 but should be taken *cum grano salis* as the obtained values for both applied techniques are not in good agreement for the heavier nuclei.

The values for D, T and ^{3}He quenching factors are obtained by the simplistic empirical *Ansatz* that the quenching factor of a nucleus scales as $\sqrt{m \times z}$. For the neutron background simulation, the quenching factors of these light nuclei are of minor interest as their associated energy deposit is much higher than the

O	Ca	W	p	D	T	^{3}He	α
12.8(5)	16(4)	> 33					
14.1(2)	27.1(9)	40.1(27)					
10.0(1)	17.9(2)	35^{+19}_{-9}					
13.5(4)	21.1(29)	40.1	1.88(8)	3.9(2)	5.9(2)	4.1(2)	5.7(1)

Table A.2: In this table, the used quenching factors of the CRESST neutron background simulation are presented. The values in the first row were obtained from neutron scattering at room temperature [Co06b]. The quenching factors in the second row are obtained by the ion – implementation method [Ni06]. In the third row quenching factors obtained from neutron scattering at mK temperatures using a cryogenic detector [Co09]. Quenching factors for D, T and ^{3}He are obtained by interpolation of the quenching factor for protons and αs using the empirical fit $Q = {}^m/_{m_{p,\alpha}}\sqrt{z_{p,\alpha}/_z}$. The value given is the mean value obtained by using the given quenching factor for protons and αs as standard. The quenching factors for protons and αs were taken from refs. [Hu06, An05].

energetic region of interest.

In the simulation, the lightyield of a detector hit has to be calculated from the raw physical data obtained in the simulation, which are the energy deposition and the type of particle responsible for the energy deposition. Each particle is assigned a nuclear quenching factor which can be found in Tab. A.2 as a starting point. The energy dependence of the lightyield according to Birks's formula is neglected for simplicity. This can be justified as we are mainly interested in a narrow region where the lightyield of the different particles does not change too wildly. Additionally, the matter constant of scintillation, i.e. the amount of light produced in the detector crystal per unit absorbed energy has to be specified. For analysis purposes throughout this work, a rather high value of $0.05\ {}^{\mathrm{MeV_{optical}}}/_{\mathrm{MeV_{dep}}}$ for γs and electrons is used for the light output.

Thus the amount of energy converted by scintillation into detectable optical photons by a particle of the species i with the quenching factor Q_i is found to be:

$$E_{\mathrm{scint}} = c_{\mathrm{scint}} Q_i^{-1} E_{\mathrm{dep}}, \tag{A.3}$$

while the remaining energy is dissipated into phonons:

$$E_{\mathrm{phonon}} = E_{\mathrm{dep}} \left(1 - c_{\mathrm{scint}} Q_i^{-1}\right). \tag{A.4}$$

For events where multiple particles deposit energy, this calculation has to be done for each particle separately. The contributions are than added up to yield the total E_{scint} and E_{phonon}. The ratio of both energies gives the quenching factor of the event.

In a real measurement no absolute scale of lightyield is available, thus the lightyield produced by γs is rescaled to unity. To include this effect into the

calculation, the lightyield is obtained by dividing the ratio of E_{scint} to E_{phonon} by c_{scint} again:

$$\mathrm{LY_{calc}} = \frac{\mathrm{E_{scint}}}{\mathrm{E_{phonon}}} \frac{1}{\mathrm{c_{scint}}}. \tag{A.5}$$

After this has be done, the quantity $\mathrm{LY_{calc}}$ for electrons and γs is larger than unity, however. If it is rescaled to unity for convenience, all other calculated lightyields are reduced, too. As the quenching factor is the inverse of the lightyield, all *calculated* quenching factors will be a bit larger than the assumed nuclear quenching factors. The deviation scales inversely to $(1 - c_{\mathrm{scint}})$ and thus the needed corrections are rather small for realistic values of c_{scint}.

In preparation for the analysis of the simulation data obtained for the CRESST – II experiment, it was found that the variation of the scintillation lightyield c_{scint} and reasonable variations of the input nuclear quenching factors do not change the picture obtained by the analysis.

Appendix B

Processes in GEANT4

This section of the appendix contains a list of the available physics processes found in GEANT4. In Sec. B.1, additional information about the data base driven `CaWO4NeutronHPInelastic` process is presented. As it uses the G4NDL3.12 nuclear data base, the available information for the various reaction channels and a comparison to reaction channels available in the ENDF – B. VII data base is presented.

B.1 Tabulated Data in for the `CaWO4NeutronHPInelastic` Process

In this section, the data files found in the subdirectories of the G4NDL3.12 and G4NDL3.13 inelastic reaction channel data is presented. This information is crucial for a physical correct treatment of inelastic scattering with the G4HPNeutronInelastic process class.

If no data files exists for an existing inelastic reaction channel, no reaction via this channel will be processed in the simulation. When the data file is only available for the natural abundance of an element, spurious reactions can occur as the reaction channels for all isotopes are mixed. Since it is not checked if the reaction is applicable for the isotope in question, it is possible to proceed along reaction channels forbidden for the energy and the isotope in question. A peculiarity of the (n, n') reaction is the chance to produce the wrong γs as the reaction does not track the cross – sections of the individual excitations, in the current implementation the highest available excitation energy is selected, which is a generally a good first estimate, however contributions of lower excitation levels do not vanish at higher energies. In Tab. B.1 the available isotope data files for the various reaction channels in the neutron data libraries G4NDL3.12 and G4NDL3.13 are presented.

Tab. B.2 shows which inelastic reaction channels are missing for the most common solid dark matter detector materials, $CaWO_4$, Ge and Xe. The listed channels can be found in the JEFF3.1 neutron scattering data base but are absent in GNDL3.12.

Directory	Reaction	Annotation
F01	(n, n)	
F02	(n, X)	This directory does not exist anymore.
F03	$(n, 2n\alpha)$	Only ^{27}Al data.
F04	$(n, 2n)$	
F05	$(n, 3n)$	
F06	$(n, n\alpha)$	
F07	$(n, 3\alpha n)$	No data.
F08	$(n, 2n\alpha)$	Only ^{27}Al,^{6,7} Li and ^{nat}C data.
F09	$(n, 3n\alpha)$	Only ^{7}Li data.
F10	(n, np)	
F11	$(n, n2\alpha)$	Only ^{27}Al data.
F12	$(n, 2n2\alpha)$	No data.
F13	(n, nD)	
F14	(n, nT)	^{27}Al,$^{\text{nat}}$ C,$^{\text{nat}}$ Sn, ^{106,108,110,111,112,113,114,116}Cd,^{140} Ba,$^{\text{nat}}$ In and ^{152}Gd.
F15	$(n, n^3\text{He})$	Only ^{nat}Sn data.
F16	$(n, nD2\alpha)$	No data.
F17	$(n, nT2\alpha)$	No data.
F18	$(n, 4n)$	^{121,123}Sb,^{127} I,^{174,176,177,178,179} Hf, ^{197}Au,^{223,224,225,226} Ra and ^{235}U.
F19	$(n, 2np)$	Only ^{27}Al and ^{nat}C data.
F20	$(n, n3p)$	Only ^{27}Al data.
F21	$(n, n2p)$	Only ^{27}Al data.
F22	$(n, np\alpha)$	Only ^{27}Al data.
F23	(n, p)	
F24	(n, D)	
F25	(n, T)	
F26	$(n, ^3\text{He})$	
F27	(n, α)	
F28	$(n, 2\alpha)$	^{14}N,^{22} Na,^{27} Al,^{36,38} Ar and ^{59}Co
F29	$(n, 3\alpha)$	No data.
F30	$(n, 2p)$	^{nat}C,^{27} Al,$^{\text{nat}}$ S,$^{\text{nat}}$ Ca,^{59} Co,^{61} Ni,$^{\text{nat}}$ Ga, ^{70,nat}Ge,^{75} As,$^{\text{nat}}$ Mo,$^{\text{nat}}$ Sn,^{124} Xe and ^{130}Ba.
F31	$(n, p\alpha)$	Only ^{nat}C,^{27} Al and ^{59}Co data.
F32	$(n, D2\alpha)$	Only ^{10}B data.
F33	$(n, T2\alpha)$	No data.
F34	(n, pD)	Only ^{nat}C and ^{27}Al data.
F35	(n, pT)	Only ^{nat}C and ^{27}Al data.
F36	$(n, D\alpha)$	Only ^{27}Al data.

Table B.1: The names of the inelastic neutron scattering reaction channel directories and the corresponding reaction channels. If no files or only a few data files for a reaction channel are available this is noted. In any case it is advisable to check the directories if a given isotope is crucial for the simulation.

Isotope	Missing Reaction Channels in GNDL3.12 compared to JEFF-3.1 database
$^{\text{nat}}$O	
^{16}O	$(n, n3\alpha)$, (n, nd), $(n, 2np)$, $(n, n2p)$, $(n, np\alpha)$, $(n, 2\alpha)$, $(n, p\alpha)$
^{17}O	
^{18}O	No cross – section in JEFF-3.1 or ENDF/B-VII.0 given
$^{\text{nat}}$Ca	
^{40}Ca	(n, n'), $(n, 2n)$, $(n, n2\alpha)$, $(n, n2p)$, $(n, np\alpha)$, (n, p), (n, d), (n, t), $\left(n,^3 He\right)$, (n, α), $(n, 2\alpha)$, $(n, 2p)$, $(n, p\alpha)$, $(n, d\alpha)$, (n, γ)
^{42}Ca	(n, n'), $(n, 2n)$, $(n, n2\alpha)$, (n, nd), (n, p), (n, d), (n, t), $\left(n,^3 He\right)$, (n, α), $(n, 2\alpha)$, $(n, 2p)$, $(n, p\alpha)$, $(n, d\alpha)$, (n, γ)
^{43}Ca	(n, n'), $(n, 2n\alpha)$, $(n, 2n)$, $(n, 3n)$, (n, nd), $(n, 2np)$, (n, p), (n, d), (n, t), $\left(n,^3 He\right)$, (n, α), $(n, 2\alpha)$, $(n, 2p)$, $(n, p\alpha)$, (n, γ)
^{44}Ca	(n, n'), $(n, 2n)$, $(n, 3n)$, (n, p), (n, d), (n, t), $\left(n,^3 He\right)$, (n, α), $(n, 2\alpha)$, $(n, 2p)$, (n, γ)
^{46}Ca	(n, n'), $(n, 2n)$, (n, p), (n, d), (n, t), $\left(n,^3 He\right)$, (n, α), (n, γ)
^{48}Ca	(n, n'), $(n, 2n)$, $(n, 3n)$, (n, p), (n, d), (n, t), $\left(n,^3 He\right)$, (n, α), (n, γ)
$^{\text{nat}}$W	
^{180}W	No cross – section in JEFF-3.1 or ENDF/B-VII.0 given.
^{182}W	(n, n'), $(n, 2n)$, $(n, 3n)$, (n, np), (n, p), (n, p), (n, α), (n, γ)
^{183}W	(n, n'), $(n, 2n)$, $(n, 3n)$, (n, np), (n, p), (n, p), (n, α), (n, γ)
^{184}W	(n, n'), $(n, 2n)$, $(n, 3n)$, (n, np), (n, p), (n, p), (n, α), (n, γ)
^{186}W	(n, n'), $(n, 2n)$, $(n, 3n)$, (n, np), (n, p), (n, p), (n, α), (n, γ)

Table B.2: The available data can be found in the GNDL3.12 data base. If reaction channels are given in the JEFF-3.1 evaluated neutron data base but not found in GNDL3.12, these channels are listed in the second column.

B.2 Hadronic Processes

In this section, the used nuclear – reactions processes used in GEANT4 are presented. Apart from the ultra high – energy processes which are needed only for the most energetic cosmogenic neutrons, two classes of hadronic processes are given in GEANT4:

The parameterization driven low – energy processes (*LE*) on the one hand, and on the other hand, the data – driven, high precision processes (*HP*).

The parameterization driven models are defined as *low* energy models in the high energy physics sense of the word, it is intended for hadronic projectiles with kinetic energies in the range of 1 GeV to 25 GeV. It is based on the GEANT3 GHEISHA package. The physics underlying this model derives from a multi – chain model in which the incident particle collides with a nucleon inside the nucleus. The final state is given by a recoil nucleon, the scattered incident particle, and possibly many hadronic secondaries. The hadron production is approximated by the formation zone concept, i.e. the interacting quark – partons require some time and thus some range to hadronize. All of these particles are able to re – interact within the nucleus, thus developing an intra – nuclear cascade.

In this model only the first hadron – nucleon collision is simulated in detail. The remaining interactions within the nucleus are simulated by generating additional hadrons and treating them as secondaries from the initial collision. The numbers, types and distribution functions of the extra hadrons are determined by parameterizing functions which were fitted to experimental data or which reproduce general trends in hadron – nucleus collisions. This leaves the model with numerous tunable parameters to obtain reasonable physical behavior. In the strict sense, this restricts the use of the LE model for hadron – nucleus interactions because it is not always clear how the parameters relate to physical quantities.

The *HP* processes described in this section are valid for energies below 20 MeV. Generally, the upper limit is set by the comprehensive evaluated neutron scattering data libraries that the simulation is based on. The final state is a set of secondary particles that is passed to the tracking sub – system for further geometric tracking within GEANT4. These models are data – driven, i.e. for each isotope there should be a data file containing at least the cross – sections for the given reaction channel on this isotope. The high precision neutron models depend on an evaluated neutron data library (G4NDL) for cross sections, angular distributions and final state information. However the library is incomplete since data for several elements is missing.

Appendix C

Modifications of the used Neutron Spectra

In this chapter, the modifications applied to the used input spectra of the primary neutrons are presented. The modifications are required to extend the spontaneous fission neutron spectra obtained by SOURCES4A which are given up to 10 MeV to the maximum energy of 20 MeV of the `G4NeutronHPElastic` and the `CaWO4NeutronHPInelastic` physical interaction class. Sec. C.1 explains how s.f. neutron spectra are extrapolated to 20 MeV by assuming either a Maxwell spectrum or an evaporation spectrum. For the (α, n) neutron spectra obtained for PE, some slight corrections have to be applied which are discussed in Sec. C.2. An estimate of the effect of the additional background neutrons due to (α, n) reactions due to alpha decay of radon on the surface of the PE shielding is given in Sec. C.3.

C.1 Extrapolation of SOURCES Spontaneous Fission Neutron Spectra

The energy spectra of the s. f. neutrons is retrieved from the SOURCES 4A code [Wi99]. This program returns the integrated neutron fluxes within energy bins of the size of 100 keV up to a maximum energy of ten MeV. Unfortunately, the part of the neutron spectra above ten MeV is interesting because the free mean path of neutrons generally rises with their kinetic energy, thus their chance to reach the shielded detectors is higher than the chance of lower energetic neutrons. An extension for the given neutron spectra to higher energies is thus desirable.

In Subsec. 4.3.4, four parameterizations of fission neutron spectra are presented. For the Maxwell spectrum and the evaporation spectrum, a extension for the given integrated fluxes can be constructed under weak assumptions with only one parameter Θ, the effective temperature of the neutron energy distribution.

The energy distribution function for the s. f. neutron spectrum is given by Eq. 4.9 for the Maxwell spectrum and Eq. 4.10 for the evaporation spectrum. In the case of s. f. , Θ is not a function of the incoming neutron energy E, as there is no incoming neutron. For the Maxwell spectrum, the ratio between the flux at two different energies E_1 and E_2 is given by:

$$\frac{f\left(E_1\right)}{f\left(E_2\right)} = \sqrt{\frac{E_1}{E_2}} \exp(-\frac{E_1 - E_2}{\Theta}), \tag{C.1}$$

for the evaporation spectrum the square root of the energies is replaced by the energies themselves:

$$\frac{f\left(E_1\right)}{f\left(E_2\right)} = \frac{E_1}{E_2} \exp(-\frac{E_1 - E_2}{\Theta}). \tag{C.2}$$

Making the assumption that the integrated flux can be linearly approximated, the integrated flux from the energy E_n up to the energy E_{n+1}, $\Phi\left(E_{n+1}\right)$, is given by:

$$\Phi\left(E_{n+1}\right) = \int_{E_n}^{E_{n+1}} f\left(E'\right) dE' \quad \approx \frac{1}{2}\left(E_{n+1} - E_n\right)\left(f\left(E_n\right) + f\left(E_{n+1}\right)\right). \tag{C.3}$$

Using Eq. C.2, the ratio of the two integrated fluxes $\Phi\left(E_{n+1}\right)$ and $\Phi\left(E_n\right)$ can be expressed for the evaporation type of spectrum:

$$\frac{\Phi\left(E_{n+1}\right)}{\Phi\left(E_n\right)} = \frac{E_{n+1} - E_n}{E_n - E_{n-1}} \frac{f\left(E_n\right)}{\left(E_{n-1}\right)} \frac{1 + \frac{E_{n+1}}{E_n} \exp\left(-\frac{E_{n+1} - E_n}{\Theta}\right)}{1 + \frac{E_n}{E_{n-1}} \exp\left(-\frac{E_n - E_{n-1}}{\Theta}\right)}, \tag{C.4}$$

for the Maxwell spectrum, the factor $\frac{E_m}{E_{m-1}}$ in front of the exponential has to be replaced by $\sqrt{(\frac{E_m}{E_{m-1}})}$. Now two assumption are made, the first requires that the distances between the E_n are equidistant, and second assumption is that the approximation:

$$\frac{1 + \frac{E_{n+1}}{E_n} \exp\left(-\frac{\Delta E}{\Theta}\right)}{1 + \frac{E_n}{E_{n-1}} \exp\left(-\frac{\Delta E}{\Theta}\right)} = 1 \tag{C.5}$$

holds true. In the equation above, ΔE replaces $E_m - E_{m-1}$. For the Maxwellian case, the factor $\frac{E_m}{E_{m-1}}$ has to be replaced by its square root again. If Θ is much larger than ΔE and ${}^{E_m}/_{E_{m-1}}$, or $\sqrt{{}^{E_m}/_{E_{m-1}}}$ in the Maxwellian case is close to unity, Eq. C.5 is valid to a high accuracy. Using the approximation, the integrated flux $\Phi\left(E_{n+1}\right)$ is obtained from the known integrated flux $\Phi\left(E_n\right)$ by the formula:

$$\Phi\left(E_{n+1}\right) = \frac{E_n}{E_{n-1}} \exp\left(-\frac{\Delta E}{\Theta}\right), \tag{C.6}$$

for an evaporation spectrum and

$$\Phi\left(E_{n+1}\right) = \sqrt{\frac{E_n}{E_{n-1}}} \exp\left(-\frac{\Delta E}{\Theta}\right), \tag{C.7}$$

for a Maxwell spectrum. The effective temperature Θ has to be obtained from the given integrated fluxes in the case of the evaporation type spectrum by:

$$\Theta = -\frac{\Delta E}{\ln\left(\frac{E_{n-1}}{E_n}\frac{\Phi(E_{n+1})}{\Phi(E_n)}\right)}, \tag{C.8}$$

for the Maxwell spectrum $^{E_{n-1}}/_{E_n}$ has to be substituted by its square root again.

For the given spectra, the extracted temperature is not constant. While the flux in the evaporation spectrum decreases faster in the case of the Maxwell spectrum, the effect is small. The difference between both spectra is less than five percent up to fission neutron energies of 20 MeV.

C.2 Preparation of a α Induced Neutron Spectrum

For the calculation of the neutron spectra induced by α – particles the energy dependent (α, xn) cross – sections in the target material and the energy loss of the α – particle in the medium have to be taken into account. While the measured neutron production cross – section of medium mass nuclei like copper raises continuously with energy for natural occurring α – particles, the (α, n) neutron production rate on light nuclei like ^{13}C extends down to low incident energies. As Fig. 5.8 reveals, pronounced resonances are found for incident energies between two and eight MeV. In such a case an elaborate calculation of the neutron production on PE is mandated. Program codes for this task are available, this work relied on the SOURCES 4A code [Wi99]. In the following paragraph, the general procedure of obtaining the neutron production rate is sketched.

The mean free path $\lambda(E)$ for (α, xn) reactions for an α – particle with a given energy E can be calculated from the density of target nuclei n and the cross – section at the incident energy $\sigma(E)$:

$$\lambda(E) = \frac{1}{n\sigma(E)} \tag{C.9}$$

The total production rate R_{prod} is then given by the integral along the track of α – particle within the target material. This integral along the track can be converted into an integral of energies, with boundaries given by the kinetic

energy the α – particle upon entry of the target material and the threshold energy of α – induced neutron production in this material:

$$R_{\mathrm{prod}} = -\int_{E_{\mathrm{thres}}}^{E_0} \left(\frac{dE}{dx}(E')\right)^{-1} \frac{1}{\lambda(E')} dE' \tag{C.10}$$

It is necessary to discretize this integral in a numerical application. For a given accuracy a sufficiently small step size of the has to be adopted. It should be ensured that a well defined medium energy of the step can be defined. The calculation of the energy loss of αs for a wide range of materials can be obtained from the NIST ASTAR alpha particle energy loss code which is available online [Be05c] . If the track length l_α of the α – particle is small in comparison to the mean free path for (α, xn) reactions, the ratio of these two quantities gives the $\alpha - n$ conversion factor along the step. Summing of the $\alpha - n$ conversion factors of the steps results in R_{prod}.

The alpha induced neutron spectrum in polyethylene used for the simulations in this work has been generated with the SOURCES4A code by V. Tomasello [To08]. As matrix material for the radioactive nuclei of the uranium – radium, the actinium – uranium and the thorium decay chain, a cube of polyethylene was specified. The concentration of the daughter nuclei has been given by their equilibrium concentration. The neutron spectrum of the α – induced neutrons on ^{13}C due to the allowed reaction channels plus the contribution of the spontaneous fission neutrons from the contaminants has been generated by the SOURCES4A code for each isotope. The initial contamination has been set to 10 ppb natural abundant uranium and 10 ppb of ^{232}Th each. Once the neutron spectrum has been acquired, it can be easily scaled for other levels of contamination.

Two issues arose with the obtained spectrum. Firstly, the generated spectrum ends at 10 MeV, thus the contributions from higher energetic spontaneous fission neutrons and the contribution of the highest energetic (α, n) – reaction on ^{212}Po were missing. Secondly, for the neutrons produced from the (α, n) – reaction on ^{212}Bi, spurious contributions were listed for energies above the kinematic endpoint of the reaction. The missing contributions of ^{215}At αs are unproblematic as the equilibrium concentration of ^{215}At is negligible.

For the first issue, a solution was found by adding the appropriate spontaneous fission neutron integrated fluxes for energies up to 20 MeV according to a Maxwellian fission spectrum. The few missing entries for the neutrons generated by ^{212}Po were added assuming that the integrated fluxes for the neutrons with energies a few hundred keV below the endpoint scale similar as in the cases of ^{214}Po and ^{212}Po with a maximum kinetic energy of the α of 7.687 MeV and 8.785 MeV.

The spurious high energy neutrons from ^{212}Bi α – particles are just subtracted from the total neutron spectrum.

C.3 An Estimate for the Radon – Induced (α, n) Contribution on PE

In this section the influence of radon induced neutrons from (α, n) processes on the surface of the PE shielding is given. An additional contribution of neutrons can be provided by additional (α, n) reactions from impinging α particles provided by the decay of radon in the air around the polyethylene shielding. While the radon activity in the air of the LNGS laboratory is known to be around 30 Bq, it is hard to determine the significance of this contribution as several key issues for this contribution cannot not easily resolved. At first, the area of the PE shielding exposed to radon is not known exactly. Secondly, the fraction of α – particles and their energetic degradation by the passage from the location of the actual radon decay to the surface of the PE shielding is hard to model, too.

The activity of 30 $^{\mathrm{Bq}}/_{\mathrm{m}^3}$ of Rn in the air in the LNGS laboratory is assumed. The natural isotopic distribution of one % of ^{219}Rn, nine % of ^{220}Rn and 90 % of ^{222}Rn is assumed. The life – times of the isotopes are given as $\tau_{^{219}\mathrm{Rn}} = 5.71$ s, $\tau_{^{220}\mathrm{Rn}} = 80.21$ s and $\tau_{^{222}\mathrm{Rn}} = 476657$ s. In secular equilibrium, the activity A of a population of N atoms of a radioactive isotope is given by:

$$N = A \cdot \tau. \tag{C.11}$$

For the three isotopes of radon with the life – times and concentrations with a total activity of 30 Bq, the following subsequent equation yields a total number N_{tot} of 10437 radioactive radon atoms:

$$30Bq = \frac{N_{^{219}\mathrm{Rn}} = 0.01 \times N_{\mathrm{tot}}}{\tau_{^{219}\mathrm{Rn}}} + \frac{N_{^{220}\mathrm{Rn}} = 0.09 \times N_{\mathrm{tot}}}{\tau_{^{220}\mathrm{Rn}}} + \frac{N_{^{222}\mathrm{Rn}} = 0.9 \times N_{\mathrm{tot}}}{\tau_{^{222}\mathrm{Rn}}}. \tag{C.12}$$

The neutron yield of energetically non – degraded α particles in polyethylene can be obtained from SOURCES 4A calculations. In Tab. C.1, the specific neutron yield of the isotopes in PE, the number of atoms of each isotope in equilibrium concentration and the maximum resulting integrated neutron flux can be found. Assuming that all α decays happen directly on the PE surface and half of the αs are emitted into the PE, the integrated neutron flux for the natural abundant radon isotopes with a total activity of 30 $^{\mathrm{Bq}}/_{\mathrm{m}^3}$ sums up to a maximum of 328.9 neutrons per year. ^{220}Rn from the Np decay chain contributes about 70 percent of all (α, n) neutrons from the source modeled here.

The main problem this the determination of radon daughter isotopes which end up on the PE surface. Even in air, the recoiling nucleus is thermalized quickly and its propagation is dominated by the physics of the air, i.e its flow, the adhesive forces between radioactive ion and surface. The distribution of contaminations on a floor, a ceiling or a wall depend on these parameters.

For the complete surface of the PE shielding of approximately 100 m^2, less than 1650 neutrons are expected per year for a radon contamination in the air

Radon Isotope	Neutron Activity in $^{n}/_{s}$ incl. daughter nuclei	Number of Atoms	Resulting Neutron Activity in $^{n}/_{s}$
^{219}Rn	6.16×10^{-8}	104.4	6.44×10^{-6}
^{220}Rn	1.54×10^{-9}	939.3	1.44×10^{-5}
^{222}Rn	1.94×10^{-12}	9393.3	1.83×10^{-8}
Total		10437	2.08×10^{-5}

Table C.1: Radon induced neutron production in polyethylene. The equilibrium concentrations of the radon isotopes given for an activity of a cubic meter of LNGS air of 30 Bq. The neutron activity per atom includes the contributions of the daughter nuclei in equilibrium concentrations. The integrated neutron fluxes per radon atom in bulk PE are obtained with the help of the SOURCES 4A code. The obtained neutron fluxes assume that all produced α particles are emitted directly from the surface of the PE into the bulk.

of the LNGS laboratory of 30 $^{\mathrm{Bq}}/_{\mathrm{m}^3}$ and the assumption that on average, 20 m^2 of PE surface are exposed to radon and the daughter nuclei of one cubic meter of air.

This is about ten percent of the neutron flux from the bulk PE shielding. If the average radon contamination in the laboratory is much higher, the primary neutron contribution is of the order of the neutrons produced in bulk PE. The low contribution of neutrons originating from the PE shielding to the relevant detector background relaxes the significance of the uncertainty in the radon induced neutron production rate.

As a caveat, it should be noted that the resulting rate does not scale linearly with the amount of primary neutrons as three quarters of the neutrons are produced on the outer surface of the PE shielding facing an enhanced moderation compared to the neutrons from the bulk PE. On the other hand, neutrons produced on the inner surface traveling into the detector setup are only moderated by the lead and the copper shielding.

Neutron production on the surface of the copper shielding is potentially dangerous as neutrons produced that close to the detectors can produce background events effectively as seen in Sec. 6.3.2 . The inner copper shielding is located within a box which is permanently flooded by nitrogen gas evaporated from liquid nitrogen. This arrangement eliminates radon contamination of the surface of the copper shielding after a short time, eliminating this neutron source.

Bibliography

[Aa08] C. E. Aalseth *et al.* (The CoGeNext Collaboration), Phys. Rev. Lett. **101** 251301 (2008); Erratum-ibid.**102**, 109903, 2009.

[Ab83] L. Abbot and P. Sikivie, Phys. Lett. **B120**, 133 (1983).

[Ab08] J. Abraham *et al.* (Pierre Auger Collaboration), Phys. Rev. Lett. **101**, 061101 (2008).

[Ab10] A. A. Abdo *et al.*, arXiv:1001.4836v1, to be published in Phys. Rev. Lett.

[Ad69] S. L. Adler, Phys. Rev. **177**, 2426 (1969).

[Ad08] P. Ade *et al.*, Astrophys. J. **674**,22 (2008).

[Ag99] M. Aglietta *et al.* (The LVD Collaboration), Proc. 26^{th} Intern. Cosmic Rays Conf, Salt Lake City (USA), Vol.2, 44 (1999).

[Ag03] S. Agostinelli *et al.*, Nucl. Instrum. Methods Phys. Res. **A506**, 250 (2003).

[Ah02] B. Aharmin *et al.* (SNO Collaboration), Phys. Rev. Lett. **89**, 011301 (2002).

[Ah09a] Z. Ahmed *et al.* (CDMS Collaboration), Phys. Rev. Lett. **103**, 141802 (2009).

[Ah09b] Z. Ahmed *et al.* (The CDMS Collaboration), arXiv:0912.3592v1.

[Al82] A. D. Albrecht and P. Steinhardt, Phys. Rev. Lett. **48**, 1220 (1982).

[Al89] R. Aleksan *et al.*, Nucl. Instrum. Meth. **A274**, 203 (1989).

[Al00] C. Alcock *et al.*, Astrophys. J. **542**. 281 (2000).

[Al06] J. Allison *et al.*, IEEE Trans. Nucl. Sci. **53**, 270 (2006).

[Al07] G. J. Alner *et al.*, Astropart. Phys. **28**, 287 (2007).

[Am08] C. Amsler *et al.*, Phys. Lett. **B667**, 1 (2008).

[An05] G. Angloher *et al.*, Astropart. Phys. **23**, 325 (2005).

[An07] S. Andriamonje *et al.* (The CAST Collaboration), JCAP **04**, 010 (2007).

[An08] J. Angle *et al.* (The XENON Collaboration), Phys. Rev. Lett. **100**, 021303 (2008).

[An09] G. Angloher *et al.* (The CRESST Collaboration), Astroparticle Phys. **31**, 270 (2009).

[Ap01] T. Appelquist, H.C. Cheng and B. A. Dobrescu, Phys. Rev. **D64**, 035002 (2001).

[Ar98] N. Arkani-Hamed, S. Dimopoulos and G. R. Dvali, Phys. Lett. **B429**, 263 (1998).

[Ar99] F. Arneodo *et al.*, Il Nuovo Cim. **112A**, 819 (1999).

[Ar05] T. Araki *et al.* (KamLAND Collaboration), Phys. Rev. Lett. **94**, 081801 (2005).

[Ar09a] E. Arik *et al.* (The CAST Collaboration), JCAP **02**, 008 (2009).

[Ar09b] E. Armengaud *et al.* (The EDELWEISS Collaboration), arXiv:0912.0805v1, submitted to Phys. Lett. **B**.

[As10] S.J. Asztalos *et al.* (The ADMX Collaboration), Phys. Rev. Lett. **104**, 041301 (2010).

[Ba81a] S. Barshay *et al.* Phys. Rev. Lett. **46**, 1361 (1981).

[Ba81b] A. Barroso and M. C. Mukhopadhyay, Phys. Lett **B106**, 91 (1981).

[Ba97] A. Bassignani *et al.*, Radiation Measurements Vol. **28**, Issues 1-6, 609 (1997).

[Ba03] H. Baer *et al.*, JHEP **0306**, 054 (2003).

[Ba07a] G. Battistoni *et al.*, Proceedings of the Hadronic Shower Simulation Workshop 2006, Fermilab 6 – 8 September 2006, AIP Conference Proceeding **896**, 31, (2007).

[Ba07b] I. Bavykina, private communication.

[Ba08] V. Barger, W. Y. Keung and G. Shaughnessy, Phys. Lett. **B664**, 190 (2008).

[Ba11] M. Bauer, Ph.D. Thesis in preparation, Eberhard – Karls – Universität Tübingen.

[Be69] J. S. Bell and R. Jackiw Nuovo Cim. **A60**,47 (1969).

[Be81] L .B. Bezrukov and E. V. Bugaev, Yad. Fiz. **33**, 1195 (1981).

[Be85] E. Bellotti *et al.*, INFN/TC – 85/19, (1985).

[Be89a] J. Bernstein *et al.*, Rev. Mod. Phys. **61**, 25 (1989).

[Be89b] P. Belli *et al.*, Il Nuovo Cim. **101A**, 959 (1989).

[Be91] K. G. Begeman, A. H. Broeils, R. H. Sanders, Mon. Not. Roy. Astron. Soc. **249**, 523 (1991).

[Be98] L. Bergström, P. Ullio and J. H. Buckley, Astropart. Phys. **9**, 137 (1998).

[Be00] L. Bergström, Rept. Prog. Phys. **63**, 793 (2000).

[Be03a] C. L. Bennett *et al.*, Astrophys. J. Supp. **148**, 1 (2003).

[Be03b] A. Benoit *et al.*, Astron. Astrophys. **399**, L19, L25 (2003).

[Be04] J. D. Bekenstein, Phys. Rev. **D70**, 083509 (2004).

[Be05a] G. Bertone, D. Hooper, J. Silk, Phys. Reports **405**, 279 (2005).

[Be05b] M. J. Berger *et al.* (2005) XCOM: Photon Cross Section Database (version 1.3). [Online] Available: http://physics.nist.gov/xcom [2010, June 17]. National Institute of Standards and Technology, Gaithersburg, MD.

[Be05c] M. J. Berger *et al.* (2005), ESTAR, PSTAR, and ASTAR: Computer Programs for Calculating Stopping-Power and Range Tables for Electrons, Protons, and Helium Ions (version 1.2.3). [Online] Available: http://physics.nist.gov/Star [2011, Feb 28]. National Institute of Standards and Technology, Gaithersburg, MD.

[Be08a] R. Bernabei *et al.*, Eur. Phys. J. **C56**, (2008).

[Be08b] E. Behnke *et al.*, Science **319**, 933 (2008).

[Be08c] P. Benetti *et al.* (The WARP Collaboration), Astropart. Phys. **28**, 495 (2008).

[Bi67] J. B. Birks, Theory and Practice of Scintillation Counting, Pergamon, 1967.

[Bi87] K. van Bibber *et al.*, Phys. Rev. Lett. **59**, 759 (1987).

[Bi89] K. van Bibber, P.M. McIntyre, D.E. Morris and G.G. Raffelt, Phys. Rev. **D39**, 2089 (1989).

[Bi03] A. Birkedal – Hansen and J.G. Wacker, Phys. Rev. **D69**, 065022 (2004).

[Bi08] C. Bischoff *et al.*, Astrophys. J. **684**, 771 (2008).

[Bl52] J. M. Blatt and V. F. Weisskopf, Theoretical Nuclear Physics, Wiley, 16–19 (1952).

[Bo97] G. Bothun, C. Impey and S. McGaugh, Publ. Astron. Soc. Pac. **109**, 745 (1997).

[Bo98] M. Bolz, W. Buchmüller and M. Plümacher, Phys. Lett. **B443**, 209 (1998).

[Bo03] A. Bottino *et al.*, Phys. Rev. **D68**, 043506 (2003).

[Bo04] S. Boughn and R. Crittenden, Nature **427**, 45 (2004).

[Bo06] M. Bonamente *et al.*, Astrophys. J. **647**, 25 (2006).

[Bo09] M. Boezio *et al.* (The PAMELA Collaboration), New J. Phys. **11**, 105023 (2009).

[Br98] D. Branch, Ann. Rev. Astron. & Astrophys. **36**, 17 (1998).

[Br06b] M. Bradač *et al.*, Astrophys. J. **652**, 937 (2006).

[Br07] J. R. Brown and J. W. Moffat, Mon. Not. Roy. Astron. Soc. **382**, 29 (2007).

[Bu00] T. Buchert, Gen. Relativ. Grav. **32**, 105 (2000).

[Bu01] S. Burles, K. M. Nollett and M. S. Turner, Phys. Rev. **D63**, 063512 (2001).

[Ca63] N. Cabibbo, Phys. Rev. Lett **10**, 531 (1963).

[Ca93] R. Cameron *et al.* (The BFRT Collaboration), Phys. Rev. **D47**, 3707 (1993).

[Ca04] M. J. Carson *et al.*, Astropart. Phys. **21**, 667 (2004).

[Ch88] M. Chen, C. Dionisi, M. Martinez and X. Tata, Phys. Reports **159**, 201 (1988).

[Ch02a] K. M. Cheung and G. Landsberg, Phys. Rev. **D65**, 076003 (2002).

[Ch02b] K. M. Cheung, K.T. Matchev and M. Schmaltz, Phys. Rev. **D66**, 036005 (2002).

[Ch02c] V. Chazal *et al.*, Nucl. Instrum. Methods Phys. Res. **A490**, 334 (2002).

[Ch03] H. C. Cheng and I. Low, JHEP **0309**, 051 (2003).

[Ch06] M. B. Chadwick *et al.*, Nucl. Data Sheets **107**, 2931, (2006).

[Ch08] A. S. Chou *et al.*, Phys. Rev. Lett. **100**, 080402 (2008).

[Ci04] A. Cimatti *et al.*, Nature, **430**, 184 (2004).

[Cl98] B. T. Cleveland *et al.*, Astrophys. J. **496**, 505 (1998).

[Cl06] D. Clowe *et al.*, Astrophys. J. **648**, 109 (2006).

[Co67] S. R. Cole and J. Mandula, Phys. Rev. **159**, 1251 (1967).

[Co01] L. Covi *et al.*, JHEP **0105**, 033 (2001).

[Co05a] A. A. Coley, N. Pelavas and R. M. Zalaletdinov Phys. Rev. Lett. **95** 155102 (2005).

[Co05b] S. Cole *et al.* Mon. Not. Roy. Astron. Soc. **362**, 505 (2005).

[Co06a] C. J. Copi, D. Huterer, D. J. Schwarz and G. D. Starkman, Mon. Not. Roy. Astron. Soc. **367**, 79 (2006).

[Co06b] C. Coppi *et al.*, Nucl. Instrum. Methods Phys. Res. **A559**, 396 (2006).

[Co09] C. Coppi, Quenching Factor Measurements for Cryogenic Dark Matter Detectors, Ph.D. Thesis, Technische Universität München (2009).

[Co10] P. Coyle (The Antares Collaboration), arXiV:1002.0754v1, to be published in Proceedings of the 31^{st} International Cosmic Ray Conference (ICRC), Łódź.

[Cr95] M. Cribier *et al.*, Astropart. Phys. **4**, 23 (1995).

[Cr99] M. Cribier *et al.* (GALLEX Collaboration), Nucl. Phys. **B70**, 284 (1999).

[De99] A. Demetyev *et al.*, Nucl. Phys. Proc. Sup. **B70**, 486 (1999), Nucl. Instrum. Methods Phys. Res. **A314**, 380 (1992).

[Di65] R. H. Dicke *et al.*, Astrophys. J. **142**, 414 (1965).

[Di83] M. Dine and W. Fischler, Phys. Lett. **B120**, 137 (1983).

[Di96] S. Dimopoulos, G. F. Giudice and A. Pomarol, Phys. Lett. **B389**, 37 (1996).

[Di97] M. Dine, Nucl. Phys. Proc. Suppl. **52A**, 201 (1997).

[Di04] C. Dickinson *et al.*, Mon. Not. Roy. Astron. Soc. **353**, 732 (2004).

[Do78] T. W. Donelli *et al.* Phys. Rev. **D18**, 1607 (1978).

[Du09] J. Dunkley *et al.*, Astrophys. J. Suppl. **180**, 306 (2009).

[Ef86] G. Efstathiou and J. R. Bond, Mon. Not. Roy. Astron. Soc. **218**, 103 (1986).

[Ei05] D. J. Eisenstein *et al.*, Astrophys. J. **633**, 560 (2005).

[El84] G. F. R. Ellis, General Relativity and Gravitation, Dordrecht: Reidel, 215 (1984).

[El00] J. Ellis, Phys. Scripta **T85**, 221 (2000).

[El03a] J. R. Ellis *et al.*, Nucl. Phys. **B652**, 259 (2003).

[El03b] J. R. Ellis *et al.*, Phys. Lett. **B565**, 176 (2003).

[Fa05] A. Fasso *et al*, CERN-2005-10, INFN/TC 05/11, SLAC-R-773, (2005).

[Fe97] M. Feast and P. Whitelock, Mon. Not. Roy. Astron. Soc. **291**, 683 (1997).

[Fi96] D. J. Fixsen, *et al.*, Astrophys. J. **473**, 576 (1996).

[Fo60] W. A. Fowler and F. Hoyle, Astrophys. J. **132**, 565 (1960).

[Fo03] P. Fosalba, E. Gaztañaga and F. Castander, Astrophys. J. **597**, L89 (2003).

[Fr01] W. L. Freedman *et al.*, Astrophys. J. **553**,47 (2001).

[Fu98] J. Fukuda *et al.*, (Super – Kamiokande Collaboration), Phys. Lett. **81**, 1562 (1998).

[Ga99] V. N. Gavrin *et al.* (SAGE Collaboration), Nucl. Phys. **B77**, 20 (1999).

[Gi82] L. Giradello and M. Grisaru, Nucl. Phys. **B194**, 65 (1982).

[Gi85] J. A. B. Gibson and E. Piesch, Neutron Monitoring for radiological protection, Technical Reports Series No. 252, IAEA, Vienna (1985).

[Gl04] K. Glazebrook *et al.*, Nature, **430**, 181 (2004).

[Gr66] K. Greisen, Phys. Rev. Lett. **16**, 748 (1966).

[Gr75] R. Grasser, E. Pitt, A. Scharmann and G. Zimmerer, Phys. Status Solidi **B69**, 359 (1975).

[Gr90] K. Griest and M. Kamionkowski , Phys. Rev. Lett. **64**, 615 (1990).

[Gr96] D. Graff and K. Freese, Astrophys.J. **456**, 49 (1996).

[Gu81] A. H. Guth, Phys. Rev. **D23**, 347 (1981).

[Gu83] A. H. Guth and E.J. Weinberg, Nucl. Phys. **B212**, 321 (1983).

[Gu07] V. G. Gurzadyan, C.L. Bianco, A.L. Kashin, H. Kuloghlian and G. Yegorian, Phys. Lett. **A363**, 121 (2007).

[Ha70] E. R. Harrison, Phys. Rev. **D1**, 2726 (1970).

[Ha75] R. Haag, J. T. Lopuszanski and M. Sohnius, Nucl. Phys. **B88**, 257 (1975).

[Ha82] S. W. Hawking, I. G. Moss and J. M. Steward, Phys. Rev. **D26**, 2681 (1982).

[Ha85a] H. E. Haber and G. Kane, Phys. Reports **117**, 75 (1985).

[Ha85b] R. M. Hazen, L.W. Finger and J. W. E. Mariathasan, J. Phys. Chem. Solids **46**, 253 (1985).

[Ha90] L. J. Hall and L. Randall, Phys. Rev. Lett. **65**, 2939 (1990).

[Ha99] P. G. Harris *et al.*, Phys. Rev. Lett. **82**, 904 (1999).

[Ha02] N. W. Halverston *et al.*, Astrophys. J. **568**, 38 (2002).

[Ha09] F. Halzen and D. Hooper, New J. Phys. **11**, 105019 (2009).

[He89] R. Heaton *et al.*, Nucl. Instrum. Methods Phys. Res. **A276**, 529 (1989).

[Hi09] G. Hinshaw *et al.*, Astrophys. J. Suppl. **180**, 225 (2009).

[Ho07a] D. Hooper, D. P. Finkbeiner and G. Dobler, Phys. Rev. **D76**, 083012 (2007).

[Ho07b] O. M. Horn, Simulations of the muon – induced neutron background of the EDELWEISS – II Experiment for Dark Matter Search, Ph.D. thesis, Universität Karlsruhe (2007).

[Hu29] E. P. Hubble, Proc. Nat. Acad. Sci. **15**, 168 (1929).

[Hu74] W. J. Hurd, IEEE Transactions on Computers **C23**,**2**, 146 (1974).

[Hu97] W. Hu and M. White, New Astron. **2**, 323 (1997).

[Hu02] W. Hu and S. Dodelson, Ann. Rev. Astron. & Astrophys. **40**, 171 (2002).

[Hu06] P. Huff, Messung der Lichtausbeute von Rückstoßkernen in $CaWO_4$, Diploma Thesis, Technische Universität München, Max – Plank – Institut für Physik (2006).

[In10] Y. Inoue *et al.*, PoS (IDM2008), 067 (2010).

[Ja99] I. Jack and D. R. T. Jones, Phys. Lett. **B457**, 101 (1999).

[Jo06] W. C. Jones *et al.*, Astrophys. J., **647**, 823 (2006).

[Ka21] T. Kaluza, Sitzungsberichte der Preussischen Akademie der Wissenschaften Physikalisch – mathematischer Klasse, 966 (1921).

[Ka08] G. Kane and S. Watson, Mod. Phys. Lett. **A23**, 2103 (2008).

[Ki79] J. E. Kim, Phys. Rev. Lett. **43**, 103 (1979).

[Ki06] J. Kisiel, Gamma ray background measurements in the underground labs, ILIAS 3^{rd} Annual Meeting, Gran Sasso, March, 2^{nd} (2006).

[Kl26] O. Klein, Zeitschrift für Physik, **37**, 895 (1926).

[Ko73] M. Kobayashi and T. Maskawa, Prog. Theor. Phys. **49**, 652 (1973).

[Ko03] L. V. Koopmans and T. Treu, Astrophys. J. **583**, 606 (2003).

[Ko08] M. Kowalski *et al.* (The Supernova Cosmology Project), Astrophys. J. **686**, 749 (2008).

[Ko09] E. Komatsu *et al.*, Astrophys. J. Suppl. **180**, 330 (2009).

[Kr86] L. M. Krauss and F. Wilczek, Phys. Lett. **B173**, 173 (1986).

[Ku04] C. L. Kuo *et al.*, Astrophys. J. **600**, 32 (2004).

[Le27] G. Lemaître, Annales de la Société Scientifique de Bruxelles, **47**, 49 (1927).

[Le01] A. T. Lee *et al.*, Astrophys. J. **561**, L1 (2001).

[Le05] E. M. Leitch *et al.*, Astrophys. J. **624**, 10 (2005).

[Le06] R. Lemrani *et al.*, Nucl. Instrum. Methods Phys. Res. **A560**, 454 (2006).

[Le07] H. S. Lee *et al.* (The KIMS Collaboration), Phys. Rev. Lett. **99**, 091301 (2007).

[Li82] A. D. Linde, Phys. Lett. **B108**, 389 (1982); **B114**, 431 (1982); Phys. Rev. Lett. **48**, 335 (1982).

[Li09] S. T. Lin (The TEXONO Collaboration), Phys. Rev. **D79**, 061101 (2009).

[LVD94] LVD Collaboration, Nucl. Phys. Proc. Sup. **B35**, 240 (1994).

[Ma99] J. C. Maher *et al.*, Astrophys. J. **512**, 511 (1999).

[Ma04] M. Markevitch *et al.*, Astrophys. J. **606**, 819 (2004).

[Ma07] A. Mahdavi, H. Hoekstra, A. Babul, D. Balam, P. Capak, Astrophys. J. **668**, 806 (2007).

[Mi83] M. Milgrom, Astrophys. J. **270**, 371 (1983).

[Mi02a] A. Miller *et al.*, Astrophys. J. Suppl. **140**, 115 (2002).

[Mi07] V. B. Mikhailin *et al.*, Phys. Rev. **B75**, 184308 (2007).

[Mo93] T. Moroi, H. Murayama, Phys. Lett. **B303**, 289 (1993).

[Mo06] T. E. Montroy *et al.*, Astrophys. J. **647**, 813 (2006).

[Mul80] J. F. Mulligan, Practical Physics: The Production and Conservation of Energy, McGraw-Hill, 1980.

[Mu04] S. Mukhanov, Int. J. Theor. Phys. **143**, 669 (2004).

[Na94] M. Nagasawa and M. Kawasaki, Phys. Rev. **D50**, 4821 (1994).

[Na98] V. Nagirnyi *et al.*, Radiat. Meas. **29**, 247 (1998).

[Na00] J. Najita, G. Tiede, and S. Carr, Astrophys. J. **541**, 977 (2000).

[Ni84] H. P. Nilles, Phys. Reports **110**, 1 (1984).

[Ni00] M. Nikl *et al.*, J. Lumin. **87 − 89**, 1136 (2000).

[Mi02b] V. V. Mikhailin *et al.*, Nucl. Instrum. Methods Phys. Res. **A486**, 496 (2002).

[Ni06] J. Ninković *et al.*, Nucl. Instrum. Methods Phys. Res. **A564**, 567 (2006).

[No09] M. R. Nolta *et al.*, Astrophys. J. Suppl. **180**, 296 (2009).

[Oo32] J. H. Oort, Bull. Astron. Inst. Netherlands **6**, 249 (1932).

[Pa05] N. Padmanabhan *et al.*, Phys. Rev. **D72**, 043525 (2005).

[Pa07] L. Pandola, V. Tomasello and V. Kudryavtsev, Neutron – and muon – induced background in underground physics experiments, ILIAS 4^{th} Annual Meeting, February, 27^{th}, Chambery (2007).

[Pe65] A. A. Penzias and R. Wilson, Astrophys. J. **142**, 419 (1965).

[Pe70] P. J. E. Peebles and J.T. Yu, Astrophys. J. **162**, 815 (1970).

[Pe77a] R. D. Peccei and H. R. Quinn, Phys. Rev. Lett **38**, 1440 (1977).

[Pe77b] R. D. Peccei and H. R. Quinn, Phys. Rev. **D16**, 1791 (1977).

[Pe98] S. Perlmutter *et al.* Astrophys. J. **517**, 565 (1998).

[Pe01] P. J. E. Peebles, Astrophys. J. **557**, 495 (2001).

[Pe03] T. J. Pearson *et al.*, Astrophys. J. **591**, 556 (2003).

[Pf10] S. E. Pfister, Suche nach Dunkler Materie mit dem CRESST – II – Experiment, Ph.D. thesis, Technische Universität München (2010).

[Pr51] H. Primakoff, Phys. Rev. **81**, 899 (1951).

[Pr83] J. Preskill, M. Wise and F. Wilczek, Phys. Lett. **B120**, 127 (1983).

[Pr11] F. Proebst, private communication.

[Ra90] G. G. Raffelt, Phys. Reports **198**, 1 (1990).

[Ra99] L. Randall and R. Sundrum, Phys. Rev. Lett **83**, 3370 (1999).

[Ra06] G. G. Raffelt, J. Phys. **A40**, 6607 (2007).

[Re04] A. C. S. Readhead *et al.*, Astrophys. J. **609**, 498 (2004).

[Re09] C. L. Reichardt *et al.*, Astrophys.J. **694**,1200 (2009).

[Ri88] A. Rindi *et al.*, Nucl. Instrum. Methods Phys. Res. **A272**, 871 (1988).

[Ri98] A. Riess *et al.*, Astron. J., **116**, 1009 (1998).

[Ri09] E. F. Ribas (The CAST Collaboration), arXiv:0912.4222v1, to be published in the proceedings of the 5^{th} Patras Workshop on Axions, WIMPs and WISPs.

[Ro04] L. Roszkowski, Pramana **62**, 389 (2004).

[Ro07] C. Robilliard *et al.*, Phys. Rev. Lett. **99**, 190403 (2007).

[Ro09] K. Rottler, private communication.

[Ru03] J. E. Ruhl *et al.*, Astrophys. J. **599**, 786 (2003).

[Sa67] R. K. Sachs and A. M. Wolfe, Astrophys. J. **147**, 73 (1967).

[Sc10] J. Schmaler, private communication.

[Se03] G. Servant and T. M. Tait, Nucl. Phys. **B650**, 391 (2003).

[Se06] U. Seljak *et al.*, JCAP **0610**, 014 (2006).

[Sh80] M. A. Shifman, A. I. Vainstein and V. I. Zakharov, Nucl. Phys. **B166**, 493 (1980).

[Si72] J. Silk, Nature **215**, 1155 (1972).

[Si85] P. Sikivie, Phys. Rev. **D32**, 2988 (1985).

[Si07a] J. L. Sievers *et al.*, Astrophys. J. **660**, 976 (2008).

[Si07b] P. Sikivie, D. B. Tanner and K. van Bibber, Phys. Rev. Lett **98**, 172002 (2007).

[Si10] B. Singh and J. C. Roediger, Nuclear Data Sheets **111**, 2081 (2010).

[Sm92] G. F. Smoot *et al.*, Astrophys. J. **396**, L1 (1992).

[Sp07] D. N. Spergel *et al.*, Astrophys. J. Suppl. Ser. **170**, 377 (2007).

[St64] P. H. Stelson and F. K. McGowan, Phys. Rev. 133B, 911 (1964).

[St06] G. Steigman, Int. J. Mod. Phys. **E15**, 1 (2006).

[Su70] R. A. Sunyaev and Y. B. Zel'dovich, Astrophysics & Space Science **7**, 3 (1970).

[Su80] R. A. Sunyaev and Y. B. Zel'dovic, Ann. Rev. Astron. Astrophys. **18**, 537 (1980).

[Su84] L. Susskind, Phys. Reports **104**, 181 (1984).

[Ta03] M. Takeda *et al.*, Astropart. Phys. **19**, 447 (2003).

[Ti07] P. Tisserand *et al.*, Astron. & Astrophys. **469**, 387 (2007).

[To08] V. Tomasello, private communication.

[Tr74] M. J. Treadway and R. C. Powell, J. Chem. Phys. **61**, 4003 (1974).

[Tu86] M. S. Turner, Phys. Rev **D33**, 889 (1986).

[Tu99] M. S. Turner in D. Caldwell, The Proceedings of Particle Physics and the Universe (COSMO – 98), A.I.P, Woodbury, NY A.I.P (1999).

[Wa67] R. V. Wagoner, W. A. Fowler, and F. Hoyle, Astrophys. J. **148**, 3 (1967).

[We78] S. Weinberg, Phys. Rev. Lett **40**, 223 (1978).

[We00] S. Weinberg, The Quantum Theory of Fields, Vol. III: Supersymmetry Cambridge University Press, 2000.

[Wh94] M. White, D. Scott and J. Silk, Ann. Rev. Astron. & Astrophys. **32**, 329 (1994).

[Wi78] F. Wilczek, Phys. Rev. Lett **40**, 279 (1978).

[Wi81] E. Witten, Nucl. Phys. **B188**, 513 (1981).

[Wi99] W .B. Wilson *et al.*, Los Alamos National Laboratory Report, LA-13639-MS, 1999.

[Wi07] D. L. Wiltshire, New J. Phys. **9**, 377 (2007).

[Wi08] L. M. Widrow, B. Pym and J. Dubinski, Astrophys. J. **679**, 1239 (2008).

[Wu04] H. Wulandari, J. Jochum, W. Rau and F. von Feilitzsch, Astropart. Phys. **22**, 313 (2004).

[Ya99] M. Yamaguchi, M. Kawasaki and J. Yokoyama, Phys. Rev. Lett. **82**, 4578 (1999).

[Za66] G. T. Zatsepin and V. A. Kuz'min, JTEP Lett **4**, 78 (1966).

[Za92] R. M. Zalaletdinov, Gen. Relativ. Grav. **24**, 1015 (1992).

[Za98] M. Zaldarriaga and U. Seljak, Phys. Rev **D58**, 023003 (1998).

[Za06] G. Zaharijas and D. Hooper, Phys. Rev. **D73**,103501 (2006).

[Ze72] Y. B. Zel'dovich, Mon. Not. Roy. Astron. Soc. **160**, 10 (1972).

[Zh80] A. R. Zhitnitsky, Sov. J. Nucl. Phys. **31**, 260 (1980).

[Zw33] F. Zwicky, Helv. Phys. Acta **6**, 110 (1933).

Danksagung

An erster Stelle möchte ich Prof. Dr. Josef Jochum dafür danken, mir die Gelegenheit gegeben zu haben diese Arbeit am Physikalischen Institut anfertigen zu können.

Dr. Franz Pröbst will ich an dieser Stelle besonders für sein Engagement für das CRESST – II Experiment danken, die Diskussionen und Gespräche mit ihm waren mir ein wichtiger Ansporn bei der Auswertung der Simulationsergebnisse.

Dr. Walter Potzel danke ich für sein Fragen zu meinen Simulationen, die mir sehr geholfen haben, die Bedeutung der Simulationen für die Analyse des Experimentes zu begreifen.

Prof. Dr. Heinz Clement und Prof. Dr. Peter Grabmayr möchte ich für die Diskussionen und ihrer Rat danken, den sie mir gegeben haben.

Prof. Dr. Goennenwein und Prof. Dr. Günter Staudt möechte ich dafür danken, mir bei meinen kernphysikalischen Fragen der Kernphysik wertvolle Hilfe gegeben zu haben.

Meinen zahlreichen Kollegen am Physikalischen Institut:
Michael Bauer, Gerhard Deuter, Dennis Dietrich, Arthur Erhard , Raphael Falkenstein, Kai Freund, Daniel Greiner, Alexander Hegai, Thorsten Hehl, Marcel Kimmerle, Markus Knapp, Claudia Oswaldt, Florian Ritter, Markus Roehling, Klemens Rottler, Christoph Sailer, Christopher Schmitt, Christian Strandhagen und Igor Usherov
verdienen meinen aufrichtigen Dank für ihre Hilfe, nicht nur in physikalischen Fragen. Desweiteren möchte ich mich fuer die Diskussionen in der Kaffeerunde bedanken.

Besonderer Dank gilt Dr. Carlo Bucci für seine Hilfe während der CRESST Schichten am LNGS.

Insbesondere möchte ich an dieser Stelle meiner Studienkollegin Petra Vergien danken.

Desweiteren gilt mein aufrichtiger Dank:

Den CRESSTlern an der TU München:
Chiara Coppi, Christian Cziemniak, Christian Isaila, Jean – Côme Lanfranchi, Sebastian Pfister, Sabine Roth und insbesondere Raimund Strauss.

Den CRESSTlern am MP für Physik in München:
Patrick Huff, Federica Petricca, Karoline Schäffner, Wolfgang Seidel und Jens Schmaler.